

Kinetics and Mechanism of Charge Carrier Transfer Reactions at TiO₂ Nanoparticles: Stopped-Flow and Laser Flash Photolysis Studies

Von der Naturwissenschaftlichen Fakultät
der Gottfried Wilhelm Leibniz Universität Hannover
zur Erlangung des Grades

Doktorin der Naturwissenschaften

Dr. rer. nat.

genehmigte Dissertation

von

M. Sc. Hanan Hussein Amin Mohamed

geboren am 24. Dezember 1977 in Gharbia, Ägypten

2011

Referent: Prof. Dr. Thomas Scheper

Korreferent: Prof. Dr. Jürgen Caro

Tag der Promotion: 30.05.2011

Erklärung zur Dissertation

Hiermit erkläre ich, das ich meine vorliegende Dissertation mit dem Titel „ **Kinetics and Mechanism of Charge Carrier Transfer Reactions at TiO₂ Nanoparticles: Stopped-Flow and Laser Flash Photolysis Studies**” selbstständig verfasst und die benutzten Hilfsmittel und Quellen sowie gegebenenfalls die zu Hilfeleistungen herangezogenen Institutionen vollständig angegeben habe.

Die Dissertation wurde nicht schon als Masterarbeit, Diplomarbeit oder andere Prüfungsarbeit verwendet.

Hannover, 23.03. 2011

M. Sc. Hanan Hussein Amin Mohamed

Acknowledgements

I would like to express my deepest gratitude to my supervisor Prof. Dr. Detlef Bahnemann, who accepted me in the group of Photocatalysis and Nanotechnology in March 2007. His patience and confidence were very important for me to develop my own thoughts, and his attitude towards science and his open-mindedness have greatly influenced my perception about scientific research. He is behind this research project and it has happened under the best conditions.

Grateful thanks are due to Prof. Dr. Thomas Scheper for accepting me as a PhD student at the Technical Chemistry Institute and for agreeing to act as the referee of my thesis.

My grateful thanks also go to Prof. Dr. Jürgen Caro for his very kind agreement to be the co-referee of my thesis.

I would like to thank all the members of the group of Photocatalysis and Nanotechnology, and the entire Technical Chemistry Institute and to express my thanks to working group of Prof. Thomas Scheper.

I would like to express my sincere appreciation to Dr. Ralf Dillert for numerous scientific discussions.

I thank PD Dr. Armin Feldhoff at Physical Chemistry Institute, Hannover University, for TEM measurements and Dr. Lars Robben at Institut of Mineralogy, Hannover University, for XRD measurements.

I am very grateful for the support of Prof. J.-E. Moser, who granted me access to all the outstanding research at the Institute of Chemical Sciences & Engineering at École Polytechnique Fédérale de Lausanne (EPFL). I am grateful to him for his fruitful scientific discussions, support, motivation and sharing his experiences, what led me to a broader understanding of ultrafast phenomena, and to his great assistance in the laboratory during my short scientific missions in his work group (July 2008 and July 2010). I express my thank to the group of Prof. J.-E. Moser for their help in the experimental setup and for their numerous scientific discussions.

I want to sincerely thank the Egyptian Ministry of Higher Education for granting me a doctoral scholarship. I am grateful also to the Department of Cultural and Education Mission of the Arab Republic of Egypt in Berlin for the removal of Finanziaal problemes and administrative difficulties. I thank the Chemistry Department, Faculty of Science, Helwan University for granting me a leave of absence.

I am very grateful to my dear parents, my sisters and brother for their support and encouragement in the last four years of ups and downs in my life. To my husband Dr. Tamer Ezzat Youssef for his support and encouragement. To my lovely kids, Youssef, Sondos and Mohannad for being the sunshine in my life.

Abstract

Photocatalytic applications employing UV irradiated TiO₂ nanoparticles for the decontamination of organic compounds as well as for the detoxification of hazardous metal ions in wastewater have become a mature field of study during the past decades. Upon band gap excitation of semiconducting TiO₂ particles electrons are promoted to their conduction band with the simultaneous generation of holes in the valence band both of which will be consumed in the photocatalytic reactions.

A fundamental understanding of the dynamics of the charge carrier transfer at TiO₂ nanoparticles is of crucial importance for the understanding and industrialization of photocatalytic reactions as well as for the rational design of photocatalytic systems. During the last decades, much effort was devoted to the study of the kinetics and the mechanistic details of the interfacial electron transfer processes at the TiO₂/water interface using the laser flash photolysis and pulse radiolysis techniques.

The work included in this thesis focuses on the study of kinetics and mechanism of charge carrier transfer from TiO₂ to a variety of acceptors utilizing two extremely useful techniques: fast mixing stopped flow technique and laser flash photolysis technique. For both techniques, nanosized TiO₂ particles have been self prepared with very small particle sizes (2-5 nm) and characterized by UV-vis spectroscopy, XRD and TEM.

This thesis is broken down into several chapters. The first chapter discusses some basic theoretical considerations about the different topics relevant to this work. The attention was drawn to semiconductor photochemistry; the focus was put on the photochemical behavior of band gap of metal oxides. And finally electron transfer dynamics in solution and at interfaces were reviewed.

The second chapter describes the materials used, the experimental methods used in the preparation of TiO₂ nanoparticles as well as of colloidal metal nanoparticles, the analytical method and finally the experimental description of the fast kinetic techniques that are used in this thesis.

The third chapter of this thesis presents and discusses the results of the study of the electron transfer dynamics at TiO₂ nanoparticles utilizing for the first time the simple and facile stopped flow technique. This study focuses on the multiple electron transfer processes from TiO₂ nanoparticles to a variety of electron acceptors. To perform these stopped flow studies, the electrons were stored on the TiO₂ nanoparticles by UV (A) photolysis of deaerated

aqueous solutions of the nanosized TiO₂ in the presence of methanol as hole scavenger. The photolysis produced the blue color of surface/bulk trapped TiO₂ electrons. Moreover, the optical properties of the stored electrons in the TiO₂ nanoparticles have been studied in detail following the UV (A) photolysis.

The electron acceptors methyl viologen dication (MV²⁺) and benzyl viologen dication (BV²⁺) have been chosen as models for the one electron acceptor process. The one electron reduction resulting in the formation of the viologen radical (V^{•+}) has been observed. Furthermore, the consecutive electron transfer from the formed viologen radicals to H⁺/H₂O forming H₂ in the presence of metal catalyst has also been examined.

The multi-electron reduction of common electron acceptors that are often present in photocatalytic system such as O₂ and H₂O₂ was investigated. The multi-electron reduction of NO₃⁻ has also been investigated and the reaction mechanism was discussed.

The kinetics of transition metal ions reduction, such as Mn²⁺, Zn²⁺, Cd²⁺, Cu²⁺, Hg²⁺, Ag⁺ and Au³⁺ has been studied after mixing with the stored TiO₂ electrons. The mechanism of the growth of metal clusters on the surfaces of TiO₂ particles was discussed in details based on the kinetic data, XRD and TEM measurements of the resulted nanocomposite. Furthermore, the kinetics of hydrogen production after the reaction of excess TiO₂ electrons with H⁺/H₂O in the presence of metal deposits has been studied under varied conditions of different pH and different metal loading.

In the fourth chapter the results of a laser flash photolysis study have been presented. Laser flash photolysis measurements were carried out in order to investigate the fast electron transfer processes that could not be detected by the stopped flow method due to its time resolution limitation and to compare kinetics of some reactions studied using stopped flow method. The dynamics of the reaction of the trapped holes through the reaction with phenolic compounds in presence of metal ions as electron scavenger have also been studied.

Keywords: TiO₂ nanoparticles, stopped flow, laser flash photolysis, charge carrier dynamics.

Zusammenfassung

Photokatalytische Anwendungen, die mit UV-Licht bestrahlte TiO_2 -Nanopartikel für die Dekontamination von organischen Verbindungen sowie für die Entgiftung von gefährlichen Metallionen im Abwasser verwenden, haben sich in den letzten Jahrzehnten zu einem wichtigen Forschungsgebiet entwickelt. Durch Anregung der Bandlücke von TiO_2 -Partikeln werden Elektronen in das Leitungsband angehoben und gleichzeitig Löcher im Valenzband erzeugt. Beide Spezies werden in der photokatalytischen Reaktion verwendet.

Ein grundlegendes Verständnis der Dynamik der Ladungsträgerübertragung an TiO_2 -Nanopartikel ist von entscheidender Bedeutung sowohl für das Verständnis und die Industrialisierung der photokatalytischen Reaktionen als auch für das rationale Design von photokatalytischen Systemen. In den letzten Jahrzehnten wurden viele Anstrengungen unternommen, um die Kinetik und die mechanistischen Details der Elektronen-Transfer-Prozesse an der Grenzfläche zwischen TiO_2 und Wasser mit Hilfe von Laserblitzphotolyse- und Pulsradiolyse-Techniken zu untersuchen.

Der Schwerpunkt dieser Arbeit ist die Untersuchung der Kinetik und des Mechanismus des Ladungsträger-Transfers von TiO_2 zu einer Vielzahl von Akzeptoren unter Verwendung von zwei äußerst nützlichen Techniken: der fast-mixing-stopped-flow-Technik und der Laserblitzphotolyse. Für beide Techniken werden nanoskalige TiO_2 -Partikel mit sehr kleinen Partikelgrößen (2-5 nm) selbst hergestellt und durch UV-Vis-Spektroskopie, XRD- und TEM-Messungen charakterisiert.

Diese Arbeit ist in mehrere Kapitel aufgeteilt. Das erste Kapitel beschäftigt sich mit einigen grundlegenden theoretischen Überlegungen zu den verschiedenen Themen, die für diese Arbeit relevant sind. Der Schwerpunkt liegt auf der Halbleiter-Photochemie, insbesondere auf dem photochemischen Verhalten der Bandlücke von Metalloxiden. Abschließend wird die Elektronentransfer-Dynamik in Lösung und an Grenzflächen behandelt.

Das zweite Kapitel beschreibt die verwendeten Materialien, die experimentellen Methoden bei der Herstellung von TiO_2 -Nanopartikeln und kolloidalen Metall-Nanopartikeln, die analytischen Methoden und schließlich die experimentellen Techniken zur Untersuchung der Kinetik.

Das dritte Kapitel dieser Arbeit präsentiert und diskutiert die Ergebnisse der Untersuchungen zur Elektronentransfer-Dynamik an TiO_2 -Nanopartikeln unter Verwendung der einfachen und leicht auszuführenden stopped-flow-Technik. Diese Untersuchungen konzentrieren sich auf Multi-Elektronen-Transfer-Prozesse von TiO_2 -Nanopartikeln auf eine Vielzahl von

Elektronenakzeptoren. In stopped-flow-Untersuchungen wurden die Elektronen auf TiO₂-Nanopartikeln durch Photolyse mit UV(A)-Licht von entgasten wässrigen Lösungen des nanoskaligen TiO₂ in Gegenwart von Methanol als Lochfänger gespeichert. Die Photolyse erzeugt die blaue Farbe von an der TiO₂-Oberfläche gefangenen Elektronen. Darüber hinaus sind die optischen Eigenschaften der gespeicherten Elektronen im TiO₂-Nanopartikel nach der UV(A)-Photolyse im Detail untersucht worden.

Die Elektronen-Akzeptoren Methylviologen-Dikation (MV²⁺) und Benzylviologen-Dikation (BV²⁺) sind als Modell Substanzen für den Ein-Elektronen-Akzeptor-Prozess ausgewählt worden. Die Ein-Elektronen-Reduktion, die zur Bildung des Viologen-Radikals (V^{•+}) führt, ist beobachtet worden. Darüber hinaus wurde der darauffolgende Elektronentransfer von gebildeten Viologen-Radikalen auf H⁺/H₂O unter Bildung von H₂ in Gegenwart von Metall-Katalysatoren untersucht.

Die Multi-Elektronen-Reduktion von herkömmlichen Elektronenakzeptoren, die wie z. B. O₂ und H₂O₂ oft in photokatalytischen Systemen vorhanden sind, wurde untersucht. Die Multi-Elektronen-Reduktion von NO³⁻ wurde ebenfalls untersucht und der Reaktionsmechanismus diskutiert.

Die Kinetik der Reduktion von Übergangsmetallionen, wie z. B. Mn²⁺, Zn²⁺, Cd²⁺, Cu²⁺, Hg²⁺, Ag⁺ und Au³⁺ wurde nach dem Mischen mit den gespeicherten TiO₂-Elektronen untersucht. Der Mechanismus des Wachstums von Metall-Clustern auf den Oberflächen der TiO₂-Partikel wurde im Detail auf der Grundlage der kinetischen Daten, sowie XRD- und TEM-Messungen der resultierenden Nanokomposite diskutiert. Außerdem wurde die Kinetik der Wasserstoff-Produktion nach der Reaktion von überschüssigem TiO₂-Elektronen mit H⁺/H₂O in Gegenwart von Metall-Ablagerungen bei verschiedenen pH-Werten und verschiedenen Metall-Beladungen untersucht.

Im vierten Kapitel werden die Ergebnisse der Laserblitzphotolyse-Studie vorgestellt. Laserblitzphotolyse-Messungen wurden durchgeführt, um die schnellen Elektronen-Transfer-Prozesse, die durch stopped-flow aufgrund seiner zeitlich begrenzten Auflösung nicht detektiert werden konnten, zu untersuchen. Die Dynamik der Reaktion der eingefangenen Löcher durch die Reaktion mit Phenol-Verbindungen in Gegenwart von Metall-Ionen als Elektronen Fänger wurde ebenfalls untersucht.

Stichworte: TiO₂ Nanopartikel, stopped-flow, Laserblitzphotolyse, Ladungsträger Dynamik.

Contents

1. Theoretical Considerations	1
1.1. Nanomaterials	1
1.1.1. Semiconductor Nanoparticles.....	2
1.1.2. Metal Nanoparticles	6
1.1.3. Metal/ Semiconductor Nanoparticles Composite System	8
1.2. Photocatalysis.....	9
1.2.1. Semiconductor Photocatalysis	11
1.2.1.1.The Semiconductor–Electrolyte Interface in the Absence of Redox Systems	11
1.2.1.2.Semiconductor–Electrolyte Interface under Illumination	12
1.2.1.3.Light Induced Charge Transfer at Semiconductor Particles	13
1.2.2. Kinetic Aspects	15
1.2.2.1.Trapped versus Free Charge Carriers in Semiconductor Particles	15
1.2.2.2.Dynamics of Charge Carrier Trapping and Recombination.	16
1.2.2.3.Dynamics of Interfacial Charge Transfer Processes at Semiconductor Nanoparticles	17
1.2.2.4.Charge Carrier Transfer Reactions at Semiconductors Nanoparticles	18
1.3. Aims of the Thesis	23
2. Materials, Analytical and Experimental Methods	25
2.1. Materials	25
2.2. Preparation of TiO ₂ Nanoparticles	25
2.3. Preparation of Noble Metal Nanoparticles.....	26
2.4. Analytical Methods	27
2.4.1. Steady State UV–vis Absorption Measurements	27
2.4.2. X–Ray Diffraction (XRD) Measurements	27
2.4.3. Transmission Electron Microscopy (TEM) Measurements	27
2.4.4. Gas Chromatography (GC) Analysis	27
2.4.5. High Performance Ion Chromatography (HPIC) Analysis	28
2.4.6. Dissolved O ₂ Concentration Measurements	28
2.4.7. H ₂ Gas Measurements.....	28
2.5. Fast Kinetic Measurements	28
2.5.1. Stopped Flow Method	28
2.5.2. Laser Flash Photolysis Method	31

3. Stopped Flow Study	33
3.1. Characterization of TiO ₂ Nanoparticles.....	33
3.2. Storing of Electrons on TiO ₂ Nanoparticles	35
3.3. Stopped Flow Investigations	42
3.3.1. Spectrum of Stored TiO ₂ Electrons	42
3.3.2. One Electron Reduction of Viologen Compounds and Ensuing Electron Transfer from the Formed Viologen Radicals to the Surface of Metal Nanoparticles	43
3.3.3. Multi–Electron Reduction of Common Electron Acceptors Employed in Photocatalytic System	56
3.3.3.1. Reaction of e ⁻ _{TiO₂} with O ₂ and H ₂ O ₂	56
3.3.3.2. Reaction of e ⁻ _{TiO₂} with Nitrate Ions	60
3.3.4. Reduction of Transition Metal Ions	65
3.3.4.1. Reduction of Toxic Metal Ions.....	65
a. Reaction of e ⁻ _{TiO₂} with Cu ²⁺	65
b. Reaction of e ⁻ _{TiO₂} with Hg ²⁺	70
c. Reaction of e ⁻ _{TiO₂} with Cd ²⁺	73
d. Reaction of e ⁻ _{TiO₂} with Zn ²⁺ and Mn ²⁺	76
3.3.4.2. Reduction of Noble Metal Ions	78
a. Reaction of e ⁻ _{TiO₂} with Ag ⁺	78
b. Reaction of e ⁻ _{TiO₂} with Au ³⁺	94
3.3.5. Relation between Interfacial Electron Transfer Rate Constants and Driving Force	108
3.3.6. Reaction of e ⁻ _{TiO₂} with H ⁺ /H ₂ O in the Presence of Noble Metal Catalysts	110
4. Laser Flash Photolysis Study	118
4.1. Primary Processes upon Band Gap Irradiation.....	119
4.1.1. Irradiation of TiO ₂ Particles in the Absence of Hole and Electron Scavengers .	119
4.1.2. Irradiation of TiO ₂ Particles in the Absence of Hole Scavengers and in the Presence of Electron Scavengers	120
4.2. Reactions of Photogenerated TiO ₂ Electrons with Methyl Viologen Dication	123
4.3. Photo- Induced Simultaneous Conversion of Phenolic Compounds and Reduction of Heavy Metal Ions in Aqueous Suspension of TiO ₂ Nanoparticles	125

5. Conclusions	132
6. References.....	135
7. Appendix	151
7.1. Derivation of the Autocatalytic Model	151
7.2. List of Abbreviations and Symbols.....	153
7.3. List of Tables.....	156
7.4. List of Figures	157
7.5. Curriculum Vitae.....	166

1. Theoretical Considerations

1.1. Nanomaterials

The nano world is a particular domain where the dimensions of the materials reach the nanometer regime, which causes a dramatic change of their behavior, characteristics and physical-chemical properties with respect to those of bulk materials.^{1, 2} Nanomaterials include all materials within a large distribution of sizes, ranging from a nanometer to as large as hundreds of nanometres. The term "nanotechnology" has evolved over the years via a terminology drift to describe "anything smaller than microtechnology," and other objects that are nanoscale in size, but not referring to mechanisms that have been purposefully built from nanoscale components. This evolved version of the term is more properly labelled "nanoscale bulk technology," while the original meaning is now more properly labelled "molecular nanotechnology" (MNT), or "nanoscale engineering," or "molecular mechanics," or "molecular machine systems," or "molecular manufacturing". Nanotechnology is considered as the technology of the 21st century, following the microtechnology development and now, even if we do not realize it yet, these materials are already taking a remarkable part in our everyday life. The interesting properties of these materials make them attractive in a variety of applications like light-emitting diode³⁻⁵ photovoltaic devices,⁶ lasers,⁷ optical memory,^{8, 9} miniaturized devices, and as fluorescent probes in biology.¹⁰⁻¹⁴ Nanoparticles (NP) can be considered as single crystals with a typical size of a few nanometers. They still contain hundreds to thousands of atoms. Due to the size quantization effect, these nanoparticles preserve some bulk material properties but, in addition, they exhibit more interesting properties. From the technological point of view, the main reason for studying nanostructured materials is the ease of tuning the optical and the electronic properties gradually by varying the particle size and shape. Nanoparticles can be prepared by different methods, and occur in various forms, including powder state materials, solid state, thin films and solutions. Nanoparticles possess a variety of properties depending on the chemical composition and size. The chemical structure of the nanoparticles can be very different. Well investigated materials include:

- a) Metals: gold,¹⁵ silver,¹⁶ palladium¹⁷
- b) Semiconductors:
 - i) Oxides: TiO₂,¹⁸ ZnO¹⁹
 - ii) II-V compounds (CdSe, CdS, CdTe, ZnSe, ZNS).²⁰⁻²³

- iii) III-V compounds (GaAs, GaP, InAs, InP).²⁴⁻²⁸
- iv) IV-VI compounds (PbS, PbSe, PbTe).²⁹

On this scale, many of the atoms are still located on the surface, or one layer removed from the surface, as opposed to the interior. The interface between substances is just now beginning to be understood. New properties are observed on this scale due to the interface that is not observed in the bulk or individual atoms. Since the properties depend on the size of the structure, instead of just the nature of the material, reliable and continual change can be achieved using a single material.

1.1.1. Semiconductors Nanomaterials

To build-up an overall picture of the mechanistic and kinetic study of the photocatalytic reactions it is essential to give an introduction to semiconductor physics.

a. Band Structure of Colloidal Semiconductors

Unlike in molecular systems, the energy levels of semiconductors are so dense that they form broad energy bands instead of discrete molecular orbital energy levels. The band theory of materials explains qualitatively the difference between these types of materials. Electrons occupy energy levels from the lowest energies upwards. However, some energy levels are forbidden because of the wave like properties of atoms in the material. The allowed energy levels tend to form bands. The highest filled level at $T = 0$ K is known as the *valence band* (VB). Electrons in the valence band do not participate in the conduction process. The first unfilled level above the valence band is known as the *conduction band* (CB). In metals, there is no forbidden gap; the conduction band and the valence band overlap, allowing free electrons to participate in the conduction process. Insulators have an energy gap that is far greater than the thermal energy of the electron, while in bulk semiconductor, due to the large number of atoms, the distance between energy levels is very small and for all practical purpose the energy levels can be described as continuous. In a bulk semiconductor the band gap is fixed; whereas in a quantum dot nanoparticle the band gap varies with the size of the nanoparticle. Figure 1.1 shows the differences between molecules, semiconductors nanoparticles (Quantum Dots) and bulk semiconductors in terms of the how the energy bands are separated.

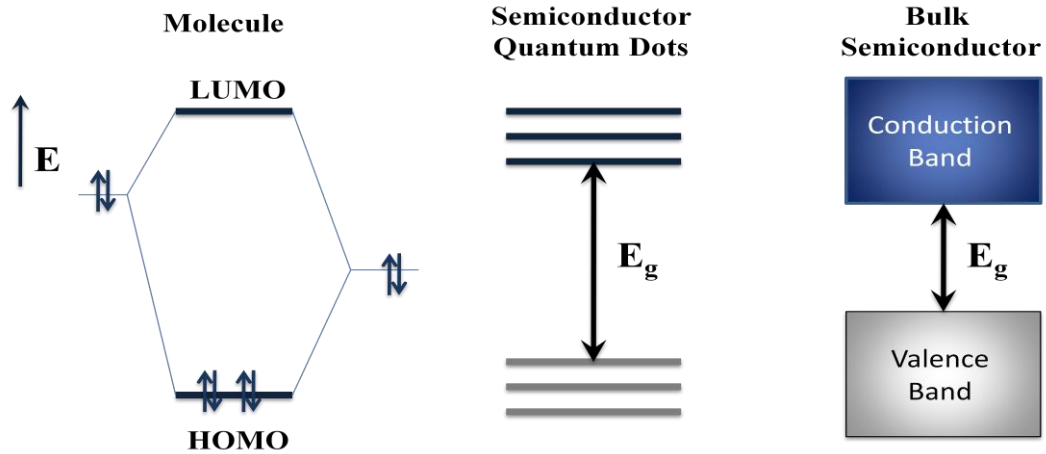


Figure 1.1: The separation of the energy bands in the molecular system, semiconductor quantum dots and bulk semiconductors.

b. Optical and Electronic Properties of Semiconductor Nanoparticles

The most pronounced property of semiconductor nanoparticles is the large change observed in their optical spectra with changing size.

Optical Absorption of Colloidal Semiconductor Particles: Mie Theory

Semiconductors absorb light below a threshold wavelength λ_g , the fundamental absorption edge, which is related to the band gap energy (E_g) via

$$\lambda_g(\text{nm}) = 1240/E_g(\text{eV}) \quad (\text{Eq. 1.1})$$

Within the semiconductor, the excitation of light follows the exponential law

$$I = I_0 \exp(-\alpha l) \quad (\text{Eq. 1.2})$$

where I is the light intensity after it passes through the sample and I_0 is the initial light intensity, l is the penetration of light and α is the reciprocal absorption length.

Optical Absorption of very Small Particles: Quantum Size Effects

At very small particle radii, deviations from the Mie equation occur which are due to the size quantization effects. In very small colloidal particles, the energy levels are quantized, the spacing between adjacent states being of the order of E_F/N , where E_F is the Fermi energy and N is the number of atoms in one particle. Since E_F has a value of a few eV, the energy levels in a particle containing about 10^4 atoms are about 10^{-4} eV. This quantization of states produces a number of anomalies in the properties of the particles, including their optical absorption. This interesting phenomenon has been addressed with success using the effective mass model. As mentioned earlier, in bulk semiconductors, light excitation results in the

formation of electron–hole pairs, which experience a Coulomb interaction and can form excitons with usually small binding energy (<0.03 eV) and large radius. The exciton radius can be calculated based on the Bohr radius of an electron in an H atom modified by introducing the dielectric constant of the semiconductor and its reduced effective mass m^* with the latter being given by

$$m^* = \left(\frac{1}{m_e^*} + \frac{1}{m_h^*} \right)^{-1} \quad (\text{Eq. 1.3})$$

Using a “particle in a box” model with an infinite potential drop at the wall as the boundary condition, and taking into account that the exciton consists of an electron– hole pair, the Schrödinger equation can be solved yielding the energy of the lowest excited state^{30, 31}, i.e., the lower edge of the conduction band, as

$$E(R) = E_g + \frac{h^2}{8m_0 m^* R^2} - \frac{1.8e^2}{\epsilon R} \quad (\text{Eq. 1.4})$$

in which m_0 is the electron mass in vacuum. According to (Eq. 1.4), when a semiconductor has a reduced effective mass significantly smaller than the free electron mass, a large variation of its band gap can be expected. Examples of such semiconductors are given: CdS ($m_e^* = 0.21 m_0$, $m_h^* = 0.80 m_0$), CdSe ($m_e^* = 0.13 m_0$, $m_h^* = 0.25 m_0$), GaAs ($m_e^* = 0.067 m_0$, $m_h^* = 0.082 m_0$) and ZnO ($m_e^* = 0.24 m_0$, $m_h^* = 0.48 m_0$).^{19, 32} There are, however, semiconductors with larger effective mass due to which quantization does only occur once particle sizes reach the molecular regime, e.g., in small clusters. One example is TiO₂ which has been the most intensively studied photocatalyst materials in the past decades. Experimentally, TiO₂ particles synthesized with an average size between 5 and 20 nm were confirmed to exhibit the bandgap properties of the bulk solid. However, when the TiO₂ particle size is controlled below 3 nm (i. e., corresponding to clusters consisting of a few hundred TiO₂ molecules), a quantum size effect could also be identified indicating a band gap increase of ~0.25 eV.¹⁸ To precisely explore the quantum size effect, it should be emphasized that the band gap shifts can only be measured with sufficient precision employing colloidal suspensions possessing a sufficiently narrow size distribution. Besides dispersed particles, techniques have also been available for fabrication of semiconductor films consisting of nanocrystalline particles.³² Such films may exhibit similar quantum-size effects as individual particles, depending on the effective mass of the semiconductor as just described. Accompanying the band gap widening due to reduced particle size, electrons at the lower

edge of the conduction band and holes at the upper edge of the valence band then possess higher negative and positive potentials, respectively. In consequence, electrons and holes can be expected to have a higher reduction and oxidation power, respectively, in such quantized particles.

c. Band Edge Positions

In Figure 1.2 band gap energies and band edge positions are given for a number of semiconductors in contact with aqueous electrolytes at pH 1. The knowledge of the band edge position is particularly useful in photocatalysis. Figure 1.2 includes the standard potential for several redox couples, which indicate the thermodynamic limitations of the photoreactions that can be carried out with the charge carriers. For example, if the reduction of the species has to be performed, the conduction band position of the semiconductor has to be positioned above the redox level. Note that the ordinate presents internal and not free energy. The free energy of an electron-hole pair is smaller than the band gap energy due to the translational entropy of the electrons and holes in the conduction and valence band, respectively. The free energy of the charge carrier generated by photoexcitation of semiconductors is directly related to their chemical potential.³³

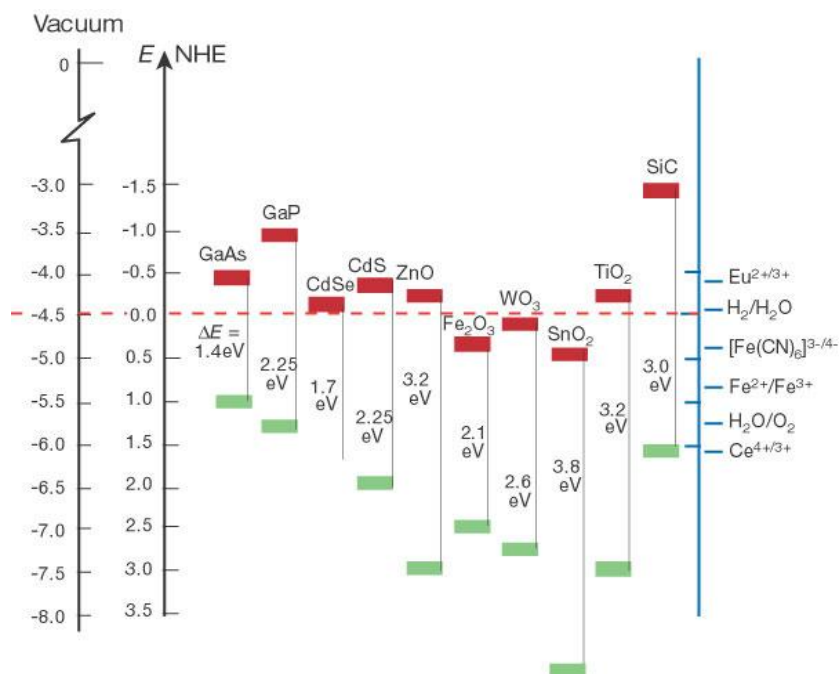


Figure 1.2: Band edge position of several semiconductors in contact with aqueous electrolyte at pH 1. The lower edge of the conduction band (red color) and upper edge of the valence band (green color) are presented along with the band gap in electron volts. The energy scale is indicated in electron volts using either the normal hydrogen electrode (NHE) or the vacuum level as a reference.³³

1.1.2. Metal Nanoparticles

In the seventeenth century, “Purple of Cassius”, a colloid of gold particles, became a popular colorant of glasses. As early as the sixteenth century, the darkening of silver compounds by light (forming silver particles) was known. The nature of these colloids remained unclear, until Faraday realized that the gold colloids he studied contained small metallic particles, which he called divided metals.³⁴ In recent years, the term “nanoparticle” has evolved. Additionally, a colloid implies that the particles are dispersed in a medium, and do not separate on long standing. The term cluster is usually used for small nanoparticles that have well-defined composition and surface structure. There has been steady progress in understanding the nature and properties of nanoparticles, especially during the last two decades. Many reviews have been published on general properties and structures of clusters and colloids.³⁵⁻⁴² Nanoparticles cannot simply be treated as minute blocks of a metal, as implied by the term divided metals. In bulk metals, the large density of states at the Fermi level forms a conduction band of continuous energy levels. However, as the particle size decreases, the valence electrons become confined, and hence, discrete energy levels occur. This phenomenon is called the size induced metal-insulator transition. It is a gradual change that occurs over a range of sizes, typically, at ambient temperature, clusters of 13 atoms are non-metallic, while clusters of 309 atoms and larger show distinct bulk metal properties.³⁶ The metal-insulator transition is readily observed through changes in electronic, optical and catalytic properties. Generally, the loss of metallic character also results in loss of catalytic activity.⁴³ The magic numbers of nuclearity (for gold nanoparticles), i.e. 13, 55, 147, 309, 561 provide energetically favorably geometries associated with closed-shell structures, resulting in a sequential series of particle sizes centered around the magic numbers.⁴¹ The fraction of surface atoms increases dramatically with decreasing particle size. A nanoparticle of 3 nm would have 45% of the atoms on the surface, compared to 76% for a 1 nm particle. Surface atoms play an especially important role in catalysis, as the reaction takes place at the surface of the particle. Furthermore, larger surface area increases the relative contribution of the surface energy, and therefore the thermodynamic stability is decreased with decreasing particle size. In nucleation studies, this phenomenon is observed as nucleation overpotential. The properties of metal nanoparticles gradually change from those of bulk material to molecular with decreasing particle size. In the intermediate range, materials with novel properties, exhibiting characteristics typical for both molecular and bulk materials are found. These materials are used to bridge the gap between the macroscopic and the microscopic world in many applications. However, applications that benefit from nano-properties require

particles with well-defined size, shape and surface properties. The greatest obstacle for the implementation of nano-devices today is the lack of techniques for mass production and assembly of nanoparticles. Neither conventional methods of controlling bulk materials nor common chemical synthetic methods are suitable for nanomaterials. These require a delicate balance between the physical forces, usually defined by their surface properties that determine their behavior. The two main approaches for building nano-devices are the “top down” and “bottom up”. In the former, nano-devices are built by miniaturization of conventional techniques, such as lithography. In the latter, nanoparticles are used as building blocks, which are assembled in a controlled fashion. The color of metal nanoparticles is due to the collective oscillation of the electrons in the conduction band, known as the surface plasmon oscillation.

Origin of Surface Plasmon Resonance

Free electrons in the metal (d electrons in silver and gold) travel through the material. The mean free path in gold and silver is ~50 nm. In particles smaller than ~50 nm, no scattering is expected from the bulk. This means interactions with the surface dominate. When the wavelength of light is much larger than the nanoparticle size it sets up standing resonance conditions as represented in Figure 1.3. Light in resonance with the surface plasmon oscillation causes the free-electrons in the metal to oscillate. As the wave front of the light passes, the electron density in the particle is polarized to one surface and oscillates in resonance with the light frequency causing a standing oscillation. The resonance condition is determined from absorption and scattering spectroscopy and is found to depend on the shape, size, and dielectric constants of both the metal and the surrounding material. This is referred to as the surface plasmon resonance, since it is located at the surface. As the shape or size of the nanoparticle changes, the surface geometry changes, causing a shift in the electric field density on the surface. This causes a change in the oscillation frequency of the electrons, generating different cross-sections for the optical properties including absorption and scattering.⁴²

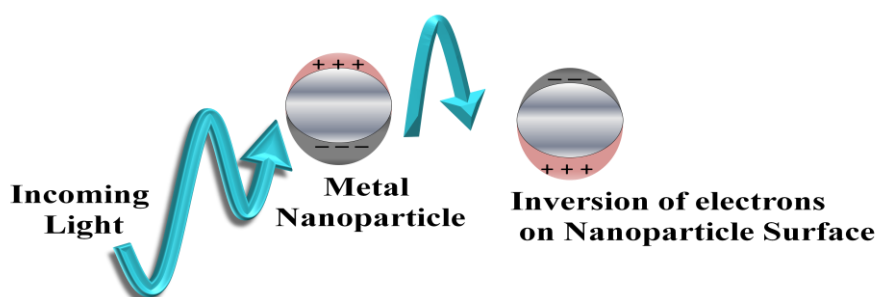


Figure 1.3: Origin of surface plasmon resonance due to coherent interaction of the electrons in the conduction band with electromagnetic field, reproduced from reference 42 (b).

1.1.3. Metal/ Semiconductor Nanoparticles Composite System

The conversion of solar energy into environmentally friendly fuel most notably by the production of hydrogen from water has been achieved utilizing semiconductor photocatalysis⁴⁴⁻⁴⁹. One of the promising strategies to attain this is the adequate deposition of a transition metal on semiconductor nanoparticles. This can be beneficial for maximizing the efficiency of photocatalytic reactions.⁵⁰⁻⁶²

Upon contact, a Schottky barrier can be formed between the semiconductor and the metal particle, leading to a rectified charge carrier transfer. For a bulk semiconductor the conduction and valance bands bend to form space charge region. The space charge layer can extend depending on the charge density. When such semiconductor–metal junction is subjected to band gap excitation, the band bending rectifies the flow of photogenerated charge carriers to produce a photocurrent. For semiconductor nanoparticles the electrons are confined. As a result the bands remain flat and the charge separation is essentially dictated by the Fermi level equilibration (cf. Figure 1.4). Different degrees of electrons accumulation can make the nanoparticles attain different energy levels creating an energy gradient.^{63, 64} Figure 1.5 shows equilibration of a semiconductor–metal nanocomposite with a redox couple before and after irradiation. Upon band gap irradiation of the semiconductor nanoparticles electrons generated in the CB raises its Fermi level to more negative values.⁶⁵ Then, the energetic difference at the semiconductor/metal interface drives the electrons from the CB of the semiconductor into the metal nanoparticles. Upon sufficient charge accumulation, the Fermi levels of the two components can equilibrate at a potential that is progressively shifted to more negative values with increasing electron density.^{66, 67} In general, only composite systems establishing ohmic metal– solution contact act as efficient catalysts for quick e^-_{CB} migration to the solution (Pt or Pd). Conversely, in the presence of non-ohmic interfaces (e.g., with Ag, Au, Cu), excess e^-_{CB} can remain stored effectively on both components of the nano-junction under suitable conditions.⁶⁶⁻⁶⁹ This altered energetic path plays a fundamental role in modulating the overall photocatalytic activity of semiconductor–metal composite systems.⁶⁶⁻⁷¹

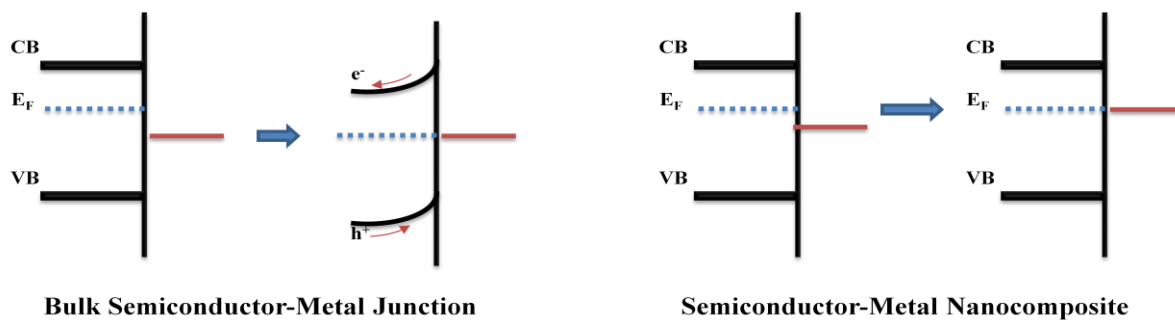


Figure 1.4: Fermi level equilibration at bulk semiconductor–metal junctions and semiconductor–metal nanocomposite systems.

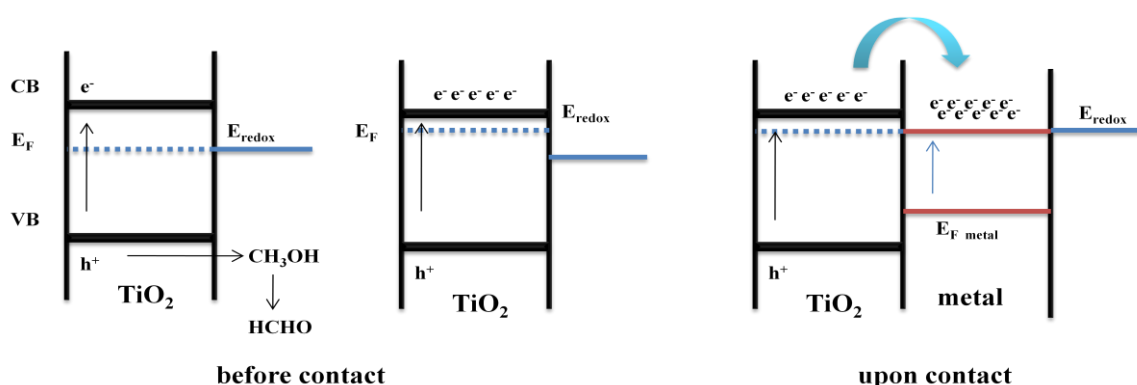


Figure 1.5: Equilibration of semiconductor–metal nanocomposites with a redox couple before and after irradiation. Electron storage in metal nanoparticles causes the Fermi level to shift closer to conduction band of the semiconductor.

1.2. Photocatalysis

Photocatalysis is generally thought of as the catalysis of a photochemical reaction at a solid surface, usually a semiconductor. This simple definition, while correct and useful, however, conceals the fact that there must be at least two reactions occurring simultaneously, the first involving oxidation, from photogenerated holes, and the second involving reduction, from photogenerated electrons (Figure 1.6 (a)). Both processes must be balanced precisely in order for the photocatalyst itself not to undergo any change, which is, after all, one of the basic requirements for a catalyst.

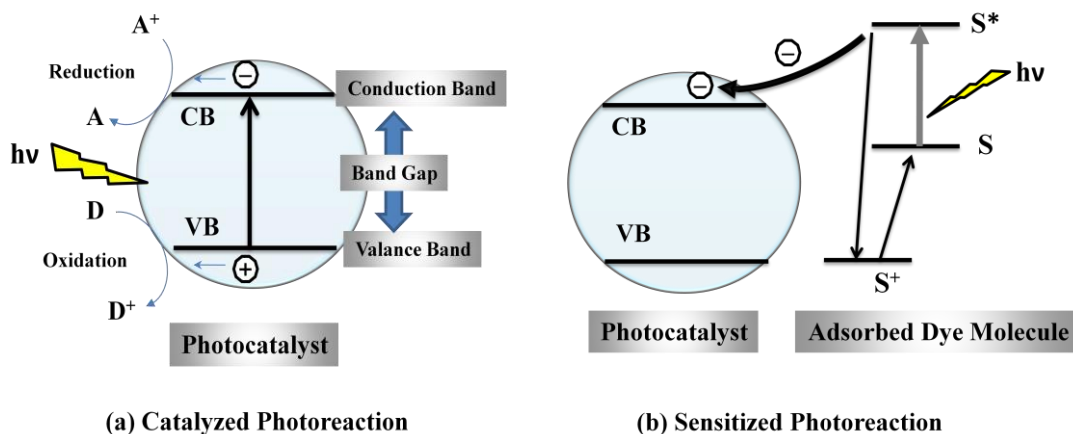


Figure 1.6: Schematic presentation of photocatalytic processes.

The photocatalytic splitting of water on TiO_2 electrodes has been discovered by Fujishima and Honda in 1972.⁷² This event marked the beginning of a new era in heterogeneous photocatalysis. Since then, research efforts in understanding the fundamental processes and in enhancing the photocatalytic efficiency of TiO_2 have come from extensive research performed by chemists, physicists, and chemical engineers. Such studies are often related to energy renewal and energy storage. In recent years, applications to environmental cleanup have been the most active areas in heterogeneous photocatalysis. This is inspired by the potential application of TiO_2 based photocatalysts for the total destruction of organic compounds in polluted air and wastewater. In a heterogeneous photocatalysis system, photoinduced molecular transformations or reactions take place at the surface of a catalyst. Depending on where the initial excitation occurs, photocatalysis can be generally divided into two classes of processes. When the initial photo excitation takes place in the catalyst substrate and the photoexcited catalyst then transfers an electron or energy into a ground state molecule, the process is referred to as a catalyzed photoreaction (Figure 1.6 (a)). When the initial photoexcitation occurs in an adsorbate molecule (e.g., dye molecules) which then interacts with the ground state catalyst substrate, the process is referred to as a sensitized photoreaction (Figure 1.6 (b)). The initial excitation of the system is followed by subsequent electron transfer and/or energy transfer. It is the subsequent excitation process (via electron transfer or energy transfer) that leads to chemical reactions in the heterogeneous photocatalysis process.

1.2.1. Semiconductor Photocatalysis

1.2.1.1. The Semiconductor–Electrolyte Interface in the Absence of Redox Systems

Extensive attention has been drawn to photocatalytic reactions in an aqueous environment. Therefore, it is essential to understand the semiconductor–electrolyte interface, preferably from an energetic point of view. A detailed analysis was done by R. Memming.⁷³ The system of a semiconductor–electrolyte interface in the absence of redox species is illustrated in Figure 1.7.⁷³

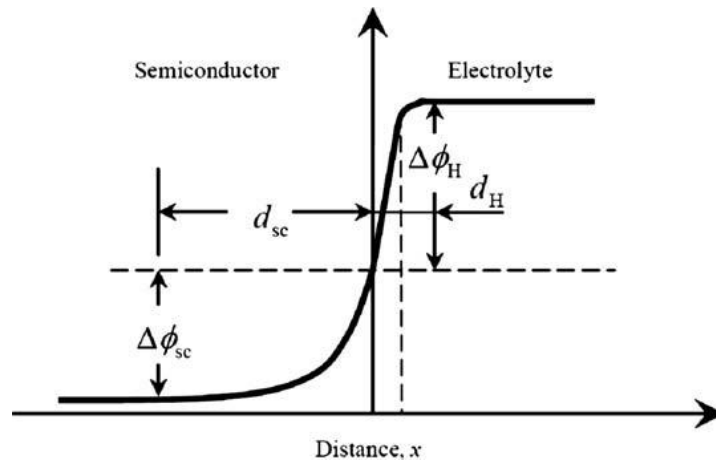


Figure 1.7: Potential distribution at the semiconductor–electrolyte interface.⁷³

When the semiconductor is brought into contact with an electrolyte, the so-called Helmholtz double layer having a potential drop of $\Delta\phi_H$ over a distance d_H is formed on the solution side. On the solid side, the counter charge (i.e., the charge to neutralize that on the solution side due to bonding or specific adsorption of, for example, hydroxyl ions) is distributed over a certain range below the surface. Correspondingly, a potential drop $\Delta\phi_{sc}$ is formed across this so-called space charge region, the dimension of which is denoted as d_{sc} , as indicated in Figure 1.7. Here the diffuse layer in the solution has been neglected assuming that a high ion concentration is applied. The potential and charge distribution within the space charge region in the solid is described by the Poisson equation as follows:

$$d^2\Delta\phi_{sc} = -\frac{1}{\varepsilon\varepsilon_0}\rho(x) \quad (\text{Eq. 1.5})$$

where ε is the dielectric constant of the material and ε_0 is the permittivity of free space. The charge density $\rho(x)$ is given by

$$\rho(x) = e[N_d - N_a - n(x) + p(x)] \quad (\text{Eq. 1.6})$$

where x is the distance from the surface and N_d and N_a are the fixed ionized donor and acceptor densities, respectively, introduced by the doping of the semiconductor.

The Boltzmann statistical distribution of electrons and holes among the available energy levels of a nondegenerated semiconductor under thermal equilibrium is expressed with the help of the concept of Fermi energy, E_f :

$$n_0(x) = N_c \exp - \left(\frac{E_c - E_f}{KT} \right) \quad (\text{Eq. 1.7})$$

$$p_0(x) = N_v \exp - \left(\frac{E_f - E_v}{KT} \right) \quad (\text{Eq. 1.8})$$

where $n_0(x)$ and $p_0(x)$ are the local equilibrium concentrations of electrons and holes at position x , E_c and E_v are the local position of the conduction and valence band edges and N_c and N_v are the effective local density of states at the bottom of the conduction band (CB) and at the top of the valence band (VB), respectively. The Fermi energy represents the electrochemical potential of electrons and holes. Since the definition of E_f takes into account the existence of internal thermal equilibrium in the sc, according to the mass action law the product of electrons and holes concentration must be constant:

$$n_0(x)p_0(x) = n_i^2 = N_c N_v \exp - \left(\frac{E_g}{KT} \right) \quad (\text{Eq. 1.9})$$

n_i being the concentration of charge carriers in the intrinsic material where n_0, p_0, n_i and E_g the band gap energy. Since the electrochemical potential of the electrolyte is defined by the redox potential $E_{redox}(A^-/A)$, according to the Fermi–Dirac statistics, the existence of thermodynamic equilibrium between the sc and the electrolyte requires that

$$E_f = E_{redox}(A^-/A) \quad (\text{Eq. 1.10})$$

The application of the principle of detailed balance under equilibrium conditions in the dark allows determining the rate constant ratios for interfacial transfer of CB electrons and VB holes.

1.2.1.2. Semiconductor–Electrolyte Interface under Illumination

If the semiconductor is illuminated by photons more energetic than its band gap energy, the equilibrium achieved at the interface in the dark is now disturbed by the excitation of electrons from the valence band to the conduction band. Besides this band–band transition, in a real, i.e., nonideal system also other electronic transitions can be induced upon light

excitation, including the excitation of an electron from a donor state or an impurity level into the conduction band, and the formation of an exciton. The latter represents a bound state between an electron and a hole due to their Coulomb attraction. Its energy is close to the conduction band, and thermal excitation can hence feasibly split the exciton into an independent electron and hole. In this section, however, only the band–band transition is considered during the analysis of charge transfer processes occurring at the semiconductor–liquid interface under illumination. The absorption of a photon results in the formation of an electron–hole pair. This process is of special interest if minority carriers, i.e., the holes in an n-type and the electrons in a p-type semiconductor, are involved in the charge transfer. Thereby, the density of the minority carriers can be increased upon light excitation, by orders of magnitude, as compared with that in the dark. For an n-type semiconductor, the minority carriers (holes) generated in the space charge region are subsequently driven to the interface by the “built-in” electric field. Those generated outside this region can only reach the space charge region by diffusion, and then continue the relayed transfer driven by the electric field. The general minority carrier transfer process across the semiconductor–solution interface occurring under illumination of an n-type semiconductor is illustrated in Figure 1.8.⁷³

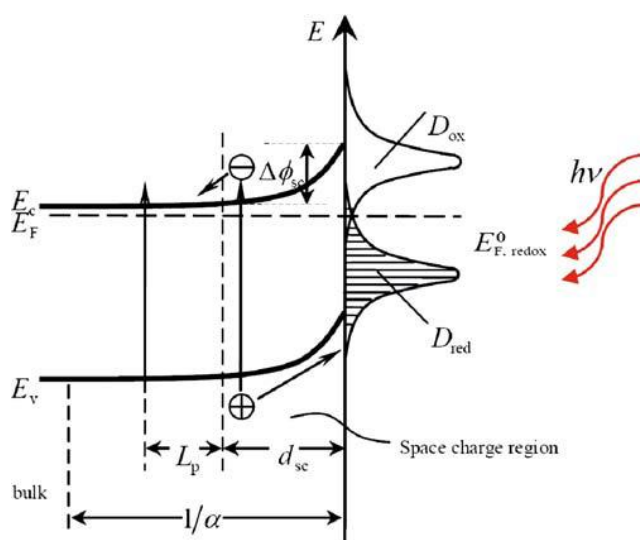


Figure 1.8: Charge transfer at the n-type semiconductor–solution interface under illumination.⁷³

1.2.1.3. Light Induced Charge Transfer at Semiconductor Particles

In photocatalytic reactions, the essential advantage of using semiconductor particles is their large surface area. Besides, the photogenerated charge carriers can easily reach the surface before they recombine, so that a high quantum yield can also be expected. However, two

reactions, an oxidation and a reduction must proceed simultaneously at the same particle surface (otherwise the particle will be charged up, eventually leading to the termination of the overall reaction), as presented in Figure 1.9 (a). The slower process then determines the overall reaction rate. In this regard, the particle behaves practically as a microelectrode kept always under open circuit potential with the anodic and cathodic current being equal in magnitude. Using larger-sized semiconductor particles, the partial currents in the dark are of rather limited magnitude under open-circuit conditions, because the majority carrier (e.g., electrons for an n-type semiconductor) density at the surface is small due to the depletion layer beneath the electrode surface, as indicated in Figure 1.9 (a). In contrast, no space charge region is formed in much smaller particles of size $d \ll d_{sc}$, (Figure 1.9 (b)). Upon light excitation, some minority carriers (e.g., holes for n-type materials) in larger particles are transferred to the electron donor in the solution, which results in a negative charging of the particle that alleviates the positive space charge. Accordingly, this event causes a flattening of energy bands (see the dashed line in Figure 1.9 (a)), equivalent to a negative shift of the rest potential of a bulk electrode under illumination.

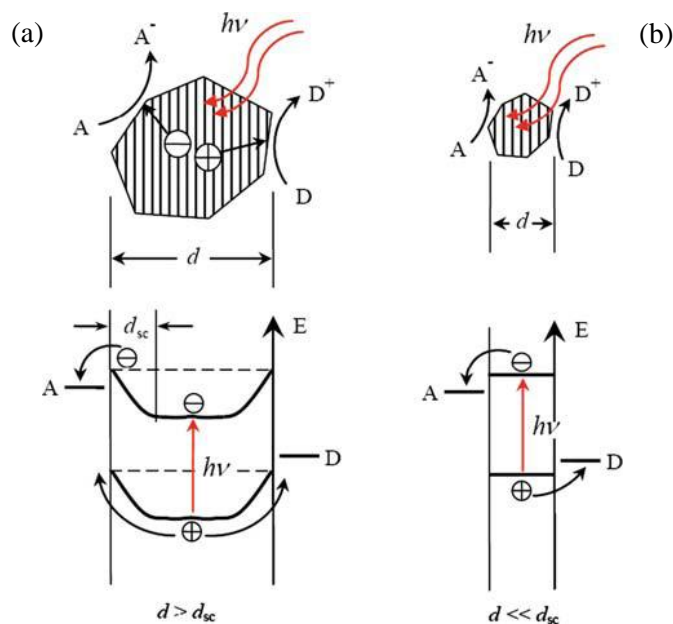


Figure 1.9: Charge-carrier transfer at large (*left*) and small (*right*) semiconductor particles in the presence of an electron donor D and an acceptor A.⁷³

Using much smaller semiconductor particles ($d \ll d_{sc}$), the photogenerated electrons and holes can be easily transferred to the surface and react with the electron and hole acceptors, provided that the energetic requirements are fulfilled. The average transit time τ_{tr} within a particle of diameter d can be obtained by solving Fick's diffusion law as

$$\tau_{tr} = \frac{d^2}{4\pi^2 D} \quad (\text{Eq. 1.11})$$

Taking typical values of $D = 0.1 \text{ cm}^2\text{s}^{-1}$ and $d = 20 \text{ nm}$, the average transit time is about 1 ps, which is much shorter than the recombination time so that most charge carriers can reach the surface before recombination.

1.2.2. Kinetic Aspects

1.2.2.1. Trapped versus Free Charge Carriers in Semiconductor Particles

The distribution of charge carriers between the conduction band and trapping states is an important phenomenon. Heterogeneous photochemical charge transfer reactions are often performed with polycrystalline semiconductors containing trapping sites in the bulk and at the surface. After charge separation in the absence of suitable adsorbed hole scavengers and the presence of molecular oxygen (i.e., an electron scavenger) the remaining holes oxidize surface water to produce adsorbed hydroxyl radicals which can subsequently induce further oxidation reactions. However, in the presence of an adsorbed hole scavenger such as methanol and in the absence of molecular oxygen the fate of the photogenerated electrons is still not clear. Bahnemann et al.⁷⁴ reported that excess electrons are trapped close to the surface of colloidal particles forming Ti^{3+} which is characterized by broad absorption spectra with $\lambda_{\text{max}} = 650 \text{ nm}$. O'Regan et al.⁷⁵ observed near infrared absorbance spectra when TiO_2 membranes were biased at a negative potential. The authors attributed these absorbance spectra to free conduction band electrons with only a small fraction of the electrons being trapped at surface sites. Boschloo and Fitzmaurice⁷⁶ reported that the optical absorption of trapped electrons produced in TiO_2 nanocrystalline layers under negative applied potential is strongest at 400 nm and gradually decreases to zero at 600 nm which is superimposed with the visible absorption spectrum of conduction band electrons that is observed when applying a more negative potential. The authors determined the extinction coefficient of an electron trapped in a surface state to be $1900 \text{ M}^{-1} \text{ cm}^{-1}$ at $\lambda_{\text{max}} = 400 \text{ nm}$, more than 3 times higher than that of conduction band electron at the same wavelength. This evince that the absorption of trapped electrons is most pronounced near 400 nm. Those authors proposed an average of 12 traps per TiO_2 nanocrystal of 12 nm diameter. Safrany et al.⁷⁷ observed a shift in the absorption spectra of TiO_2 electrons to longer wavelength after longer time illumination. They attributed this to the storing of electrons in the conduction band after the traps have been filled.

1.2.2.2. Dynamics of Charge Carrier Trapping and Recombination

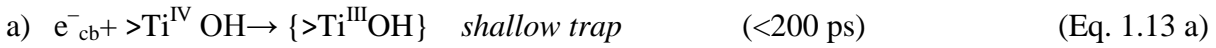
Exciting a semiconductor with any light source causes interband transition, excitonic transition or below-band gap transitions. If the photon energy is larger than the band gap, interband transitions dominate, exciting electrons from the valence band into the conduction band. The recombination of electrons and holes is an important electronic process in semiconductors. Rectification, photoconductivity, and transistor behavior are critically dependent on the life time of the injected mobile carriers. The recombination rate also plays a critical role in photocatalytic reactions with semiconductor particles.

The general mechanism of heterogeneous photocatalysis on TiO₂ can be summarized by the following steps⁷⁸ (cf. Figure 1.10):

(1) Charge carrier generation



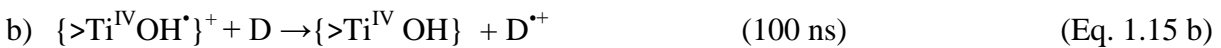
(2) Charge carrier trapping



(3) Charge carrier recombination



(4) Interfacial charge transfer



According to the above mechanism the interfacial charge transfer efficiency is determined by two important processes: the competition between charge carrier recombination and trapping followed by the competition between trapped carrier recombination and interfacial charge transfer.

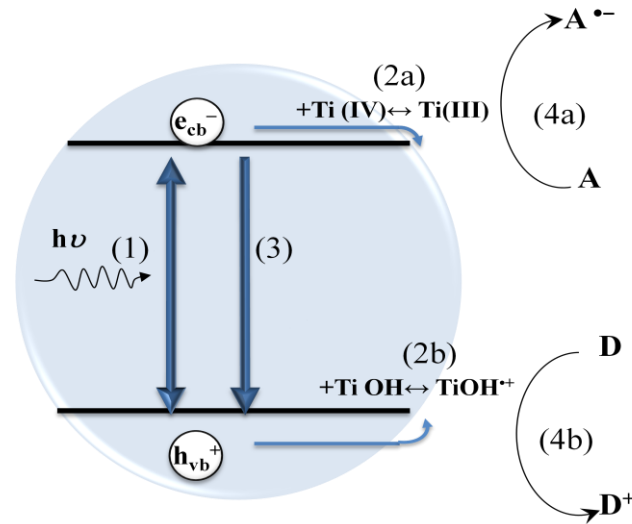


Figure 1.10: Schematic representation of the general mechanistic steps in heterogeneous photocatalysis on TiO₂ nanoparticles.

1.2.2.3. Dynamics of Interfacial Charge Transfer Processes at Semiconductor Nanoparticles

The dynamics of interfacial charge transfer have been early studied.^{79, 80} When either hole or electron traps by surface adsorbed catalyst or acceptor, the non-trapped electrons or holes might react with a suitable acceptor molecule in solution. The overall reaction composed of two steps:

1. Formation of an encounter complex of the electron (or hole) acceptor with the semiconductor particle. The rate of this process is diffusion limited.
2. Interfacial electron transfer which is an electrochemical step involves a Faradic current across semiconductor-solution interface and is characterized by the rate parameter k_{ct} (cm^{s-1}).

The detailed kinetic treatment of the above reaction steps was done by Grätzel et al.⁷⁹ and was expressed by the following Equation:

$$\frac{1}{k^{obs}} = \frac{1}{4\pi R^2} \left(\frac{1}{k_{ct}} + \frac{R}{D} \right) \quad (\text{Eq. 1.16})$$

where R is the sum of the radii of the semiconductor particle and electron (or hole) and D is the sum of their respective diffusion coefficient, k^{obs} is the familiar rate constant obtained experimentally and k_{ct} is the electrochemical rate parameter. There are two limiting cases of Eq. 1.16:

- a) Heterogeneous charge transfer is rate determining and much slower than diffusion ($k_{ct} \ll D/R$). In this case Eq. 1.16 reduces to:

$$k^{obs} = 4\pi R^2 k_{ct} \quad (\text{Eq. 1.17})$$

b) Heterogeneous charge transfer is faster than diffusion, which controls the overall reaction rate ($k_{ct} \ll D/R$). In this case the well known Smoluchowski expression is obtained from Eq. 1.16:

$$k^{obs} = 4\pi DR \quad (\text{Eq. 1.18})$$

Diffusion effects can be eliminated by adsorption or chemical fixation of the acceptor at the semiconductor particle surface by the following relation:

$$k_{ct} = \delta/\tau_{ct} \quad (\text{Eq. 1.19})$$

where τ_{ct} is the average time required for the charge carrier to tunnel across the interface and δ is the reaction layer thickness.

1.2.2.4. Charge Carrier Transfer Reactions at Semiconductors Nanoparticles

a. Reduction of Viologen Compounds

Viologen compounds were chosen as model electron acceptors to study the interfacial electron transfer at semiconductor nanoparticles.⁷⁹⁻⁸¹ Viologen compounds (N,N'-dialkyl-4,4'-dipyridinium dichloride) are well known to be subjected to one-electron reduction which produces the blue radical cation ($V^{\bullet+}$) from the colorless dication (V^{2+}) (Eq. 1.20). Viologen radical cations have attracted much attention because of their strong redox ability. They are capable of reducing protons to produce molecular hydrogen. In view of this, there has been a surge of interest directed to photocatalytic generation of $V^{\bullet+}$ as a possible means of light-to-chemical energy conversion.⁸²⁻⁸⁸ Viologen compounds are known also for their diverse applications, as a herbicidal and toxicological agent.⁸⁹ The herbicidal activity of viologen compounds is related to the facile reaction of their radical cations with oxygen generating superoxide radical anions.⁸⁹⁻⁹¹



b. Photocatalytic Reduction of Transition Metal Ions

The photocatalytic reduction of transition metal ions is an important process because of two effects: 1. the transformation of the ions to less toxic species and 2. the deposition of the reduced metals on the semiconductor catalyst surface for recovery of expensive and useful metals. Moreover, noble metal islands deposited on semiconductor surfaces have unusual catalytic and optoelectronic properties.⁹² It is well known that at the nanometer scale, the optical, electronic and catalytic properties of transition-metal nanoclusters are highly sensitive

to their size and shape. Whereas deposition of metal nanoparticles improves both charge separation as well as interfacial charge transfer kinetics the mechanism responsible for such an improvement is yet to be understood fully on the nanoscale. One main reason for this paucity of mechanistic information is the lack of the experimental methods able to follow these processes in real time.⁹³ A fundamental understanding of the kinetics and mechanisms involved in the deposition of metal nanoclusters on nanometer-scale semiconductors is important in three ways: (i) fundamentally, (ii) to gain better control over catalyst syntheses, and (iii) practically, since key catalytic properties including selectivity,⁹⁴ activity,⁹⁵ lifetime and stability⁹⁵ depend on the catalyst size,⁹⁶ surface composition,⁹⁷ and structure,⁹⁸ which in turn require greater control over heterogeneous-catalyst syntheses. The reduction of the metal ions by semiconductor photocatalysis technology is based on the reduction of the metals by the generated electrons in the system:



One of the most important parameters that affects the efficiency of the process is the standard redox potential of the involved metallic couple related to the V_{fb} because only those species with reduction potentials much more positive than the CB edge can be photoreduced (see Figure 1.11).

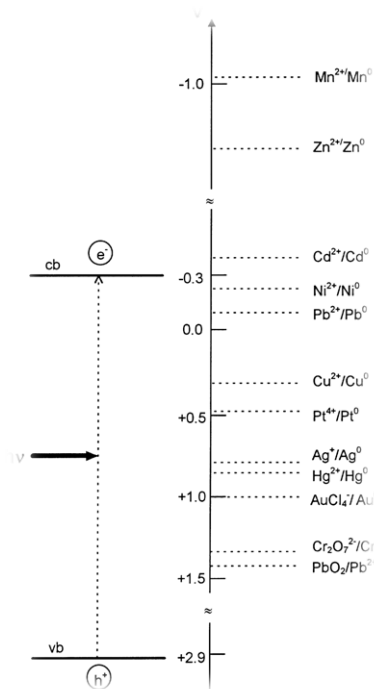


Figure 1.11: Positions of the redox potentials of various metallic couples related to the energy levels of the conduction and valence bands of TiO_2 (P25).⁹⁹ (a)

Reduction of Cu²⁺, Cd²⁺ and Hg²⁺

Effluents from electroplating, electrical industry, machinery and military supplies often contain high concentrations of copper ions. This places Cu²⁺ on the list of strategically important metals as its continuous demand tends to eliminate the known reserves. Moreover, environmental pollution caused by copper contamination must not be neglected.⁹⁹ The detailed understanding of the kinetics and the mechanism of the photocatalytic reduction of Cu²⁺ ions is thus of crucial importance in order to develop respective systems for the removal of these metal ions from waste streams. It has been reported that Cu²⁺ can be reduced to Cu⁰ by TiO₂ electrons.^{100, 101} Herrmann et al.¹⁰² suggested that in the presence of TiO₂ suspensions Cu²⁺ ions are not reduced to Cu⁰ but to Cu⁺ instead even in the absence of molecular oxygen. For the past several decades, mercury has received increasing attention as one of the most dangerous metals to be removed due to its toxic and bio-accumulative properties.^{103, 104} It is used mainly in electrical equipment, catalysts, metallurgy, the paint and color industry, pharmaceuticals, and pesticides, etc. Its removal from wastewaters is of crucial importance because it is harmful to biological systems and can easily get into the food chain. Photocatalysts such as TiO₂,¹⁰⁵ WO₃¹⁰⁶ and magnitide¹⁰⁷ are able to reduce Hg²⁺ to Hg⁰ under UV and visible irradiation.

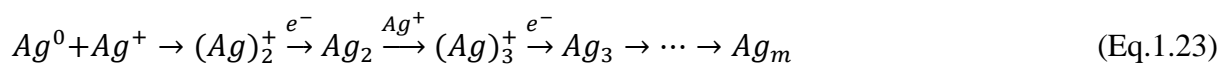
Cadmium does not exist freely in nature. It is used in electroplating, alloys, paints, insecticides, batteries and as a neutron absorber in nuclear reactors. It is very toxic and can enter the human body through food contaminated with residues of fertilizers. The recommended level in drinking waters is <5 ppb and it is included in the list of priority pollutants by the US EPA, together with lead and thallium.¹⁰⁷

Reduction of Ag⁺

Large amounts of silver are present in effluents from photographic processes and waste water from silver jewellers. The toxic effects of silver are not completely understood, but it is known as an effective bactericide, and consequently can damage biological systems. The photocatalytic deposition of metallic silver on semiconductors is amply documented for recovery, principally from waste photographic effluents, for the modification of semiconductors and also as the basis for photoimaging processes. Two limiting cases for the mechanism of colloidal metal particle formation have been proposed:^{99 (a)} (a) aggregation of concurrently formed silver atoms:



(b) a sequence of alternating electronic and ionic events which build up the Ag^0 particle in a similar way as the latent image cluster in silver halide photography:



Recently, the primary events in the photocatalytic deposition of silver on nanoparticulate TiO_2 from ethanol solutions have been analyzed by picosecond-resolved laser flash photolysis.¹⁰⁸ Surface-trapped photoelectron states, probably Ti^{III} , and silver deposition could be observed on the same time scale. It was inferred that one-electron, inner sphere reduction of Ag^I by Ti^{III} is rate determining in the formation of the colloidal silver deposit, and that the particles grow by a sequence of alternating electronic and ionic events, as those proposed in Eq. (56). Other investigation focused on nanosecond laser flash photolysis studies of the reduction of silver ions by the TiO_2 conduction band electrons has also been reported.¹⁰⁹ Friedmann et al.¹⁰⁹ have studied the primary processes during irradiating the system of TiO_2 nanoparticles and silver ions in presence of polyvinyl alcohol (PVA) using nanosecond XeF laser. They detected the photo deposition of metallic silver cluster on TiO_2 by detecting their absorption spectra with a maximum at 380 nm.

Reduction of Au^{3+}

Gold is widely used in the manufacture of jewellery and in plating. It is a material of extreme economic importance in several industrial applications, and ways for its recovery are constantly under investigation. Photocatalysis appears to be an excellent technique for this purpose. Borgarello et al.¹¹⁰ reported the rapid photochemical deposition of gold (III) from aqueous chloride media in the presence of TiO_2 (UV light) or WO_3 (visible light) at pH 3.1. Air and argon purging gave the same results, indicating that oxygen did not affect the rate of deposition. Immobilized TiO_2 supported on glass beads was found to be active also for the photoreduction and recovery of Au^{3+} .¹¹¹ It was possible to follow the two-step mechanism of the photoreduction of noble metals on titania, i.e. the nucleation and the growth of the metallic crystallites. A mechanism similar to that of silver (Eq. 1.22 and 1.23) can also be proposed

In the present study, aqueous solutions of metal ions were mixed with stored TiO_2 electrons and the reaction products were detected by steady state absorption measurements as well as by following the reaction kinetics by stopped flow measurements.

c. Multiple Electron Transfer Reactions

Upon incidence of high light intensities, the charge can accumulate at the semiconductor–electrolyte interface. Depending on the surface pre-treatment, the presence of surface states and the kinetics facilitate the interfacial electron transfer, the accumulated charge may sometimes be used to induce multiple electron transfer to or from an adsorbed substrate. This charge accumulation is critical in the redox reactions of simple inorganic molecule such as water oxidation, oxygen reduction, nitrogen reduction, nitrate reduction or CO₂ reduction. Multi-electron transfer reactions are important processes which avoid high-energy free radical intermediates and can yield desired reaction products under mild conditions. Multi-electron storage and hydrogen generation by light was achieved in aqueous dispersions of ultrafine TiO₂ particles when the amphiphilic viologen derivative N-tetradecyl-N'-methyl-4,4'-dipyridinium dichloride (C₁₄MV²⁺) was used as an electron relay.⁸¹ Two-electron reduction of C₁₄MV²⁺ was coupled with H₂ generation in alkaline medium in the presence of Pt catalyst co-deposited onto the TiO₂ particle.

S. O. Obare et al.¹¹² studied multi-electron transfer reaction of organohalide pollutants at heme-functionalized nanocrystalline TiO₂. Using of this catalyst leads to the formation of stable carbene products in greater than 60 % yield.

Gao et al.^{113(a)} studied the reactions of excess electrons in TiO₂ produced by radiolysis employing steady state and pulse radiolysis techniques. The authors analysed the kinetics of the electron transfer reactions with several scavengers including Cu²⁺, NO₂⁻, NO₃⁻, O₂, H₂O₂ using different nanocrystal sizes. They found that the rate of the reduction of the different scavengers tend to increase with the driving force.

In recent publications,^{113(b-d)} the reaction of electrons in TiO₂ with H⁺ and water in the presence of noble metal coatings and employing pulse radiolysis technique have been investigated. Kasarevic-Popovic et al.^{113(b)} found that the reaction of TiO₂ electrons with H⁺/H₂O is a pseudo first order reaction depending on Pt⁰ and H⁺ concentration. It was shown that the energy of the adsorbed hydrogen atoms on the Pt⁰ surface is not sufficient to abstract hydrogen from 2-propanol. A similar observation was reported in Au/TiO₂ by Hussein and Rudham.^{113(c)} Behar and Rabani^{113(d)} studied the kinetics of hydrogen production upon the reaction of TiO₂ electrons with H⁺ and water in presence of different surface metal catalyst (Pd⁰, Pt⁰ and Au⁰). They found that when the TiO₂ nanoparticles are partially coated with Au⁰ instead of Pd⁰ or Pt⁰, a higher than expected molecular hydrogen level is observed attributing this to a short chain reaction involving hydrogen abstraction from 2-propanol.

1.3. Aims of the Thesis

Charge carrier transfer reactions have been widely acclaimed to be very important as they play a pivotal role in photocatalytic processes. The fundamental study of the dynamics of the charge transfer processes is important in the design of new photocatalysts as well as for the industrialization of the photocatalytic processes. During the past decades, extensive investigations have been performed concerning the study of the kinetics and of the mechanistic details of the interfacial electron transfer processes at the semiconductor/water interface using the laser photolysis^{74,79,80} and the pulse radiolysis technique.¹¹³

The main objective of the present thesis is to study the dynamics of the charge carrier transfer processes induced by light at TiO₂ nanoparticle/liquid (metal ions, organic molecules, O₂, ...) interfaces and to elucidate the mechanistic models in accordance with the kinetic data for a better understanding of photocatalytic reactions.

Our approach was to use for the first time the stopped flow technique to study the dynamics of the transfer of the trapped electrons on TiO₂ nanoparticles. This is one of the most frequently used methods to monitor and evaluate rapid kinetics reactions using absorption or fluorescence spectroscopy. It is applicable to reactions with half lives in the range 10⁻³ to 10³ seconds which is the typical time of electron transfer processes. The basic concept of this study is straightforward, the electrons are generated on TiO₂ nanoparticles by UV illumination in the presence of hole scavengers, stored on them in the absence of molecular oxygen and subsequently used for the reduction of various acceptors. The kinetics of these reactions can be determined after mixing of aqueous suspensions of TiO₂ loaded with electrons and aqueous solutions of the acceptor in the stopped flow chamber following the decay of the absorbance of these stored electrons as well as analyzing the build-up of the absorbance of the respective products. The study of the optical properties of the stored electrons is of interest for their quantification and qualification. Several reactions have been studied utilizing this technique:

- a) Reduction of viologen compounds as models for one- electron transfer reactions.
- b) Multi-electron reduction of common electron acceptor frequently employed in the photocatalytic systems, e.g., O₂, H₂O₂, NO₃⁻.
- c) Reduction of transition metal ions such as Cd²⁺, Cu²⁺, Hg²⁺, Ag⁺ and Au³⁺ and deposition of the corresponding metal clusters on the TiO₂ nanoparticles.
- d) The reduction of H⁺/H₂O in the presence of metal nanoparticles as catalysts.

Additional information arises from using the nanosecond laser flash photolysis technique. In this technique short laser pulses (7 ns, 355 nm) are used to excite the TiO₂ nanoparticles generating electron/hole pairs. The reaction of the photogenerated electrons and/or holes with the adsorbed species can be monitored immediately after the laser pulse excitation by following the decay in the absorbance of electrons or the build-up of the absorbance of the products.

The laser flash photolysis technique was used to study the dynamics of the reaction of the trapped holes through their reaction with phenolic compounds in the presence of electron scavengers as well as to compare the rates of electron transfer reactions with those obtained in the stopped flow studies.

2. Materials, Analytical and Experimental Methods

2.1. Materials

All chemicals were of the highest purity available and were used as received without further purification. They were all purchased from the Sigma-Aldrich Company. All metal salts were chlorides or perchlorates: AgClO_4 (99.5%), $\text{HAuCl}_4 \cdot 3\text{H}_2\text{O}$ (99, 9%), $\text{H}_2\text{PtCl}_6 \cdot x\text{H}_2\text{O}$ (99, 99.5%), HgCl_2 (99.5%), $\text{Cd}(\text{ClO}_4)_2 \cdot x\text{H}_2\text{O}$ (99.999%), CuCl_2 (99.99 %), MnCl_2 (99.9), ZnCl_2 (99.9). Gold nanoparticles (average particle size 5 nm) and polyvinyl alcohol (PVA, 10.000 g/mol) were purchased from Sigma.

Methyl viologen dichloride ($\text{C}_{12}\text{H}_{14}\text{Cl}_2\text{N}_2 \cdot x\text{H}_2\text{O}$) and benzyl viologen dichloride ($\text{C}_{24}\text{H}_{22}\text{Cl}_2\text{N}_2$) were recrystallized from absolute methanol.

TiCl_4 (99,9%), Titan(IV)-isopropoxid ($\text{Ti}[\text{OCH}(\text{CH}_3)_2]_4$) (99.999%), Methanol (99,99 %), NaNO_3 (99.995%), NaNO_2 (99.5%), NaClO_4 (99.5%), (H_2O_2 ,30%) and Nessler's reagent were used as received. All solutions were prepared with deionized water from a SARTORIUS ARIUM 611 apparatus (resistivity = 18.2 Ω cm).

2.2. Preparation of TiO_2 Nanoparticles

For transient absorption measurements in the stopped flow studies, it is important that light scattering of the particles is negligible, which can be achieved using transparent colloidal suspensions of extremely small particle size. For that transparent TiO_2 nanoparticles (2-3 nm particle size) have been prepared from the inorganic precursor following the recipe reported by Kormann et al.¹⁸ A 9 ml quantity of titanium tetrachloride TiCl_4 prechilled to -20°C was added slowly to 750 ml of vigorously stirred deionized water at 0°C . After being continuously stirred for 1 hour, the resulting transparent colloidal solution was dialyzed using deionized water to change the pH to 2-3. In the experiments of silver ions reduction the obtained colloid was then dialyzed using perchloric acid solutions of the same pH several times until $[\text{Cl}^-] = 1.8 \times 10^{-5}$ M (determined by HPIC), for the purpose of reducing the chloride ion concentration to minimize the possibility that formation and reduction of AgCl on the catalyst surface might be intermediate in the observable electron transfer reaction. The colloid was dried by vacuum evaporation at 20 mbar at 27°C . Off white shining crystals were obtained which can be resuspended in pure water to obtain perfectly transparent colloidal TiO_2 suspensions. TiO_2 was also prepared from organic precursor (Titan(IV)-isopropoxid) according to Bahnemann et

al.⁷⁴ as following: dropwise addition of titanium tetraisopropoxide dissolved in 2-propanol to perchloric acid solution of pH 1.5. This mixture was stirred overnight until it was virtually clear. The pH was changed to 2–3 by dialyses against pure water. After vacuum evaporation of the solvent a white powder of TiO₂ remained. The final solution was made by dissolving appropriate weight of the powder in pure water. Figure 2.1 shows the schematic presentation of TiO₂ preparations either from organic- (Titan(IV)-isopropoxide) or inorganic- (TiCl₄) precursor.

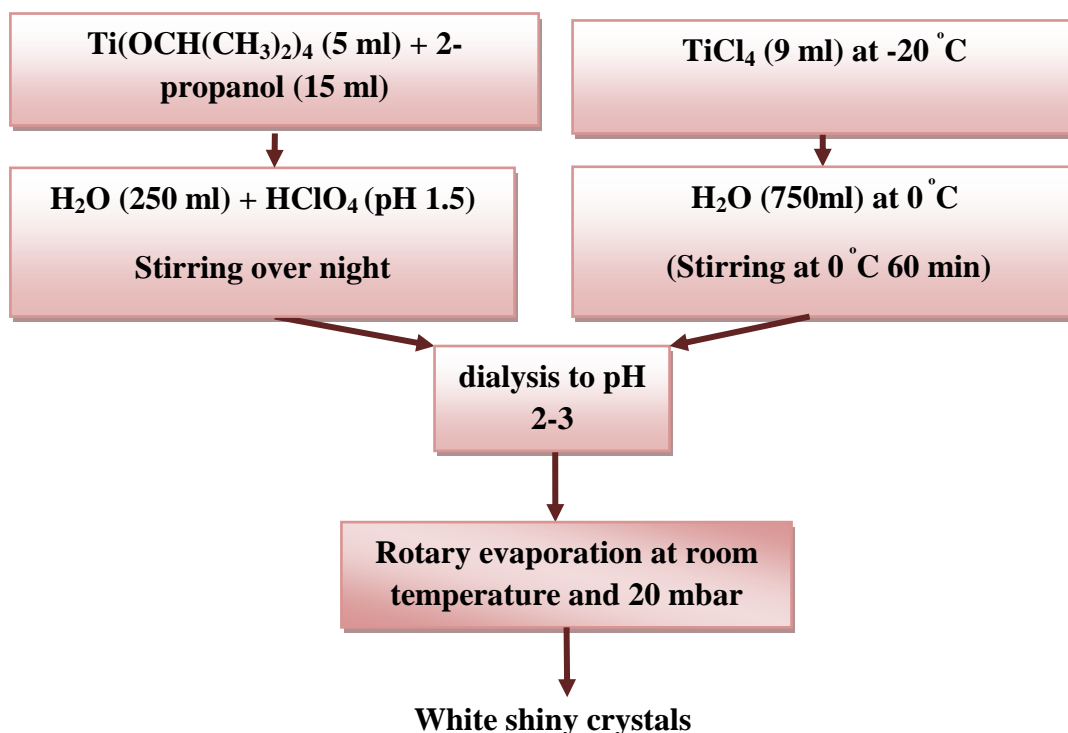


Figure 2.1: TiO₂ preparation from organic- (Titan (IV)-isopropoxid) and inorganic precursor (TiCl₄).

2.3. Preparation of Noble Metal Nanoparticles

Colloidal noble metal particles (Platinum and gold) were thermally prepared by reducing the metal salt H₂PtCl₆ or HAuCl₄ solution with sodium citrate.¹¹⁴ 25 ml of a 3.4×10^{-3} M sodium citrate solution was added to 500 ml of a boiling 1×10^{-3} M solution of metal salt (H₂PtCl₆ or HAuCl₄). After boiling for 1 h, the solution exhibited brown or red color, respectively, indicating the formation of colloidal platinum or colloidal gold nanoparticles respectively.

The colloids were cooled to room temperature and deionized with Amberlite MB1ion-exchange resin until a specific conductivity of 3–5 $\mu\text{s cm}^{-1}$ was reached.

2.4. Analytical Methods

2.4.1. Steady State UV–vis Absorption Measurements

The UV–vis spectra over a range of 200–800 nm were recorded employing a Varian Cary 100 Scan UV–vis system.

2.4.2. X- Ray Diffraction (XRD) Measurements

XRD (WXR) data were acquired on a Bruker AXS D4 Endeavor X diffractometer using Cu $K\alpha_{1/2}$, $\lambda_{\alpha 1} = 154.060$ pm, $\lambda_{\alpha 2} = 154.439$ pm radiation. X-ray diffraction (XRD) data for the Rietveld phase analysis of TiO_2 have been recorded on a Phillips PW1800 diffractometer using reflection geometry with variable divergence slits, Cu KR1, 2 radiations, and a secondary monochromator. For each measurement 3000 data points were collected with a step width of 0.02° and 2 s measurement time per step in the 2θ range from 20 to 80° . Phase analysis by the Rietveld method was carried out by using the TOPAS 2.0 (Bruker AXS) software.

2.4.3. Transmission Electron Microscopy (TEM) Measurements

TEM measurement was conducted at 200 kV with a JEOL JEM-2100F-UHR field-emission instrument equipped with a GatanGIF 2001 energy filter and a 1k-CCD camera. Sample preparation was made by dispersing the powder in ethanol and dropping ca. 10 μl of the suspension onto a copper-supported perforated carbon film of the type Multi A (Quantifoil Micro Tools GmbH, Jena, Germany), on which it was dried.

2.4.4. Gas Chromatography (GC) Analysis

The GC measurements are carried out using a Shimadzu GC (Shimadzu 8A) equipped with a molecular sieve 5 Å packed column for analysis of inorganic gases (H_2 and N_2). Argon was used as the carrier gas. A Thermal Conductivity Detector (TCD) was employed for the gas detection.

2.4.5. High Performance Ion Chromatography (HPIC) Analysis

The HPIC measurements were performed using a high performance DIONEX ICS-1000 ion chromatograph equipped with a 2×50 mm Ion Pac AS9-HC column and a conductivity detector and an electro-regenerator- suppressor. The mobile phase was an alkaline solution of 0.008 mol l⁻¹ Na₂CO₃ and 0.0015 mol l⁻¹NaHCO₃. No temperature control was applied to the compartment of the separation column, but the temperature of the detector conductivity cell was kept constant at 35.00±0.05 °C.

2.4.6. Dissolved O₂ Concentration Measurements

The concentration of dissolved oxygen in water has been determined using a Microprocessor Oximeter oxi 2000 providing Trioximatic EO 200 electrode.

2.4.7. H₂ Gas Measurements

The concentration of the evolved H₂ gas was determined as following: to a sealed glass tube (25 ml) containing 10 ml Ar-saturated aqueous solutions of metal nanoparticles prepared in advance by citrate method a 10 ml of TiO₂ aqueous suspension loaded with electrons ($[e^-_{\text{TiO}_2}] = 5 \times 10^{-4}$ M) (a detailed discription of loading of electrons on TiO₂ nanoparticles will be present in the following Section 2.5.1) was injected. The resulted mixture was vigoursly shaken to ensure the equilibration between the liquid mixture and the gas phase. A given volume from the headspace of the tube was injected to the gas chromatograph to measure the H₂ concentration. This experiment was performed at different pH (2.2–3.2) and different metal concentrations (1×10^{-4} – 5×10^{-4} M).

2.5. Fast kinetics Measurements

2.5.1. Stopped Flow Measurements

Stopped Flow Instrument: One of the most frequently used rapid kinetics techniques is the stopped–flow technique. Small volumes of solutions are rapidly driven from syringes into a high efficiency mixer to initiate a fast reaction. The resultant reaction volume then displaces the contents of an observation cell thus filling it with freshly mixed reagents. The volume injected is limited by the stop syringe which provides the “stopped-flow”. Just prior to stopping, a steady state flow is achieved. The solution entering the flow cell is only milliseconds old. The age of this reaction volume is also known as the dead time of the stopped–flow system.

The stopped flow experiments presented in this thesis were performed using a SX.17MV-R Rapid Mixing Spectrophotometer (Applied Photophysics, United Kingdom). The 150 W arc Xenon lamp used as light source and Spectra Kinetic monochromator fitted with a 250 nm holographic diffraction grating giving useful operating wavelength range of 200 to 700 nm. The dead time of the work is 1 ms and the optical path length of the measuring cuvette is 0.2 cm. Unless otherwise stated, the measurements were carried out under anaerobic condition at ambient temperature. Figure 2.2 shows the schematic of a typical stopped-flow apparatus. Two reactant solutions are rapidly mixed by being forced into a mixing chamber, and then through an observation cell. At some point in time, the flow fills the stop-syringe, until the plunger hits the trigger-switch. This simultaneously stops, and the reaction monitored using a suitable spectroscopic probe, such as absorbance or fluorescence. The change in the absorbance signals as a function of time is recorded.

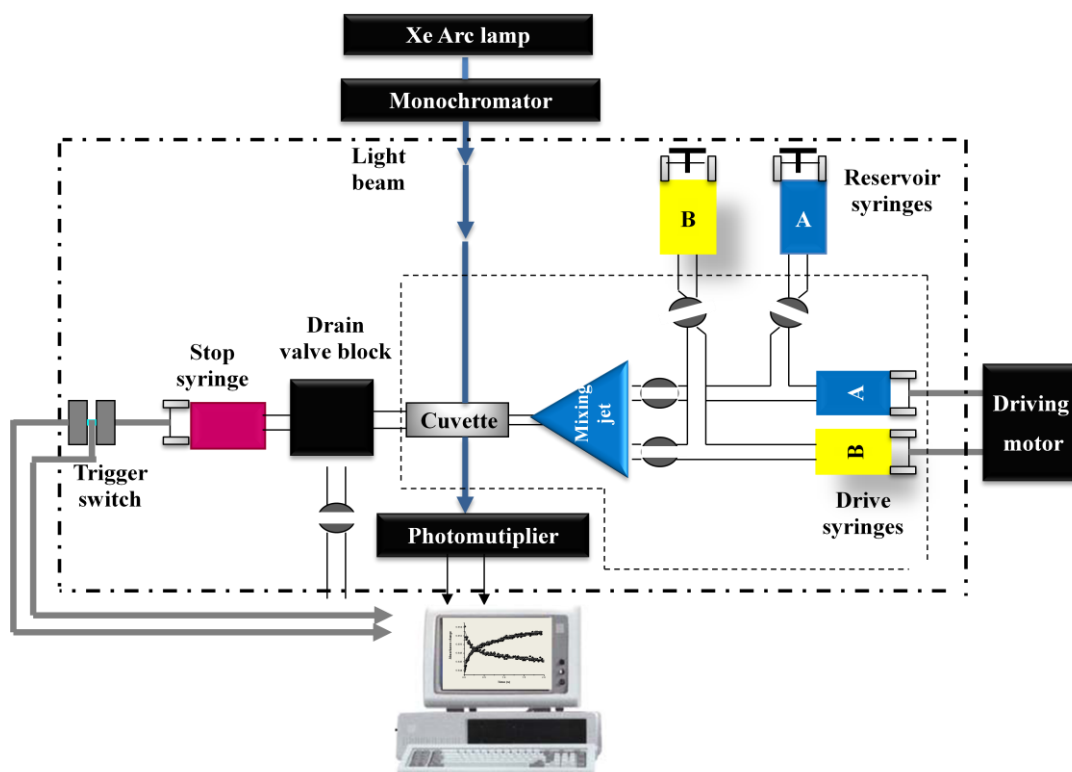


Figure 2.2: Schematic representation of the stopped flow apparatus set up.

Storing of Electrons on TiO₂ Nanoparticles

The electrons are stored on the TiO₂ nanoparticles by illuminating a deaerated (Argon purged) freshly prepared transparent suspension of 3g l⁻¹ (3.8×10⁻² M) of the nanoparticles for 2-8 hours in the presence of 0.02 M methanol as a hole scavenger (cf. Figure 2.3 (a)). The illumination was performed using a double jacket Duran glass reactor (110 cm³) with two outlets for gas purging and using a high-pressure Xe-lamp (OSRAM HBO- 500W) placed inside a quartz jacket and equipped with a cooling tube. The employed UV (A) light intensity was 2.6 ×10⁻³ J cm⁻² s⁻¹.

Stopped Flow Experiments

In a typical stopped flow experiment (cf. Figure 2.3 (b)), nanosized TiO₂ particles loaded with electrons were injected in one of the stopped flow syringes and the electron acceptor (metal ions, O₂ (H₂O), H₂O₂, N₂(H₂O), ...) was injected in the other syringe. A 1:1 mixing of the two reactants takes place and the resulting reactant mixture travels to the optical cell where the change in the absorbance with time is measured. The kinetics of the electron transfer reactions was studied by following the decay of the absorbance of TiO₂ electrons at 600 nm or the build-up of the absorption signals of products, e. g., the plasmonic bands of nano-sized metal particles with time. The rate constants which define the reaction kinetics can be measured by fitting the data using a suitable model.

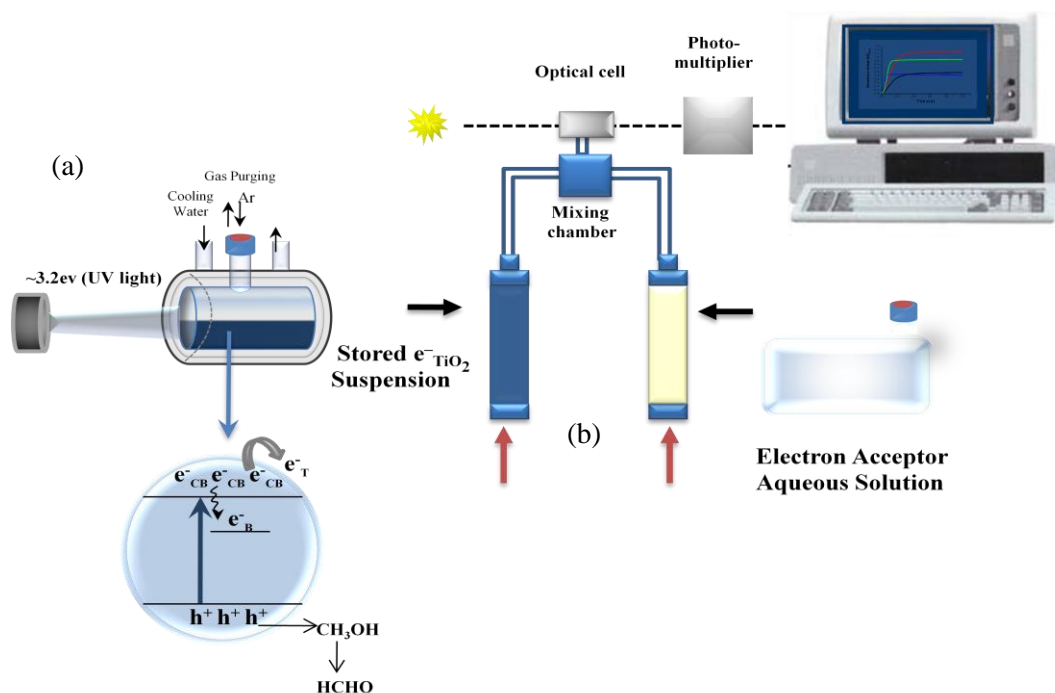


Figure 2.3: Schematic illustration of the stopped flow experiment for the multi-electron transfer reactions induced by stored electrons in TiO₂ nanoparticles.

2.5.2. Laser Flash Photolysis Measurements

Flash photolysis is a pump-probe technique developed by Ronald George, Wreyford Norrish and George Porter, who won the 1967 Nobel Prize in Chemistry for this invention together with Manfred Eigen. The sample is primarily excited by a relatively energetic nanosecond laser pulse. This light pulse induces a change in the electronic configuration that can lead to a photochemical reaction. A continuous light beam probes the sample and allows for the recording of a transient trace related to the optical perturbation. This is in practice recorded with an oscilloscope measuring the transient response of a photodiode or photo-multiplier tube. Figure 2.4 presents a scheme of the setup used in the framework of this thesis. The excitation source is provided by Nd: YAG Q-switched laser (Continuum Powerlite-7030) with a frequency-tripled output (355 nm). The diameter of the laser beam at the entrance of the 1 cm measuring quartz cuvette was 4 ± 1 mm. The laser intensity ranging from 0.6 to 0.8 J s⁻¹, the repetition rate was 30 Hz and the energy output ranging from 20 to 27 mJ/pulse. The pulse duration was 7 ns. The photon flux was ranging from 2×10^{-5} mol photon l⁻¹ to 5×10^{-5} mol photon l⁻¹. The samples are probed by continuous light provided by a CW 450W Xe arc lamp. The output of a Xenon arc lamp, filtered through various filters, constitutes the probe beam. It is focused onto the sample and then collected in a monochromator. The monochromator is tuned at the desired probe wavelength. The photo-detection is finally achieved by a fast photomultiplier tube (R9110, Hamamatsu) supplied with 750 V. The induced transient voltage signal is then recorded into a digital signal analyzer (DSA 602 A, Tektronix). The device is triggered by a small fraction of the excitation beam driven into a fast photodiode. Absorbance changes following laser excitation are monitored over the chosen time window and a satisfactory signal-to-noise ratio is obtained by averaging over 200-1000 shots. The stability of the system is good enough to measure transient spectra by accumulation of traces at selected wavelengths. Data analysis is then performed by Origin and a series of Igor Pro macros that load and process the data. The rate constants which define the reaction kinetics can be measured by fitting the data using a suitable model.

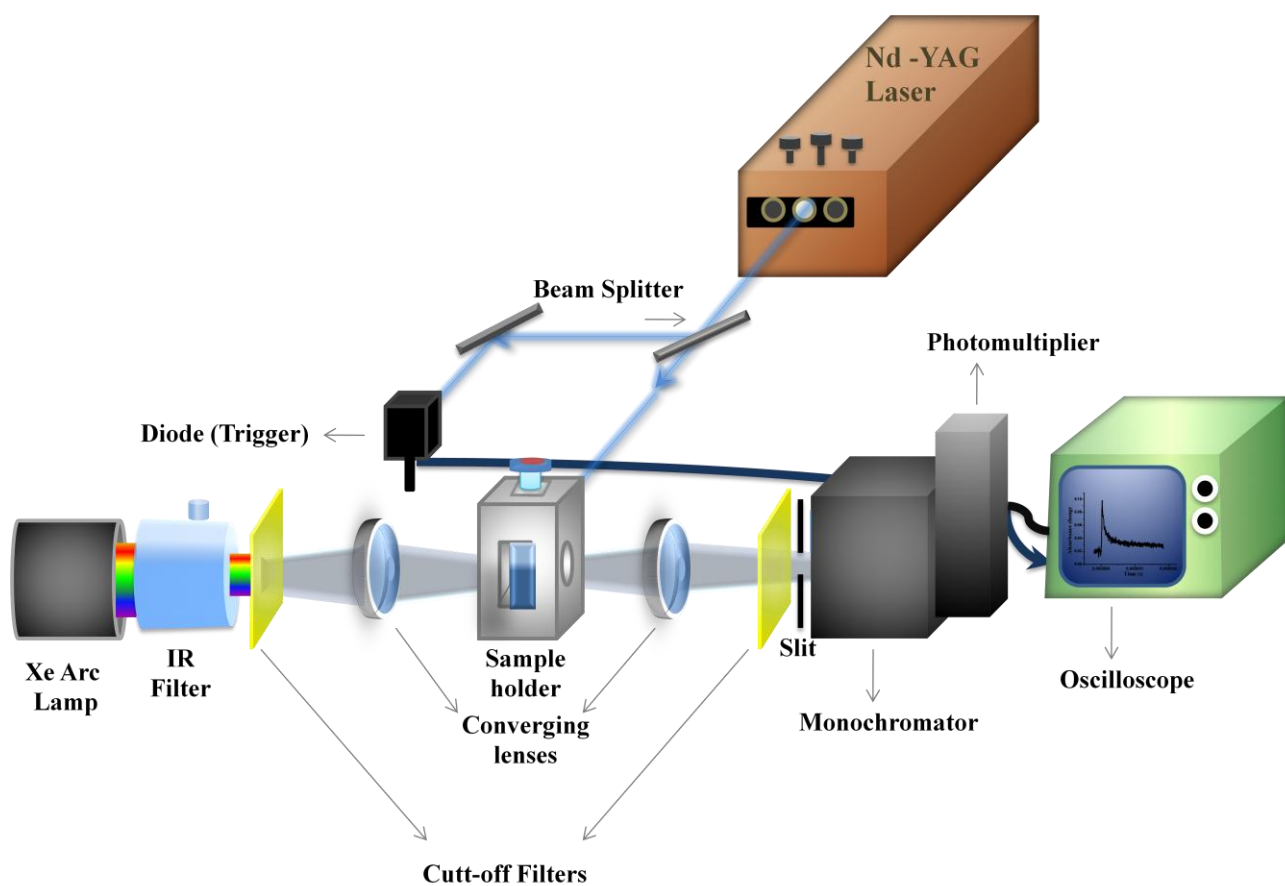


Figure 2.4: Schematic representation of the set up of a Nanosecond laser flash photolysis spectrometer.

3. Stopped Flow Study

This chapter presents a comprehensive and detailed study of the kinetics and the mechanism of a variety of electron transfer reactions at TiO₂ nanoparticles employing the simple and facile stopped flow technique. Moreover, the optical properties of the stored electrons in the TiO₂ nanoparticles have been studied in detail following the UV (A) photolysis of deaerated aqueous suspensions of nanosized TiO₂ in the presence of methanol. The basic concept of this work is rather straightforward, the electrons are generated on the TiO₂ nanoparticles by UV illumination in the presence of a hole scavenger, stored on them in the absence of molecular oxygen and subsequently used for one- or multi- electron transfer reduction of various oxidants such as viologen dication (V²⁺), O₂, H₂O₂ and NO₃⁻. The reduction of toxic metal ions Hg²⁺, Cu²⁺, Cd²⁺, Zn²⁺ and Mn²⁺ as well as noble metal ions Ag⁺ and Au³⁺ has also been studied. The kinetic of these reactions were investigated not only by following the decay of the transient absorbance of the trapped electrons but also by the detection of the respective surface plasmon (SP) absorbance band of the resulting metal clusters. Furthermore, the reduction of H⁺/H₂O in presence of metal deposits has been examined under varied conditions of different pH and different metal loading. The underlying reaction mechanisms are discussed in detail.

3.1. Characterization of TiO₂ Nanoparticles

The TiO₂ nanoparticles used in this study were prepared from the hydrolysis of TiCl₄ (see Section 2.2). The absorption spectrum of 3 g l⁻¹ TiO₂ nanoparticles re-suspended in pure water is shown in Figure 3.1 (a). The absence of any light absorption above 400 nm evinces the presence of very small, i. e., non- light scattering particles. Due to the band gap energy of TiO₂ (E_g= 3.2 V for anatase)¹¹⁵ the absorption rises rapidly at wavelengths shorter than 390 nm. The crystalline character of the nanoparticles was investigated by XRD (cf. Figure 3.1 (b)). The samples exhibit broad diffraction pattern characteristic of the crystal phase of pure anatase of 3 nm particle size (as calculated from the XRD line broadening). The size of the TiO₂ particles was also determined using TEM measurements to be 2–3 nm which is consistent with the XRD measurements (cf. Figure 3.1 (c)).

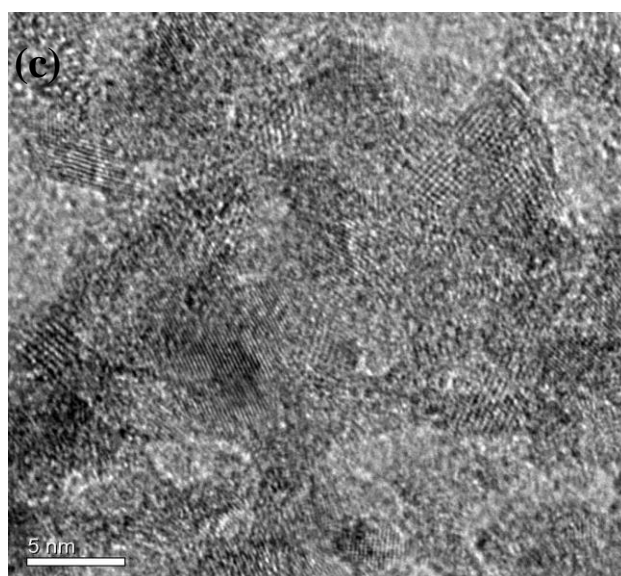
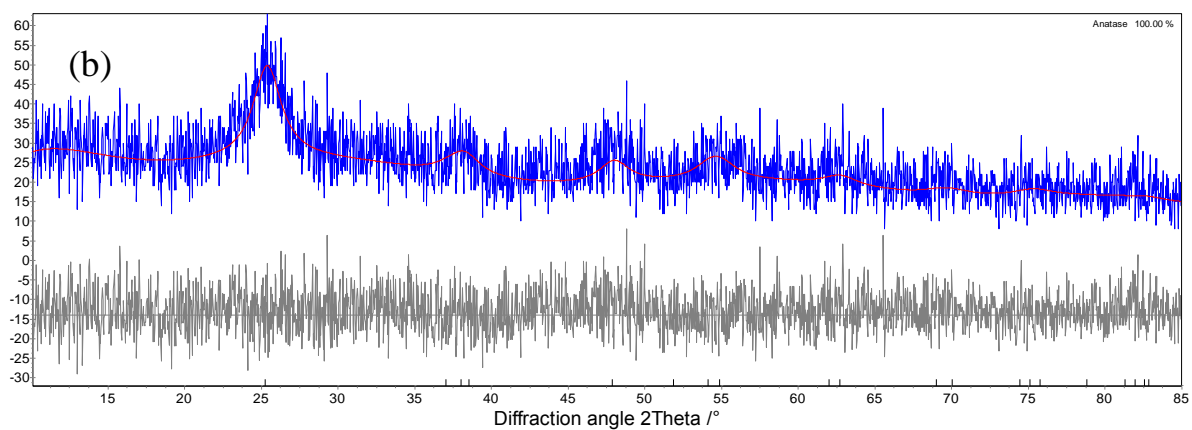
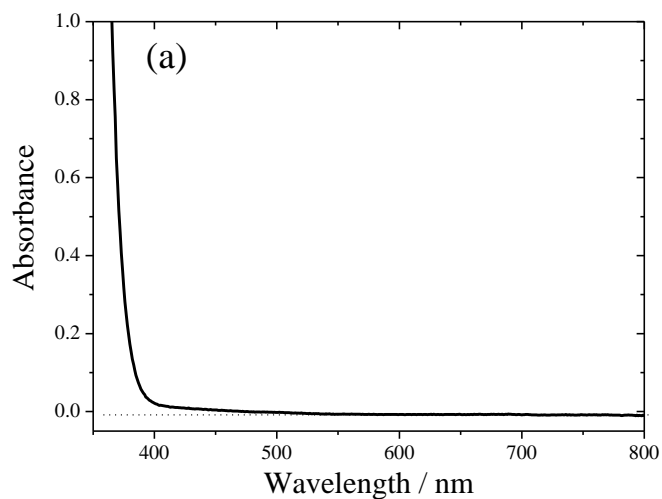


Figure 3.1: (a) UV-vis absorbance of an aqueous suspension of as prepared TiO₂ nanoparticles (3 g l⁻¹), (b) XRD pattern of as-prepared TiO₂ (blue line), XRD of pure anatase (red line), difference between pure anatase and sample (grey line), (c) TEM micrograph of as prepared TiO₂.

3.2. Storing of Electrons on TiO₂ Nanoparticles

The UV (A) photolysis of a system containing TiO₂ (3.8×10^{-2} M) and methanol (2×10^{-2} M) as hole scavenger in the absence of molecular oxygen (purged with Argon gas before illumination to remove all dissolved oxygen) results in the formation of a transparent blue suspension indicating the generation of the stored electrons in the TiO₂ particles. The blue coloration is characterized by a broad absorption band in the visible region (400–800 nm) with a maximum observed after 25 min of illumination at 523 nm, which is then slightly shifted to longer wavelengths with increasing irradiation time to finally reach 627 nm after 480 min of illumination. Figure 3.2 (a) shows the absorption spectra of the aqueous TiO₂ suspension observed after different UV irradiation periods. Figure 3.2 (b) shows the change of the absorption maximum of the stored electrons with irradiation time.

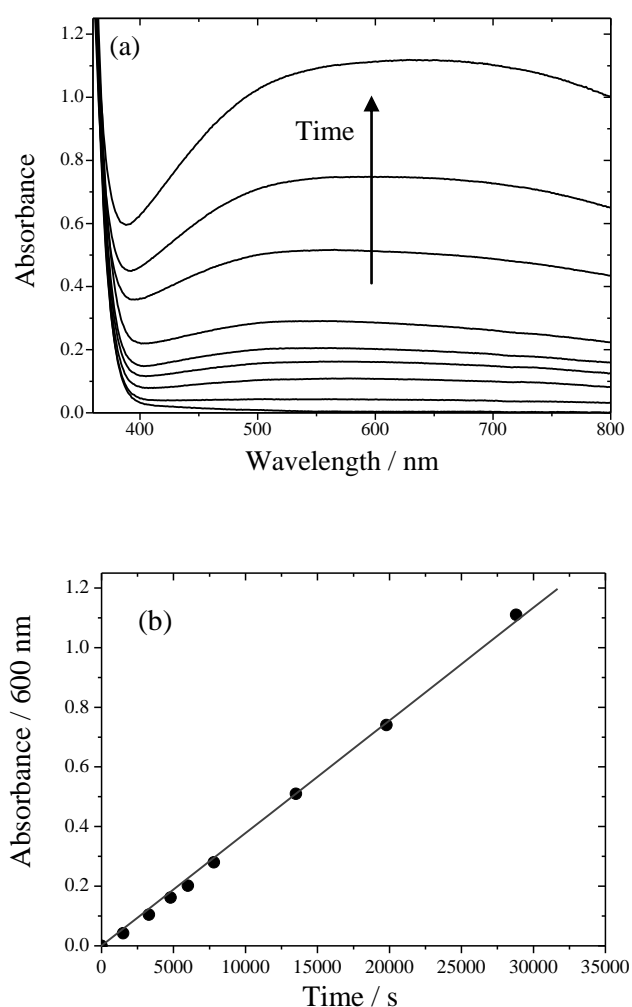


Figure 3.2: (a) Build up of the TiO₂ electron spectrum of a 3.8×10^{-2} M deaerated aqueous TiO₂ suspension (freshly prepared) in the presence of 0.02 M methanol at pH 2.3 recorded following different periods of UV irradiation. (b) Change in absorbance at 600 nm as a function of the employed irradiation time.

The absorption spectra of stored TiO₂ electrons (Figure 3.2 (a)) show a peak at 532 nm upon illumination of freshly prepared TiO₂ colloidal suspension which is red shifted to 627 nm when the illumination time was increased to 480 min. In accordance with the mechanisms proposed in the literature⁷⁴ it is concluded that the TiO₂ electrons (e_t⁻) are trapped as Ti (III) states, i.e., that the conduction band electrons get trapped at Ti (IV) sites. These trapped TiO₂ electrons exhibit broad absorption in the visible region of the spectrum with a maximum at around 600 nm. Therefore, it is believed here that the observed absorption spectra are assigned to the absorption of trapped electrons.

For further understanding of the factors causing the shifting in the absorption of the trapped TiO₂ electrons with increasing the illumination time the TiO₂ suspension was aged for 2 weeks and then illuminated by UV (A) light. The spectra evolved after different period of irradiation is illustrated in Figure 3.3.

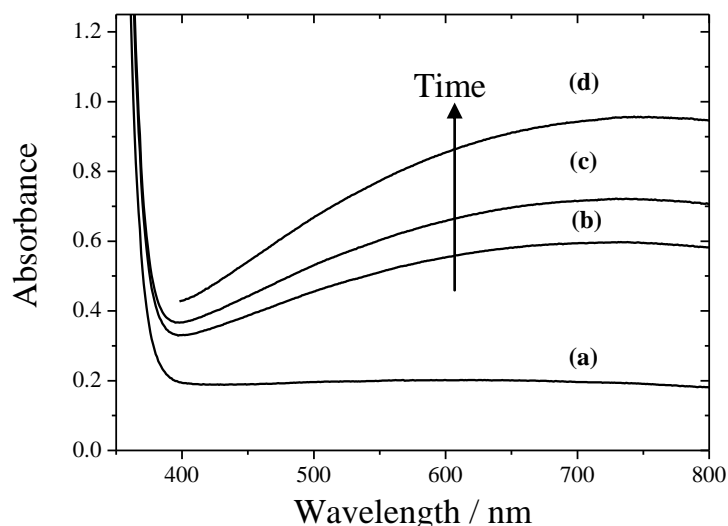
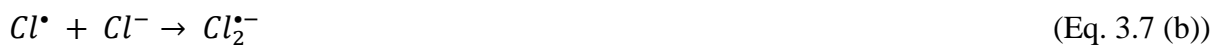


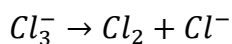
Figure 3.3: Build-up of the TiO₂ electron spectrum of a 3.8×10^{-2} M deaerated aqueous TiO₂ suspension (aged for 2 weeks) in the presence of 0.02 M methanol at pH 2.3 recorded following different periods of UV irradiation, (a) 100, (b) 200, (c) 250, (d) 400 min.

As clearly seen from Figure 3.3 the spectra of electrons are different from that of freshly prepared suspension (Figure 3.2 (a)); the absorption increases from 360 nm to 800 nm with a maximum shifting from 625 nm after 100 min of illumination to 730 nm after 400 min of illumination. This red shifting in the absorption maximum is similar to that reported previously by Safrany et al.⁷⁷ when they illuminated the TiO₂ particles aged for 24 months. The authors attributed these red shifted spectra of the aged particles to the spectra of conduction band electrons.⁷⁶ Therefore, it can be concluded here that the shift in the optical absorbance of stored TiO₂ electrons to longer wavelengths is attributed to the storing of the

excess electrons in the conduction band of TiO₂ after the available surface traps have been filled⁷⁷ (or decreased upon ageing) or by the trapping of the electrons in bulk rather than in surface traps, i. e., assuming that bulk electron traps exhibit slightly red shifted absorption spectra.

The mechanism of electron storing can be summarized as follows (Eq. 3.1– 3.7): upon band gap illumination electrons are promoted from the valance to the conduction band leaving holes behind in the valance band (Eq. 3.1). While the electrons are trapped at Ti (IV) sites as Ti (III) (Eq. 3.2) the valence band holes migrate to the surface of the particles where they react with the adsorbed methanol molecules producing α -hydroxyl methyl radicals (Eq. 3.3). The latter can directly inject electrons to the conduction band of the TiO₂ nanoparticle (Eq. 3.4) or react with another hole producing formaldehyde (Eq. 3.5). The former process (Eq. 3.3) followed by (Eq. 3.4) is known as current doubling.¹¹⁶ The valance band holes can also react with adsorbed chloride ions producing chlorine atoms (Eq. 3.6) and finally chlorine gas (Eq. 3.7). This gas can either be produced by a termination reaction between two chlorine atoms (Eq. 3.7 (a)) or involve the production of other radical intermediates with a high oxidative power such as Cl₂^{•-} (Eq. (3.7 (b)–3.7(d)). Indirect indications of a loss of chloride ions by conversion to chlorine are (i) the decrease in the chloride ion concentration measured after illumination, and (ii) the blue coloration obtained by illuminating an aqueous TiO₂ suspension in the absence of methanol, due to the stored TiO₂ electrons (cf. Figure 3.4).





(Eq. 3.7 (d))

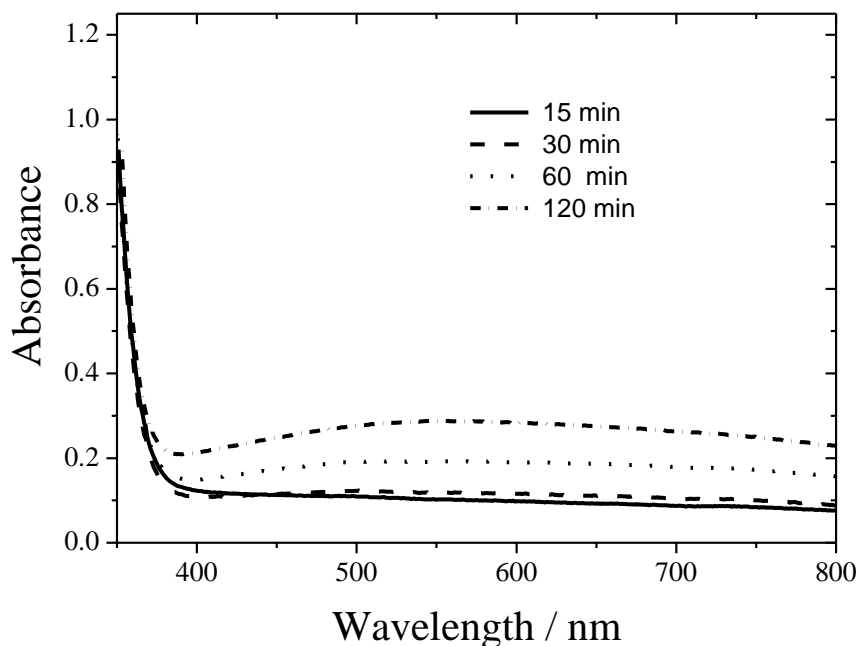


Figure 3.4: Build-up of the TiO₂ electrons spectra of a 3.8×10^{-2} M deaerated aqueous TiO₂ suspension in the absence of methanol at pH 2.3 recorded following different periods of UV irradiation.

It is important to notice here that the pH of all experiments was in the range of 2-3.5. Under our experimental conditions of using high concentration of TiO₂ particles (3 g l^{-1}) it was found that when the pH is below 1.5 or raised above 3.5 either by titration of the aqueous suspension with NaOH or by dialysis, the particles coagulated. So that it was not possible to follow the effect of changing the pH on the kinetics of the reactions beyond this range.

Determining of the Number of Electrons per TiO₂ Nanoparticle

Assuming that the TiO₂ nanoparticles have a spherical shape, the volume of one TiO₂ particle with a diameter of 3 nm is calculated to be $1.41 \times 10^{-20} \text{ cm}^3$. Considering that the mass density of anatase TiO₂ is 3.894 g cm^{-3} , the average weight of one 3 nm TiO₂ nanoparticle is readily calculated to be $5.43 \times 10^{-20} \text{ g}$. In our system of 3 g l^{-1} TiO₂, the number of TiO₂ particles will consequently be $5.53 \times 10^{19} \text{ particles l}^{-1}$ which is equivalent to $9.2 \times 10^{-5} \text{ mol particles l}^{-1}$.

The TiO₂ electron concentration was calculated from the absorbance measurements (see Figure 3.2) and providing that the extinction coefficient is known according to Beer's law:

$$A = \epsilon bc \quad (\text{Eq. 3.8})$$

where A is the absorbance, b is the optical path length (1 cm), and ϵ is the extinction coefficient.

The extinction coefficient of stored TiO_2 electrons was determined at 600 nm from the titration with Benzoquinone (BQ)⁷⁷, which reacts with TiO_2 electrons according to Eq.3.9:



It was observed that the absorbance of stored electrons at 600 nm decreases linearly with an increase of the BQ concentration. Table 3.1 summarizes the extinction coefficient values determined for different TiO_2 particles. An average value $\epsilon_{600\text{nm}} = (600 \pm 20) \text{ M}^{-1} \text{ cm}^{-1}$ was determined from different titration experiments (cf. Table 3.1 and Figure 3.5). This value agrees rather well with the values of $470 \text{ M}^{-1} \text{ cm}^{-1}$ ⁷⁷ determined in acidic solution or $800 \text{ M}^{-1} \text{ cm}^{-1}$ determined in alkaline solution.¹¹⁷ According to the determined value of $600 \text{ M}^{-1} \text{ cm}^{-1}$, the concentration of stored electrons in the reported experiments is found to range from 1×10^{-4} to $2.5 \times 10^{-3} \text{ M}$ (6×10^{19} – 150×10^{19} electrons l^{-1}), corresponding to an average of about 1– 27 electrons / TiO_2 particle.

Table 3.1: Summary of the extinction coefficient values determined for different TiO_2 suspensions.

TiO_2 particles	Extinction coefficient at 600 nm ($\epsilon_{600\text{nm}}$) / $\text{M}^{-1} \text{ cm}^{-1}$
Fresh prepared aqueous suspension (particles 1)	600
Fresh prepared aqueous suspension (particles 2)	625
1 week aged aqueous suspension of particles 1	585
2 weeks aged aqueous suspension of particles 1	578

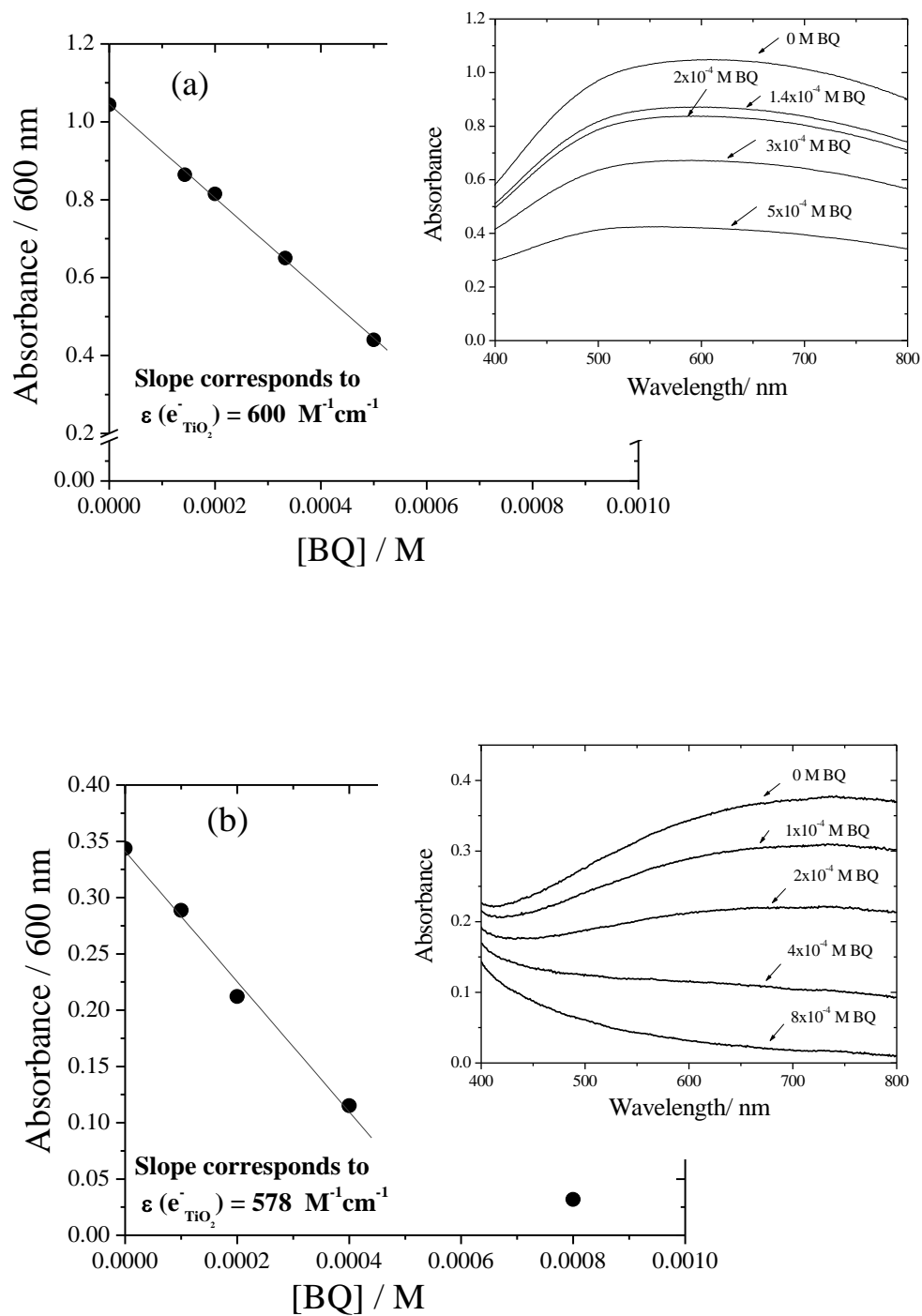


Figure 3.5: The dependency of the absorbance change of TiO₂ electrons at 600 nm due to the titration of the stored electrons with different concentration of benzoquinone on BQ concentrations (a) using freshly prepared aqueous TiO₂ suspension and (b) 2 weeks aged TiO₂ suspensions (b). Insets show the final absorbance of stored electrons after their titration with different BQ concentrations.

The Photonic Efficiency for the TiO₂ Electron Storing

The photonic efficiency ζ of the storing of the TiO₂ electrons is calculated from the ratio of the rate of the build-up of the stored electrons (R) and the incident photon flux (J_0)¹¹⁸ (see Eq. 3.10 and 3.11),

$$\zeta (\%) = \frac{R.V}{J_0.A} .100 \quad (\text{Eq. 3.10})$$

where

$$J_0 = \frac{I.\lambda}{N_A .h.c.} \quad (\text{Eq. 3.11})$$

The rate of the formation of the stored electrons (R) is calculated from the slope obtained from the build-up of the stored TiO₂ electrons concentration as a function of the illumination time (Figure 3.6) to be $6 \times 10^{-8} \text{ mol l}^{-1} \text{ s}^{-1}$. The illumination of the deaerated TiO₂ aqueous suspension in presence of methanol was performed using a double jacket Duran glass reactor (110 cm³) with two outlets for gas purging (see section 2.5.2 and Figure 2.3 (a)). The TiO₂ electron concentration values shown in Figure 3.6 were calculated according to Beer's law as shown in the previous section according to the absorbance values presented in Figure 3.2 and using the extinction coefficient of $600 \text{ M}^{-1}\text{s}^{-1}$.

The light intensity (I) was calculated based on the UV light meter measurement to be $2.6 \times 10^{-3} \text{ J s}^{-1} \text{ cm}^{-2}$ at an average wavelength (λ) of 350 nm with N_A : Avogadro's number, h is Planck's constant, c: light velocity and the volume (V) being $6 \times 10^{-2} \text{ l}$; the irradiated surface area (A) was 12.56 cm^2 . The average photonic efficiency measured under the above conditions was 3.8 %.

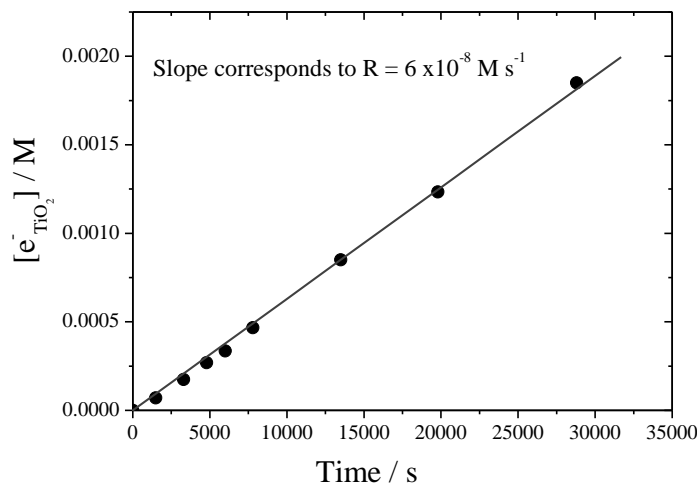


Figure 3.6: Change in concentrations of TiO₂ stored electrons as a function of the employed irradiation time, the concentration data were obtained from the absorbance measurements shown in Figure 3.2 and providing that the average extinction coefficient is $600 \text{ M}^{-1}\text{s}^{-1}$.

3.3. Stopped Flow Investigations

3.3.1. Spectrum of the Stored Electrons

As a blank experiment, the absorption spectrum of the stored electrons on TiO_2 was measured using the stopped flow instrument. The blue colloidal suspension of the stored TiO_2 electrons at pH 2.3 was mixed with a deaerated aqueous HCl solution at the same pH in the stopped flow apparatus and the change of absorption with time was recorded. Figure 3.7 (a) shows the transient absorbance spectrum (400–640 nm) that is recorded 5 ms after the mixing. A broad absorption spectrum is observed with an absorption maximum around 600 nm. The inset of Figure 3.7 (a) shows the transient absorption vs. Time signal at 600 nm (mixing occurred at $t = 0$ s), it is obvious that the signal remains unchanged during the entire measurement time of 1 s. Figure 3.7 (b) shows the typical absorption spectrum of stored TiO_2 electrons prepared under the same conditions, *i.e.*, after 1:1 dilution of the stored TiO_2 electron suspension with deaerated aqueous HCl solution. It is important to clarify that the absorption spectrum obtained from the stopped flow measurements is measured in a cuvette with an optical path length of 0.2 cm, while that obtained from the steady state UV–vis spectrophotometer is measured with an optical path length of 1.0 cm. As can be seen from Figure 3.7 (b), the absorbance of the electrons is 5 times higher (using the 1 cm cuvette) in comparison with the stopped flow measurements reflecting the difference in the optical path length (10 mm vs. 2 mm).

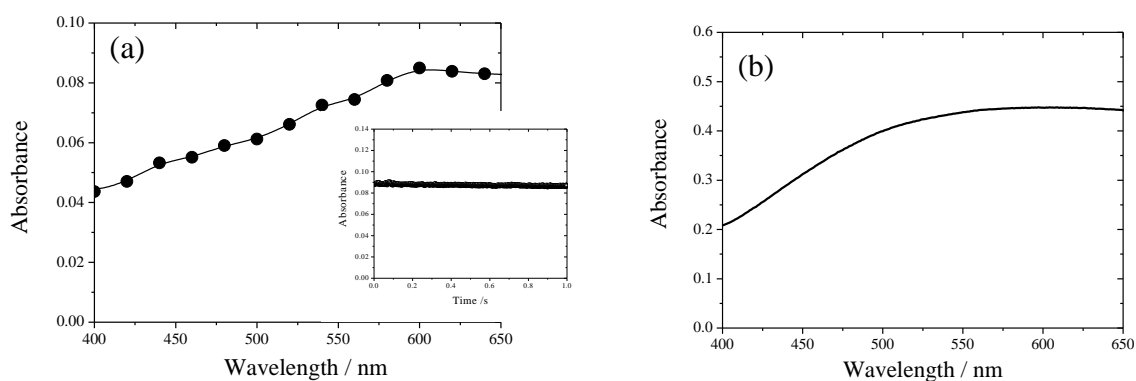
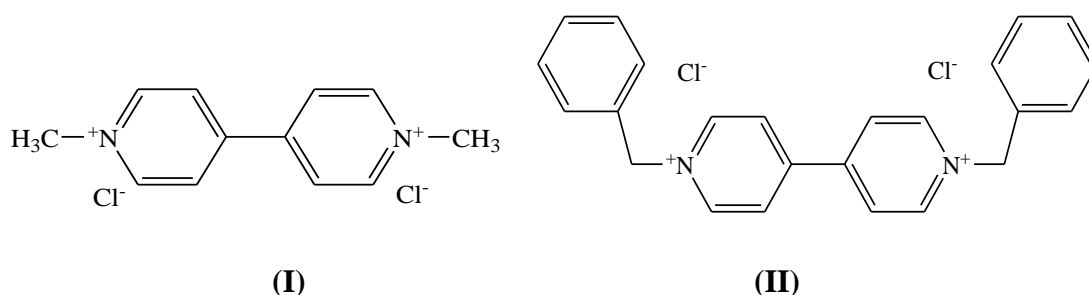


Figure 3.7: (a) Transient absorption spectrum measured after 5 ms of mixing a deaerated aqueous suspension of 3.8×10^{-2} M TiO_2 molecules (9.2×10^{-5} mol TiO_2 particles l^{-1} loaded with about 7.7 electrons per TiO_2 particle) at pH 2.3, inset shows transient absorbance vs. time signals observed at 600 nm after mixing of an aqueous TiO_2 electrons suspension with deaerated water at pH 2.3 (HCl), (b) Steady state absorbance of a deaerated aqueous TiO_2 electron suspension after 1:1 mixing with deaerated H_2O at pH 2.3 under the identical experimental conditions of (a).

3.3.2. One Electron Reduction of Viologen Compounds and Ensuing Electron Transfer from Viologen Radicals to the Surface of Metal Nanoparticles

The following study represents and discusses the one electron reduction of viologen compounds (methyl viologen (MV²⁺) (I) and benzyl viologen (BV²⁺) (II)) in aqueous solution at acidic pH (2.7) using the electrons loaded on TiO₂ nanoparticles. The electron transfer rate constants were obtained and compared with the published values using laser flash photolysis technique. The factors influencing the formation kinetics of V^{•+} such as the initial concentration of V²⁺ compounds and the ionic strength as well as the factors influencing the decay kinetics of the formed viologen radical cations such as the presence of metal particles have been studied.



UV-vis Absorption Measurements

Figure 3.8 shows the steady state UV-vis absorption spectra observed for methyl viologen and benzyl viologen radical cations that are formed after mixing of the corresponding dications (2×10^{-3} M) with electrons loaded TiO₂ nanoparticles ($[e^-_{\text{TiO}_2}] = 1 \times 10^{-4}$ M) at pH 2.7. The typical absorption bands with peaks at 605 ($\epsilon_{605} = 11000 \text{ M}^{-1} \text{ cm}^{-1}$)^{119(a)} and 394 nm are attributed to methyl viologen radical cation, and bands with peaks at 600 and 399 nm are attributed to benzyl viologen radical cation ($\epsilon_{605} = 13000 \text{ M}^{-1} \text{ cm}^{-1}$).^{119(b)} These spectra are resulting from the one electron reduction of viologen dications to their corresponding radical cations



However, further reduction of MV^{•+} was reported at alkaline aqueous solution (pH 13)¹²⁰ leading to the disappearance of the blue colouration of MV^{•+} and the appearance of the yellow coloration of MV⁰ with a characteristic absorption band at 385 nm. This second electron transfer reaction was not observed in our system at acidic pH. It is estimated from the final

height of the absorbance maxima at 600 nm of $V^{\bullet+}$ (Figure 3.8) and the extinction coefficient values that the final concentration of $V^{\bullet+}$ generated from the one electron reduction of V^{2+} have the values of $\sim 9 \times 10^{-5}$ M and 8.5×10^{-5} M for $MV^{\bullet+}$ and $BV^{\bullet+}$ respectively. Since the initial electron concentration is 1×10^{-4} M, about 10 % of electrons in case of MV^{2+} and 15% of electrons in case of BV^{2+} did not contribute to the one electron reduction.

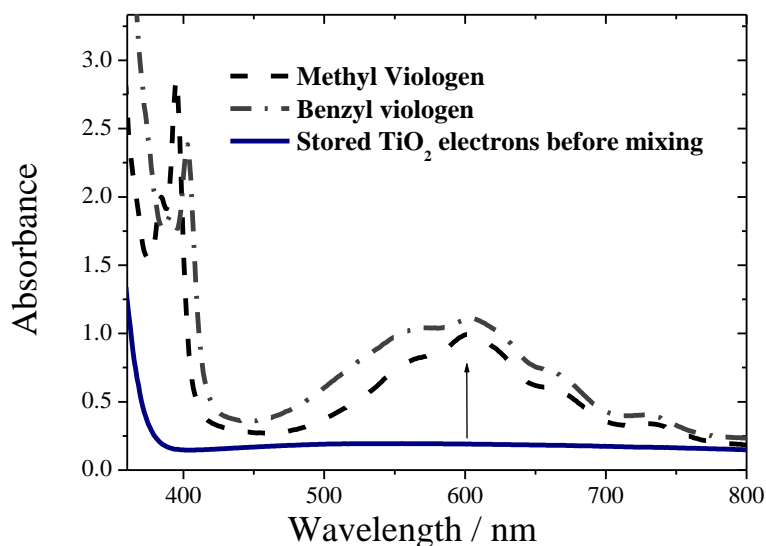


Figure 3.8: Steady state UV-vis absorbance spectra of the methylviologen radical ($MV^{\bullet+}$) and the benzylviologen radical ($BV^{\bullet+}$) measured after mixing of electrons loaded TiO_2 suspension ($[TiO_2] = 9.2 \times 10^{-5}$ M (particles), $[e^-_{TiO_2}] = 1 \times 10^{-4}$ M, ~ 1 electron/ particle) with an Ar-saturated aqueous solutions of the corresponding dication ($[V^{2+}] = 1 \times 10^{-3}$ M) at pH 2.7, the final concentration of viologen radicals calculated from the final absorbance value and the corresponding extinction coefficient values are 9×10^{-5} M and 8.5×10^{-5} M, respectively, for $MV^{\bullet+}$ and $BV^{\bullet+}$, respectively.

Stopped Flow Investigations. The kinetics of the electron transfer from TiO_2 nanoparticles to the methyl viologen dications were investigated by mixing the electron loaded TiO_2 suspension with deaerated aqueous viologen solution in the stopped flow apparatus and following the change in the absorbance of the resulting solution with time. The concentration of the viologen dication was chosen to be in excess compared to the TiO_2 electrons concentration in order to simplify the kinetic analysis. For the one electron reduction according to Eq. 3. 12, the rate is given by

$$R = k_2[V^{2+}][e^-_{TiO_2}]$$

Since the concentration of viologen dication was in large excess ($[V^{2+}] \gg [e^-_{TiO_2}]$), as the reaction progresses only a small amount of V^{2+} is consumed and its concentration can be considered to stay constant. So that,

$$R = k' [e^-_{TiO_2}]$$

where $k' = k_2 [V^{2+}]_0$ (k' or k^{obs} with units s^{-1})

By collecting k^{obs} for many reactions with different concentrations of $[V^{2+}]$; a plot of k^{obs} versus $[V^{2+}]$ gives k_2 ($M^{-1} s^{-1}$), the regular second order rate constant as the slope.

Figure 3.9 shows the kinetic curves of the build-up of the absorbance vs. time signal at 600 nm after mixing. The initial concentration of loaded electrons and that of the viologen compounds are identical to that in the steady state experiment. The individual electron transfer rate constants (k^{obs}) were extracted by the single exponential fitting of the transient absorbance shown in Figure 3.9 to the expression for the pseudo first order reaction.

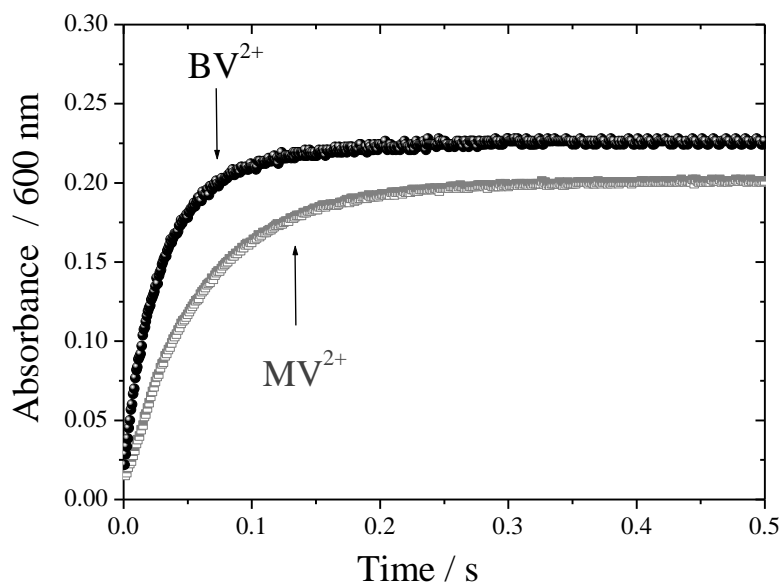


Figure 3.9: Time profiles of the build-up of methylviologen radical and benzylviologen radical absorbance at 600 nm observed upon mixing of electrons loaded TiO_2 suspension ($[TiO_2] = 9.2 \times 10^{-5}$ mol particles l^{-1} , $[e^-_{TiO_2}] = 1 \times 10^{-4}$ M, 1 electron/particle) with an Ar-saturated aqueous solutions of the corresponding dication ($[V^{2+}] = 1 \times 10^{-3}$ M) at pH 2.7, the final concentration of viologen radicals calculated from the final absorbance value and the corresponding extinction coefficient values are 9×10^{-5} M and 8.6×10^{-5} M, respectively, for $MV^{•+}$ and $BV^{•+}$, respectively.

The observed rate constant for the one electron reduction of benzyl viologen ($k^{obs} = 31.2 \text{ s}^{-1}$) is found to be higher than that for the one electron reduction of methyl viologen ($k^{obs} = 16.7 \text{ s}^{-1}$) under identical experimental conditions. This can be readily attributed to the fact that the redox potential of benzyl viologen E ($\text{BV}^{2+}/\text{BV}^{•+}$) = -0.374 V vs. NHE ¹²¹ is more positive than that of methyl viologen E ($\text{MV}^{2+}/\text{MV}^{•+}$) = -0.450 V vs. NHE .¹²² On other hand this difference in the rate can be attributed to the higher electron withdrawing effect of benzyl group in benzyl viologen than that of methyl group in methyl viologen. Figure 3.10 shows the evolution of the time resolved UV-vis spectra of methyl viologen radical cation recorded at different reaction times at the wavelength range of 380 nm– 640 nm after mixing of the TiO_2 electron suspension with the aqueous methyl viologen solution under identical conditions as those used for the experiments reported in Figure 3.8. The observed spectra were typically assigned to $\text{MV}^{•+}$ with the two maxima at 605 nm and 395 nm.

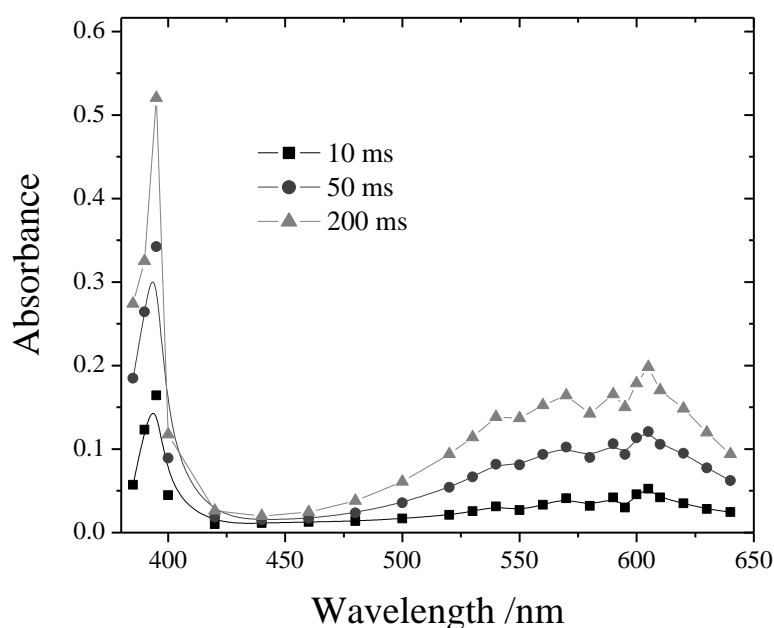


Figure 3.10: Transient absorption spectra measured after various times of mixing of an Ar-saturated aqueous solution of the methylviologen dication ($1 \times 10^{-3} \text{ M}$) with TiO_2 electron suspension ($[\text{e}^-_{\text{TiO}_2}] = 1 \times 10^{-4} \text{ M}$) at pH 2.7, experimental conditions are identical to those in Figure 3.8 and 3.9.

Figure 3.11 (a) and (b) show the kinetic curves of the build-up of the absorbance vs. time signals at 600 nm observed upon mixing the aqueous suspension of TiO_2 loaded with electrons ($[\text{TiO}_2] = 9.2 \times 10^{-5} \text{ M}$ (particles), $[\text{e}^-_{\text{TiO}_2}] = 1 \times 10^{-4} \text{ M}$, corresponds to 1 electron/particle) with aqueous solutions of different concentrations of the methyl viologen dication

and the benzyl viologen dication, respectively. The second order rate constants $2.06 \times 10^4 \text{ M}^{-1} \text{ s}^{-1}$ and $2.86 \times 10^4 \text{ M}^{-1} \text{ s}^{-1}$ for methyl viologen and benzyl viologen, respectively, were determined from the linear relationship of the corresponding dication concentrations and the observed pseudo first order rate constant values (cf. Figure 3.12). The rate of the reaction in the milliseconds time range reveal that the electron transfer occurs from TiO_2 to viologen dications in the bulk.

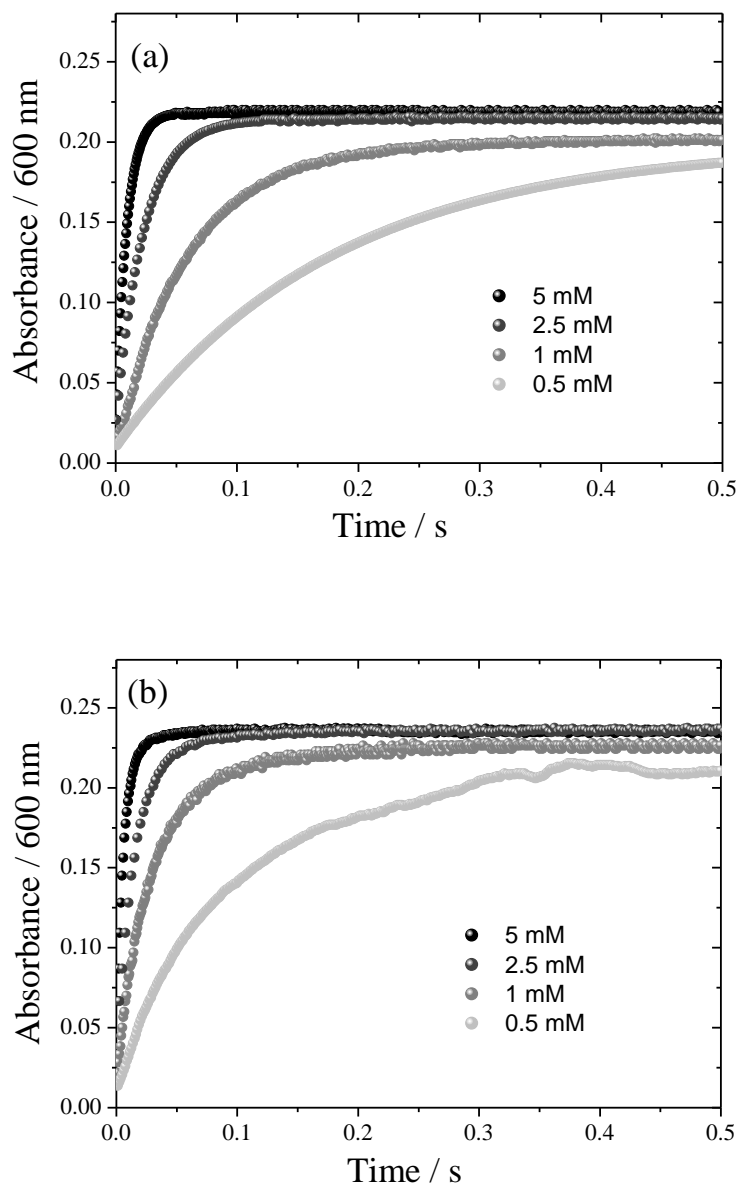


Figure 3.11: Time profiles of the build-up of viologen radicals absorbance at 600 nm observed upon mixing of aqueous suspensions of TiO_2 nanoparticles loaded with electrons ($[\text{TiO}_2] = 9.2 \times 10^{-5} \text{ M}$ (particles), $[\text{e}^-_{\text{TiO}_2}] = 1 \times 10^{-4} \text{ M}$, 1 electron/ particle) with Ar-saturated aqueous solutions containing different concentrations of viologen dication at pH 2.7.

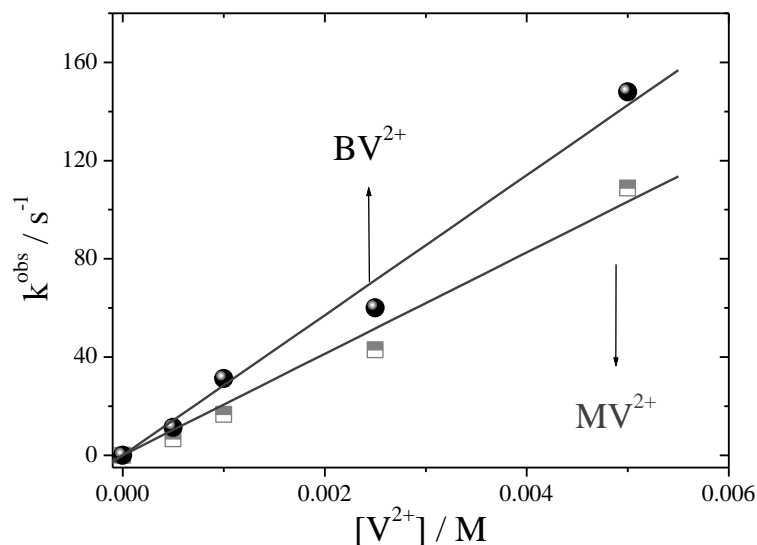


Figure 3.12: Linear dependency of the observed first order rate constants on the V^{2+} concentrations. First order rate constants k^{obs} were determined from the data analysis according to Figure 3.11.

Viologen compounds were extensively used as a model for electron acceptors in the early studies of the dynamic of interfacial electron transfer in colloidal semiconductors using laser flash photolysis technique.^{79, 80} The rate constants of the build-up of methyl viologen radical were obtained from the laser flash photolysis of the solution containing 5 g l^{-1} TiO_2 and 10^{-3} M MV^{2+} at various pH values.⁷⁹ The authors found that the first order rate constants of the MV^{+} formation increased dramatically over a pH region from 3 to 8. Increasing the rate constant with increasing the pH was explained in terms of the negative shift of the conduction-band position of the TiO_2 particle with increasing the pH. The authors used polyvinyl alcohol for stabilizing the TiO_2 particles above pH 3. However, it was not possible to follow the effect of changing pH with our naked particles since they were only stable below pH 3.5. The second order rate constant obtained here at pH 2.7 ($2.06 \times 10^4 \text{ M}^{-1} \text{ s}^{-1}$) (Figure 3.8) was found to be smaller than the value obtained by Duonghong et al.^{79 (b)} (estimated from the data in Figure 6^{79(b)} to be about $1 \times 10^5 \text{ M}^{-1} \text{ s}^{-1}$ at pH 3 (using the data of the first order rate constant of 10^2 s^{-1} and $[\text{MV}^{2+}]$ of 10^{-3} M). However, in both techniques a one electron transfer reaction occurred, in the laser flash photolysis experiments the TiO_2 colloidal suspension are in equilibrium with adsorbed and bulk MV^{2+} while there is no adsorbed MV^{2+} on the TiO_2 surfaces employing the stopped flow technique.

It is estimated from the final height of the absorbance of $V^{\bullet+}$ (Figure 3.11) and the extinction coefficient values that the maximum concentration of $V^{\bullet+}$ generated from the one electron reduction of V^{2+} were independent on the initial concentration of V^{2+} and attaining a limit of $\sim 9 \times 10^{-5}$ M and 8.6×10^{-5} M for $MV^{\bullet+}$ and $BV^{\bullet+}$ respectively. Since the initial electron concentration is 1×10^{-4} M, about 10 % of electrons in case of MV^{2+} and 14% of electrons in case of BV^{2+} did not contribute to the one electron reduction.

Duonghong et al.^{79 (b)} reported a yield of only $\sim 10\%$ $MV^{\bullet+}$ upon the reduction of MV^{2+} by $e^-_{TiO_2}$ at pH 2.7 (estimated from the data presented in Figure 4^{1 (a)}). One possible explanation for these considerable differences is the different size of the employed TiO_2 particles in both studies. While Duonghong et al.^{79 (b)} have used rather large TiO_2 particles with a diameter of 20 nm exhibiting bulk electronic properties, the particles employed here are much smaller (2-3 nm). This is the size regime when even titanium dioxide starts to exhibit quantum size properties.¹⁴ From the calculations performed by Kormann et al. one can conclude that in the present study where the TiO_2 particles are within the quantum size regime a negative shift of the position of the conduction band of about 0.15 eV relative to the bulk anatase particle can be expected.¹⁴ According to the Nernst Equation, this shift is equivalent to a pH change of almost 3 units. Thus, the driving force for the reduction of MV^{2+} by the $e^-_{TiO_2}$ particles employed here at pH 2.7 should be almost identical to that of the larger TiO_2 particles employed by Duonghong et al. at pH 6 (where these authors also observed an almost quantitative $MV^{\bullet+}$ formation).

Effect of Ionic Strength

The effect of ionic strength on the formation kinetics of methyl viologen radical was studied by performing another kinetic stopped flow experiment by mixing deaerated aqueous solutions of methyl viologen dication at different concentration of NaCl with electron loaded aqueous TiO_2 suspensions. Figure 3.13 shows the kinetic curves of the formation of the methyl viologen radical after mixing of methyl viologen dication solution (1×10^{-3} M) containing various concentration of sodium chloride (0 M, 1×10^{-3} M, 2.5×10^{-3} M, 4×10^{-3} M) and electron loaded TiO_2 aqueous suspension ($[e^-_{TiO_2}] = 1 \times 10^{-4}$ M).

The effect of ionic strength on the rate of MV^{2+} reduction can be expressed by the Brønsted – Bjerrum equation, based on the limiting law of Debye–Hückel (Eq. 3.13).

$$\log k = \log k_0 + 1.02 z_A z_B I^{1/2} \quad (\text{Eq. 3.13})$$

where k is the second order rate constant, k_0 is the second order rate constant at infinite dilution and z_A and z_B are the charges of the ions involved in the rate determining step. For more concentrated solutions the Brønsted–Bjerrum and the extended law of Debye–Hückel can be combined to obtain the following expression:

$$\log k = \log k_0 + 1.02 z_A z_B [I^{1/2}/1 + I^{1/2}]^{1.22(b-d)} \quad (\text{Eq. 3.14})$$

The second order rate constants (k) can be calculated from the half life time ($t_{1/2}$) obtained from the data in Figure 3.13(a) and knowing the initial concentrations of MV^{2+} (C_0) according to Eq. 3.15. The calculated second order rate constant values are presented in Table 3.2.

$$k = 1/t_{1/2}C_0 \quad (\text{Eq. 3.15})$$

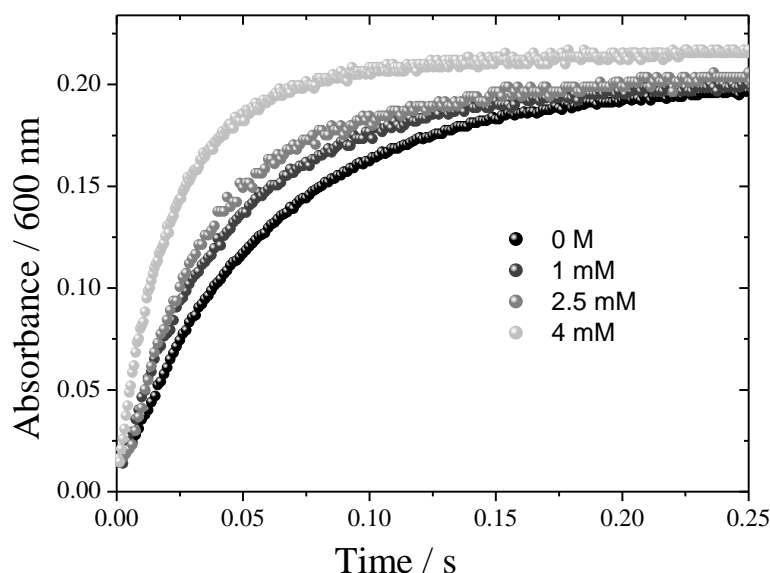


Figure 3.13: Time profiles of the formation of methylviologen radical absorbance at 600 nm observed upon mixing of electrons loaded TiO_2 suspension ($[e^-_{TiO_2}] = 1 \times 10^{-4}$ M) with Ar-saturated methylviologen dication aqueous solutions (1×10^{-3} M) at various NaCl concentrations at pH 2.7.

Table 3.2: Second order rate constant values obtained from the half life time at $[MV^{2+}]_0 = 1 \times 10^{-3}$ M and various ionic strengths.

$I / 10^{-3}$ M	$t_{1/2} /$ s	$k / 10^4$ M ⁻¹ s ⁻¹
0	0.06	1.66
1	0.045	2.2
2.5	0.038	2.6
4	0.027	3.7

From the data in Table 3.2 it can be observed that the higher rate constants are attained at higher ionic strengths. At low pH the surface of TiO_2 particles are positively charged and increasing the chloride ions reduced the electrostatic repulsion between MV^{2+} and the positively charged particles leading to increasing the chance of a successful reaction. It was suggested that this effect is due to ions in the diffuse double layer, rather than ions specifically adsorbed on the particles.¹²³ Particles with high positive charge will bind the counter ions close to their surfaces which may reduce the effective charge experienced by positive viologen dication.

Using the rate constant data at different ionic strengths, a graph was obtained employing the Brønsted–Bjerrum, based on the limiting law of Debye–Hückel (Figure 3.14 (a)). The product of the charges $z_A z_B$ is 5. Considering the extended law of Debye–Hückel (Figure 3.14 (b)) $z_A z_B$ is 5.2. It is not possible to correlate the values of $z_A z_B$ to the theoretical number of charges of the ions involved in the reaction since the number of charges of the TiO_2 particle surface is not known yet and its determination is beyond this study.

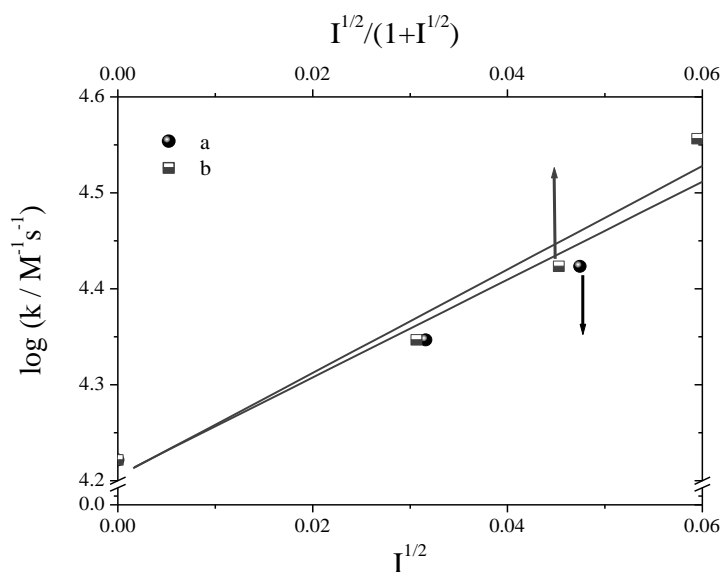


Figure 3.14: Effect of ionic strength on the rate of reaction applying limiting Debye–Hückel law (a) and extended Debye–Hückel law (b).

Effect of Metal Nanoparticles

Previous laser flash photolysis studies have shown that when a system containing $\text{Pt/TiO}_2/\text{V}^{2+}$ is irradiated, no color formation indicating the formation of viologen radicals was observed.

Instead, small amounts of H_2 were generated.¹²⁴ The authors attributed this to the reoxidation of the formed viologen radicals according to the following reaction



Therefore, the effect of the presence of metal particles on the reoxidation of the methylviologen radical cation has been investigated under our experimental conditions. The results obtained in the presence and the absence of Au_n^0 particles, respectively (average particle size ~ 5 nm, Sigma) are shown in Figure 3.15 (a). Obviously, the absorption signals of the methylviologen radical cation at 600 nm remain constant for seconds in the absence of gold particles, while the absorbance signals decay following first order kinetics when gold particles are present. The measurements performed at different metal concentrations show a linear dependency of the first order rate constants of the $MV^{\bullet+}$ decay on the concentration of Au_n^0 particles (Figure 3.15 (b)).

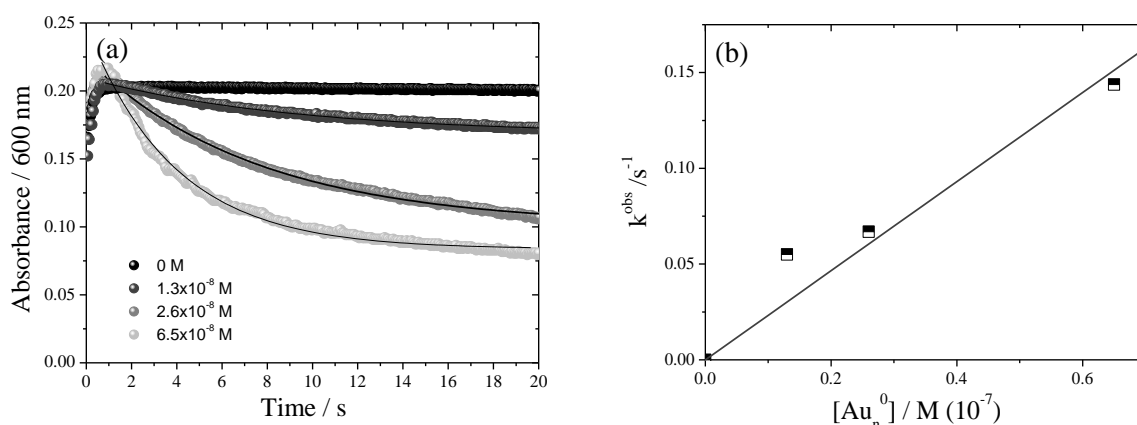


Figure 3.15: (a) Time profiles of the formation and decay of the methylviologen radical absorbance at 600 nm observed upon mixing of electron loaded TiO_2 suspension ($[e^-_{TiO_2}] = 1 \times 10^{-4}$ M) with Ar-saturated methylviologen dication aqueous solutions (1×10^{-3} M) at pH 2.7 ($[H^+] = 3.2 \times 10^{-3}$ M) in the absence and in the presence of various concentrations of gold metal particles, solid lines represent the first order fits. (b) Linear dependency of the concentration of the gold particles on the observed rate constant of the methylviologen radical decay at 600 nm, the slope corresponding to $2.6 \times 10^6 \text{ M}^{-1} \text{ s}^{-1}$.

$MV^{\bullet+}$ apparently acts as an electron relay for the hydrogen production process thus transferring the electrons from the TiO_2 to the adsorbed H^+ on the surface of the catalyst (i. e., the metal particles) being reoxidized in turn. The decay of the absorbance signal of $MV^{\bullet+}$ in the presence of gold particles (Figure 3.15 (a)) is therefore suggested to be caused by their reaction with adsorbed H^+ on the surface of the Au_n^0 particles, i. e., forming molecular

hydrogen through an electron transfer process. Increasing the decay rate with increasing the concentration of gold metal particles can thus be explained by the increasing number of the active sites (metal catalyst) for these reactions. It is important to notice that the final absorbance observed in Figure 3.15 (a) can be attributed to the absorbance of the gold nanoparticles at this wavelength implying that MV^{2+} has been reoxidized completely. A bimolecular rate constant of $k = 2.6 \times 10^6 \text{ M}^{-1} \text{ s}^{-1}$ is obtained from the data analysis of Figure 3.15 (b). A direct transfer of $e^-_{\text{TiO}_2}$ to adsorbed H^+ on the Au_n^0 particle surfaces can be ruled out in this work even at low pH (2.7). Under the employed experimental conditions this reaction is found to have a much lower rate constant ($k^{obs} = 0.05 \text{ s}^{-1}$) than the one electron reduction of methyl viologen ($k^{obs} = 16.7 \text{ s}^{-1}$). Figure 3.16 shows the kinetic curve observed upon mixing the $e^-_{\text{TiO}_2}$ suspension with an aqueous solution of gold metal particles ($6.5 \times 10^{-8} \text{ M}$ (particles)) in the absence of MV^{2+} under otherwise identical experimental conditions to those employed for the experiments presented in Figure 3.15 (a). A second order rate constant of $k = 7.7 \times 10^5 \text{ M}^{-1} \text{ s}^{-1}$ is thus obtained for the direct transfer of $e^-_{\text{TiO}_2}$ to the Au_n^0 particle (analyzing the data shown in Figure 3.16). Accordingly, the rate constant of H^+ reduction in the presence of MV^{2+} ($2.6 \times 10^6 \text{ M}^{-1} \text{ s}^{-1}$) is more than 3 times higher than that in the MV^{2+} free system ($7.7 \times 10^5 \text{ M}^{-1} \text{ s}^{-1}$). A detailed kinetic study of the electron transfer to various noble metal particles will be presented later (Section 3.1.3.5). It is important to note that neither the reaction between TiO_2 and MV^{2+} nor that between TiO_2 and Au_n^0 is diffusion controlled. According to the so-called Smoluchowski equation the rate constant of a diffusion-controlled second order reaction ($k_{AB} / \text{M}^{-1} \text{ s}^{-1}$) can be calculated as follows

$$k_{AB} = \frac{4\pi r_{AB} D_{AB} N_{Av}}{1000} \quad (\text{Eq. 3.17})$$

where r_{AB} is the encounter distance between the TiO_2 and the metal particles (i.e., the sum of the radii of the TiO_2 and the metal particle), D_{AB} is the sum of the diffusion coefficients of the TiO_2 and the metal particle ($D_{\text{TiO}_2\text{Au}^0} = D_{\text{TiO}_2} + D_{\text{Au}^0}$) and N_{Av} is Avogadro's number. The diffusion coefficient D_A can be calculated according to the Stokes- Einstein equation (Eq. 3.17)

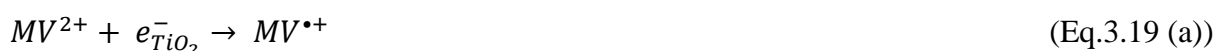
$$D_A = \frac{kT}{6\pi\eta r} \quad (\text{Eq. 3.18})$$

where k is the Boltzmann constant = $1.381 \times 10^{-23} \text{ m}^2 \text{ kg s}^{-2} \text{ K}^{-1}$, T is the temperature in Kelvin = 293 K, η is the dynamic viscosity of water = $1.002 \times 10^{-3} \text{ Kg m}^{-1} \text{ s}^{-1}$ and r is the radius of the reacting molecule or particle.

According to Eq. 3.17 and considering that $r_{MV^{2+}} = 150$ pm, $r_{TiO_2} = 1.25$ nm and $r_{Au_n^0} = 2.5$ nm are the radii of the MV^{2+} molecule, the TiO_2 particle and the Au_n^0 particle, respectively, the diffusion coefficients were calculated to be $D_{MV^{2+}} = 1.47 \times 10^{-5} \text{ cm}^2 \text{ s}^{-1}$, $D_{TiO_2} = 0.176 \times 10^{-5} \text{ cm}^2 \text{ s}^{-1}$ and $D_{Au_n^0} = 0.088 \times 10^{-5} \text{ cm}^2 \text{ s}^{-1}$ for the MV^{2+} molecule, the TiO_2 particle and the Au_n^0 particle, respectively. Taking these values the diffusion controlled rate constant calculated from Eq. 6 for the reaction between the TiO_2 particle and the MV^{2+} molecule is $k_{TiO_2-MV^{2+}} = 1.74 \times 10^{10} \text{ M}^{-1} \text{ s}^{-1}$ and that for the reaction between TiO_2 particle and Au^0 particle is $k_{TiO_2-Au^0} = 7.5 \times 10^9 \text{ M}^{-1} \text{ s}^{-1}$. Clearly, these rate constants are considerably higher than the second order rate constants measured for the reduction of MV^{2+} by $e^-_{TiO_2}$ ($2.06 \times 10^4 \text{ M}^{-1} \text{ s}^{-1}$) or for the reduction of the adsorbed H^+ on the metal surface by $e^-_{TiO_2}$ ($7.7 \times 10^5 \text{ M}^{-1} \text{ s}^{-1}$ (calculated from $k^{obs} = 0.05 \text{ s}^{-1}$ at $[Au_n^0] = 6.5 \times 10^{-8} \text{ M}$)).

Hence, it can be concluded that MV^{2+} acts as an electron relay accepting electrons from the TiO_2 nanoparticles and subsequently donating these electrons to H^+/H_2O on the surface of the gold particles generating H_2 gas. This will accelerate the rate of H_2 gas generation since MV^{2+} molecules can move freely in the solution transferring the electrons from the TiO_2 to the metal particles.

The reaction mechanism of the one electron reduction of the methyl viologen dication in the presence of noble metal particles can therefore be described as follows: MV^{2+} is firstly generated by the reaction with the stored TiO_2 electrons and then reacts with H^+ to produce H_2 . The mechanism is illustrated in Figure 3.17 and expressed by the following equations:



Eq. 3.19 (b) and (c) have been verified experimentally by measuring the evolved H_2 gas after 1:1 mixing of an aqueous TiO_2 suspension ($[e^-_{TiO_2}] = 1 \times 10^{-4} \text{ M}$) with an Ar-saturated aqueous methylviologen solution ($1 \times 10^{-3} \text{ M}$) at pH 2.7 ($[H^+] = 3.2 \times 10^{-3} \text{ M}$) in the presence of gold particles ($6.5 \times 10^{-8} \text{ M}$ (particles)) in a sealed tube under argon atmosphere to be $4.6 \times 10^{-5} \text{ M}$ corresponding to 92% of the initial electron concentration. The value of unreacted $MV^{\bullet+}$ can be assumed within the experimental error. Hence, our experimental results show that almost all $MV^{\bullet+}$ are able to react with Au particles generating H_2 gas.

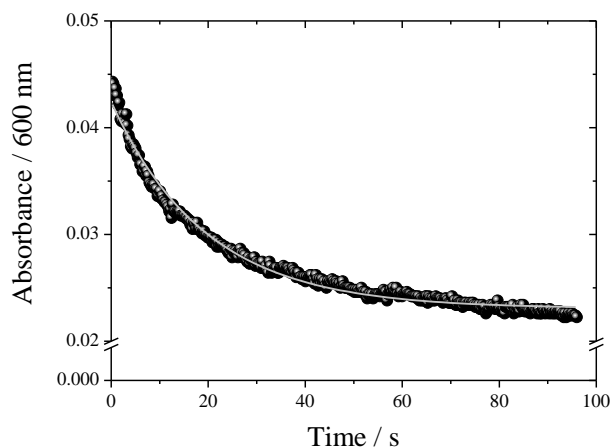


Figure 3.16: Time profile of the absorbance decay at 600 nm observed after mixing of an electron loaded TiO₂ suspension ($[e^-_{\text{TiO}_2}] = 2 \times 10^{-4}$ M, $2 e^-_{\text{TiO}_2}/\text{particles}$) with an Ar-saturated aqueous colloidal gold solution (6.5×10^{-8} M (particles)). The solid line shows the first order fit.

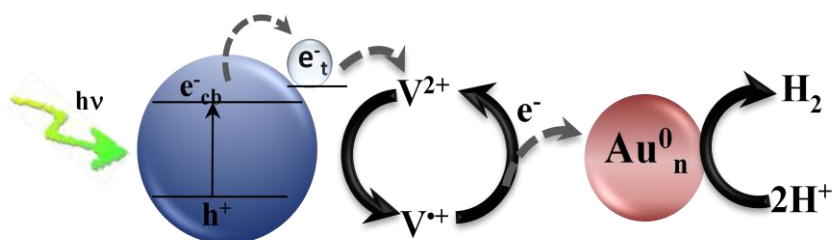


Figure 3.17: Schematic illustration of the electron transfer processes from TiO₂ nanoparticles to the viologen dication forming the viologen radical cation and the ensuing electron transfer from the radical cation to the metal particles forming H₂ gas.

3.3.3. Multi-Electron Reduction of Common Electron Acceptors Employed in Photocatalytic System

3.3.3.1. Reaction of $e^-_{\text{TiO}_2}$ with O_2 and H_2O_2

Oxygen is the usual electron acceptor employed in studies of photocatalytic reactions for environmental remediation. Hence, its role in these reactions has been the focus of attention of several theoretical and experimental studies.¹²⁵⁻¹²⁹ It is generally agreed that photogenerated electrons can reduce molecular oxygen to $\text{O}_2^{\cdot-}$ which can subsequently transform to other chemical species, such as HO_2^{\cdot} , HO_2^- , H_2O_2 , and most likely, finally to OH^{\cdot} radicals. These activated oxygen species may therefore play an important role in the oxidation of the organic electron donor. Moreover, hydrogen peroxide has been found to improve the rates of photocatalytic reactions based on the generation of highly reactive hydroxyl radicals upon its reaction with photogenerated electrons resulting in the oxidation and subsequently the complete mineralization of organic species.¹³⁰ Therefore, the reaction of both O_2 and H_2O_2 with the stored electrons on TiO_2 have been studied here in details.

Figure 3.18 (a) shows the transient absorption signals observed upon mixing aqueous stored TiO_2 electron suspensions ($[e^-_{\text{TiO}_2}] = 5.7 \times 10^{-4} \text{ M}$) at pH 2.3 with aqueous solutions containing different concentrations of O_2 ($0.65 \times 10^{-4} \text{ M}$, air-saturated ($1.25 \times 10^{-4} \text{ M}$), O_2 -saturated ($6.25 \times 10^{-4} \text{ M}$), and Argon saturated H_2O). Similar kinetic experiments for the reduction of hydrogen peroxide by the stored TiO_2 electrons were also performed. Figure 3.19 (a) shows the transient absorption signals observed upon mixing the blue suspension of TiO_2 electrons ($[e^-_{\text{TiO}_2}] = 6.9 \times 10^{-4} \text{ M}$) at pH 2.3 with different concentrations of aqueous H_2O_2 solutions, i. e., 1.56×10^{-4} , 3.12×10^{-4} and $6.25 \times 10^{-4} \text{ M}$. It is observed that in Argon flushed solution the absorbance signals are decreasing very slowly with a rate of 0.0012 s^{-1} , while in solutions containing dissolved O_2 or H_2O_2 the electron absorbance is fading rapidly, with the rate depending on the concentration of O_2 or H_2O_2 , respectively. The kinetic curves were analyzed according to double exponential decay fitting. The observed first order rate constants were found to increase linearly with increasing the concentration of the electron acceptors (O_2 , H_2O_2) and the respective second order rate constants were obtained from the slope of the linear dependencies (Figure 3.18 (b) and Figure 3.19 (b) for O_2 and H_2O_2 respectively). The values of the resulting second order rate constants are summarized in Table 3.3.

The rate constant of the first initial decay ($k_I^{\text{obs}} = 2.0 \times 10^4 \text{ M}^{-1} \text{ s}^{-1}$) and that of the second decay ($k_{II}^{\text{obs}} = 5.7 \times 10^3 \text{ M}^{-1} \text{ s}^{-1}$) for the reaction of the stored TiO_2 electrons with molecular oxygen were found to be similar to the values of the rate constants of the two slower processes k_{III}

($7.3 \pm 1.5 \times 10^3 \text{ M}^{-1} \text{ s}^{-1}$) and k_{IV} ($1.0 \pm 0.2 \times 10^3 \text{ M}^{-1} \text{ s}^{-1}$) as reported by Gao et al.¹¹³ who studied the reaction of electrons formed by radiation chemical processes in small TiO_2 particles and who suggested that these slow processes are due to the reaction of excess TiO_2 electrons with molecular oxygen in the bulk.

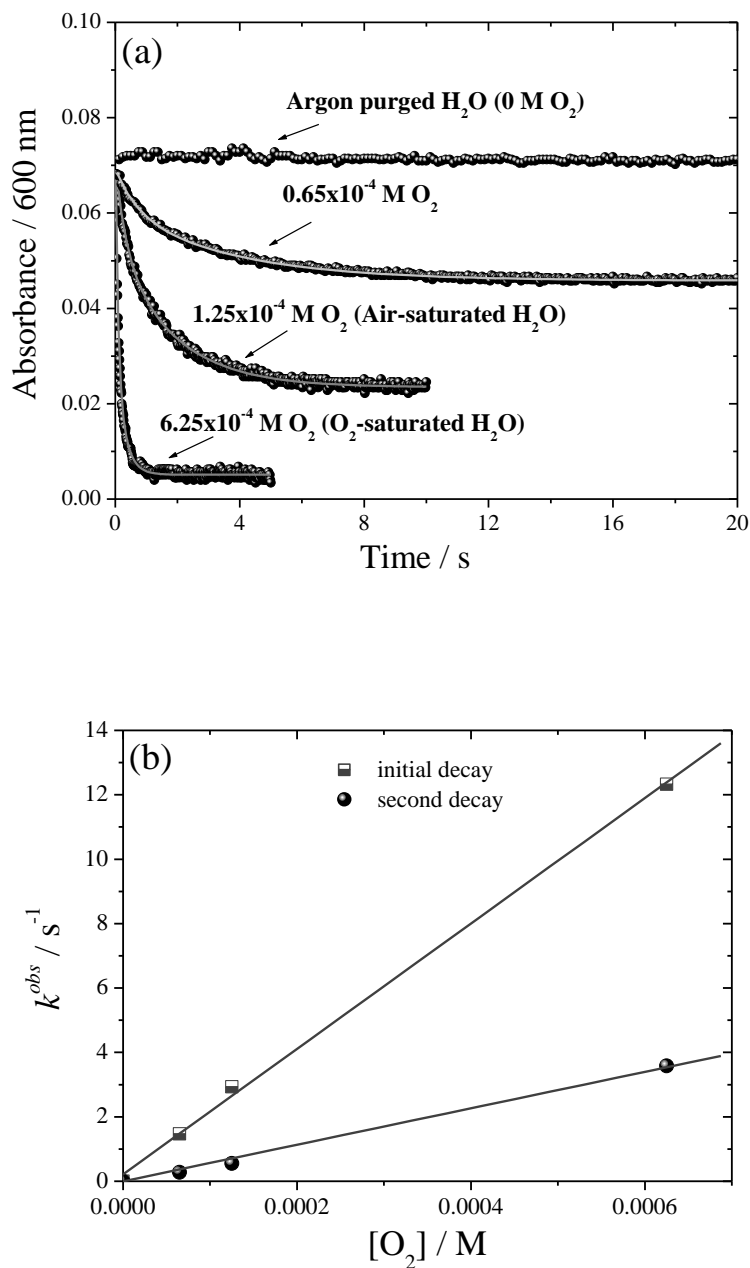


Figure 3.18: (a) Time profiles of the decay of the $e^-_{\text{TiO}_2}$ absorbance at 600 nm ($[e^-_{\text{TiO}_2}] = 5.7 \times 10^{-4} \text{ M}$, $6 e^-_{\text{TiO}_2}/\text{particle}$) observed upon mixing of their aqueous suspension with different concentration of dissolved O_2 saturated aqueous solutions at pH 2.3 (HCl). The solid lines show the double exponential fits, (b) Linear dependency of the observed first order rate constants on the O_2 concentrations. First-order rate constants determined from the data analysis according to (a).

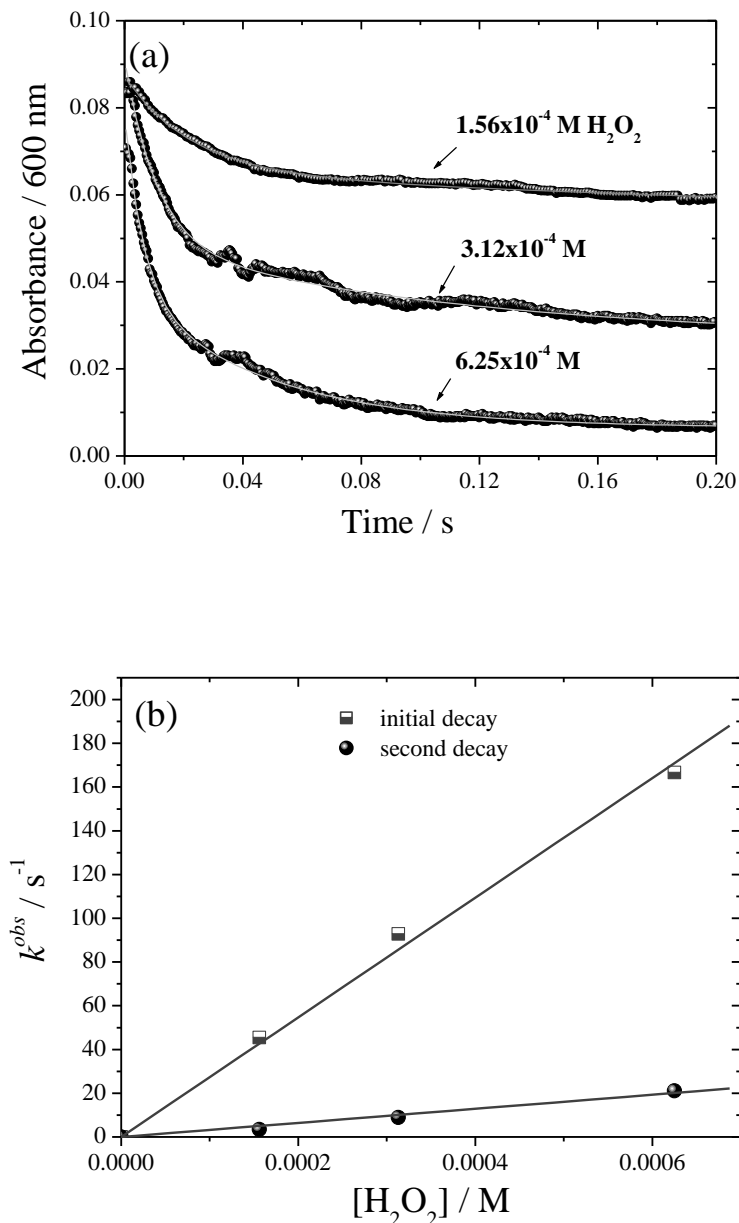


Figure 3.19: (a) Time profiles of the decay of the $e^-_{\text{TiO}_2}$ absorbance at 600 nm ($[e^-_{\text{TiO}_2}] = 6.9 \times 10^{-4}$ M, $7 e^-_{\text{TiO}_2}/\text{particle}$) observed upon mixing of their aqueous suspension with Ar-saturated H_2O_2 aqueous solutions at pH 2.3 (HCl), (b) Linear dependency of the observed first order rate constants on the H_2O_2 concentrations. First-order rate constants determined from the data analysis according to (a).

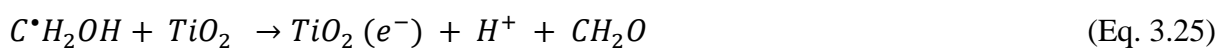
Bahnemann et al.¹³¹ determined a reaction rate constant of $7.6 \times 10^7 \text{ M}^{-1} \text{ s}^{-1}$ for the reaction of trapped electrons produced by laser flash photolysis of platinumized TiO_2 nanoparticles with molecular oxygen producing the superoxide radical which is considerably higher than the present value. However, it is important to note that the employed experimental conditions differ considerably between the laser flash photolysis study and the present stopped flow

experiments. While in the former just one electron/hole pair was generated in each TiO₂ nanoparticle during each single laser pulse, in the present study the TiO₂ particles contained between 6 and 9 electrons each. Consequently, the observed differences can be attributed to multi-electron transfer processes that are supposed to occur in the present system. Moreover, while the laser flash experiments were carried out employing colloidal TiO₂ suspension with equilibrium of adsorbed and dissolved O₂ molecules, there is no molecular oxygen present on the surface of the TiO₂ particles here. Hence, all observed electron transfer processes clearly reflect reactions with dissolved electron acceptors. The present results can therefore be regarded as an experimental proof for the assumption of Gao et al.¹¹³ that the “slow processes” are indeed reflecting the electron transfer to dissolved O₂ molecules.

The rate constant of the first initial decay ($k_I^{obs} = 2.7 \times 10^5 \text{ M}^{-1} \text{ s}^{-1}$) and that of the second decay ($k_{II}^{obs} = 3.2 \times 10^4 \text{ M}^{-1} \text{ s}^{-1}$) for the reaction of the stored TiO₂ electrons with hydrogen peroxide are found to be in very good agreement with the respective k_I and k_{II} values obtained by Gao et al.¹¹³ for small TiO₂ particles. In the latter study, the fast and slow decay rate constants, respectively, were suggested to be due to the reaction of stored electrons with adsorbed H₂O₂ molecules and H₂O₂ molecules in the bulk, respectively.

The number of consumed electrons was also determined from the kinetic curves shown in Figures 3.18 (a) and 3.19 (a) for the case that the initial concentration of the electron acceptor is lower than the initial concentration of the stored electrons. Thereby, it is found that in the presence of molecular oxygen an average of 3.1 electrons are transferred per O₂ molecule while in the presence of hydrogen peroxide an average of 1.6 electrons are transferred to each H₂O₂ molecule. Safrany et al.⁷⁷ estimated a similar value of 3.3 electrons consumed during the reduction of one oxygen molecule employing radiation induced TiO₂ electrons. The authors attributed this to the occurrence of two parallel pathways, *i.e.*, the two and the four electron reduction of O₂ to water which can be explained as following: in acidic medium molecular oxygen reacts with one electron producing HO₂[•] radicals (Eq. 3.20), which are known to disproportionate to O₂ and H₂O₂ (Eq. 3.21). Thus, oxygen effectively reacts with 2 electrons to produce H₂O₂. However, no H₂O₂ could be detected here after mixing suspensions of stored e⁻_{TiO₂ with acidic aqueous solutions containing O₂ using a very sensitive enzymatic analytical method.¹³² Presumably, H₂O₂ remains on the TiO₂ surface where it rapidly reacts with another electron producing an [•]OH radical along with an OH⁻ ion (Eq. 3.22), which is neutralized in acidic solution (Eq. 3.23). The [•]OH radical reacts with methanol by hydrogen abstraction resulting in the formation of a [•]CH₂OH radical (Eq. 3.24)}

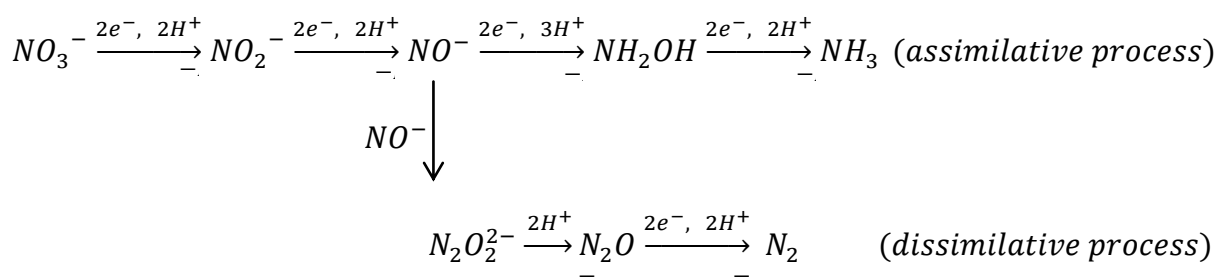
which can in turn transfer an electron to TiO₂ (Eq. 3.25). This pathway results in the reduction of one oxygen molecule to water consuming a net amount of only two electrons. On the other hand, when hydrogen peroxide reacts with two electrons (Eq. 3.26), the reduction of oxygen to water requires a net amount of 4 electrons.



3.3.3.2. Reaction of $e_{TiO_2}^-$ with Nitrate Ions

The photocatalytic reduction of nitrate has recently received special attention in view of pollution control.¹³³⁻¹³⁸ Therefore it is of particular interest to study the kinetics of these reduction reactions by the stored TiO₂ electrons.

There are two ways of reducing nitrate and nitrite ions, i. e., the dissimilative and the assimilative process yielding dinitrogen gas and ammonia, respectively, according to the following scheme.¹³⁹



According to this scheme, it is obvious that 5 or 8 electrons, respectively, are required to reduce nitrate to dinitrogen or ammonia, respectively. Moreover, also the one-electron reduction of nitrate ions is feasible in photocatalytic systems:



In aqueous solutions NO_2 will, however, disproportionate according to the following equation:



Thus, Eq.3.27 and 3.28 cannot be easily distinguished from the 2-electron reduction of nitrate forming nitrite.

In the presence of excess electrons nitrate can rather react by a five electron transfer step to form dinitrogen *via*



N_2 in turn can be reacting by a 2 electron transfer reaction to produce N_2H_5^+ ions



N_2H_5^+ will further react with two electrons to produce 2 NH_4^+ ions



In the present kinetic study, stopped flow experiments were performed by mixing an aqueous suspension of the stored electrons on TiO_2 and aqueous nitrate solution from sodium nitrate at acidic pH (2.3). The transient decay curves of the absorbance of the TiO_2 electrons ($[\text{e}_{\text{TiO}_2}^-] = 5.5 \times 10^{-4} \text{ M}$) upon mixing with various concentrations of sodium nitrate in aqueous solution are shown in Figure 3.20 (a). The kinetic curves were analyzed according to double exponential decays (cf. solid lines in Figure 3.20). The observed first order rate constants of both decay processes are found to increase linearly with increasing nitrate ion concentrations. The respective second order rate constants were obtained from the slope of the linear dependencies Figure 3.20 (b) and are summarized in Table 3.3.

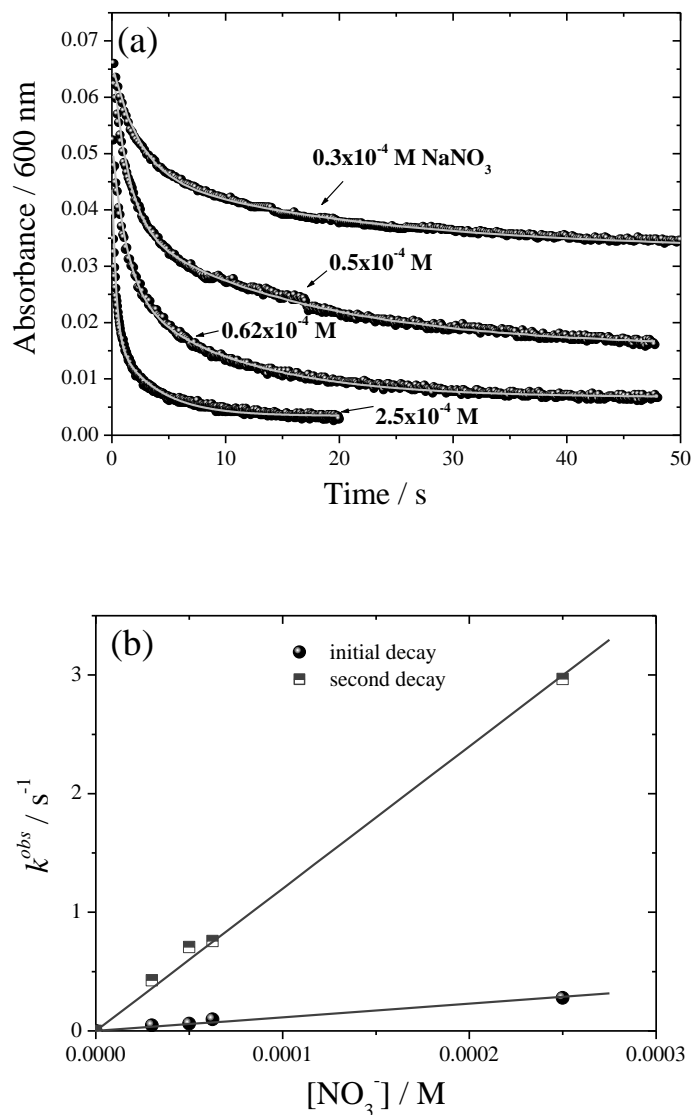


Figure 3.20: (a) Time profiles of the decay of $e^-_{\text{TiO}_2}$ absorbance at 600 nm ($[e^-_{\text{TiO}_2}] = 5.5 \times 10^{-4}$ M, 6 $e^-_{\text{TiO}_2}$ /particle) observed upon mixing of their aqueous suspension with Argon-saturated aqueous NaNO_3 solutions at pH 2.3, the solid lines show the double exponential fits. (b) Linear dependency of the observed first order rate constants on the NO_3^- concentrations. First order rate constants determined from the data analysis according to (a).

The values of the second order rate constants obtained here differ considerably from those reported by Gao et al.¹¹³ This is readily explained by the fact that these authors observed the one electron reduction of nitrate ions while in the present study a multi-electron transfer is occurring (the concentration of electrons employed in their experiments are considerably lower than the electron concentration employed here). It is in fact estimated that an overall of about 8 electrons are consumed per NO_3^- ion which is in consistence with the stoichiometry

of the assimilative pathway of reduction of nitrate ions to ammonia. According to the observed results and the estimated number of electrons for each decay step (see Table 3.3), the mechanism can be described as follows: in the presence of excess electrons initially a five electron transfer process occurs leading to the reduction of nitrate to dinitrogen (Eq. 3.29), the latter can be further reduced to ammonia through Eq. 3.30 and 3.31. In order to confirm the reaction of dinitrogen gas with excess $e^-_{\text{TiO}_2}$, a stopped flow experiment was performed mixing an aqueous TiO_2 electron suspension ($2.5 \times 10^{-3} \text{ M } e^-_{\text{TiO}_2}$) with a N_2 saturated aqueous solution ($[\text{N}_{2\text{aq}}] = 3.35 \times 10^{-4} \text{ M}$)¹⁴¹ at pH 2.3. The $e^-_{\text{TiO}_2}$ absorbance decays according to a first order rate law (cf. Figure 3.21). From the resulting first order rate constant of 5.9 s^{-1} a second order rate constant $k_2 = 1.8 \times 10^4 \text{ M}^{-1} \text{ s}^{-1}$ is calculated. This rate constant is faster than that obtained for the slow process in the reduction of nitrate which is expected to be due to the reduction of molecular nitrogen to ammonia (Eq. 3.30 and 3.31). This can be readily understood as the steady state concentration of dinitrogen gas that is reduced during the reduction of nitrate ions will be much lower than the N_2 concentration employed in the experiment of $e^-_{\text{TiO}_2}$ and molecular nitrogen ($e^-_{\text{TiO}_2} + \text{N}_2$). From the calculated second order rate constant for the slow process in the reduction of nitrate ($1.6 \times 10^3 \text{ M}$) and that for N_2 reduction ($k_2 = 1.8 \times 10^4 \text{ M}^{-1} \text{ s}^{-1}$) with ($[\text{N}_{2\text{aq}}] = 3.35 \times 10^{-4} \text{ M}$, the steady state concentration of N_2 was calculated to be $2.97 \times 10^{-5} \text{ M}$.

It is calculated that ~ 6 electrons were consumed per N_2 molecule which is in good agreement with the theoretical number of electrons required for the reduction of dinitrogen gas to ammonia.

The formation of ammonia was confirmed by performing separate experiments, i. e., by the 1:1 mixing of aqueous suspensions of TiO_2 electrons and NaNO_3 solutions (under the conditions identical to those of the kinetic experiments) in a closed reactor and measuring the evolved ammonia by Nessler's method.¹⁴² The pH of resulting mixed solutions were adjusted to 9 by adding NaOH , then the solutions were cooled to 4°C . Nessler's reagent (0.09 M solution of potassium tetraiodomercurate (II) ($\text{K}_2[\text{HgI}_4]$) in 2.5 M potassium hydroxide) was then added slowly to the cooled solutions. Strong yellow-brown colorations were observed indicating the presence of ammonia. In addition, GC measurements of the headspace above the mixed solutions indicated the absence of any measurable amount of dinitrogen gas.

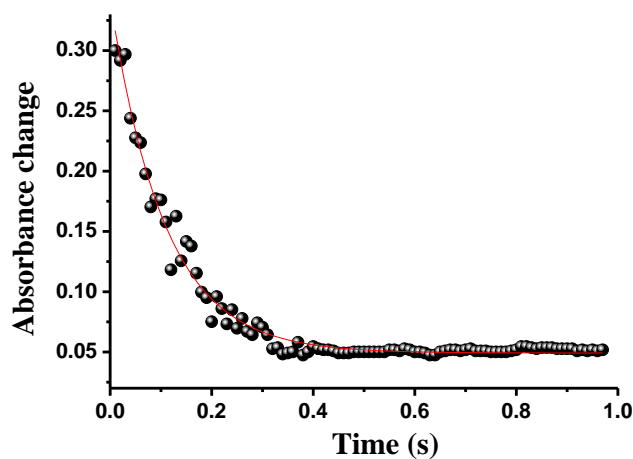


Figure 3. 21: Time profile of the decay of $e^-_{\text{TiO}_2}$ absorbance at 600 nm ($[e^-_{\text{TiO}_2}] = 2.5 \times 10^{-3}$ M, 27 $e^-_{\text{TiO}_2}$ /particle) observed upon mixing of their aqueous suspension with a N_2 saturated aqueous solution at pH 2.3.

Table 3.3: Summary of rate constants of the reaction of TiO_2 electrons with different electron acceptors and their corresponding reactions.

Electron acceptors	Reaction Pathway	$[e^-_{\text{TiO}_2}] / \text{M}$	Number of transferred electrons	$k_2 / \text{M}^{-1}\text{s}^{-1}$
O_2	$e^-_{\text{TiO}_2} + \text{O}_2 + \text{H}^+ \rightarrow \text{HO}_2^\bullet$	5.7×10^{-4}	1.1	2×10^4
	$e^-_{\text{TiO}_2} + \text{HO}_2^\bullet + \text{H}^+ \rightarrow \text{H}_2\text{O}_2$		2	5.6×10^3
	$\begin{cases} \text{H}_2\text{O}_2 + e^-_{\text{TiO}_2} \rightarrow \text{OH}^- + \text{OH}^\bullet \\ 2e^-_{\text{TiO}_2} + \text{H}_2\text{O}_2 \rightarrow 2 \text{OH}^- \end{cases}$		Total (3.1)	
H_2O_2	$\text{H}_2\text{O}_2 + e^-_{\text{TiO}_2} \rightarrow \text{OH}^- + \text{OH}^\bullet$	6.9×10^{-4}	1.1	2.7×10^5
	$2e^-_{\text{TiO}_2} + \text{H}_2\text{O}_2 \rightarrow 2 \text{OH}^-$		0.5	3.2×10^4
			Total (1.6)	
NO_3^-	$2\text{NO}_3^- + 12 \text{H}^+ + 10e^-_{\text{TiO}_2} \rightarrow \text{N}_2 + 6\text{H}_2\text{O}$	5.5×10^{-4}	4.6	1.7×10^4
	$\text{N}_2 + 4e^-_{\text{TiO}_2} + 5\text{H}^+ \rightarrow \text{N}_2\text{H}_5^+$		3.3	1.6×10^3
	$\text{N}_2\text{H}_5^+ + 2e^-_{\text{TiO}_2} + 3\text{H}^+ \rightarrow 2 \text{NH}_4^+$		Total (7.9)	

3.3.4. Reduction of Transition Metal Ions

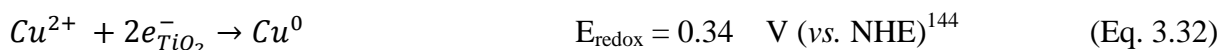
The stopped flow study presented in this thesis involves the study of the kinetics and the mechanism of the reduction of various metal ions including toxic metal ions such as Mn^{2+} , Zn^{2+} , Cd^{2+} , Cu^{2+} , Hg^{2+} and noble metal ions such as Ag^+ and Au^{3+} using the stored TiO_2 electrons.

3.3.4.1. Reduction of Toxic Metal Ions

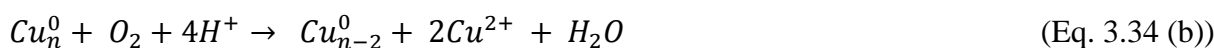
a) Reaction of $e^-_{TiO_2}$ with Cu^{2+}

Figure 3.22 shows the steady state UV-vis spectra recorded immediately and after various times of 1:1 mixing of an aqueous suspension of TiO_2 electrons and an Ar-saturated aqueous solution of $CuCl_2$ in a sealed cuvette. Since the reduction of Cu^{2+} ions depends strongly on the presence of molecular oxygen, great care was taken to exclude molecular oxygen as far as possible during the manipulation of the solutions. Obviously, as the broad absorption of TiO_2 electrons decays (Figure 3.22 (a)), a new band develops with a maximum at 570 nm (Figure 3.22 (b)-(c)). This band is assigned to the surface plasmon absorbance of copper nanoparticles. Henglein^{143 (a)} reported the spectra with maxima ranging from 578 nm to 581 nm assigned to copper nanoparticles prepared from the pulse radiolysis of copper salt. P.K. Khanna et al.^{143 (c)} reported spectra of colloidal copper with a maximum ranging from 595 nm to 612 nm which resulted from the reduction of copper salt by sodium citrate/SFS and myristic acid/SFS.

The blue suspension of TiO_2 electrons turned to the ruby-red color of colloidal copper after mixing with an aqueous solution of Cu^{2+} ions. A two electron transfer reaction is thus assumed to take place resulting in the formation of copper atoms (Eq. 3.32), which then coalesce to form colloidal copper nanoparticles (Eq. 3.33),



It was also observed that the color of the resulted copper metal deposits disappeared yielding a colorless suspension after exposure to air (Figure 3.22 (e)). This may be attributed to the oxidation of the copper deposits giving back copper ions and forming the corresponding reduced oxygen species (Eq. 3.34 (a) and Eq. 3.34 (b)). The kinetics of the reaction of the copper deposits with molecular oxygen will be presented later.



It was difficult to determine the size of the deposited copper particles by TEM measurements since the particles were very sensitive towards molecular oxygen and completely dissolved by exposure to air within a few minutes. Moreover, no theoretical correlation between the size of the copper particles and the position of their surface plasmon band could be found in the literature. Hence, the particle size of the Cu_n^0 could also not be deduced from the UV-vis spectra obtained here (cf. Figure 3.22).

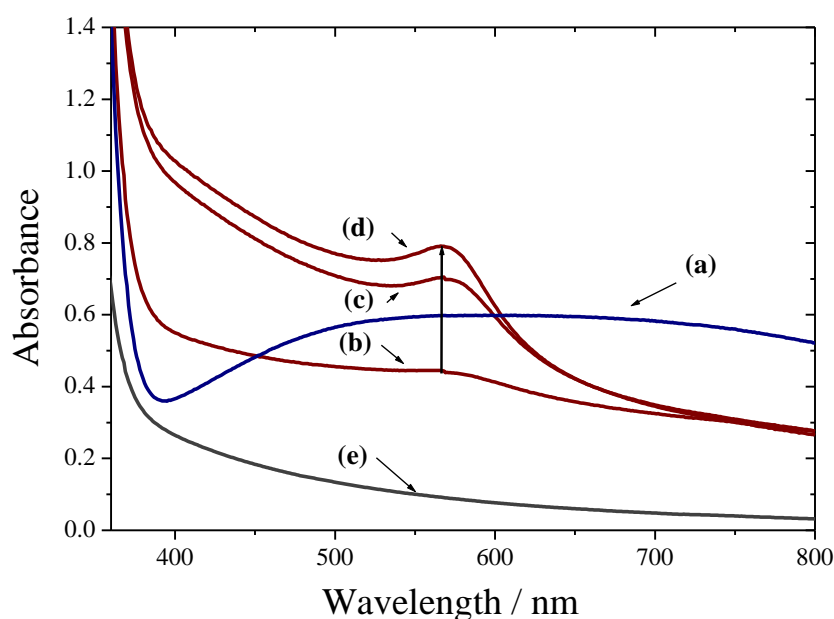


Figure 3.22: Steady state UV-vis measurements showing the growth of the Cu^0 nanoparticle absorption as indicated from the surface plasmon absorbance with max. at 570 nm after mixing of an aqueous suspension of TiO_2 electrons ($[\text{e}^-_{\text{TiO}_2}] = 5.5 \times 10^{-4} \text{ M}$, $6 \text{ e}^-_{\text{TiO}_2}/\text{particle}$) with an Ar-saturated aqueous solution of Cu^{2+} (CuCl_2), $[\text{Cu}^{2+}] = 2.5 \times 10^{-4} \text{ M}$, (a) stored TiO_2 electrons before mixing (b) immediately after mixing, (c) after 2 min, (d) after 4 min of mixing with Cu^{2+} ions, (e) after the exposure of the final colloidal metal deposits to air. The light scattering above 400 nm can be attributed to a coagulation of TiO_2 particles.

The kinetics of the electron transfer reaction from TiO_2 electrons to Cu^{2+} ions was studied by performing stopped flow mixing experiments of TiO_2 electron suspensions with various concentrations of CuCl_2 in aqueous solutions in the absence of oxygen (Figure 3.23). The employed concentrations of copper ions (0.5×10^{-3} – $4 \times 10^{-3} \text{ M}$) were in excess compared to the concentration of the stored TiO_2 electrons ($0.15 \times 10^{-3} \text{ M}$) (i. e., $\text{Cu}^{2+} \gg \text{e}^-_{\text{TiO}_2}$), so that a

pseudo first order rate law was obeyed at all Cu^{2+} concentrations. Figure 3.24 shows the linear dependency of the observed first order rate constants on the Cu^{2+} concentrations. The second order rate constant obtained from the slope of this linear dependency is $k_2 = 3.5 \times 10^4 \text{ M}^{-1} \text{ s}^{-1}$. This value is smaller than the value obtained by Gao *et al.*¹¹³ ($1.3 \pm 0.3 \times 10^5 \text{ M}^{-1} \text{ s}^{-1}$). The authors attributed this rate constant to the one electron reduction of Cu^{2+} to Cu^+ .

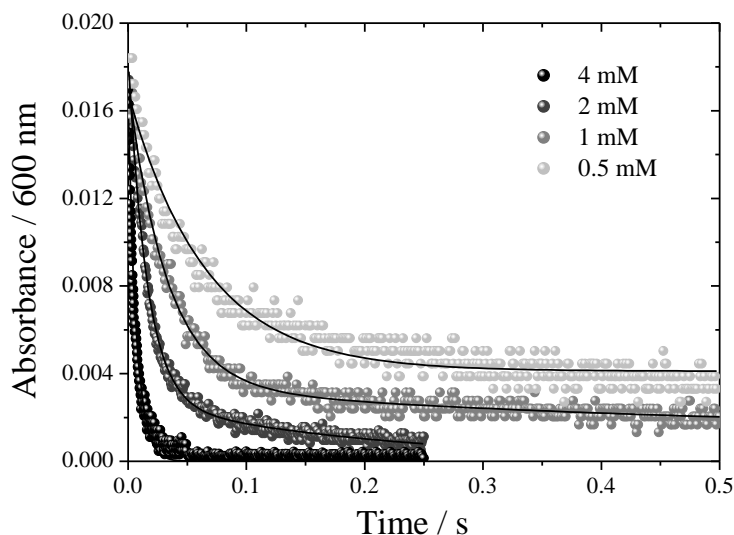


Figure 3.23: Time profiles of the decay of the $e^-_{\text{TiO}_2}$ absorbance at 600 nm ($[e^-_{\text{TiO}_2}] = 1.5 \times 10^{-4} \text{ M}$, $1.6 e^-_{\text{TiO}_2}/\text{particle}$) observed after mixing of their aqueous suspension with Ar-saturated aqueous CuCl_2 solutions at pH 2.3, solid lines show the first order fits.

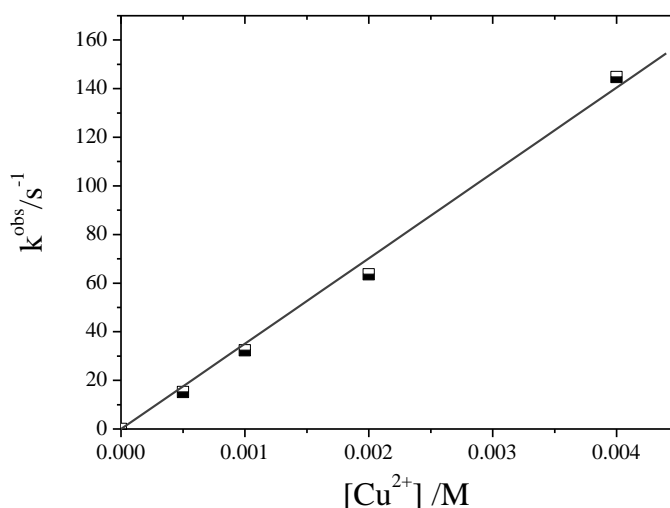


Figure 3.24: Linear dependency of the observed first order rate constants on the Cu^{2+} concentrations. First-order rate constants determined from the data analysis according to Figure 3.23.

Following the fast initial decay a slow build-up of a transient absorbance is observed in the wavelength range 380-620 nm. Figure 3.25 shows the long scale time profile of the build-up of the absorbance observed at 570 nm after mixing of stored TiO₂ electrons suspension ($[e^-_{\text{TiO}_2}] = 1.5 \times 10^{-4} \text{ M}$) with deaerated aqueous CuCl₂ solutions with $[\text{Cu}^{2+}] = 1 \times 10^{-3} \text{ M}$. The build-up of the absorbance signals can be fitted by the first order kinetic law. It was found that the kinetics of the build-up does not depend on the concentration of Cu²⁺ ions at the same electron concentration. This observation can confirm Eq. 3.33 since the growth step involves the coalescence of the reduced Cu⁰ atoms. The second order rate constant of the TiO₂ electron absorbance decay and the first order rate constant of the Cu⁰ particles growth are summarized in Table 3.4.

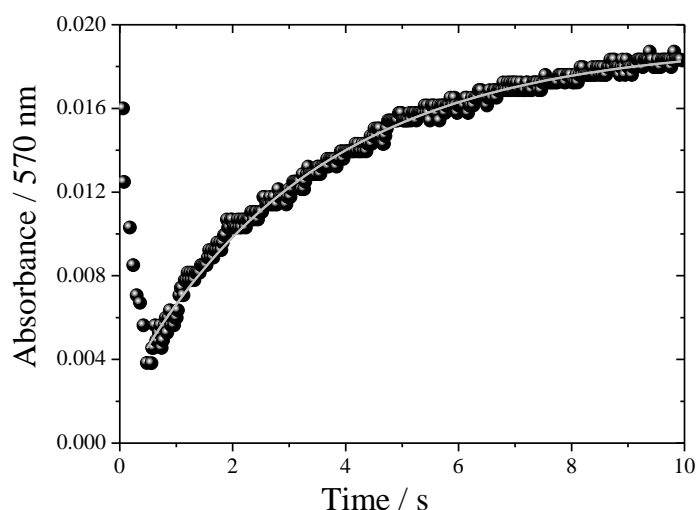


Figure 3.25: Long time scale profile at 570 nm observed after mixing of stored TiO₂ electrons suspension ($[e^-_{\text{TiO}_2}] = 1.5 \times 10^{-4} \text{ M}$, $1.6 e^-_{\text{TiO}_2}/\text{particle}$) with deaerated aqueous CuCl₂ solution ($[\text{Cu}^{2+}] = 1 \times 10^{-3} \text{ M}$) at pH 2.3, solid line shows data fitting.

The time resolved UV–vis spectra measured at different times after mixing of stored TiO₂ electrons suspension ($[e^-_{\text{TiO}_2}] = 1.5 \times 10^{-4} \text{ M}$, $1.6 e^-_{\text{TiO}_2}/\text{particle}$) with deaerated aqueous CuCl₂ solution ($[\text{Cu}^{2+}] = 1 \times 10^{-3} \text{ M}$) at pH 2.3 is illustrated in Figure 3.26.

Obviously, at the height of the signals the broad spectrum assigned to the absorbance of TiO₂ electrons decayed and at 500 ms giving a featureless spectrum and then increased showing the evolution of the Cu⁰ absorbance with increasing the absorption in the shorter wavelength. By the comparison with the steady state absorption spectra (Figure 3.22) the final spectrum obtained at 10 s can be assigned to the absorbance of the early formed small copper clusters.

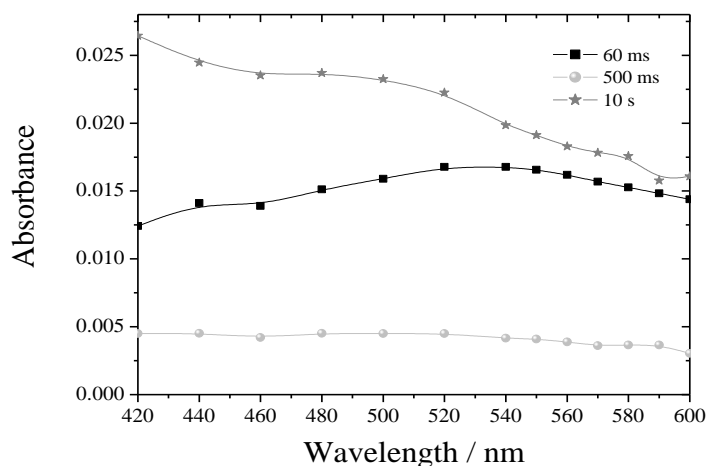


Figure 3.26: Time resolved absorption spectra measured at different time after 1:1 mixing of stored TiO_2 electrons suspension ($[\text{e}^-_{\text{TiO}_2}] = 1.5 \times 10^{-4} \text{ M}$, $1.6 \text{ e}^-_{\text{TiO}_2}/\text{particle}$) with deaerated aqueous CuCl_2 solution ($[\text{Cu}^{2+}] = 1 \times 10^{-3} \text{ M}$) at pH 2.3.

Effect of O_2

The effect of molecular oxygen on the deposited copper particles was investigated by mixing an aqueous solution of copper deposits (Cu/TiO_2) which was prepared in advance by mixing of $2.5 \times 10^{-4} \text{ M}$ CuCl_2 with an aqueous TiO_2 suspension of $5.5 \times 10^{-4} \text{ M}$ $\text{e}^-_{\text{TiO}_2}$ (cf. Figure 3.27).

It was observed that the original absorbance at 570 nm decay exponentially with rate constant $k^{obs} = 0.36 \text{ s}^{-1}$. This decay can be assigned to (Eq. 3.34 (a) and (b)).

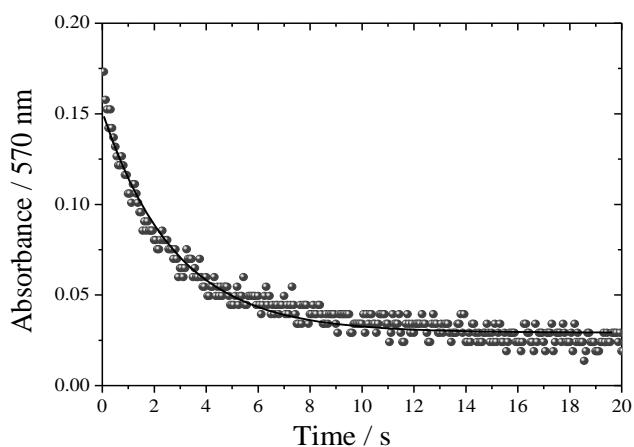
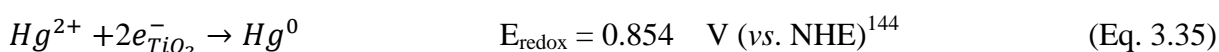


Figure 3.27: Time profile of the decay of the SP absorbance of copper particles observed at 570 nm after 1:1 mixing of oxygen saturated aqueous solution with an aqueous solution of Cu/TiO_2 which was prepared in advance by mixing of $2.5 \times 10^{-4} \text{ M}$ CuCl_2 with an aqueous suspension of $5.5 \times 10^{-4} \text{ M}$ $\text{e}^-_{\text{TiO}_2}$.

a. Reaction of $e^-_{\text{TiO}_2}$ with Hg^{2+}

A steady state UV–vis experiment has been performed by 1:1 mixing of an aqueous suspension of TiO_2 electrons ($8.3 \times 10^{-3} \text{M}$) with deaerated aqueous HgCl_2 solution ($0.5 \times 10^{-3} \text{M}$) in a sealed cuvette. The spectra are illustrated in Figure 3.28. The transparent blue coloration of the TiO_2 electrons suspension turned to yellow brown coloration after the addition of the HgCl_2 solution. The broad spectrum of TiO_2 electron absorbance (Figure 3.28 (a)) decayed and a featureless spectrum is observed which increased with time to give a shoulder at 400–480 nm (Figure 3.28 (b)– (c)) confirming the two electron reduction of Hg^{2+} ions into their corresponding Hg^0 (Eq. 3.35)



It was reported that mercury metal nanoparticles have a brown and strongly opalescent coloration whose spectrum exhibits a broad maximum with an intense plasmon absorption band at 300 nm and a weak absorption over the whole range of the visible and UV.^{143 (d), (e)}

The spectrum observed in Figure 3.28 (b) is similar to the reported broad UV–vis spectra with a maximum at 300 nm for Hg^0 nanoparticles^{143 (d)}, however, it was not possible to detect the band at 300 nm here since TiO_2 absorbs strongly in this region. Additionally, the broad absorption band was observed at 400–480 nm (Figure 3.28 (c)). The later absorption band was not reported before.

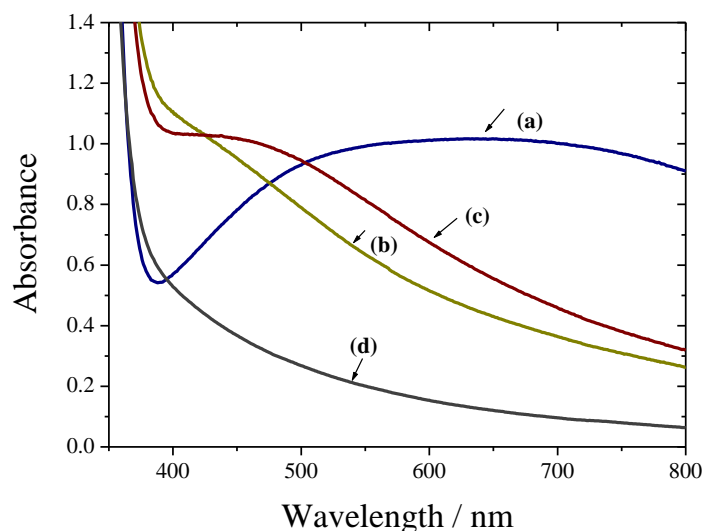


Figure 3.28: Steady state UV–vis measurements showing the growth of the Hg^0 nanoparticles as indicated from its absorbance after mixing of an aqueous suspension of TiO_2 electrons ($[e^-_{\text{TiO}_2}] = 8.3 \times 10^{-4} \text{M}$, $9 e^-_{\text{TiO}_2}/\text{particle}$) with an Ar-saturated aqueous solution of HgCl_2 ($5 \times 10^{-4} \text{M}$). (a) Stored TiO_2 electrons before mixing (b) immediately after mixing, (c) after 2 min, (d) after the exposure of the final colloidal metal deposits to air.

Similar to the copper deposits, the deposited mercury nanoparticles were found to be sensitive towards molecular oxygen. The intensity of the color of the final deposited metal suspension decreased after the exposure to air. The absorbance measurement after the exposure to air (Figure 3.28 (d)) shows that the broad absorption band is decreased which can be assigned to the oxidation of Hg^0 particles.

To follow the kinetics of Hg^{2+} reduction, the typical stopped flow experiments have been performed by mixing the TiO_2 electrons (1.5×10^{-4} M) with aqueous solutions of Hg^{2+} ions from HgCl_2 at a concentration range of 5×10^{-4} – 2×10^{-3} M. Figure 3.29 shows the time profiles of the decay of the absorbance signals at 600 nm upon the reaction of $e^-_{\text{TiO}_2}$ with different concentration of Hg^{2+} ions. Pseudo first order rate constants were obtained from the single exponential fits of the all kinetic decays. A second order rate constant ($7.5 \times 10^4 \text{ M}^{-1} \text{ s}^{-1}$) is obtained from the linear dependency of the observed first order rate constants on the metal ion concentrations (cf. Figure 3.30).

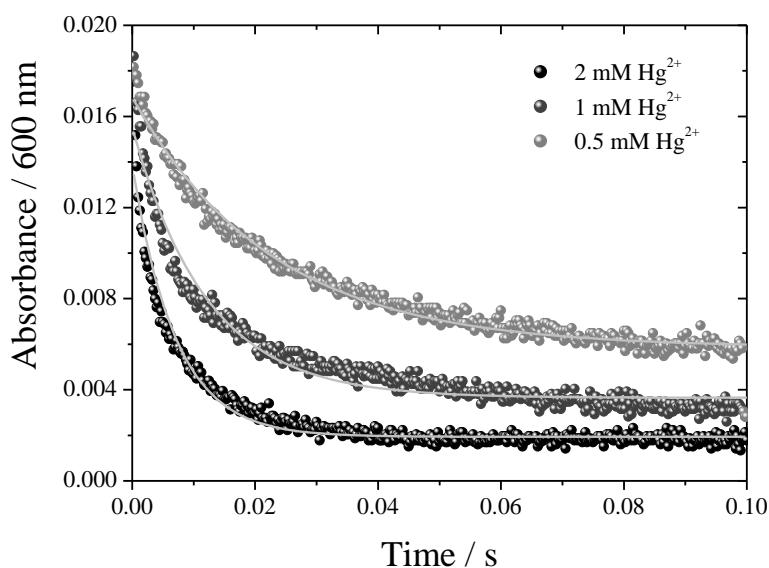


Figure 3.29: Time profiles of the decay of the $e^-_{\text{TiO}_2}$ absorbance at 600 nm ($[e^-_{\text{TiO}_2}] = 1.5 \times 10^{-4}$ M, $1.6 e^-_{\text{TiO}_2}/\text{particle}$), observed after mixing of their aqueous suspension with Ar-saturated HgCl_2 aqueous solutions containing different concentrations of Hg^{2+} at pH 2.3. Solid lines show the single exponential fits.

Following the decay a build-up were observed at the wavelength range of 380-480 nm. Figure 3.31 shows the change in the absorbance signals at 420 nm, initially first order decay is observed followed by a sigmoidal build-up. The sigmoidal build-up rate depends on the

concentrations of Hg^0 . Hence, the growth of Hg^0 deposits can be described by an autocatalytic process



The obtained rate constants of the electron decays and the autocatalytic growth of the Hg^0 particles are summarized in Table 3.4.

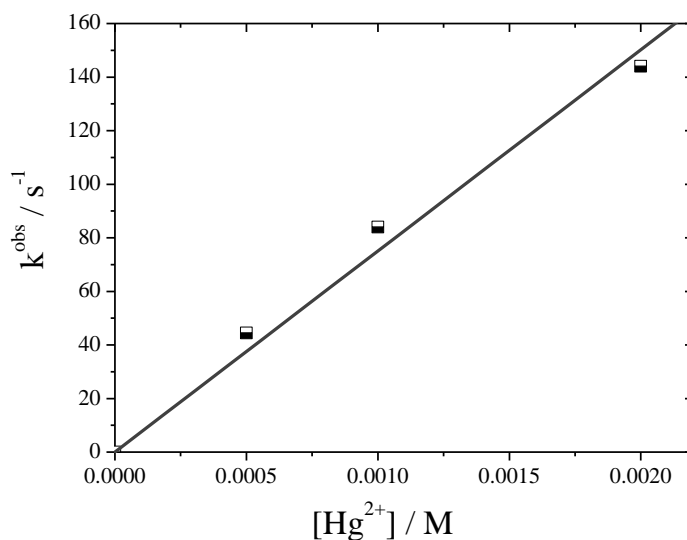


Figure 3.30: Linear dependency of the observed first order rate constants on the Hg^{2+} concentrations. First order rate constants determined from the data analysis according to Figure 3.29.

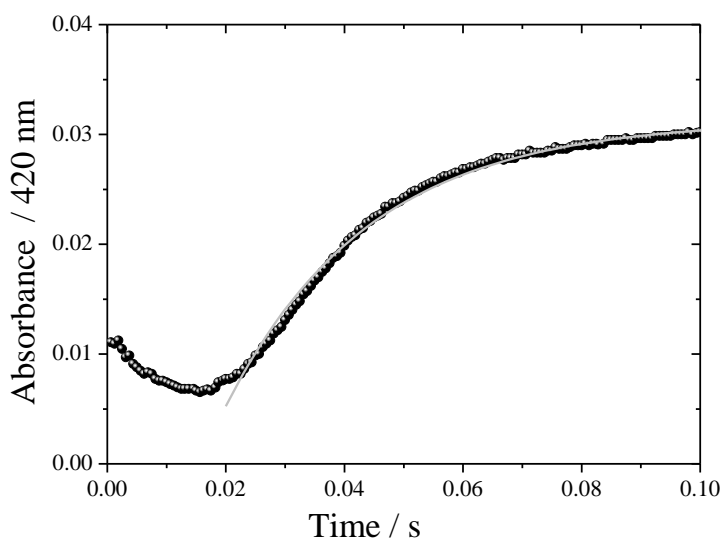


Figure 3.31: Time profile of the absorbance build-up at 420 nm observed upon mixing of an aqueous suspension of TiO_2 electrons ($[e_{\text{TiO}_2}^-] = 1.5 \times 10^{-4} \text{ M}$) with an Ar-saturated HgCl_2 aqueous solution ($2 \times 10^{-3} \text{ M}$) at pH 2.3.

The time resolved UV–vis spectra measured at different times after mixing of stored TiO₂ electrons suspension ($[e^-_{\text{TiO}_2}] = 1.5 \times 10^{-4} \text{ M}$, $1.6 e^-_{\text{TiO}_2}/\text{particle}$) with deaerated aqueous HgCl₂ solution ($[\text{Hg}^{2+}] = 2 \times 10^{-3} \text{ M}$) at pH 2.3 are illustrated in Figure 3.32.

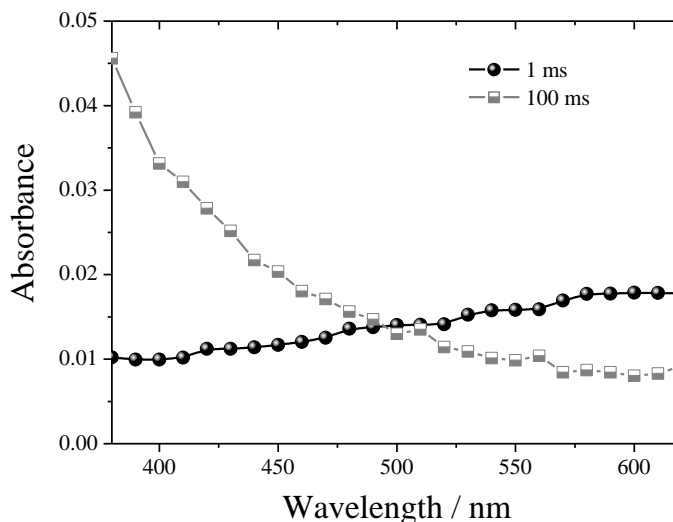


Figure 3.32: Time resolved absorption spectra measured at different time after 1:1 mixing of an aqueous suspension of TiO₂ electrons ($[e^-_{\text{TiO}_2}] = 1.5 \times 10^{-4} \text{ M}$) with an Ar-saturated HgCl₂ aqueous solution ($2 \times 10^{-3} \text{ M}$) at pH 2.3.

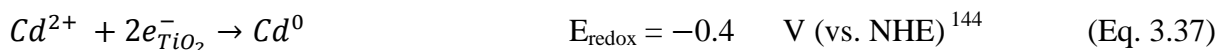
It was observed that after 1 ms of mixing a broad spectrum which is assigned to the absorbance of TiO₂ electrons decayed and a featureless spectrum evolved which does not exhibit any characteristic maximum on the measured region of 380–620 nm but the absorption increases on going to the shorter wavelength range. The transient spectra were found to be in agreement with the steady state spectra (Figure 3.28).

b. Reaction of $e^-_{\text{TiO}_2}$ with Cd^{2+}

A typical steady state UV–vis experiment was performed by mixing an aqueous suspension of TiO₂ electrons ($5 \times 10^{-4} \text{ M}$) with a deaerated aqueous Cd(ClO₄)₂ solution ($2 \times 10^{-4} \text{ M}$). The spectra are illustrated in Figure 3.33. The transparent blue coloration of the TiO₂ electron suspension turned to yellow coloration after the mixing. A featureless spectrum is observed with increasing the absorbance in the shorter wavelength range. However, no surface plasmon band of Cd⁰ was observed under our experimental condition.

The number of consumed electrons have been calculated from the decrease in the initial absorbance of electrons at 600 nm ($5 \times 10^{-4} \text{ M}$) and its final absorbance ($1.38 \times 10^{-4} \text{ M}$) (cf. Figure 3.33 (a) and (b) respectively) which is corresponding to 1.8 electrons per Cd²⁺ ion.

This confirms the two electron reduction of Cd^{2+} ions into their corresponding metal atoms (Eq. 3.37). There is no surface plasmon absorbance observed in the visible region under our experimental conditions. This is found to be in agreement with the reported spectra of Cd^0 particles.^{143 (f)} It was also observed that the resulting spectrum decays after exposure to air which may be due to the reaction of the formed metal particles with molecular oxygen (similar to copper and mercury metal deposits).



The kinetics of the reaction between TiO_2 electrons and Cd^{2+} ions were studied by performing stopped flow experiments of TiO_2 electron suspensions with various concentrations of Cd^{2+} in aqueous $\text{Cd}(\text{ClO}_4)_2$ solutions in the absence of oxygen (Figure 3.34). The concentrations of cadmium ions ($1 \times 10^{-3} \text{ M}$ – $4 \times 10^{-3} \text{ M}$) were in excess compared to the concentration of stored TiO_2 electrons ($0.25 \times 10^{-3} \text{ M}$). The decay of the signals obey first order kinetics and the second order rate constant is obtained from the linear dependency of the observed pseudo first order rate constants on the Cd^{2+} concentrations to be $k_2 = 4.38 \times 10^2 \text{ M}^{-1} \text{ s}^{-1}$ (Figure 3.35).

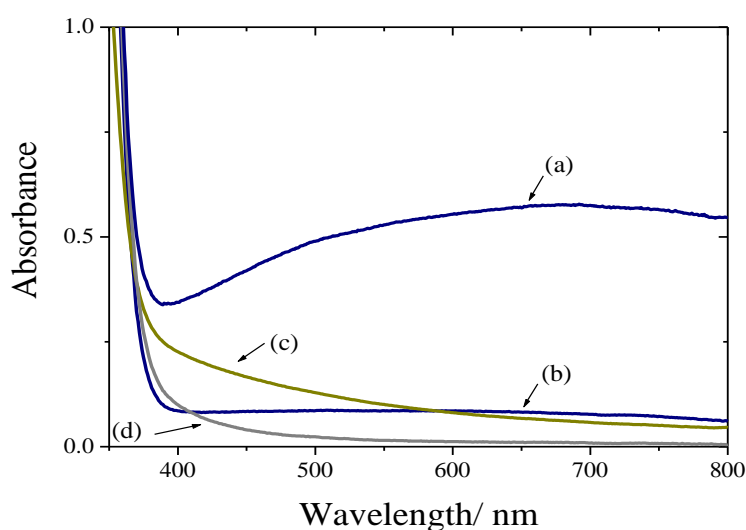


Figure 3.33: Steady state UV–vis measurements showing the growth of the Cd^0 nanoparticles as indicated from its absorbance after mixing of an aqueous suspension of TiO_2 electrons ($[\text{e}_{\text{TiO}_2}^-] = 5 \times 10^{-4} \text{ M}$, $5.5 \text{ e}_{\text{TiO}_2}^-/\text{particle}$) with an Ar-saturated aqueous solution of $\text{Cd}(\text{ClO}_4)_2$ ($2 \times 10^{-4} \text{ M}$). (a) Stored TiO_2 electrons before mixing (b) after 1 min, (c) after 2 min, (d) after the exposure of the final colloidal metal deposits to air.

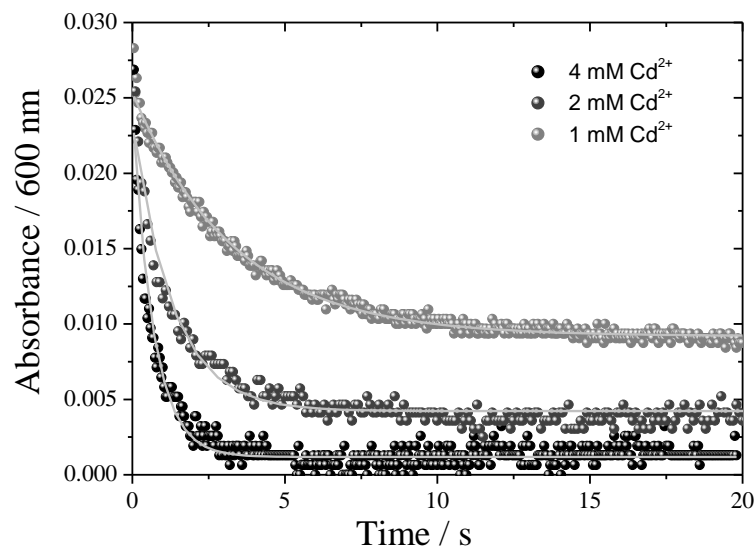


Figure 3.34: Time profiles of the decay of $e^-_{TiO_2}$ ($[e^-_{TiO_2}] = 2.5 \times 10^{-4}$ M, $2.7 e^-_{TiO_2}/particle$) absorbance at 600 nm, upon mixing of their aqueous suspension with deaerated aqueous $Cd(ClO_4)_2$ solutions containing different concentrations of Cd^{2+} , pH 2.3.

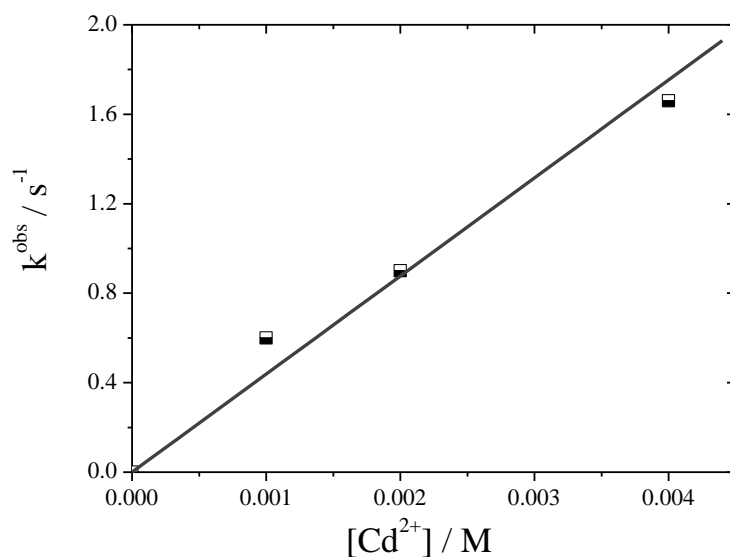


Figure 3.35: Linear dependency of the observed first order rate constants on the Cd^{2+} concentrations. First order rate constants determined from the data analysis according to Figure 3.34.

Following the initial decay of electron absorbance, a slow build up of a transient absorbance was observed in the wavelength range of 380–550 nm. Figure 3.36 shows the build-up of the absorbance signals at 420 nm. This build-up can be fitted by first order rate kinetics with rate constant $0.024 s^{-1}$. The rate constant of the build-up of the absorbance of Cd^0 particles at 420

nm was found to be independent on the Cd^{2+} concentrations. Hence the growth of the Cd^0 particles can be assumed as a coalescence of the reduced metal atoms (Eq. 3.38).



The second order rate constant of the TiO_2 electron absorbance decay and the first order rate constant of the Cd^0 clusters growth are summarized in Table 3.4.

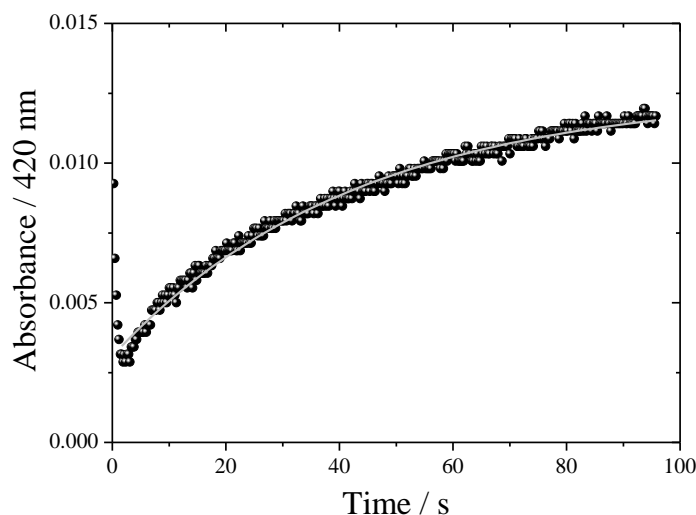


Figure 3.36: Build-up of the transient absorbance at 420 nm showing the growth of Cd^0 clusters observed after mixing of stored TiO_2 electrons suspension ($[\text{e}^-_{\text{TiO}_2}] = 2.5 \times 10^{-4} \text{ M}$, $2.7 \text{ e}^-_{\text{TiO}_2}/\text{particle}$) with deaerated aqueous $\text{Cd}(\text{ClO}_4)_2$ solutions ($[\text{Cd}^{2+}] = 2 \times 10^{-3} \text{ M}$) at pH 2.3, solid line shows first order data fitting.

c. Reaction of $\text{e}^-_{\text{TiO}_2}$ with Zn^{2+} and Mn^{2+}

It was observed that after mixing of aqueous suspensions of stored TiO_2 electrons ($2 \times 10^{-3} \text{ M}$) with acidic solutions containing either Zn^{2+} ($0.5 \times 10^{-3} \text{ M ZnCl}_2$) or with Mn^{2+} ($0.5 \times 10^{-3} \text{ M MnCl}_2$), the absorbance signals of TiO_2 electrons remains stable even over 200 s. Thus, the reactions in Eq. 3.39 and 3.40 did not occur.



This can be attributed to the fact that the values of the redox potentials of Zn^{2+} and Mn^{2+} are considerably more negative than the potential of the stored electrons on the TiO_2 (-0.5 V vs. NHE).¹³⁸

Table 3.4: Summary of rate constants of the reaction of TiO_2 electrons with different metal ions and their corresponding reactions.

Electron acceptors	Reaction Pathway	$[\text{e}^-_{\text{TiO}_2}] / \text{M}$	$k_2 / \text{M}^{-1}\text{s}^{-1}$
Cd^{2+}	$\text{Cd}^{2+} + 2 \text{e}^-_{\text{TiO}_2} \rightarrow \text{Cd}^0$	2.5×10^{-4}	4.38×10^2
	$n\text{Cd}^0 \rightarrow \text{Cd}^0_n$		
Cu^{2+}	$\text{Cu}^{2+} + 2 \text{e}^-_{\text{TiO}_2} \rightarrow \text{Cu}^0$	1.5×10^{-4}	3.5×10^4
	$n\text{Cu}^0 \rightarrow \text{Cu}^0_n$		
Hg^{2+}	$\text{Hg}^{2+} + 2 \text{e}^-_{\text{TiO}_2} \rightarrow \text{Hg}^0$	1.6×10^{-4}	7.5×10^4
	$\text{Hg}^0 + \text{Hg}^{2+} + 2 \text{e}^-_{\text{TiO}_2} \rightarrow \text{Hg}^0_2$		

3.3.4.2. Reduction of Noble Metal Ions

The kinetics and the mechanism of the reaction of the stored electrons on TiO₂ nanoparticles with the noble metal ions Ag⁺ and Au³⁺ in aqueous solution have also been studied employing the UV–vis steady state absorption as well as the stopped flow technique. The formation of the noble metal nanoparticles was detected by their typical surface plasmonic (SP) absorption band at 400 nm and 540 nm, respectively, for Ag and Au nanoparticles, respectively. The following topics were of special interest in these studies: 1. The kinetics and the mechanism of the reduction of the noble metal ions as well as the growth of the corresponding noble metal nanoparticles on the surface of the nano-sized TiO₂. 2. The changes in the optical properties of the deposited noble metal nanoparticles upon the transfer of excess electrons to the deposited metal particles. 3. The reactivity of the charged metal deposits for hydrogen production. 4. The effect of polymer chains such as polyvinyl alcohol (PVA) on the stabilization of the deposited metal particles. 5. The effect of molecular oxygen on the deposited metal particles.

a. Reaction of e⁻_{TiO₂ with Ag⁺}

Steady State UV–vis Absorption Measurements

Reaction of TiO₂ Electrons with Silver Ions

The UV–vis spectra recorded after mixing of TiO₂ loaded with electrons and Ag⁺ ions are shown in Figure 3.37. The spectra show the damping of the TiO₂ electrons absorbance between 400 nm and 650 nm, and the evolution of an absorbance maximum at 400 nm, which is typically ascribed to the plasmon resonance of silver nanoparticles.¹⁴⁵⁻¹⁴⁸ These observations reveal that the silver ions are reduced by stored TiO₂ electrons to silver atoms (Eq. 3.41) followed by the growth of these atoms to form silver particles (the mechanism of the growth process will be discussed later).

Furthermore, it is observed that the peak maximum is subsequently shifted slightly from 400 nm to about 395 nm. It was also observed that when the resulting suspension of Ag/TiO₂ nanoparticles was purged with O₂ gas the height of the SP band decreased to about 70% of the original absorbance indicating a decrease in the concentration of the reduced silver atoms on the Ag⁰ particles.



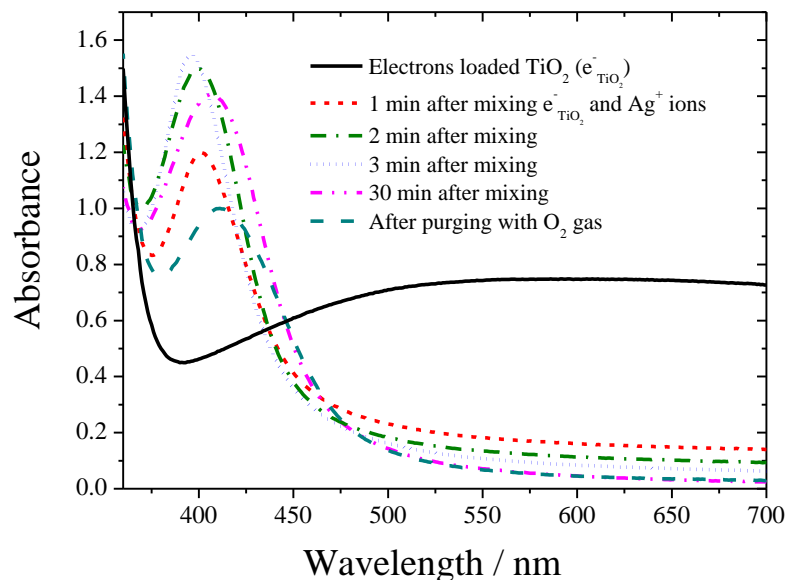


Figure 3.37: Steady state UV–vis measurements of the growth of the Ag^0 nanoparticles as indicated from the evolution of the surface plasmon absorbance with a maximum at 400 nm after mixing of electrons loaded TiO_2 ($[\text{e}^-_{\text{TiO}_2}] = 1.2 \times 10^{-3} \text{ M}$, $13 \text{ e}^-_{\text{TiO}_2}/\text{particle}$) with an Ar-saturated AgClO_4 aqueous solution ($[\text{Ag}^+] = 1 \times 10^{-4} \text{ M}$) at pH 2.7 and the effect of O_2 on the formed Ag^0 particles.

Effect of PVA

The presence of PVA and other polymers during the formation of metal nanoparticles is known to limit their particle size as well as to stabilize them and preventing them from coagulation.^{149, 150} Therefore, it was of importance to study the effect of the presence of polyvinyl alcohol (PVA) on the formation and growth of silver particles on the TiO_2 surfaces. Figure 3.38 shows the UV–vis absorption spectra recorded after mixing of TiO_2 electrons with Ag^+ ions in the absence and the presence of PVA ($0.5 \times 10^{-3} \text{ M}$). It is observed that the intensity of the surface plasmon peak is lower in presence of the polymer than in the polymer free solution. It was also observed that the SP band of the absorption spectra recorded 4 days after the particle formation has disappeared in the PVA free solution while the height of the band decreased to about 65 % of its original value when PVA was present.

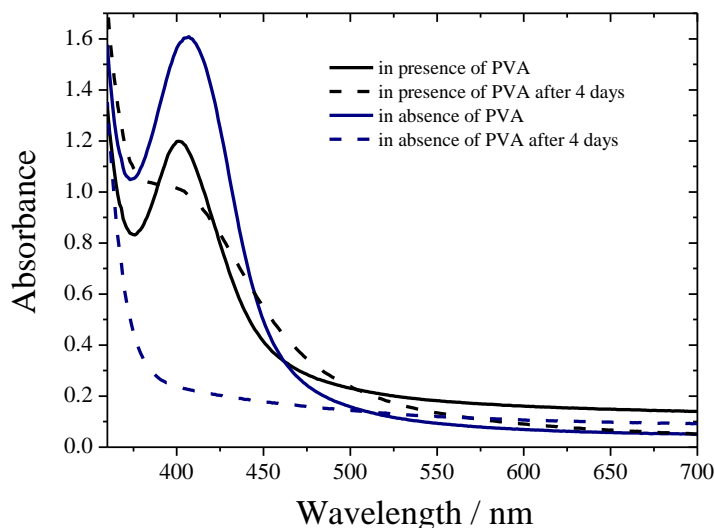


Figure 3.38: Steady state UV-vis absorption spectra recorded after mixing of electrons loaded TiO_2 suspension ($[\text{e}^-_{\text{TiO}_2}] = 1.2 \times 10^{-3} \text{ M}$, $13 \text{ e}^-_{\text{TiO}_2}/\text{particle}$) with an Ar-saturated AgClO_4 aqueous solution ($[\text{Ag}^+] = 1 \times 10^{-4} \text{ M}$) in the presence and the absence of PVA ($0.5 \times 10^{-3} \text{ M}$) at pH 2.7.

Stopped Flow Kinetic Measurements

Reaction of TiO_2 Electrons with Silver Ions

For the following experiments the colloidal TiO_2 electron suspensions were mixed with aqueous solutions of silver ions in the form of silver perchlorate (AgClO_4) in the stopped flow chamber and the kinetics were studied by following the decay of the absorbance of the TiO_2 electrons as well as the build up of the surface plasmon absorbance of the deposited silver particles. Two experimental conditions were applied, one working at $[\text{e}^-_{\text{TiO}_2}] > [\text{Ag}^+]$ and the other at $[\text{Ag}^+] \gg [\text{e}^-_{\text{TiO}_2}]$.

In the first case the concentration of electrons was $0.9 \times 10^{-3} \text{ M}$ and that of silver ions was $0.25 \times 10^{-3} \text{ M}$. The change in the absorbance vs. time was recorded in the wavelength range 360– 640 nm. Kinetic decay curves consisting of three phases were observed in the wavelength range from 500 to 640 nm in all experimental runs, while a three phase kinetic build-up has been observed in the wavelength range from 480 to 360 nm.

Figure 3.39 (a) shows the change in the absorbance vs. time signal at 600 nm for a typical experimental run. Clearly, three phases of the kinetic decay are observed, which are well separated in time. Figure 3.39 (b) shows the change of the absorbance vs. time signal at 400 nm. The curve starts with a fast initial build up of an absorbing species followed by a

continuous sigmoidal growth which finally leads to a slow growth domain. It was also observed that both the first initial decay at 600 nm and the first initial build-up at 400 nm occur simultaneously (phase 1). In addition, the second slower decay and the sigmoidal build-up also happen in the same time domain (phase 2).

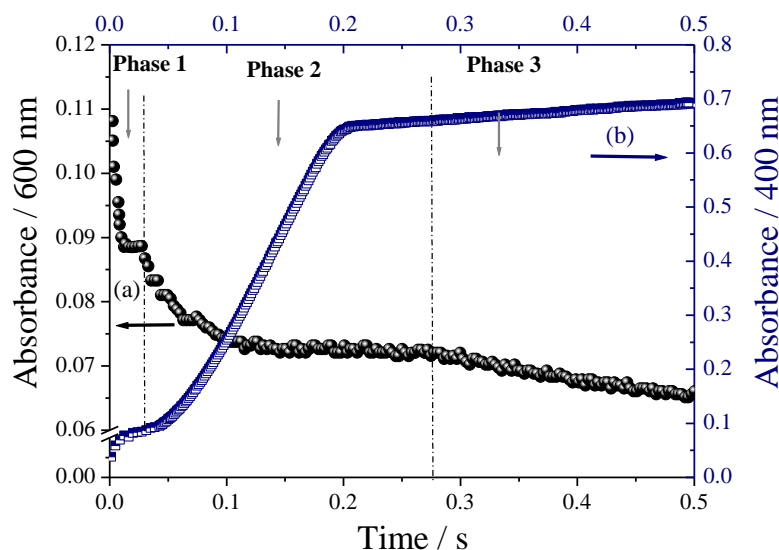


Figure 3.39: Change in the absorbance vs. time signals at 600 nm (a) and at 400 nm (b) observed after 1:1 mixing of electrons loaded TiO_2 suspension ($[\text{e}^-_{\text{TiO}_2}] = 9 \times 10^{-4} \text{ M}$, $10 \text{ e}^-_{\text{TiO}_2}$ /particle) with an Ar-saturated AgClO_4 aqueous solution ($[\text{Ag}^+] = 2.5 \times 10^{-4} \text{ M}$) at pH 2.7.

From the calculated concentration of the consumed electrons for each phase (cf. Figure 3.39), it is found that at the end of phase 1 only part of the silver ions have been consumed, while the number of consumed electrons at the end of the phase 2 corresponds to the entire amount of silver ions originally present in the solution. This observation can be interpreted as follows: In phase 1 a fraction of the silver ions is reduced to form silver nuclei. In phase 2 the formed silver nuclei are growing to form silver particles. In phase 3 the silver particles partly coalesce with each other to form bigger particles. Moreover, according to the observed results and the estimated concentration of electrons for each decay step, the kinetic decay at 600 nm in phase 3 is suggested to be due to the transfer of electrons to the formed silver particles. If indeed phase 3 can be described to the transfer of electrons to the deposited silver particles it should be possible to detect the reaction of these electrons with water or adsorbed hydrogen ions to produce molecular hydrogen. This was confirmed by measuring the amount of the evolved H_2 gas upon mixing of TiO_2 electrons ($0.9 \times 10^{-4} \text{ M}$) and different concentrations of silver ions ($0.08 \times 10^{-3} \text{ M}$ – $0.25 \times 10^{-3} \text{ M}$) in a closed reactor (see Table 3.5). It was found that the amount

of evolved hydrogen gas increases with an increasing concentration of silver ions (which will most likely result in the increase of the catalyst surface area (i.e., Ag^0 deposits) required for H^+ reduction).

Table 3.5: Variation of the amount of H_2 gas measured after mixing of an aqueous suspension of TiO_2 electrons ($0.9 \times 10^{-4} \text{ M}$) and aqueous Ag^+ solution with various of silver ion concentrations at pH 2.7.

$[\text{Ag}^+] / 10^{-3} \text{ M}$	Amount of $\text{H}_2 / 10^{-6} \text{ mol}$ measured after 30 min of mixing
0	0
0.08	4.5
0.125	12
0.25	19

The UV–vis spectra measured at different times after mixing are shown in Figure 3.40. A spectrum of the TiO_2 electrons is obtained immediately, i. e., 5 ms after the mixing followed by the growth of the typical SP absorbance of silver particles at 400 nm with time and the decay of the $e^-_{\text{TiO}_2}$ absorbance at 600 nm. Absorption maximum slightly shifts from 400 nm (100 ms) to 390 nm at 0.5 s after the mixing. This plasmon band arises from surface oscillations of the electron gas in the Ag^0 metal nanoparticles and should be sensitive to the changes on the metal surface.⁴²

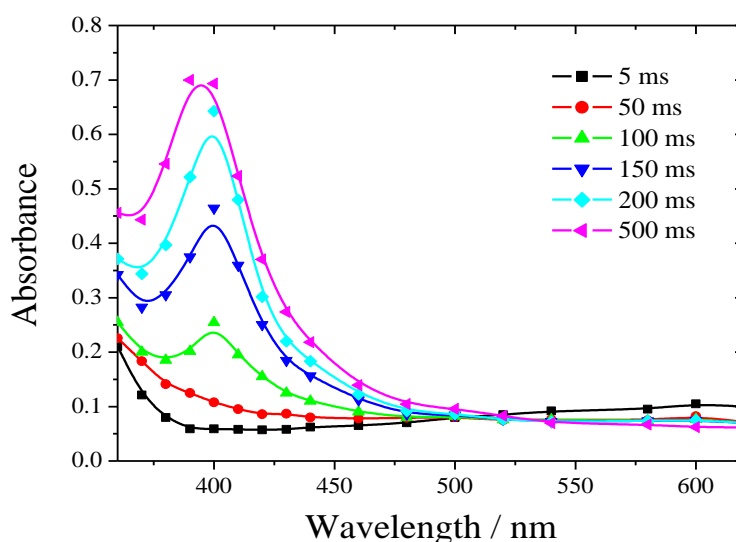


Figure 3.40: Time resolved absorption spectra measured at different times after 1:1 mixing of electron loaded TiO_2 suspension ($[\text{e}^-_{\text{TiO}_2}] = 9 \times 10^{-4} \text{ M}$, $10 \text{ e}^-_{\text{TiO}_2} / \text{particle}$) and an Ar-saturated AgClO_4 aqueous solution ($[\text{Ag}^+] = 2.5 \times 10^{-4} \text{ M}$) at pH 2.7.

Gaddy et al.¹⁵¹ assigned absorption bands at 250 nm and at 500 nm as being due to Ag clusters and Ag particles respectively with the surface plasmon resonance band of spherical silver particles which are less than 20 nm in size located at around 410 nm. Sahyun and Serpone¹⁰⁸ observed absorption spectra with maxima in the range of 420– 465 nm in their laser flash photolysis study concerning the initial stages of the photodeposition of silver on TiO₂ particles. They attributed these spectral features to metallic silver particles. Friedmann et al.¹⁰⁹ observed absorption spectra with a maximum at 380 nm at 1 μs after irradiating transparent colloidal TiO₂ suspensions in the presence of Ag⁺ ions and polyvinyl alcohol by an XeF laser (351 nm wavelength) with photon fluxes equivalent to 60 or 2 photons/TiO₂ particle, respectively. They attributed this band to the absorption of silver clusters containing more than 12 silver atoms. The authors concluded that the formation of such “larger than expected silver clusters” even at low photon fluxes is a result of an electron transfer within the TiO₂ aggregate similar to an antenna effect. Moreover, the authors observed that when the spectrum obtained 1 μs after the laser pulse is compared with the spectrum obtained after 5 ms, there is a clear decrease in absorption at shorter wavelengths and an increase at longer wavelengths. They attributed this shift in absorption towards the longer wavelengths in the millisecond time range to the cluster growth due to the diffusion of Ag⁺ ions from the solution to the metal clusters with the subsequent reduction of these silver ions and the growth of the silver clusters to form silver particles.

In comparison with our observation in the millisecond time scale the 400 nm band which is formed upon the reduction of silver ions with stored TiO₂ electrons, is attributed to rather large Ag⁰ particles while the deposits observed by Friedmann et al.¹⁰⁹ were small silver clusters and were formed at a very early stages of the reaction. Furthermore, the experimental condition differ considerably between the laser flash photolysis study and the present stopped flow experiments concerning both the concentration of TiO₂ particles as well as that of the silver ions.

The shift in the SP band to shorter wavelength observed here is supposed to be due to the transfer of TiO₂ electrons to the surface of the deposited silver particles and the subsequent accumulation on them leading to the equilibration of the Fermi level of the resulting Ag/TiO₂ composite nanoparticles. Mulvaney and co-workers¹⁵² studied the influence of the surface charge of silver particles within silica shells on the position and the intensity of the SP band. They observed a blue shift in the SP band of the silver particles after injection of electrons

chemically using borohydride ions as a reductant. Kamat and co-workers¹⁵³ observed a blue shift in the SP band of silver particles in Ag@TiO₂ core shell structures after injection of electrons from pre-irradiated TiO₂ suspensions. Furthermore, they studied the reproducibility of charging and discharging by repeated cycles of UV- irradiation of deaerated Ag@TiO₂ suspensions followed by exposure to air. They found that the SP band regains the original spectral features when the stored electrons are discharged by exposure to air. Therefore, it is believed here that the blue shift in the SP band is due to the accumulation of excess TiO₂ electrons on the silver particles surfaces. This is in fact attributed to the Fermi Level Equilibration in the semiconductor-metal nanojunction. Once the silver ions are completely reduced, the Fermi level in the Ag island still lies well within the band gap, probably close to +0.15 V vs. NHE.¹⁵² (b) As the excess electrons are transferred to the Ag islands a slow increase in the Fermi energy can be expected, i.e., inducing a more negative redox potential through an accumulation of excess electrons on the silver islands.

In other kinetic experiments the concentration of silver ions was in excess (5×10^{-3} M) compared to the concentration of TiO₂ electrons (2.2×10^{-4} M). Figure 3.41 (a) and (b) show the change in the absorbance vs. time signals at 600 nm and at 400 nm, respectively, for a typical experimental run.

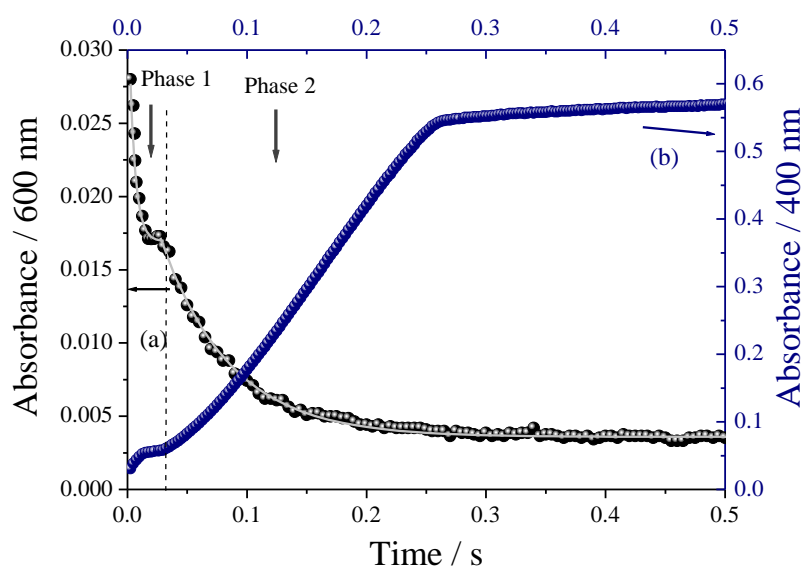


Figure 3.41: Change in the absorbance vs. time signals at 600 nm (a) and at 400 nm (b) observed after 1:1 mixing of electrons loaded TiO₂ suspension ($[e^-_{\text{TiO}_2}] = 2.2 \times 10^{-4}$ M, $2.4 e^-_{\text{TiO}_2}$ / particle) with an Ar-saturated AgClO₄ aqueous solution ($[Ag^+] = 5 \times 10^{-3}$ M) at pH 2.7.

A fast initial decay at 600 nm is accompanied by a fast initial build-up at 400 nm. The fast decay at 600 nm (phase 1) is followed by a second slower decay until a plateau is reached

(phase 2). The fast initial build up at 400 nm is followed by a continuous sigmoidal growth followed by a slow growth course similar to that observed in Figure 3.39. The first two phases observed here are similar to those observed working under the condition where $[e^-_{\text{TiO}_2}] > [\text{Ag}^+]$, while a third decay at 600 nm (phase 3) was not observed here. These observations support the assumption that the decay of electron absorbance at 600 nm in phase 3 (Figure 3.39) is due to the transfer of the excess electrons to the deposited silver particles after all silver ions were reduced.

The time resolved UV-vis spectra measured at different times after mixing are illustrated in Figure 3.42. A broad spectrum is observed followed by the formation of a peak at 390 nm that is shifted to 410 nm with time indicating the subsequent growth of the silver deposits.

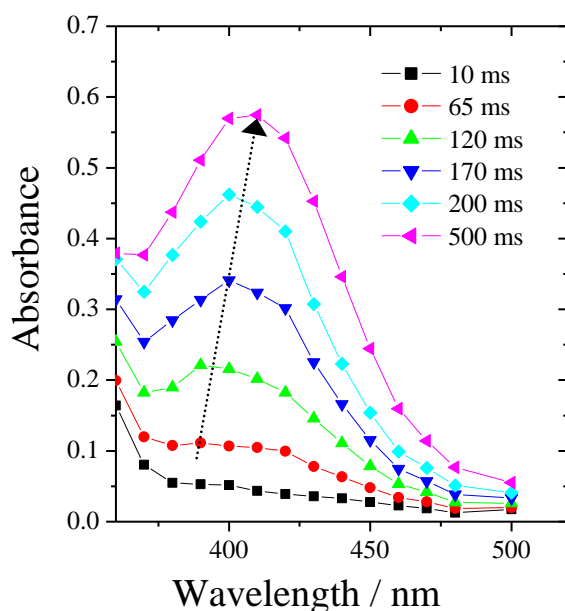


Figure 3.42: Time resolved absorption spectra measured at different times after 1:1 mixing of electron loaded TiO_2 suspension ($[e^-_{\text{TiO}_2}] = 2.2 \times 10^{-4} \text{ M}$, $2.4 e^-_{\text{TiO}_2}/ \text{particle}$) with deaerated aqueous AgClO_4 solution ($[\text{Ag}^+] = 5 \times 10^{-3} \text{ M}$) at pH 2.7.

The electron transfer rate constants due to the reduction of silver ions by the stored TiO_2 electrons were obtained by performing the kinetic experiment at different silver ions concentrations. Figure 3.43 (a) and 3.44 (a) show the absorbance decay at 600 nm and the absorbance build-up at 400 nm, respectively, observed after the reaction of the stored electrons with different Ag^+ concentrations. The pseudo first order rate constants of the decay of the kinetics curves at 600 nm in the two phases were found to correlate linearly with the

concentration of silver ions (Figure 3.43 (b)) and second order rate constants obtained from the slope of these linear relationships are $k_{ph1} = 3.74 \times 10^4 \text{ M}^{-1} \text{ s}^{-1}$, and $k_{ph2} = 3.86 \times 10^3 \text{ M}^{-1} \text{ s}^{-1}$ for phase 1 and phase 2 respectively. The first order rate constants of the fast initial build-up (phase 1) observed at 400 nm were found to increase linearly with increasing the concentration of silver ions and the obtained second order rate constant ($k_{ph1} = 3.34 \times 10^3 \text{ M}^{-1} \text{ s}^{-1}$) is in good agreement with the second order rate constant of the fast initial decay (phase 1) observed at 600 nm (Figure 3.44(b)).

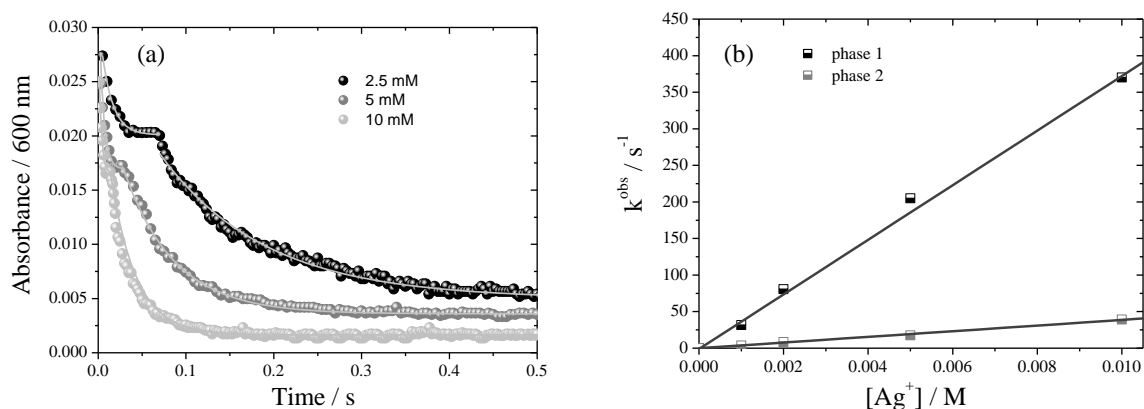


Figure 3.43: (a) Changes in the absorbance vs. time signals at 600 nm observed after 1:1 mixing of electrons loaded TiO_2 suspension ($[\text{e}^-_{\text{TiO}_2}] = 2.2 \times 10^{-4} \text{ M}$, $2.4 \text{ e}^-_{\text{TiO}_2} / \text{particle}$) with Ar-saturated AgClO_4 aqueous solution with different concentrations of Ag^+ ions, pH 2.7, solid lines present the first order fits. (b) Linear dependency of the observed first order rate constants for phase 1 and 2 on the Ag^+ concentrations.

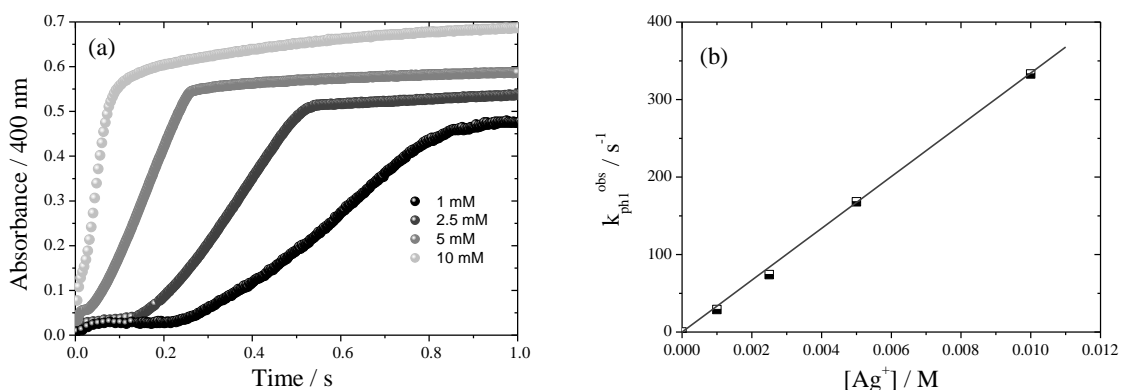


Figure 3.44: (a) Changes in the absorbance vs. time signals at 400 nm observed after 1:1 mixing of electrons loaded TiO_2 suspension ($[\text{e}^-_{\text{TiO}_2}] = 2.2 \times 10^{-4} \text{ M}$, $2.4 \text{ e}^-_{\text{TiO}_2} / \text{particle}$) with Ar-saturated AgClO_4 aqueous solutions with different concentrations of Ag^+ ions, pH 2.7. (b) Linear dependency of the observed first order rate constants for phase 1 on the Ag^+ concentrations.

The sigmoidal shape of the phase 2 as shown in Figure 3.44 (a) (as well as in Figures 3.39 and 3.41) suggests that autocatalysis is involved in phase 2 according to the following Equation:



Smaller Ag_n clusters act as catalysts for the growth of larger ones by transferring $e^-_{TiO_2}$ at their surfaces to Ag^+ ions adsorbing there from the bulk solution.

It has been suggested that $\ln(a/(1-a))$ should change linearly with the reaction time in the case of a simple autocatalysis,¹⁵⁴ according to the following equation

$$\ln(a/(1-a)) = (k[Ag^+])t - \ln([Ag^+]/n[Ag_n]) \quad (\text{Eq. 3.43})$$

where $a = A_t/A_\infty$ and A_t and A_∞ are the absorbance at time t and ∞ , respectively. The derivation of Eq.3.43 is presented in the Appendix 7.1 (page 150)

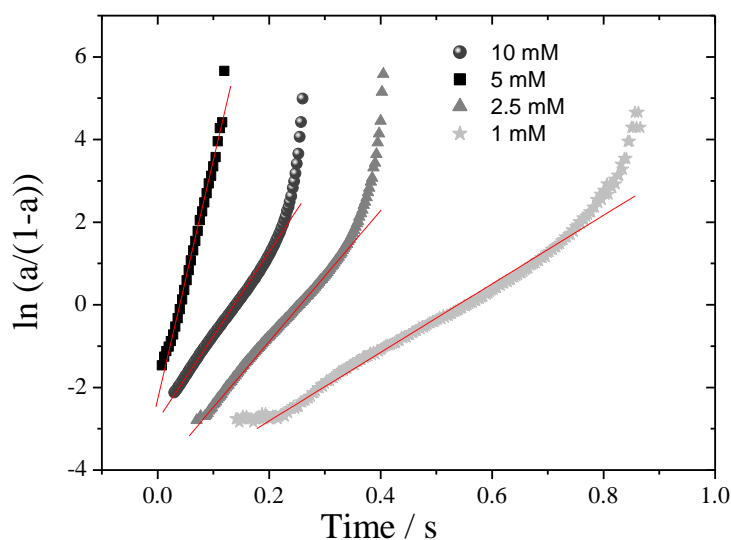


Figure 3.45: Autocatalytic plot of $\ln(a/(1-a))$ vs. reaction time using the data obtained in Figure 3.44 (a).

Actually, the fit was very good ($R^2 = 0.998$) over almost the entire duration of phase 2 and the straight line obtained by plotting $\ln(a/(1-a))$ vs. reaction time up to 88 % conversion (Figure 3.45) suggests that the assumption of an autocatalytic reaction is correct. The apparent rate constants of the sigmoidal growth (phase 2) of the SP absorbance of the silver nanoparticles at 400 nm at different concentration of silver ions are summarized in Table 3.6. From Eq. 3.42 the autocatalytic rate constant (k_{ph2}) is expected to vary linearly with the initial

concentration of silver ions ($[\text{Ag}^+]$) since $k_{\text{ph2}} = k[\text{Ag}^+]$. The linear dependency of the observed autocatalytic rate constant $k_{\text{ph2}/400 \text{ nm}}$ on the initial concentration of Ag^+ is illustrated in Figure 3.46 and the second order autocatalytic rate constant $k_a = 5.55 \times 10^3 \text{ M}^{-1} \text{ s}^{-1}$ is obtained.

Table 3.6: The rate constants of the build-up of SP at 400 nm obtained from the data represented in Figure 3.45.

$[\text{Ag}^+] / 10^{-3} \text{ M}$	$k_{\text{ph2}/400 \text{ nm}} / \text{s}^{-1}$ Autocatalytic Growth (Phase 2)
1	8.3
2	13.2
5	25.1
10	57.8

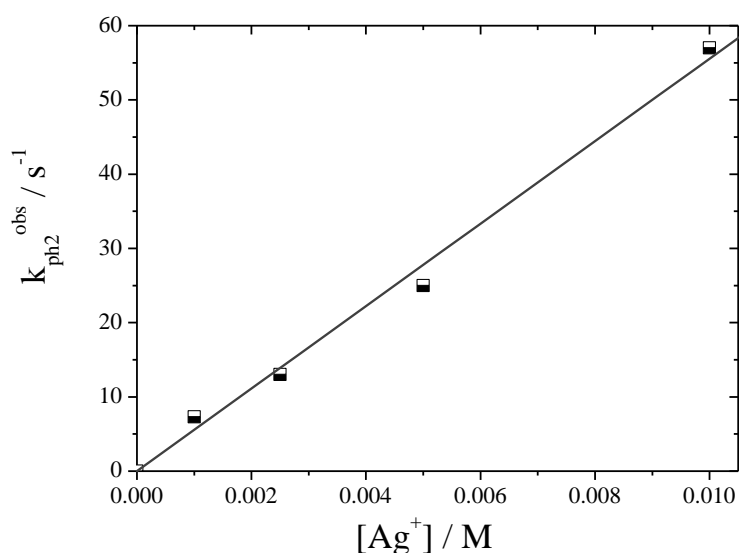


Figure 3.46: Linear dependency of the observed autocatalytic first order rate constants (phase 2) on the Ag^+ concentrations, the rate constants data obtained from the autocatalytic fits in Figure 3.45.

Effect of PVA on the Growth of Ag^0 Deposits

To study the effect of the presence of the polymer PVA on the kinetics of the formation and growth of silver deposits stopped flow experiments were performed by mixing the stored electrons with silver ions in the presence of PVA and comparing the kinetic curves with those for the experiments performed in the absence of PVA. Figure 3.47 shows the change in the absorbance vs. time signals recorded at 400 nm after mixing of TiO_2 electrons ($9 \times 10^{-4} \text{ M}$) and

Ag^+ ions (2.5×10^{-4} M) in the absence and the presence of PVA (5×10^{-4} M, 1×10^{-3} M). The rate constants are summarized in Table 3.7. It is obvious that the rate of the initial reduction and the autocatalytic growth of silver particles are decreased when PVA is present. It is also observed that the final absorbance at the saturation range at 1 s for the solution containing PVA is considerably lower than that observed in the PVA free solution. These experimental observations can be readily explained by the steric stabilization of the silver particles by the polymeric chain which isolate the particles and prevent them from coalescence and aggregation.

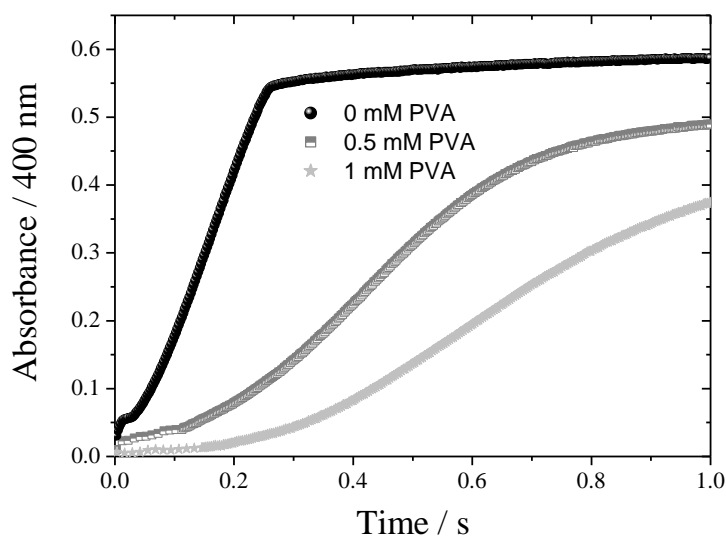


Figure 3.47: Change in the absorbance vs. time signals at 400 nm observed after 1:1 mixing of electrons loaded TiO_2 suspension ($[\text{e}^-_{\text{TiO}_2}] = 2.2 \times 10^{-4}$ M, $2.4 \text{ e}^-_{\text{TiO}_2}/\text{particle}$) and AgClO_4 solution ($[\text{Ag}^+]_0 = 2.5 \times 10^{-4}$ M) in the absence and the presence of PVA at pH 2.7.

Table 3.7: The rate constants of the build-up of SP at 400 nm ($[\text{e}^-_{\text{TiO}_2}] = 2.2 \times 10^{-4}$ M, $2.4 \text{ e}^-_{\text{TiO}_2}/\text{particle}$) and AgClO_4 solution ($[\text{Ag}^+]_0 = 5 \times 10^{-3}$ M) in the absence and the presence of PVA obtained from the data represented in Figure 3.47.

$[\text{PVA}] / 10^{-3} \text{ M}$	$k_{\text{ph1}} / \text{s}^{-1}$	$k_{\text{ph2}} / \text{s}^{-1}$
0	168	25.1
0.5	67.4	12.1
1	25.2	10.6

Effect of Oxygen

For further understanding of the factors influencing the formation kinetics of silver deposits it is important to study the effect of the presence of molecular oxygen. Kinetic experiments were performed by saturating the solution of Ag^+ ions with O_2 gas and then mixing it with TiO_2 loaded with electrons in the stopped flow chamber. The transient absorption spectra (370–540 nm) and the transient absorbance vs. time signal at 410 and 420 nm are shown in Figure 3.48 and the inset of Figure 3.48 respectively. It is obvious that the absorbance of SP band at 410 nm was developed followed by a slow decay ($k^{obs} = 0.21 \text{ s}^{-1}$). Moreover, the transient spectra show a red shift of the plasmon band from 410 nm to 420 nm. These observations reveal that the deposited silver particles in aqueous solution are sensitive toward oxygen, molecular oxygen acts as an electron acceptor resulting in the dissolution of the silver particles according to Eq. 3.44 (a). The reaction of the silver deposits with molecular oxygen is indicated by a damping and a red shift of the SP absorbance band. Henglein et al.⁹⁸ found that small silver clusters are sensitive towards oxygen and upon exposure of a cluster solution to air the cluster absorption bands disappearing within seconds.

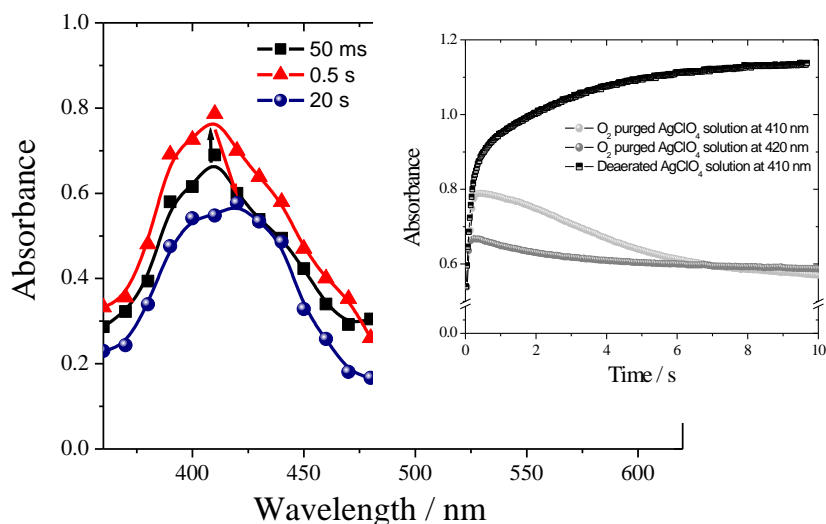


Figure 3.48: Time resolved absorption spectra measured after 1:1 mixing of electrons loaded TiO_2 suspension ($[\text{e}^-_{\text{TiO}_2}] = 5 \times 10^{-4} \text{ M}$, $5.4 \text{ e}^-_{\text{TiO}_2}/\text{particle}$) at pH 2.7 and oxygen saturated aqueous AgClO_4 solution ($[\text{Ag}^+] = 3 \times 10^{-4} \text{ M}$). Inset shows the decay of the build-up signals of the plasmon absorbance of silver particles at 420 and 410 nm in absence and presence of oxygen.

The oxidation of silver particles by molecular oxygen can also occur according to the four electron oxidation process (Eq. 3.44 (b)).



Furthermore, the kinetics of the reaction of deposited silver particles with molecular oxygen was studied by mixing an O₂-saturated aqueous solution with an aqueous solution of silver deposits (Ag/TiO₂) which was prepared in advance by mixing of 3×10⁻⁴ M AgClO₄ with an aqueous suspension of e⁻_{TiO₂} (5×10⁻⁴ M). The kinetic results is shown in Figure 3.49. It was observed that about 15 % of the original absorbance at 400 nm was decayed obeying first order kinetics with rate constant $k^{obs} = 0.06 \text{ s}^{-1}$. This slow decay can be assigned to (Eq. 3.44 (a) and (b)). This rate constant is smaller than that obtained from the analysis of the data in the inset of Figure 3.48 (0.21 s⁻¹). This can be explained in terms of the effect of particle size. The oxidation of the small particles during the early stages of the formation (i. e., the experimental conditions of Figure 3.48) is expected to be faster than the oxidation of the bigger particles that have been already formed and then brought in contact with molecular oxygen (i. e., the experimental condition of Figure 3.49).

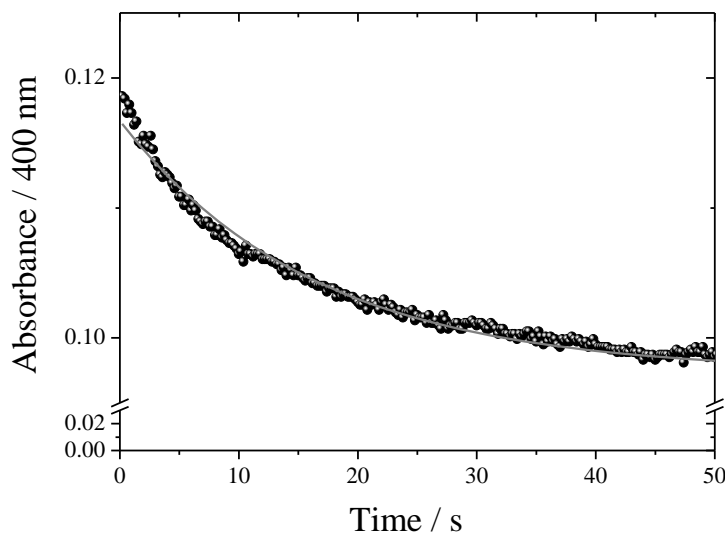


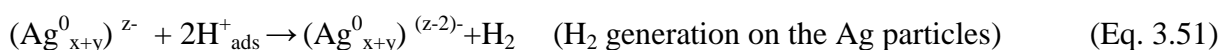
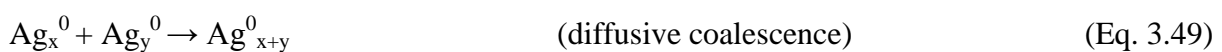
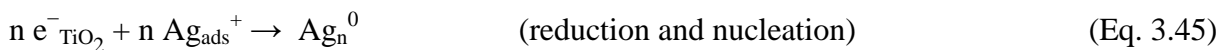
Figure 3.49: Time profile of the decay of the SP absorbance signals observed at 400 nm after 1:1 mixing of oxygen saturated aqueous solution with an aqueous solution of Ag/TiO₂ which was prepared in advance by mixing of 3×10⁻⁴ M AgClO₄ with an aqueous suspension of 5×10⁻⁴ M e⁻_{TiO₂}.

Eq. 3.44 (a) and (b) have been confirmed by the reaction of the colloidal silver deposits before and after saturation with molecular oxygen with 1 mM NaCl. It was observed that the reaction of the colloidal silver deposits saturated with oxygen resulted in a turbid solution. In contrast turbidity was not observed for the colloidal silver deposits in the absence of oxygen. These results indicate that essentially Ag^+ ions resulting from Eq. 3.44 reacted with Cl^- ions to form AgCl particles.

Mechanism of Formation and Subsequent Growth of Silver Particles on the Surface of TiO_2

The presented experimental results suggest a sequential process of the formation of silver nanoparticles on the surface of TiO_2 using the stored electrons on the TiO_2 nanoparticles as reductants. The mechanism can be proposed as: initial rapid reduction of a fraction of the Ag^+ ions to form silver atoms, which are aggregating to form silver nuclei, this step is followed by an autocatalytic growth of these silver nuclei forming silver nanoparticles. The growth step was suggested to occur by a sequence of alternating electronic and ionic events with the association of species such as Ag_{n+1}^+ , Ag_{n+1}^0 , Ag_{n+2}^+ , Ag_{n+2}^0 , Ag_{n+3}^+ , and Ag_{n+3}^0 analogous to those hypothesized to be involved in latent image formation in silver halide photography.¹⁰⁸ The autocatalytic growth is followed by a slow diffusion coalescence of the formed silver particles on the surface of TiO_2 to form even bigger silver particles.

After all the silver ions are consumed (ending of the growth step and starting of the aggregation step), the excess electrons are transferred via a Schottky barrier contact to the formed silver particles (this step is accompanying in the coalescence step) and stored on them, where they are used in the reduction of H^+ ions/water to produce molecular hydrogen. The above mechanism can be described by the following equations:



Furthermore, according to the theoretical calculations for the relation between the peak position and the radius of the formed particle reported by A. Slistan-Grijalva et al¹⁵⁵ and concerning the observed absorption maximum of the formed silver particle at 400 nm, the radius of the deposited silver particles is estimated to be about 5 nm which is corresponding to 3×10^4 silver atoms. For $9 \times 10^{-4} \text{ M } e^-_{\text{TiO}_2}$ it was calculated that each TiO_2 particle was charged with about 15 electrons. This means that the formation of each 5 nm silver particle require an association of 2000 TiO_2 particles. Hence, it is proposed that interparticle electron transfer mechanism is responsible for such high yield of the coalesced silver atoms to form the large silver particles.

b. Reaction of $e^-_{\text{TiO}_2}$ with Au^{3+}

Steady State UV–vis Absorption Measurements

Figure 3.50 shows the steady state UV–vis spectra of the blue suspension of stored electrons in TiO_2 nanoparticles (1×10^{-3} M) marked by the broad absorption in the visible region with a maximum around ~ 600 nm and the spectrum recorded after mixing of an aqueous solution of Au^{3+} ions (3×10^{-4} M) with TiO_2 electrons (1×10^{-3} M). Obviously, after mixing of the two solutions the broad absorbance of TiO_2 electrons disappears and a new absorption band with a maximum at 533 nm appears. The band at 533 nm resembles the typical surface plasmon band of gold nanoparticles.^{156,157} Recording of the spectra evinces the formation of stable particles with very little change in the absorbance after 5 min of formation. It was also found that the colloidal gold deposits were stable upon purge with air. These results reveal that the Au^{3+} ions are reduced by TiO_2 electrons to Au^0 atoms (Eq. 3.52) followed by the growth of these atoms to form gold particles.

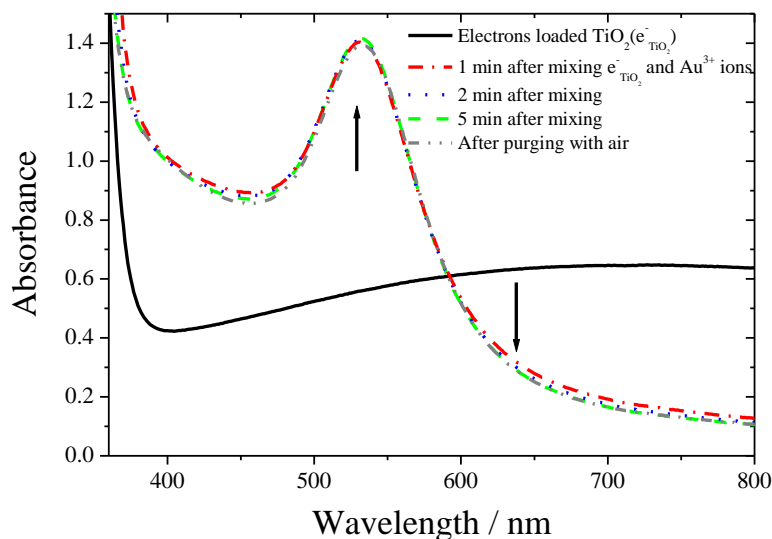


Figure 3.50: Steady state UV–vis spectra of the growth of Au^0 nanoparticles observed after mixing electron loaded TiO_2 aqueous suspension (1×10^{-3} M, $11 e^-_{\text{TiO}_2}$ /particle) with Au^{3+} ions from HAuCl_4 (3×10^{-4} M) at pH 2.2 and the effect of O_2 on the Au^0 deposits.

Stopped Flow Studies

The time resolved transient absorption spectra over the wavelength range of interest (380–600 nm) observed after mixing of the stored electrons of TiO_2 and Au^{3+} solution are shown in

Figure 3.51. Featureless spectra are observed during the induction period which is followed by the appearance of an absorption band at 550 nm with a small shoulder at 520 nm (which may result from clustering of different sizes of the particles). The bands are finally developed (at ~ 50 ms) and coalesced to give a broad band with a maximum around 540 nm. This band resembles the typical surface plasmon band of gold nanoparticles. The band maximum is slightly shifted to longer wavelength compared to the band observed in the steady state absorption spectra (Figure 3.50). The blue shift in the steady state spectra might be attributed to the the transfer of the TiO_2 electron to the surface of the gold deposits.

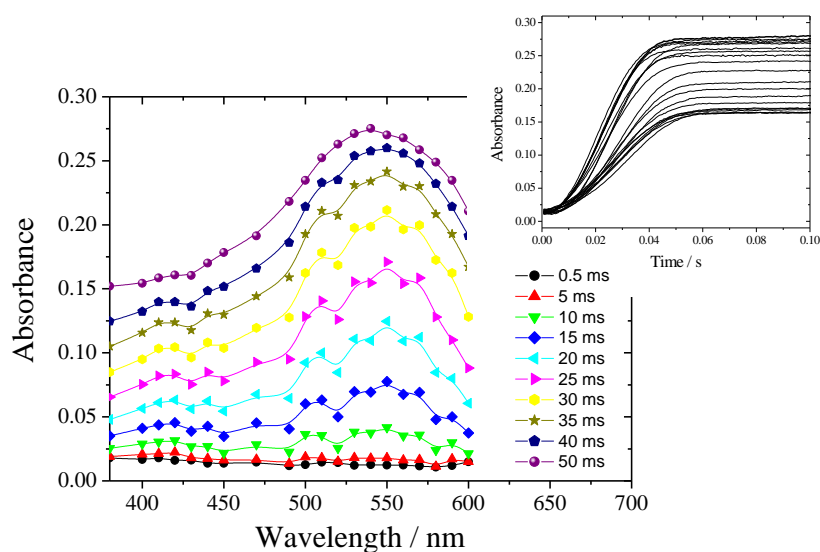


Figure 3.51: Time resolved spectra measured after mixing of an Ar-saturated Au^{3+} solution (3×10^{-4} M) with stored TiO_2 electrons suspension ($[\text{e}^-_{\text{TiO}_2}] = 1 \times 10^{-3}$ M, $11 \text{ e}^-_{\text{TiO}_2}/\text{particle}$) at pH 2.2. Inset shows the transients build-up at the whole wavelength range.

The transient absorption vs. time signals for the build-up of the absorbance at 540 nm observed after mixing of an aqueous solution of the Au^{3+} ions (3×10^{-4} M) with stored TiO_2 electrons (1×10^{-3} M) is shown in Figure 3.52. It is obvious that the kinetic curves exhibit a sigmoidal form: they start with a slow induction phase, then rise sharply and finally reach a constant saturation value, indicative of an autocatalytic reaction.¹⁵⁸⁻¹⁶⁰

If the process is indeed autocatalytic, the function quantitatively describing the progress of reduction, $\ln(a/(1-a))$ should have a linear time dependence where $a = A_t/A_\infty$ and A_t and A_∞ are the absorbance at time t and ∞ , respectively (cf. Eq. 3.43).¹⁵⁴

It was found that the kinetic curves observed here were successfully fitted with this model. The inset of Figure 3.52 shows the linear dependency of $\ln(a/(1-a))$ as a function of time for the data in Figure 3.52.

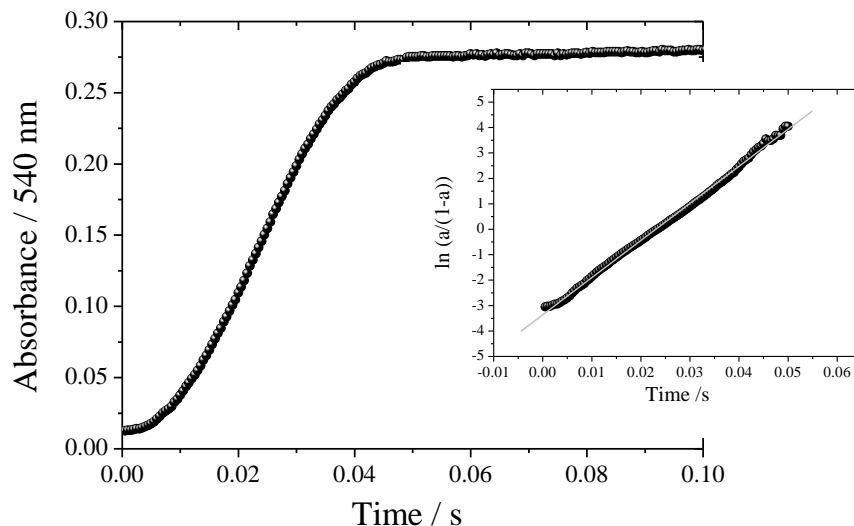


Figure 3.52: Time profile of the build-up of the absorbance of Au nanoclusters at 540 nm observed after mixing of an Ar-saturated HAuCl_4 solution ($[\text{Au}^{3+}] = 3 \times 10^{-4} \text{ M}$) with a stored TiO_2 electrons suspension ($[\text{e}^-_{\text{TiO}_2}] = 1 \times 10^{-3} \text{ M}$, $11 \text{ e}^-_{\text{TiO}_2}/\text{particle}$) at pH 2.2. Inset shows the plot of $\ln(a/(1-a))$ vs. time.

Unfortunately, it was not possible to observe the decay of the absorbance of TiO_2 electrons (until 620 nm) due to the reduction of Au^{3+} ions under our experimental conditions. The initial decay of electrons to form metal atoms is supposed to be faster than the limited resolution time of the stopped flow. The nucleation of the formed atoms is rather indicated from the induction time observed before the autocatalytic growth.

Effect of Initial Electron Concentration

In order to establish the mechanism of the reaction, it is necessary to determine the influence of the reductant concentration on the kinetics. Figure 3.53 shows the kinetic characterization of the formation of Au^0 nanoparticles at different electron concentrations. The initial concentration of Au^{3+} ions was kept constant ($3 \times 10^{-4} \text{ M}$). It is obvious that the induction time decreases and the growth rate increases as the concentration of the loaded electrons in TiO_2 increases. The rate constants are summarized in Table 3.8.

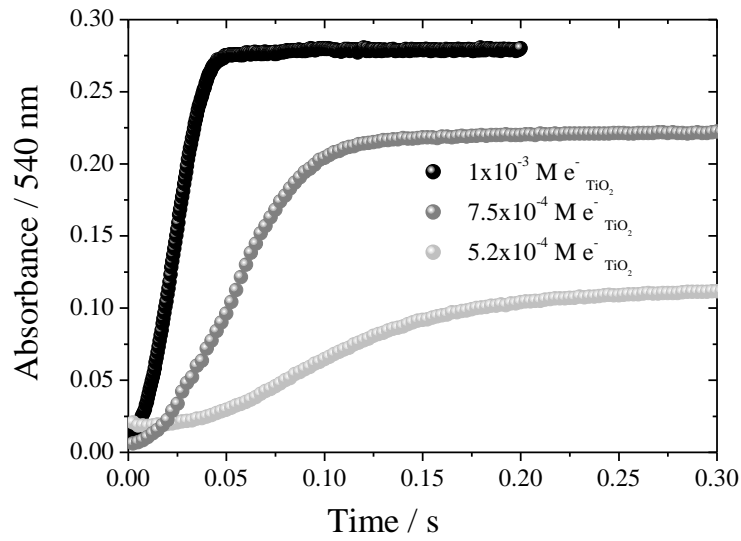
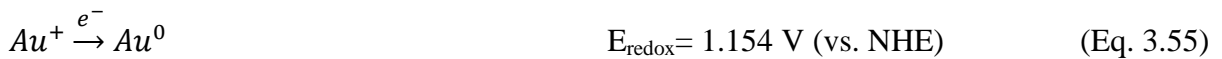
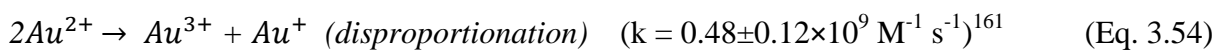


Figure 3.53: Time profiles of the build-up of the absorbance of Au nanoclusters at 540 nm after mixing of Ar-saturated 3×10^{-4} M Au^{3+} solutions with different concentrations of stored TiO_2 electrons suspensions at pH 2.2.

Effect of Initial Au^{3+} Ions Concentration

In order to learn more about the kinetics as well as the mechanism of the reduction of Au^{3+} ions and the formation of metallic Au_n^0 particles, the influence of the initial concentration of Au^{3+} ions at constant $e_{\text{TiO}_2}^-$ concentration on the rate of the reaction was studied. Figure 3.54 shows the time profiles of the build-up of the SP absorbance at 540 nm at different concentration of Au^{3+} . It is observed that the final absorption value increases with an increasing the initial gold ion concentration from 1.25×10^{-4} M to 3×10^{-4} M until reach limiting value at 3×10^{-4} M when $3e_{\text{TiO}_2}^- = \text{Au}^{3+}$. Interestingly, the autocatalytic growth rate decreases as the initial concentration of Au^{3+} increases. The rate constants are summarized in Table 3.8.

The decreasing of the autocatalytic growth rate with initial Au^{3+} concentration can be discussed, tentatively, in terms of the sequential steps reduction of Au^{3+} to Au^0 :



When the initial concentration of Au^{3+} increases, the production of Au^+ requires a larger amount of electrons (Eq. 3.53 and 3.54), so that the concentration of the remaining electrons required for the reduction of Au^+ to Au^0 (i. e., Eq. 3.55) is decreasing and consequently, the concentration of produced Au^0 nuclei should be decreasing. Hence, the autocatalytic growth rate will be decreasing as the amount of Au^0 nuclei acting as active centres for further growth is decreasing. Jacqueline Belloni^{160 (b)} and co-workers reported that the low valence Au^+ ions are somewhat protected by the more concentrated Au^{3+} ions from reduction.

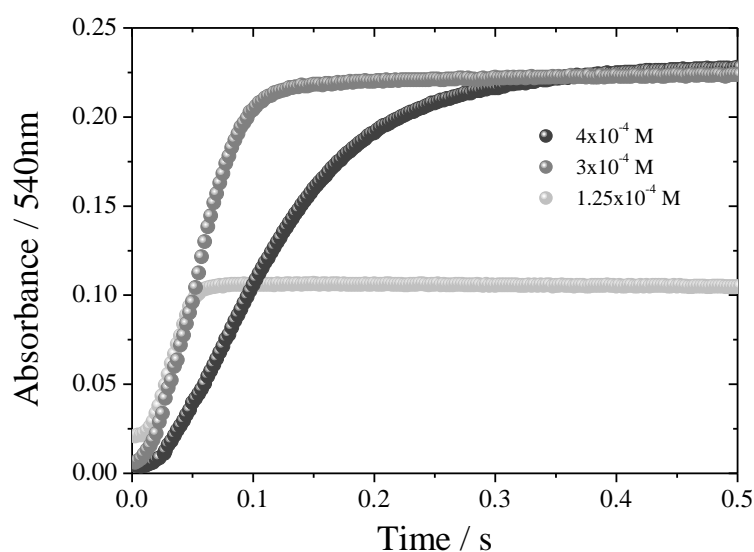


Figure 3.54: Time profiles of the build-up of the absorbance of Au nanoclusters at 540 nm observed after mixing of an Ar-saturated aqueous HAuCl_4 solutions containing different concentrations of the Au^{3+} ions with 7.5×10^{-4} M of stored TiO_2 electrons suspension ($8 e^-_{\text{TiO}_2}$ /particle) at pH 2.2.

Effect of PVA

Reduction of Au^{3+} ions was studied in polymer free solution as well as in systems containing the Au^{3+} salt dissolved in PVA solution. Figure 3.55 shows the kinetic characterization of the formation of gold nanoclusters in the absence of PVA and in the presence of PVA. It is obvious that the induction time increases and the autocatalytic growth rate decreases as the PVA concentration increases. In addition, the gold nanoclusters concentration decreases (as indicated from the final absorbance of the SP band) with increasing the polymer concentration. The effect of PVA in increasing the induction time can be explained in the light of the steric stabilization of the polymeric chain to the gold ions. Reduction of metal ions in the presence of the polymer is most often chosen because of the complexation of the metal

cations by the ligand atoms of the polymer which is crucial before reduction. It has been shown that polymers favor the isolation of Au nanoparticles¹⁶²⁻¹⁶⁴ as well as they protect the metal nanoparticles from coagulation and limit their particle size.⁴¹ The shapes and sizes of metal nanoparticles are controlled by changing in the ratio of the concentration of the polymer material to the concentration of the metal cations used.¹⁶⁵ Values of rate constants obtained at different polymer additions are gathered in Table 3.8.

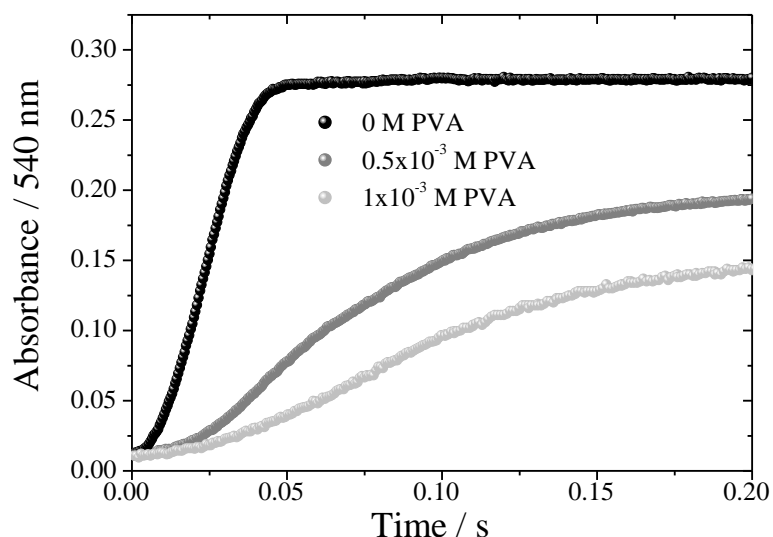


Figure 3.55: Time profiles of the build-up of the absorbance of Au nanoclusters at 540 nm observed after mixing an Ar-saturated aqueous HAuCl_4 solution (3×10^{-4} M) with an aqueous suspension of stored TiO_2 electrons (1×10^{-3} M, $11 e^-_{\text{TiO}_2}$ /particle) at pH 2.2 in the absence and in the presence of PVA.

Table 3.8: Rate constants of growth of Au at different concentrations of Au^{3+} , $e^-_{\text{TiO}_2}$ and PVA obtained from the slope of the linear dependency of $\ln(a/(1-a))$ vs. time.

$[\text{Au}^{3+}]_0 / 10^{-3}$ M	$[e^-_{\text{TiO}_2}] / 10^{-4}$ M	[PVA] / 10^{-3} M	k^{obs} / s^{-1}
1	7.5 ($8 e^-_{\text{TiO}_2}$ /particle)	0	20.3
0.4	7.5	0	27.4
0.3	5.2 ($5.7 e^-_{\text{TiO}_2}$ /particle)	0	28.2
		0	61
	10 ($11 e^-_{\text{TiO}_2}$ /particle)	0	140
		0.5	30
0.125	7.5	1	26.5
		0	92

Effect of Oxygen

To study the effect of molecular oxygen on the kinetics of the growth of Au⁰ nanoclusters on TiO₂ kinetic experiments were performed by saturating the solution of Au³⁺ ions with O₂ gas and then mixing it with TiO₂ loaded with electrons in the stopped flow chamber. It is found that the observed autocatalytic rate constant of the build-up of absorbance signals at 540 nm in the deaerated solution ($k^{obs} = 25.1 \text{ s}^{-1}$) is higher than that for the O₂ purged solution ($k^{obs} = 17.2 \text{ s}^{-1}$) as shown in Figure 3.56. These results presumably present the competition of gold nuclei growth and molecular oxygen reduction by the stored TiO₂ electrons during the growth step, which reduces the stored electrons concentration resulting in the decreasing of the growth rate as well as of the final SP absorbance. However, no decay in the absorbance signals is observed even over longer time scale, demonstrating the high stability of the deposited Au⁰ nanoclusters in presence of O₂.

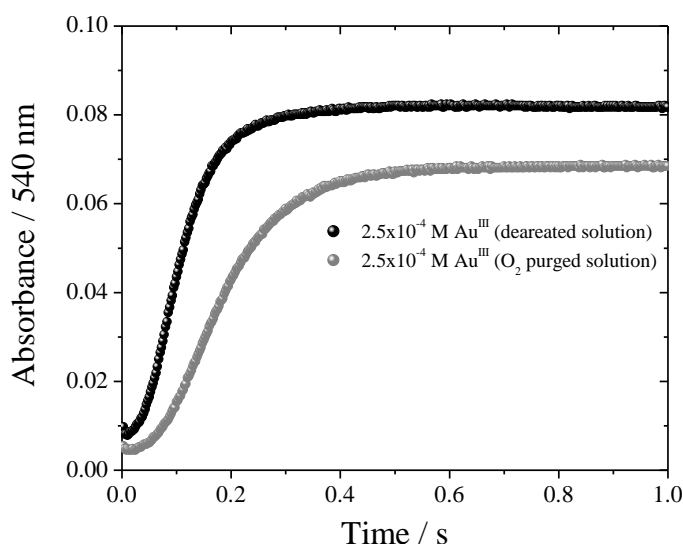


Figure 3.56: Time profiles of the build-up of the absorbance of Au nanoclusters at 540 nm observed after mixing stored TiO₂ electrons suspension ($[e^-_{\text{TiO}_2}] = 5 \times 10^{-4} \text{ M}$, $5.4 \text{ e}^-_{\text{TiO}_2}/\text{particle}$) with Ar-saturated aqueous HAuCl₄ solutions ($2.5 \times 10^{-4} \text{ M}$) at pH 2.2 in the absence and in the presence of oxygen.

Reaction of Excess TiO₂ Electrons with Au³⁺ Ions

In the following experiment the concentration of TiO₂ electrons was in excess ($1 \times 10^{-3} \text{ M}$) as compared to the Au³⁺ ($1 \times 10^{-4} \text{ M}$) ions concentration. Figure 3.57 shows the development of the UV-vis spectra under the strict exclusion of oxygen. Interestingly, after mixing the SP

band at 540 nm appeared immediately but was then bleached with time until it reached a constant absorbance without any further decay.

In order to investigate the process on a fast time scale, rapid mixing stopped flow experiments were performed. Figure 3.58 shows the transient absorption vs. time signal at 540 and 600 nm, it is obvious that the build-up signals of the SP absorbance (see the inset of Figure 3.60) followed by slow first order decay ($k^{obs} = 1.123 \text{ s}^{-1}$). The time resolved spectrum is shown in Figure 3.59. A broad absorption with peak at 540 nm is evolved after 75 ms followed by a damping without significant spectral changes.

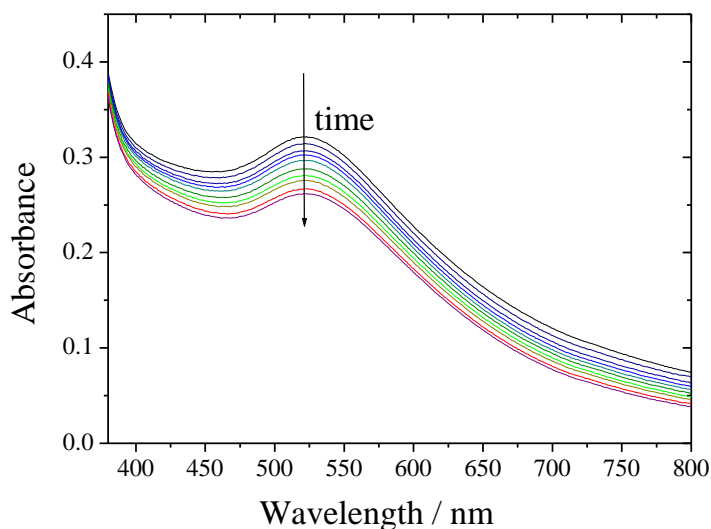


Figure 3.57: Steady state UV-vis spectra show the damping of the spectra of Au nanoclusters with time (time interval is 1 min) observed after mixing of an Ar-saturated aqueous HAuCl_4 solution ($1 \times 10^{-4} \text{ M}$) with an aqueous suspension of TiO_2 loaded with electrons ($[\text{e}^-_{\text{TiO}_2}] = 1 \times 10^{-3} \text{ M}$, $11 \text{ e}^-_{\text{TiO}_2}/\text{particle}$) at pH 2.2.

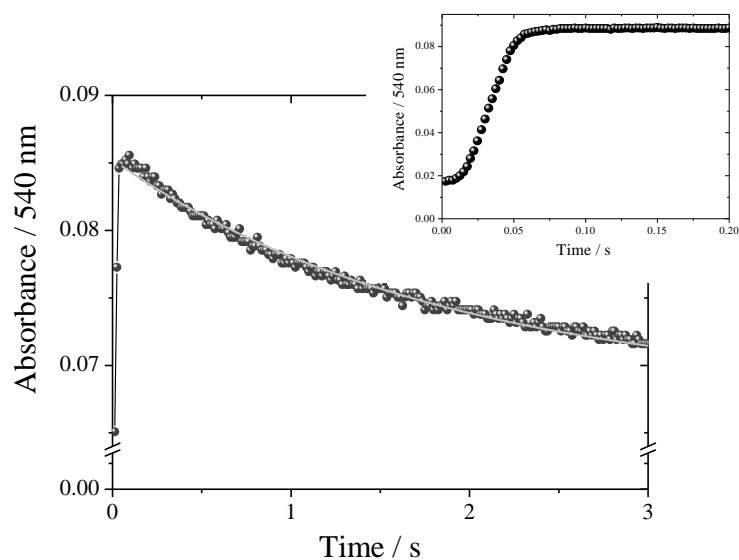


Figure 3.58: Time profiles of the build up and decay of absorbance of Au nanoclusters at 540 nm observed after mixing of Au^{3+} aqueous solution (1×10^{-4} M) with stored TiO_2 electrons suspension (1×10^{-3} M, $11 e^-_{\text{TiO}_2/\text{particle}}$) at pH 2.2, solid lines represent the first order fits of the decay signals. The inset shows the same data in the millisecond time scale.

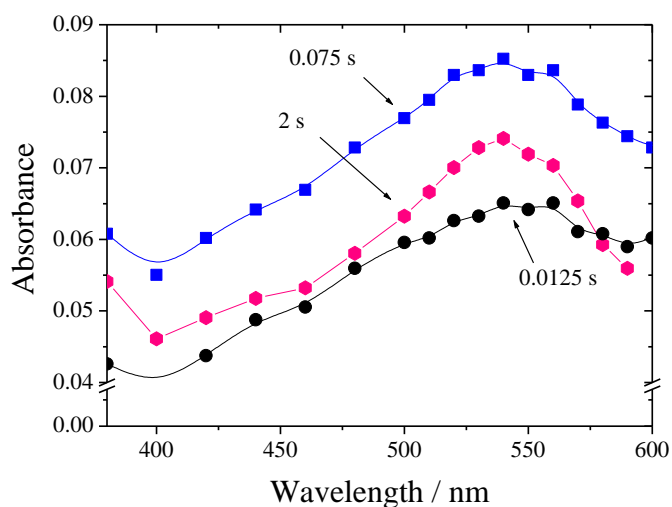


Figure 3.59: Time resolved spectra measured after mixing of 1×10^{-4} M Au^{3+} solution with 1×10^{-3} M stored TiO_2 electrons suspension ($11 e^-_{\text{TiO}_2/\text{particles}}$) at pH 2.2.

Proposed Mechanism of the Formation of Gold Nanoparticles on TiO_2 Surfaces

Reduction process is occurred at the interface of solution/substrate. Since the pH value of the solution in the experiments (around 2.5) was lower than the pH_{PZC} (7.5)^{165(b)}, AuCl_4^- ions

adsorb on the positively charged TiO₂ particles due to the electrostatic attracting. Summarizing all results obtained from studying the formation of the gold nanoparticles on TiO₂ under different conditions, one can suggest the mechanism as following:

- a) Reduction of metal ions by loaded electrons on TiO₂ colloidal suspension forming gold atoms which is supposed to be faster than the detection time of the stopped flow:

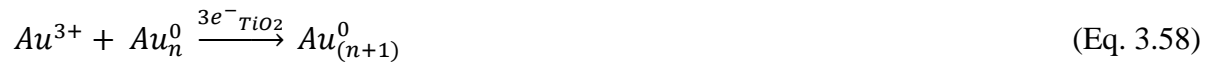


The electron transfer rate constant of the reduction of Au³⁺ ions (Eq. 3.54) can be later (Section 3.3.4.3) predicted theoretically from the linear relationship between the driving force and the interfacial electron transfer rate constants obtained for various metal ions (Figure 3.65) to be $k^{obs} = 1.18 \times 10^6 \text{ M}^{-1} \text{ s}^{-1}$, assuming that $E^0_{(Au^{3+}/Au^0)} = 1.52 \text{ V}_{NHE}$.

- b) The nucleation of the reduced gold atoms is supposed to be occur during the induction time:



- c) Growth of metal nuclei on the surface of TiO₂ forming gold particles:



Similar to the proposed mechanism of the silver particles growth, the growth of the gold particles on the TiO₂ surfaces (Eq. 3.58) will be composed of hundreds of elementary steps. The association of gold atoms with gold ions has been investigated for the radiolytic reduction mechanism of monovalent silver ions¹⁶⁶⁻¹⁶⁸ as well as for other ions.¹⁶⁹

Each growth step should be a diffusion controlled step, gold ions adsorb on the deposited gold clusters before getting reduced by the stored TiO₂ electrons.

Watzky and Finke¹⁷⁰ proposed two steps mechanism in their studies of the formation of transition metal nanoclusters using hydrogen as the reductant, the first step is corresponding to a slow continuous nucleation followed by fast autocatalytic surface growth of the metal clusters.

In the present system, the stored electrons were transferred from TiO₂ to Au³⁺ ions resulting in the reduction to gold atoms. After the Au³⁺ ions were reduced to Au atoms, the metal atoms form nuclei which act as core in promoting the reduction of further metal ions until all the gold ions are consumed, the growth phase stopped and reaching a plateau. The induction

time period represents the nucleation time. The role of metal core has been discussed in earlier studies of the formation of metal nanoparticles.¹⁷¹⁻¹⁷³

The deposition of gold particles on TiO₂ surfaces was confirmed by XRD and TEM measurements. Figure 3.60 shows the XRD reflection pattern of pure TiO₂ and Au/TiO₂ nanocomposite formed after mixing of blue suspension pre-loaded TiO₂ with electrons 1×10^{-3} M and Au³⁺ ions from HAuCl₄ solution (3×10^{-4} M) at pH 2.2. Au (111) and (200) diffraction planes are recognizable in the Au/TiO₂ sample, while anatase TiO₂ (101) and (200) lattice planes are detectable in the two samples.

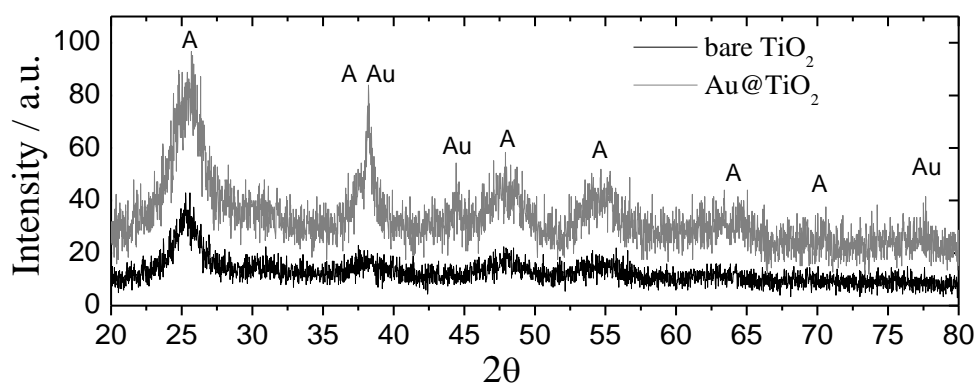


Figure 3.60: XRD patterns for as prepared Au/TiO₂ and pure TiO₂. Au (111) and (200) diffraction planes are recognizable in the Au/TiO₂ sample, while anatase TiO₂ (101) and (200) lattice planes are detectable in the two samples.

Figure 3.61 shows the TEM micrograph of Au/TiO₂ nanocomposite formed by mixing of blue suspension pre-loaded TiO₂ with electrons 1×10^{-3} M and Au³⁺ ions from HAuCl₄ solutions (3×10^{-4} M) at pH 2.2. The TEM pictures showing a distribution of deposited gold particles of about 5 nm on an agglomeration of smaller TiO₂ nanocrystals of about 2–3 nm size.

According to the TEM measurement the number of Au⁰ atoms in 5 nm particle is 6.35×10^3 atom/particle. Since each TiO₂ particle is charged with about 10 electrons. Thus it can be readily calculated that the formation of one Au⁰ particle require the association of 635 TiO₂ particles. These investigations reveal that the inter-particles electron transfer mechanism is responsible for the deposition of such large particles.⁶¹

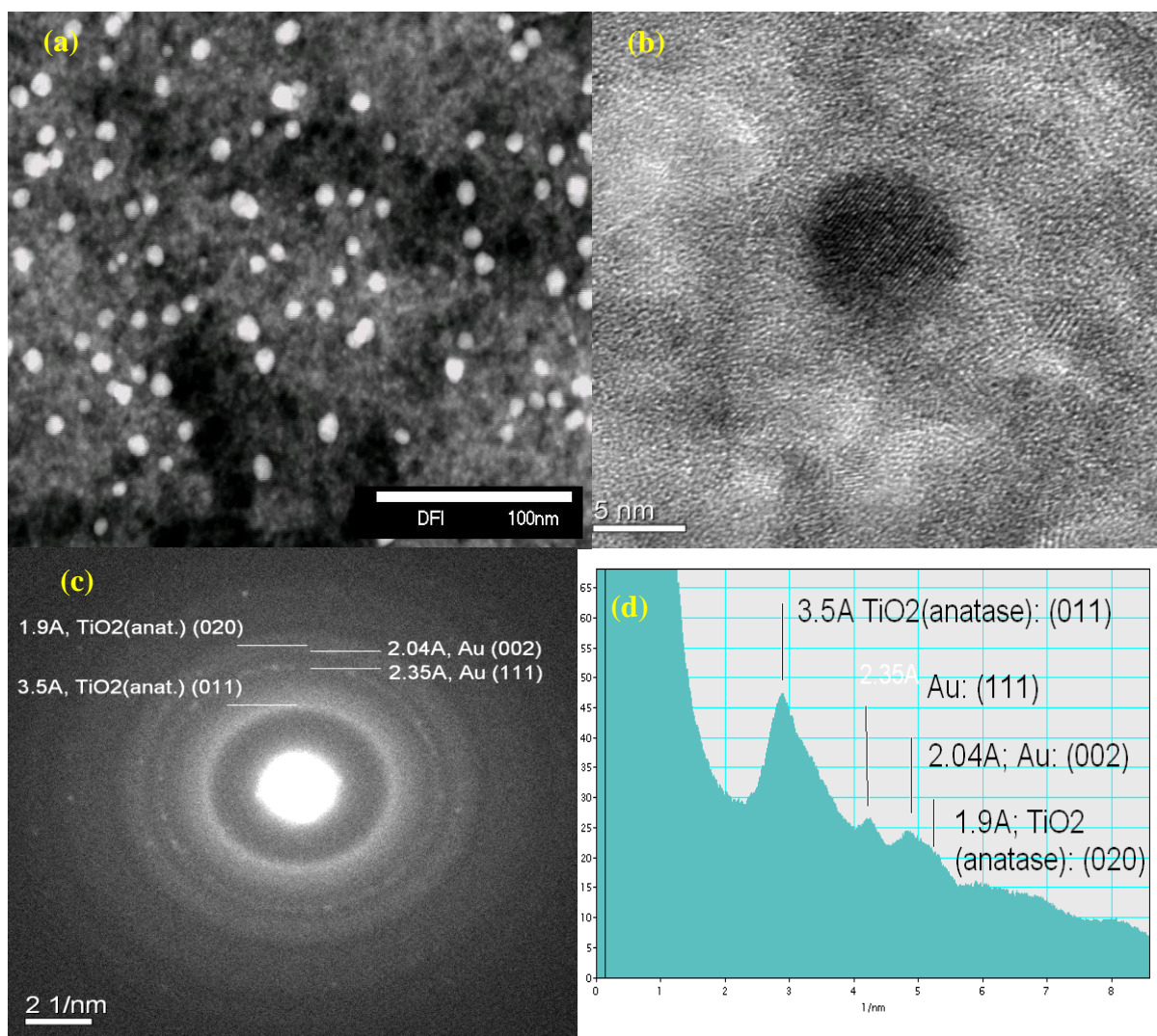


Figure 3.61: (a) STEM dark field micrograph showing gold particles (ca. 5nm diameter) by bright contrast and an agglomerated carpet of smaller TiO₂ nanocrystals (ca. 2-3nm) by grey contrast. (b): HR-TEM micrograph showing (111) lattice fringes of a gold nanocrystal, surrounded by smaller TiO₂ crystallites. (c): SAED pattern of a 560 nm circular specimen area showing two sets of Debye Scherrer rings, as a consequence of crystal structures and crystallite sizes. The rings corresponding to (002) and (111) of Au are relatively narrow. The rings corresponding to (020) and (011) of TiO₂ in the anatase modification are relatively broad. (d): Radial intensity distribution of the SAED pattern.

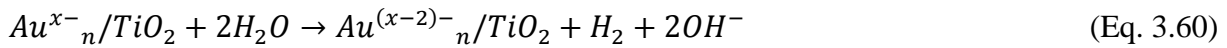
Transfer of the Excess Electrons from TiO₂ to the Deposited Gold Particles

In the case that the TiO₂ electrons are in excess compared to Au³⁺ ions, the electrons are initially transferred to the Au³⁺ ions forming gold nanoparticles, the excess electrons are then transferred to the reduced gold nanoclusters and stored on them causing the surface plasmon absorption to bleach. The bleaching of the surface plasmon band of gold nanoparticles results from the Fermi level equilibration of Au/TiO₂ nanocomposites, raising the quasi-Fermi level

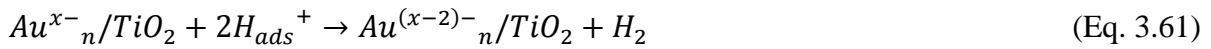
of gold deposits close to the conduction band level of the TiO₂. However, the surface plasmon bleaching observed with direct laser pulse excitation is due to the heating of the electronic gas of the metal nanoparticles.^{174, 175}

If indeed, such bleaching in the plasmon band is due to the storing of electrons in gold nanoparticles shifting the Fermi level of nanocomposite to more negative potential, we should be then able to detect the reaction of these electrons with water or adsorbed hydrogen ions to produce molecular hydrogen. It has been shown previously that the shift is often large enough to enable the stored electrons to form H₂ from the aqueous solution, i.e. the colloidal particles act as catalysts for the two-electron reduction of water.¹⁷⁶

Eq. 3.59 and 3.60 describe the processes of the charging of deposited gold nanoparticles by the stored TiO₂ electrons and the discharging of them by the reduction of water molecules.



Alternatively, the stored electrons can transfer to the adsorbed hydrogen ions:



Eq. 3.60 was inferred from the measured hydrogen yield which is found to be 3×10^{-4} M H₂, measured after 30 min of injecting the excess TiO₂ electrons (1×10^{-3} M) in an deaerated aqueous Au³⁺ solution (1×10^{-4} M). This value is close to the expected theoretical value of 3.5×10^{-4} M H₂, assuming that the concentration of the excess electrons reacted with H⁺/H₂O is 7×10^{-4} M.

Since Eq. 3.60 and 3.61 are accompanied by the decrease in the hydrogen ion in the solution, they could be proved by measuring the pH of the solutions. It is found that the pH of the resulted mixture of Au/TiO₂ nanocomposite suspension changed from 2.26 to 2.32 after 4 hours of injecting the TiO₂ electrons confirming Eq.3.60 and 3.61. Summarizing all the results a general scheme illustrate the multistep electron transfer mechanism is illustrated in Figure 3.62.

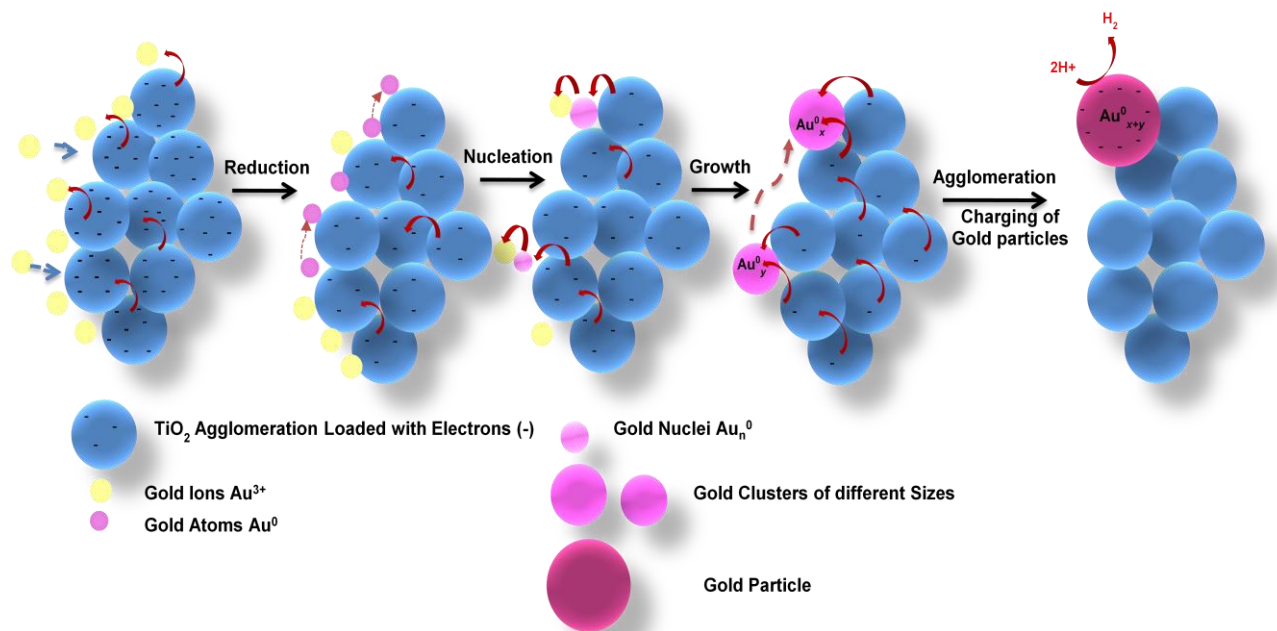


Figure 3.62: Schematic illustration of the deduced mechanism of the formation and growth of gold nanoparticles on TiO_2 surfaces using stored electrons.

3.3.4.3. Relation between Interfacial Electron Transfer Rate Constants and Driving Force

One of the most important parameters that affects the efficiency of the photocatalytic reduction of transition metal ions is the standard redox potential of the involved metallic couple related to the standard redox potential of the conduction band electron because only those species with reduction potentials much more positive than the conduction band edge can be photoreduced.

The difference between the standard redox potential of the metallic couple ($E^0_{(Mn+/M0)}$) and the standard redox potential of the conduction band electrons corresponding to the Fermi energy (E_{CB}) is defined as the driving force of the electron transfer reaction.

The interfacial electron transfer rate constant k_{et} (cm s^{-1}) changes with the driving force ($E^0_{(Mn+/M0)} - E_{CB}$) according to Tafel Equation (Eq.3.62)

$$\log k_{et} = \log k_{et}^0 + \frac{\alpha}{0.059} (E^0_{(M^{n+}/M^0)} - E_{CB}) \quad (\text{Eq. 3.62})$$

where α is the transfer coefficient and k_{et}^0 the value of the rate constant for $E^0_{(M^{n+}/M^0)} - E_{CB} = 0$. The interfacial electron transfer rate constant k_{et} is given by

$$k'_2 = 4\pi R^2 k_{et} \quad (R \text{ is the sum of the radii of TiO}_2 \text{ particle and the acceptor}) \quad (\text{Eq. 1.17})$$

where k'_2 expressed in the unit $\text{cm}^3 \text{s}^{-1}$, is related to the observed second order rate constant k_2^{obs} ($\text{M}^{-1} \text{s}^{-1}$) by

$$k'_2 = k_2^{obs} \times 1000/N_A \quad (N_A = \text{the Avogadro's number}) \quad (\text{Eq. 3.63})$$

Table 3.9 summarize the reactions, their redox potential, their observed second order rate constants (k_2^{obs}) obtained from stopped flow kinetic data and the electron transfer rate constants (k_{et}).

As no reaction between $e^-_{\text{TiO}_2}$ and Zn^{2+} or Mn^{2+} has been realized due to thermodynamic unfeasibility, the results of the reduction of other metal ions show the expected trend concerning the relationship between $\log k_{et}$ and the driving force of the electron transfer

reaction taking the value of $E_{CB} = -0.5 V_{NHE}$. This means that the electron transfer rate constants tend to increase with the driving force as illustrated in Figure 3.63.

The electron transfer rate constant of the reduction of Au^{3+} ions (Eq. 3.54) can be predicted theoretically from the linear relationship between the driving force and the interfacial electron transfer rate constants obtained for various metal ions (Figure 3.65) to be $k^{obs} = 1.18 \times 10^6 M^{-1} s^{-1}$, assuming that $E^0_{(Au^{3+}/Au^0)} = 1.52 V_{NHE}$.¹⁴⁴

Table 3.9: Summary of the electron transfer rate constants of the reaction of stored TiO_2 electrons with transition metal ions, their corresponding reactions and the corresponding redox potentials.

Reaction	$E^0(V_{NHE})$	$k_2 / M^{-1} s^{-1}$	$k_{et} / cm s^{-1}$
$Mn^{2+} + 2e^-_{TiO_2} \rightarrow Mn^0$	-1.18	(no reaction observed)	—
$Zn^{2+} + 2e^-_{TiO_2} \rightarrow Zn^0$	-0.76	(no reaction observed)	—
$Cd^{2+} + 2e^-_{TiO_2} \rightarrow Cd^0$	-0.4	6.38×10^2	2.28×10^{-6}
$Cu^{2+} + 2e^-_{TiO_2} \rightarrow Cu^0$	+0.34	3.5×10^4	1.87×10^{-4}
$Hg^{2+} + 2e^-_{TiO_2} \rightarrow Hg^0$	+0.85	7.5×10^4	1.91×10^{-4}
$Ag^+ + e^-_{TiO_2} \rightarrow Ag^0$	+0.8	3.77×10^4 (phase 1)	3.87×10^{-4}
$Au^{3+} + 3e^-_{TiO_2} \rightarrow Au^0$	+1.52	1.18×10^6 (predicted from Figure 3.65)	6.2×10^{-3}

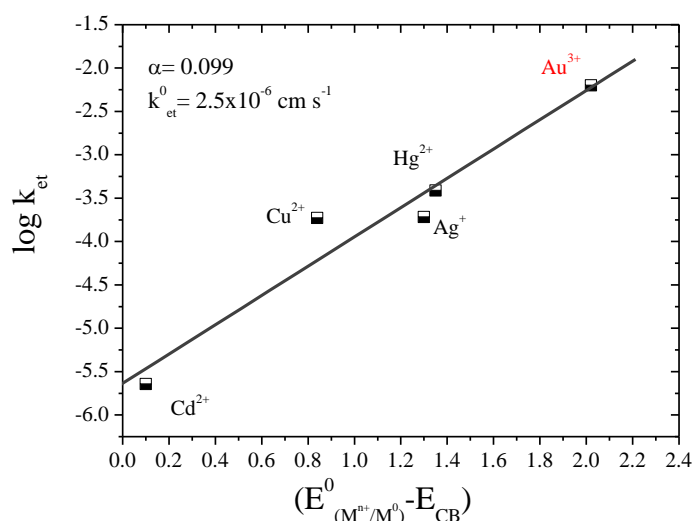


Figure 3.63: Dependency of interfacial electron transfer rates on the driving forces.

3.3.5. Reaction of $e^-_{TiO_2}$ with H^+/H_2O in Presence of Noble Metal Catalyst

Characterization of Metal Nanoparticles

Figure 3.64 (a) and (b) show the UV–vis absorption measurements of colloidal platinum (Pt^0) and colloidal gold (Au^0) nanoparticles respectively, prepared by citrate method reduction (section 2.3). The spectrum of colloidal platinum (a) stretches over the whole wavelength with a maximum at 225 nm in accordance with the spectra reported by Henglein et al. for platinum nanoparticles prepared by pulse radiolysis technique with a maximum at 215 nm.¹⁷⁷ It was reported that the particles prepared by this method had a mean diameter of 2.5- 3 nm.^{178, 179} The spectrum of colloidal gold nanoparticle with a typical surface plasmon band at 555 nm is shown in Figure 3.64 (b). The particles had a mean diameter of about 15-20 nm according to the reported method.^{178, 179} The pH of the colloidal metal particles was adjusted by HCl.

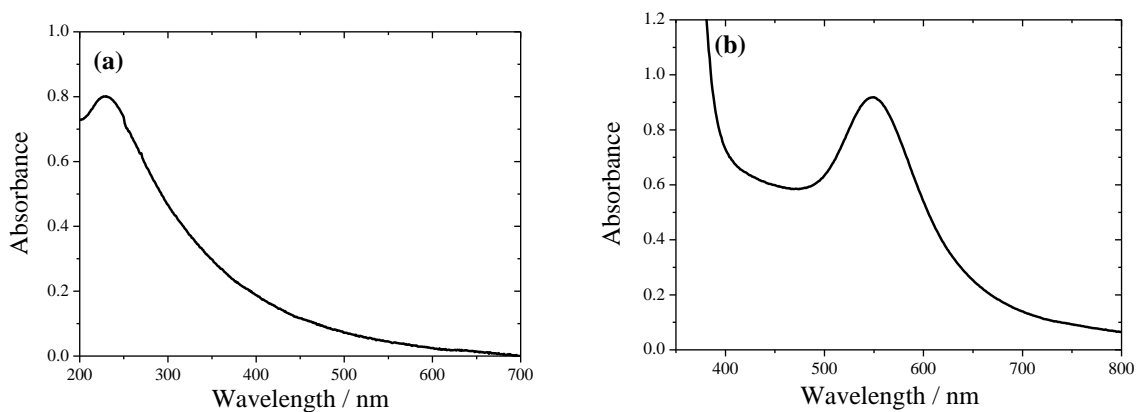


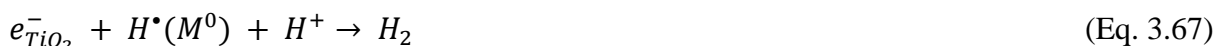
Figure 3.64: UV–vis absorption spectra of (a) colloidal platinum and (b) colloidal gold nanoparticles prepared by citrate method (Section 2.3) : 3.4×10^{-3} M sodium citrate, 1×10^{-3} M metal salt (H_2PtCl_6 , $HAuCl_4$)

Stopped Flow Kinetic Experiments

It was shown previously (Section 3.1.3.4 (b)) that the stored TiO_2 electrons reduce the noble metal ions (Ag^+ and Au^{3+}) to their metallic form. Interestingly, a consequence transfer of the excess electrons to the deposited metal particles has been observed and the reduction the adsorbed H^+/H_2O on their surfaces has been proved. Moreover, the role of MV^{2+} as an electron relay for H^+ reduction on the surface of Au^0 particles by the TiO_2 electrons has been investigated in Section 3.1.3.2. The following section represents a detailed kinetic study of the reaction of the $e^-_{TiO_2}$ with H^+ and water. Kaserevic-Popovic et al. showed that the typical blue color of colloidal $e^-_{TiO_2}$ in Argon saturated acid solution, disappears within several hours when the TiO_2 is coated with Pt^0 due to the reaction of $e^-_{TiO_2}$ with H^+ and H_2O .^{113(b)}



The adsorbed hydrogen radicals in Eq. 3.61 and 3.62 produce molecular hydrogen via radicals combination or by a reaction with further electron.



The kinetics of these reactions were studied by following the decay of the $e_{\text{TiO}_2}^-$ absorbance at 600 nm after the pulse radiolysis of the system $\text{TiO}_2/M^0/2$ -propanol.^{113(b,d)}

In the present work the decay kinetics of $e_{\text{TiO}_2}^-$ absorbance at 600 nm is followed after mixing of the electrons loaded TiO_2 aqueous suspension with aqueous suspensions of metal nanoparticles in the stopped flow chamber. Kinetic measurements are performed using different metals, Pt⁰ and Au⁰, at different metal concentrations and different pH. Figure 3.65 show the comparison of the decay kinetics of $e_{\text{TiO}_2}^-$ absorbance at 600 nm after mixing with an aqueous colloidal suspension of Pt⁰ and Au⁰.

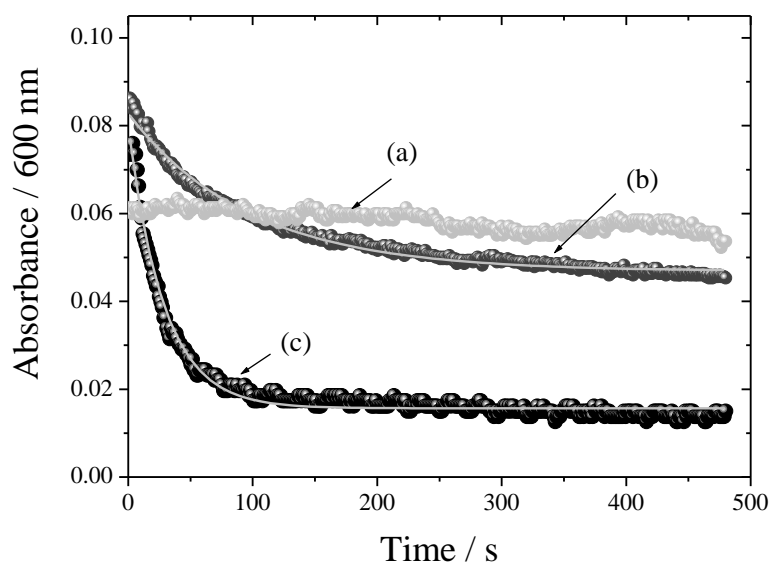


Figure 3.65: Time profiles of the decay of $e_{\text{TiO}_2}^-$ absorbance at 600 nm observed after mixing aqueous suspension of stored TiO_2 electrons (5×10^{-4} M, $5.4 e_{\text{TiO}_2}^-/\text{particle}$) with an Ar-saturated water in the absence of metal particles (a), Ar-saturated aqueous colloidal gold solution (5×10^{-10} M (particles)) (b), or colloidal platinum solution (9.1×10^{-7} M (particles)) (c) at pH 2.5. The solid lines represent the first order fit.

It is observed that in an Ar-saturated solution and in the absence of the metal particles the absorbance signals decay very slowly with a rate constant of 0.00149 s^{-1} , while in solutions containing gold particles or platinum particles the electron absorbance is fading faster. The decays obey first order rate law in both cases with rate constants of 0.010 s^{-1} and 0.035 s^{-1} for the Au^0 and Pt^0 respectively.

Bamwende et al.¹⁸⁰ studied photocatalytic H_2 generation in the system of Au^0/TiO_2 and Pt^0/TiO_2 in aqueous 5 M ethanol solution. They reported that the overall activity in Au^0/TiO_2 system is 30% lower compared to Pt^0/TiO_2 with H_2 yield depends on the metal content. In contrast, Behar and Rabani^{113(d)} reported higher than expected rate of H^+ reduction when TiO_2 particles coated with Au^0 instead of Pd^0 or Pt^0 which was attributed to a short chain reaction involving hydrogen abstraction from 2-propanol. This contradiction can be attributed to the different techniques performed and the different preparation method of the metal nanoparticles. According to our preparation method the gold particles had larger particle size (15-20 nm) than the colloidal platinum particles (2.5-3 nm), so that higher surface area of the later can reflect the higher rate constant of the reaction on their surfaces.

Figure 3.66 shows the kinetic measurements at different gold metal concentrations. The decay rate constants are increasing with the metal concentrations and a linear dependency was obtained from plotting the decay rate constants with metal concentrations (Figure 3.67). Similar linearity was obtained by Behar and Rabani^{113(d)} which was attributed to increasing the number of active sites rather than the surface area of the metal particles.

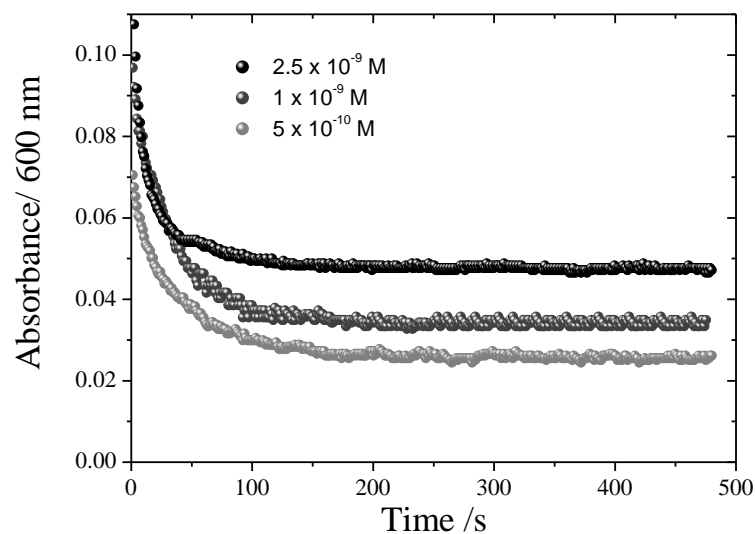


Figure 3.66: Time profiles of the decay of the $e^-_{\text{TiO}_2}$ absorbance at 600 nm observed after mixing aqueous suspension of the stored TiO_2 electrons ($5 \times 10^{-4} \text{ M}$, $5.4 e^-_{\text{TiO}_2}/\text{particle}$) with Ar-saturated aqueous colloidal gold solutions with different metal particles concentrations at pH 2.2.

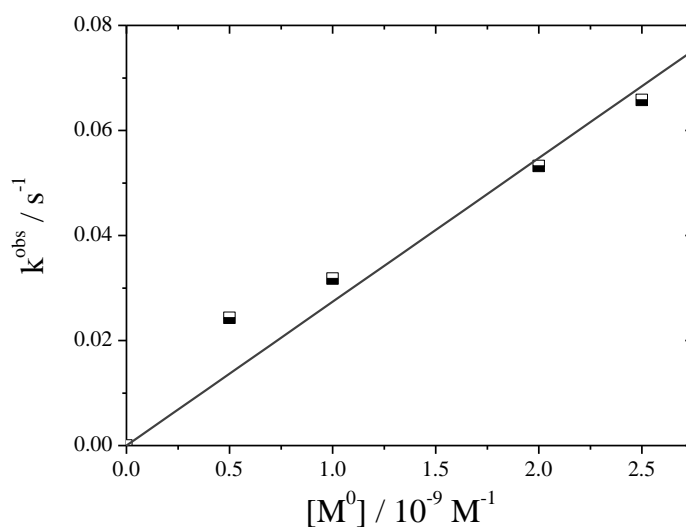


Figure 3.67: Linear dependency of the observed first order rate constants (obtained from the kinetic analysis of the data in Figure 3.66 and the concentrations of gold metal atoms). The slope = $2.7 \times 10^7 \text{ M}^{-1} \text{ s}^{-1}$.

Kinetic measurements performed at different pH at a given metal concentration are shown in Figure 3.68. It is observed that as the pH decreasing the rate of electron decay increasing.

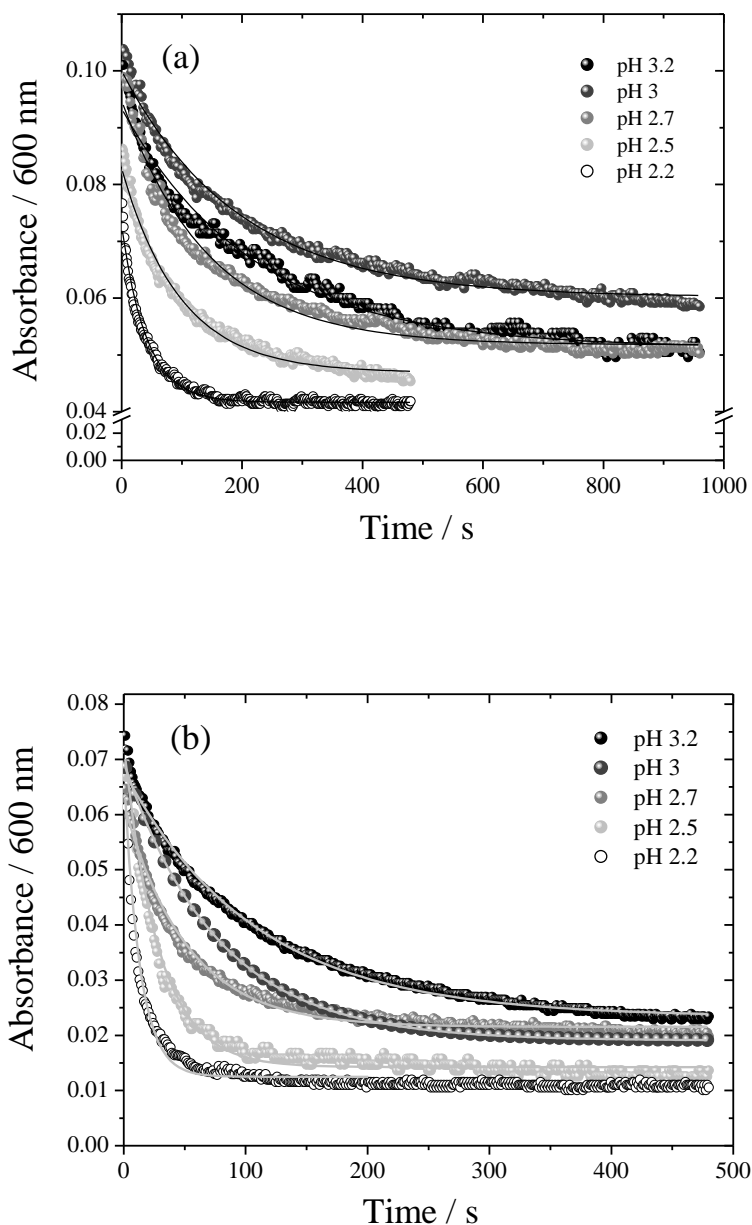


Figure 3.68: Time profiles of the decay of $e^-_{TiO_2}$ absorbance at 600 nm observed after mixing aqueous suspension of stored TiO_2 electrons (5×10^{-4} M, $5.4 e^-_{TiO_2}/particle$) with (a) an Ar-saturated aqueous colloidal gold solution (5×10^{-10} M (particles)), (b) an Ar-saturated aqueous colloidal platinum solution (9.1×10^{-7} M (particles)) at different pH, solid lines represent the first order fit.

The rate of the electron transfer reaction increases linearly with H^+ concentrations (Figure 3.69) confirming Eq.3.64, while the intercepts evincing a much smaller contribution of water reduction (Eq.3.65). According to Eq. 3.64, the hydrogen production is third order reaction:

$$R = k [e^-_{TiO_2}] [H^+] [M^0]$$

Since the concentrations of H^+ and M^0 are in excess compared to the concentration of electrons, they can be considered constant,

$$R = k^{\wedge} [e^-_{TiO_2}] \quad \text{where } k^{\wedge} = k [H^+] [M^0]$$

k^{\wedge} is the observed rate constants obtained from the pseudo first order fitting of the decay of electrons.

The slopes obtained from the linear dependency of the pseudo first order rate constants of the electrons decay and H^+ concentrations calculated from the data in Figure 3.69 are corresponding $k^{\wedge} [M^0]$ and third order rate constants for the reaction on Au^0 surfaces and Pt^0 surfaces are $k_{Au} = 3.5 \times 10^4 [Au^0] M^{-1} s^{-1}$, and $k_{Pt} = 9.8 \times 10^4 [Pt^0] M^{-1} s^{-1}$ respectively. The rate constants obtained here are correspondingly higher than the rate constants obtained by Behar and Rabani^{113 (b)} ($k_{Au} = 7 \times 10^2 [Au^0] M^{-1} s^{-1}$, $k_{Pt} = 1 \times 10^2 [Pt^0] M^{-1} s^{-1}$). This might be attributed to the different preparation method of metal nanoparticles, different sizes and different TiO_2 particles.

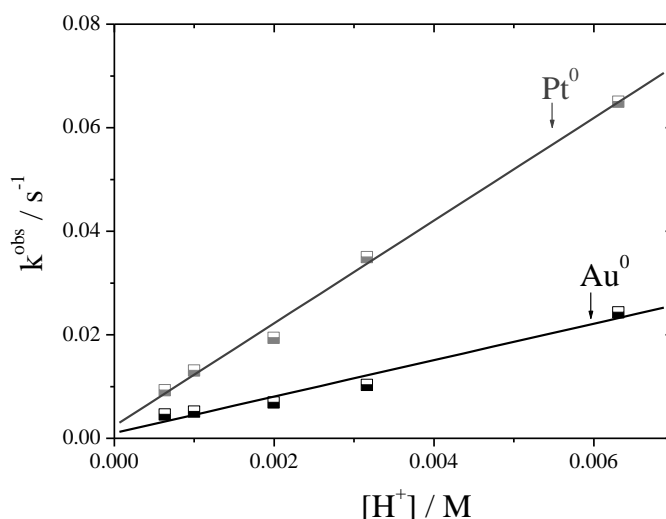


Figure 3.69: Linear dependency of the observed first order rate constants (obtained from the kinetic analysis of the data in Figure 3.68 and H^+ concentrations).

Such law rate constants can be understood by considering the diffusion of the big metal particles and TiO_2 particles in the solution before the successful electron transfer reaction occur.

On this basis, Smoluchowski¹⁸¹ provided an equation for the diffusion-controlled second order rate constant ($k_{AB} / M^{-1} s^{-1}$) as following

$$k_{AB} = \frac{4\pi r_{AB} D_{AB} N_{Av}}{1000} \quad (\text{Eq. 3.68})$$

where r_{AB} is the encounter distance between TiO_2 and the metal particles (i.e., the sum of the radii of the TiO_2 and the metal particle), D_{AB} is the sum of the diffusion coefficients of the TiO_2 and the metal particle ($D_{\text{TiO}_2\text{Au}^0} = D_{\text{TiO}_2} + D_{\text{Au}^0}$) and N_{Av} is the Avogadro's number. The diffusion coefficient D_A is calculated according to the following equation

$$D_A = \frac{KT}{6\pi\eta r} \quad (\text{Eq. 3.69})$$

where K is Boltzmann constant = $1.3806503 \times 10^{-23} \text{ m}^2 \text{ kg s}^{-2} \text{ K}^{-1}$, T is the temperature in Kelvin = 297 K, η is the viscosity of water = $8.9 \times 10^{-4} \text{ Kg m}^{-1} \text{ s}^{-1}$ and the r is the radius of A.

The diffusion controlled rate constant calculated from Eq. 3.65 and 3.66 for the reaction between TiO_2 particle (3 nm) and Au^0 particle (15 nm) is $1.33 \times 10^8 \text{ M}^{-1} \text{ s}^{-1}$.

According to the above calculations it is clear that the reaction between the TiO_2 particle and the metal particle is not a diffusion controlled rate reaction.

H₂ Measurements

The concentration of molecular hydrogen produced from the reaction of $e^-_{\text{TiO}_2}$ with $\text{H}^+/\text{H}_2\text{O}$ have been determined after mixing of electrons loaded TiO_2 aqueous suspensions with Ar-saturated aqueous solutions containing metal nanoparticles under various conditions of metal nanoparticles concentrations (detailed experimental description was shown in the Experimental Section (Section 2.4)). All measurements have been carried out under argon atmosphere and a reference measurement was taken by mixing the electron suspension with an Ar-saturated aqueous solution in the absence of metal particles. The results are summarized in Table 3.10.

Table 3.10: Comparison of produced hydrogen concentrations at different metals and different metal concentrations.

Metal	$[\text{M}^0] / 10^{-4} \text{ M}$	pH	$[\text{H}_2] / 10^{-4} \text{ M}$ (measured after 15 min of mixing)
Au	0	2.2	0
	1	2.2	1.2
	5	2.2	1.8
Pt	0	2.2	0
	1	2.2	2.1
	5	2.2	2.2

Assuming that the Pt particles have a spherical shape, the volume of one Pt particle with a diameter of 2.5 nm is calculated to be $8.18 \times 10^{-21} \text{ cm}^3$. Considering that the mass density of Pt is 21.45 g cm^{-3} , the average weight of one Pt particle is readily calculated to be $1.75 \times 10^{-19} \text{ g}$. In our system of $5 \times 10^{-4} \text{ M}$, the number of Pt particles will consequently be 5.47×10^{17} particles l^{-1} . Similarly, assuming that Au particle have a spherical shape, the volume of Au particle with a mean diameter of 15 nm is $1.77 \times 10^{-18} \text{ cm}^3$, the average weight of one Au particle is readily calculated to be $3.4 \times 10^{-17} \text{ g}$. At Au concentration of $2.5 \times 10^{-4} \text{ M}$, the number of Au particles will consequently be 1.5×10^{15} particles l^{-1} . In our system of 5.53×10^{19} TiO_2 particles l^{-1} , for each 100 TiO_2 particle there is one Pt particle, while for each 3.7×10^4 TiO_2 particle there is one Au particle. Therefore, most of the TiO_2 particles don't contain metal particle and hence a partial transfer of electrons is expected. However, this is contradicted to the concentration of consumed electrons calculated here.

In our system the concentration of TiO_2 electrons is $5 \times 10^{-4} \text{ M}$, for the TiO_2 particles of 3 nm mean diameter, this is corresponding to 5 electrons per TiO_2 particle. The concentrations of the produced H_2 presented in Table 3.10 reveal that most TiO_2 electrons have been reacted to produce molecular hydrogen. At the highest concentration of metal ($5 \times 10^{-4} \text{ M}$) about 88% of electrons have been reacted in presence of Pt metal and about 72 % of electrons have been reacted in presence of Au metal. These values are in a good agreement with the concentrations of consumed electrons calculated from the kinetic curves.

These results might be explained by the interparticle transfer mechanism,⁶¹ the stored electrons on the TiO_2 particle can be move freely from one particle to another within the TiO_2 agglomerate until reaching the surface of metal particle.

4. Laser Flash Photolysis Study

Chemical Procedures

The TiO₂ nanoparticles used in laser flash photolysis study was prepared from the hydrolysis of titanium tetra isopropoxide in 2-propanol. The pH was adjusted using perchloric acid (Section 2.2). The XRD analysis of the resulted powder indicating the anatase crystals of 5 nm particle sizes. The aqueous colloidal suspensions were freshly prepared in deionized water immediately prior to each experiment. The solutions were deaerated by purge with Argon gas for 30 min before measurements. Prior to the laser flash photolysis experiment the steady state absorption spectrum was measured using a Cary 1E (Varian) UV–Vis spectrometer to ensure the absence of any stray light above 400 nm.

The absorbance spectra of 2 g l⁻¹ of TiO₂ nanoparticles re-suspended in pure water at pH 2.5 is shown in Figure 4.1. The TiO₂ colloidal suspensions absorb below 380 nm with no absorption in the visible range. The crystalline character of the nanoparticles was investigated by XRD (Figure 4.2). The sample exhibit broad diffraction pattern characteristic of the crystal phase of pure anatase of 5 nm particle size (as calculated from the XRD line broadening).

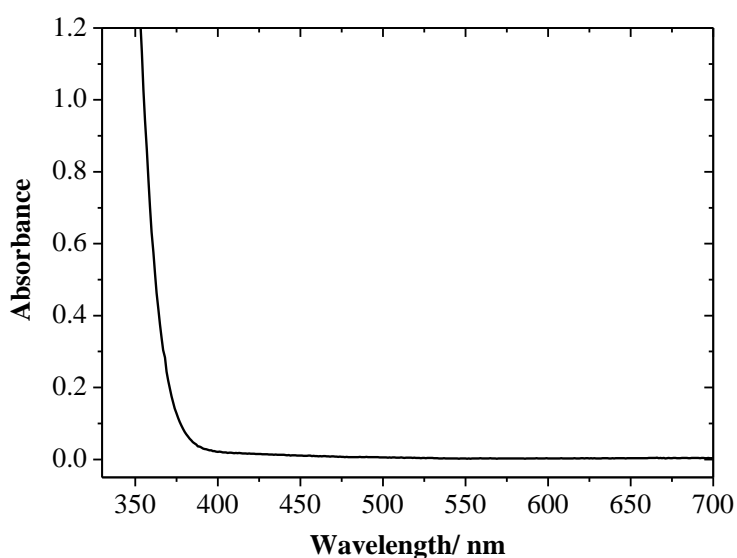


Figure 4.1: Absorption spectrum of freshly prepared 2 g l⁻¹ colloidal TiO₂ aqueous suspension at pH 2.5.

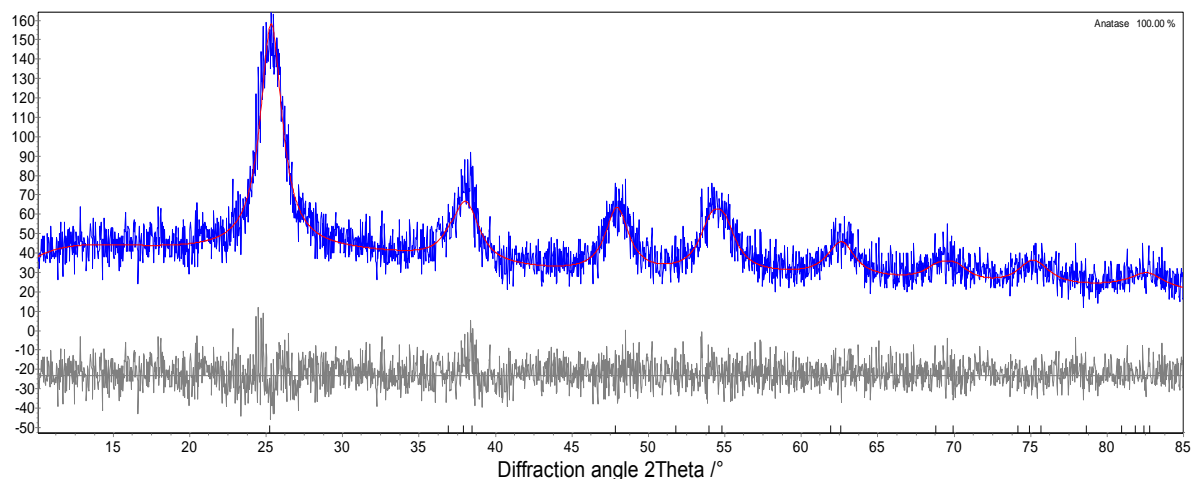


Figure 4.2: XRD pattern of as-prepared TiO₂ powder.

Based on the concentration of the TiO₂ particles of 2 g l⁻¹ and on the average particle size of 5 nm, TiO₂ particles concentration is: 1.3×10⁻⁵ mol particles l⁻¹. According to the values of the calculated photon fluxes from 2×10⁻⁵ mol photons l⁻¹ to 5×10⁻⁵ mol photons l⁻¹, this is corresponding to the range from 1 to 4 photons / particle.

Laser Flash Photolysis Experiments

In the laser flash photolysis experiments the changes of the optical absorbance of irradiated colloidal TiO₂ suspensions was measured after laser pulses under varied conditions. In all cases the absorbing transient species were characterized by recording their transient absorption spectra over the time range of interest (nanosecond to millisecond). The laser flash photolysis experiments performed here are aiming to investigate the primary processes upon band gap irradiation including the reactions of photogenerated electrons and holes in TiO₂ nanoparticles.

4.1. Primary Processes upon Band Gap Irradiation

4.1.1. Irradiation of TiO₂ Particles in the Absence of Hole and Electron Scavengers

The system of aqueous suspension of TiO₂ (6.3×10⁻³ M) was purged for 30 min with argon gas and excited with laser pulses (an average 600 pulses). The photon flux of 5×10⁻⁵ mol photons l⁻¹ was used which is equivalent to ~ 4 photon/particle. The typical transient absorbance vs. time signal observed at 580 nm and 400 nm upon band gap irradiation ($\lambda_{\text{max}} = 355$ nm) of the deaerated aqueous TiO₂ colloidal suspension are shown in Figure 4.3.

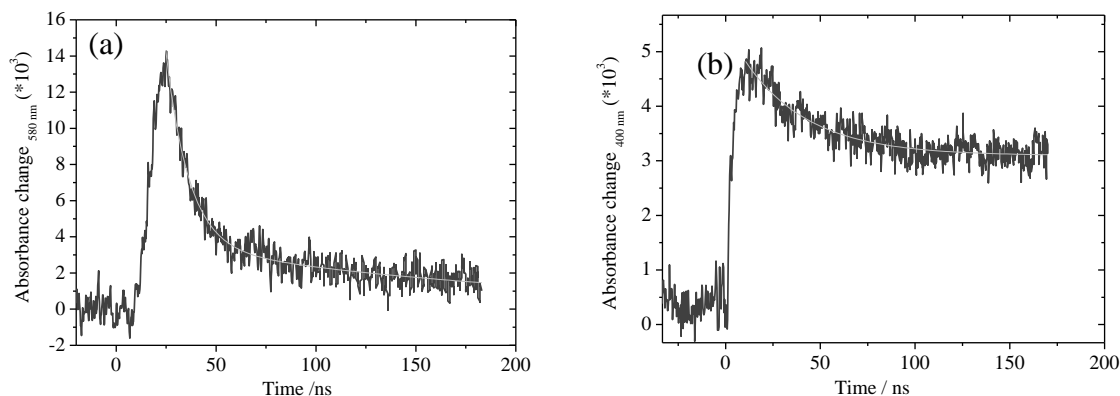


Figure 4.3: Transient absorption vs. time signals at 580 nm (a) and 400 nm (b) observed upon laser excitation of a deaerated aqueous suspension of TiO_2 particles (1.3×10^{-5} mol particles l^{-1}) at pH 2.5, absorbed photon concentration is 5×10^{-5} mol photons l^{-1} .

It is obvious that about 85 % of the signal decays very rapidly within about 50 ns until a plateau is reached a further slow decay is observed. The fast initial decay obeys first order kinetic and a rate constant $k_1 = 1.08 \times 10^8 \text{ s}^{-1}$ is obtained from exponential fitting of the absorption/time signal at 580 nm. Similar decays were observed at the entire wavelength regime of interest (400-640 nm) with decreasing the decay rate on going to the shorter wavelength regime.

In general, the basic processes of the TiO_2 photocatalysis can be summarized as follows: when a photon of energy higher or equal to the band gap energy is absorbed by a TiO_2 nanoparticle, an electron from the VB is promoted to the CB with simultaneous generation of a hole in the VB (Eq.4.1). In absence of electron and hole acceptors the e^-_{cb} and the h^+_{vb} can recombine on the surface or in the bulk of the particle in a few nanoseconds (and the energy dissipated as heat) (Eq. 4.2) or can be trapped in surface states where they can react with donor or acceptor species adsorbed or close to the surface of the particle (Eq. 4.3 and 4.4).



The photogenerated electrons trapped at Ti^{IV} sites in less than 20 ps⁷⁹ giving rise to the absorption in the visible regime with absorption maximum at around 600–620 nm.^{74, 79} The change in the absorption of these trapped electrons was used to explain the decay kinetics.

It is clear from Figure 4.3 that the absorption of trapped electrons decays initially rapidly followed by further slow decay. According to Moser and Grätzel¹⁷⁹ the fast initial decay is

indeed attributed to the electron hole pair recombination while the second slow decay can be attributed to the reaction with trapped holes or the reaction with impurities. The transient absorption spectra plotted at the initial height of the signal (at 25 ns) for the wavelength range from 400-600 nm is shown in Figure 4.4. The transient absorption exhibits a very broad peak in the visible with a maximum around 580 nm which is readily attributed to the absorption of the trapped electrons. The spectrum is in good agreement with earlier publications.^{74, 131}

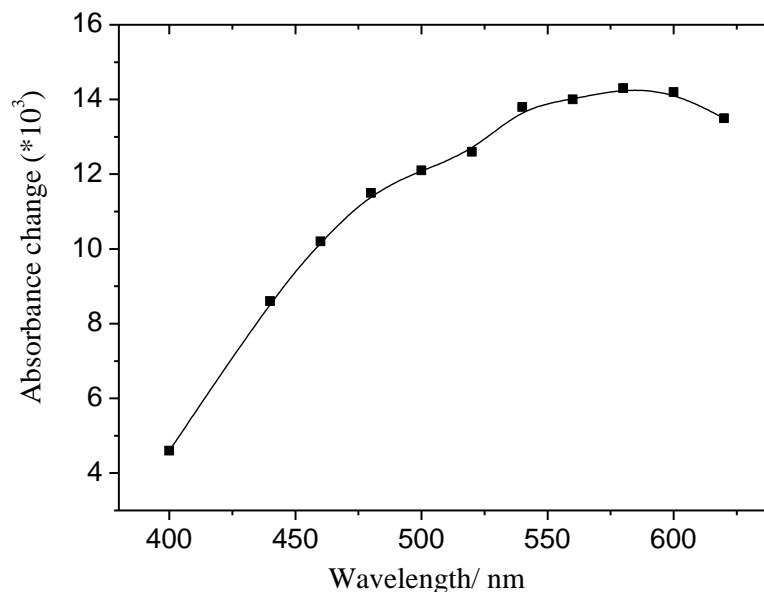


Figure 4.4: Transient absorption spectrum measured at the height of the absorbance signals (25 ns) under the experimental conditions in Figure 4.3.

4.1.2. Irradiation of TiO₂ Particles in the Absence of Hole Scavenger and the Presence of Electron Scavenger

To clarify the kinetics of the charge carrier upon band gap excitation of TiO₂ nanoparticles in the presence of electron scavenger we carried out the experiments where aqueous suspensions of TiO₂ (1.3×10^{-5} mol particles l⁻¹) in the presence of gold particles (5 nm, 4×10^{-8} mol particles l⁻¹) were excited with laser pulses (average of 600 pulses). Figure 4.5 (a) and (b) show the transient absorption vs. time signal observed after the laser excitation at 560 and 480 nm respectively. The transient decay observed in the nanosecond time scale after laser excitation shows that the absorbance signals remain almost unchanged (cf. Inset Figure 4.5 (a)) while a double exponential decay was observed in the microsecond time with rate constants $k_1^{obs} = 1.36 \times 10^{-6}$ s⁻¹ and $k_2^{obs} = 1.25 \times 10^{-4}$ s⁻¹. Similar decays were observed at the whole wavelength range.

The transient absorption spectra measured at different time after laser excitation are shown in Figure 4.6. The transient absorbance spectrum obtained from the measured absorbance at the height of the signal exhibits a broad absorption band with maximum at 560 nm, the band shifted to 480 nm at the end of the signal.

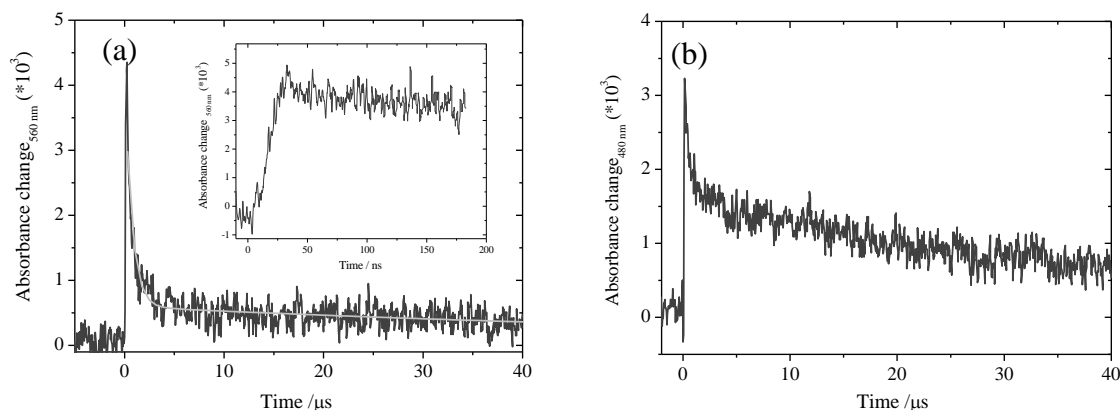
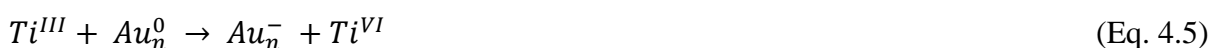


Figure 4.5: Transient absorption vs. time signals at 560 nm, the inset shows the same data in the ns time scale (a) and 480 nm (b) observed upon laser excitation ($\lambda = 355$ nm) of aqueous suspension of TiO_2 (1.3×10^{-5} mol particles l^{-1}) /colloidal gold (5×10^{-5} M) at pH 2.5, absorbed photon concentration 5×10^{-5} mol photons l^{-1} .

When colloidal gold is added to the TiO_2 suspension in the absence of any hole scavenger the gold particles act as electron traps via Eq. 4.5, while the holes will remain in the valance band to oxidize eventually the surface water producing the surface adsorbed hydroxyl radical (Eq. 4.6), the later leading to the increases in the absorption at 460 nm (cf. Figure 4.6).



Bahnemann et al.¹³¹ have published transient absorption spectrum with a maximum at 450 nm after the laser excitation of colloidal TiO_2 in presence of 1% of colloidal Pt particles. They attributed this absorption to the trapped valance band holes by the surface hydroxyl groups of TiO_2 . On the other hand this observation can be assigned to the surface bound peroxidase resulting from the trapping of hole to the TiO_2 surface OH^- group.^{79, 80}

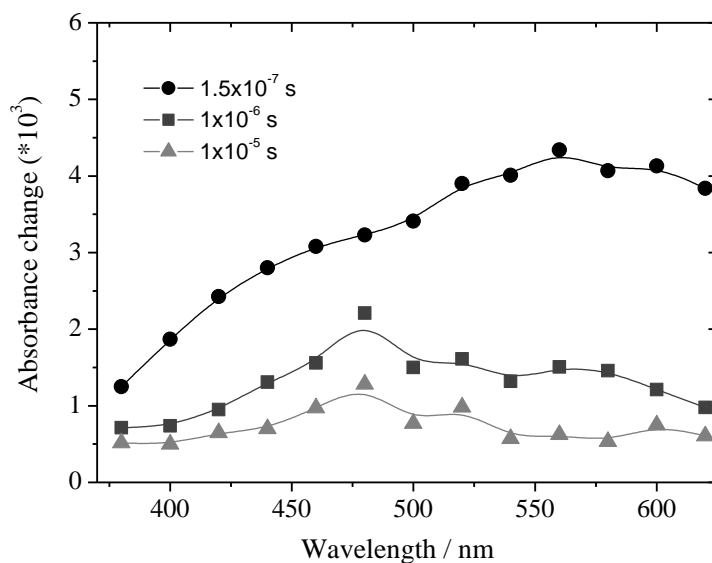
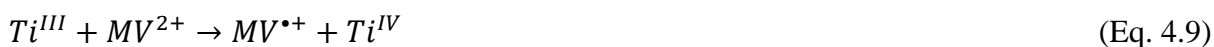
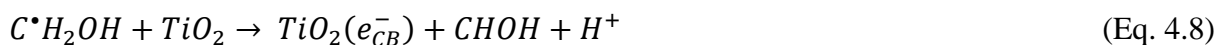


Figure 4.6: Transient absorption spectra measured various time after the laser excitation ($\lambda=355$ nm) of aqueous suspension of TiO_2 (1.3×10^{-5} mol particles l^{-1}) /colloidal gold (4×10^{-8} mol particles l^{-1}) at pH 2.5, absorbed photon concentration 5×10^{-5} mol photons l^{-1} .

4.2. Reactions of Photogenerated TiO_2 Electrons with Methyl Viologen Dication in the Presence of Hole Scavenger

In this study the experiments were carried out to study the kinetics of on electron transfer reduction of MV^{2+} at TiO_2 nanoparticles in the presence of methanol as hole scavenger. The one electron reduction of MV^{2+} has been investigated in chapter 3 using stored electrons on TiO_2 and employing stopped flow technique. Here the laser pulses are used to excite deaerated aqueous suspensions containing TiO_2 / MV^{2+} / methanol at pH 2.5. The laser pulses excitation results in the formation of the blue color which is characterized by the typical $\text{MV}^{•+}$ absorption with maxima at 602 nm and 395 nm (Section 3.1.3.2). Upon laser excitation the electron/hole pair will be generated (Eq. 4.1). While the electrons are trapped at Ti^{IV} sites as Ti^{III} (Eq. 4.3) the valence band holes migrate to the surface of the particles where they react with the adsorbed methanol molecules producing α -hydroxyl methyl radicals (Eq. 4.7). The latter can directly inject electrons to the conduction band of the TiO_2 nanoparticle (Eq. 4.8). The trapped electrons can react with MV^{2+} by one electron transfer producing $\text{MV}^{•+}$ (Eq. 4.9).





To clarify the one electron reduction kinetics of MV^{2+} , the formation rate constants of the MV^{*+} are investigated at various MV^{2+} concentrations. Figure 4.7 (a) shows the typical build-up of transient absorbance at 600 nm for MV^{*+} observed at concentration range of 1–10 mM MV^{2+} . Individual electron-transfer rate constants (k^{obs}) were extracted by the single-exponential fitting of the formation kinetics of MV^{*+} in the kinetic traces (Figure 4.7 (a)) to the expression for a pseudo first order reaction and second order rate constant ($k_2 = 1.64 \times 10^5 \text{ M}^{-1} \text{ s}^{-1}$) was then determined from the linear relationship between the MV^{2+} concentrations (1–10 mM) and the k^{obs} values (see Figure 4.7 (b)). This value is in good agreement with those obtained by Duonghong et al.^{79 (b)} ($1 \times 10^5 \text{ M}^{-1} \text{ s}^{-1}$ at pH 3) but is higher than the value obtained from the stopped flow experiment (Section 3.3.2). However, in both technique one electron transfer reaction is occurred, in the laser flash photolysis experiment the TiO_2 colloidal suspension are in equilibrium with adsorbed and bulk MV^{2+} while using the stopped flow technique it is assumed that the trapped electrons react with the free MV^{2+} molecule in the bulk.

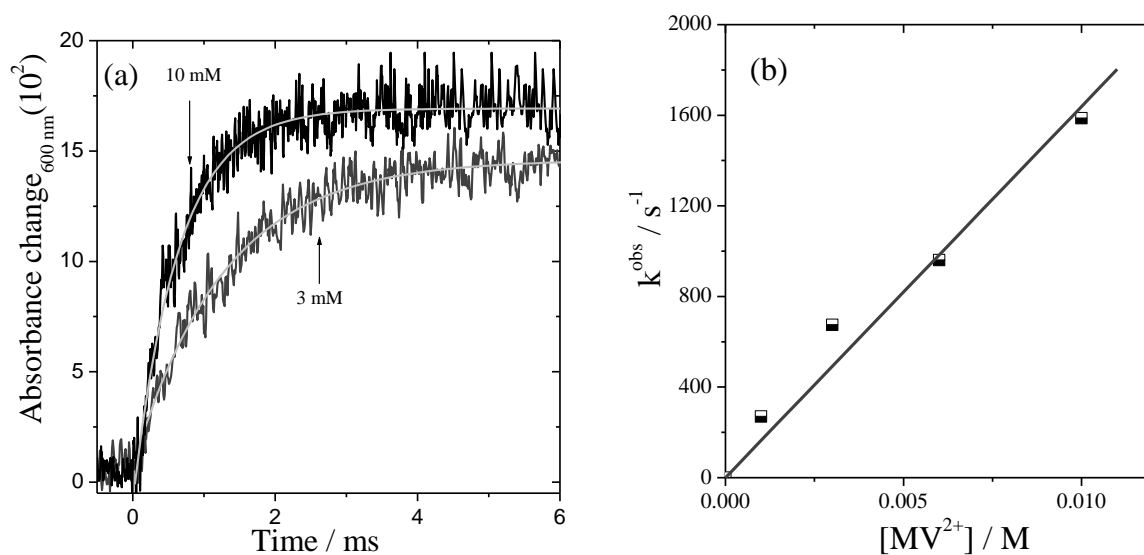


Figure 4.7: (a) Time profiles at 600 nm observed upon laser excitation (355 nm) of the system of TiO_2 ($1.3 \times 10^{-5} \text{ mol particles l}^{-1}$) / MV^{2+} at different concentrations of MV^{2+} , absorbed photon concentration is $2 \times 10^{-5} \text{ mol photons l}^{-1}$, pH 2.7, (b) Linear dependency of the observed first order rate constants obtained from the data analysis of the kinetic curves in (a) on the initial concentration of MV^{2+} .

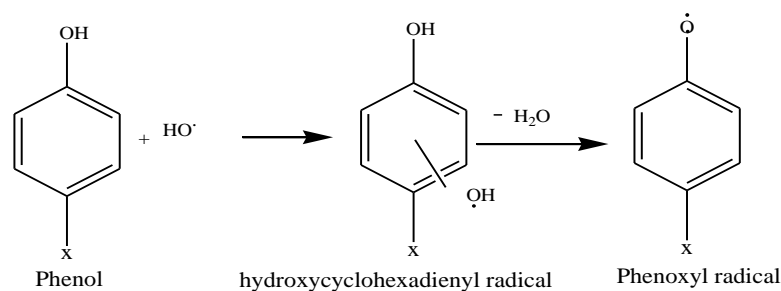
The amount of MV^{*+} produced after the completion of the growth process was independent on the initial MV^{2+} concentration present in the solution and approach a limit.

At high MV^{2+} concentration where $[e^-_{CB} / h^+] \ll [MV^{2+}]$ the reduction of MV^{2+} is incomplete and reaches a limit when $[e^-_{CB}] = [MV^{*+}]$. This allows us to derive the electron-hole pair concentration produced by the light flash, which according to Figure 4.7 is around 1.36×10^{-5} M.

4.3. Photo- Induced Simultaneous Conversion of Phenolic Compounds and Reduction of Heavy Metal Ions in Aqueous Suspension of TiO_2 Nanoparticles

Upon laser pulse excitation (355 nm wavelength) the photogenerated CB electrons consumed in reaction that reduces the metal ion, while VB hole was filled via oxidation reaction of phenol compound. The one electron oxidation of hydroquinone or resorcinol was chosen as a model for the reaction of the trapped holes while the reduction of Cu (II) was chosen as a model for the reaction of trapped electrons. The dynamics of the electron reaction resulting in the reduction of metal ions was investigated following the decay of the absorbance signals of the TiO_2 trapped electrons at 600 nm, while the dynamics of hole reaction resulting from the oxidation of phenolic compounds was investigated following the formation of transient intermediate during the oxidation process.

It has been investigated in pulse radiolysis study that the hydroxyl radical react with phenolic compounds preferentially by an addition reaction yielding hydroxycyclohexadienyl radicals (OH adduct) with rate constant $k_2 = 1.4 \times 10^{10} \text{ M}^{-1} \text{ s}^{-1}$ which has spectrum with distinct maximum around 330 nm.¹⁸² The acid-catalyzed water elimination reactions from these $\cdot OH$ adducts produce phenoxy radical (Eq. 4.10) which is characterized by a spectrum with an maximum around 400–440 nm.^{182, 183} Since it has been suggested that hydroxyl radical is formed due to the trapping of photogenerated holes on TiO_2 nanoparticles (Eq. 1.13 (c)), the oxidation of phenolic compounds is supposed to be due to their reaction with the surface trapped holes upon band excitation (Eq. 4.11).



(Eq. 4.10)



In the following experiments a system of $\text{TiO}_2/\text{Cu}^{2+}$ /hydroquinone were excited by laser pulses (355 nm) and the change in the absorbance vs. time was followed at the wavelength regime of interest (380-620 nm). Significant build-up was observed in the wavelength range of 380-480 nm. Figure 4.8 shows the build-up of the transient absorption vs. time signal at 410 nm observed after laser pulse excitation of deaerated aqueous TiO_2 suspension (1.3×10^{-5} mol particles l^{-1}) in presence of hydroquinone (5×10^{-4} M) and CuCl_2 (1×10^{-3} M). The kinetics of the build-up obeys pseudo first order rate law.

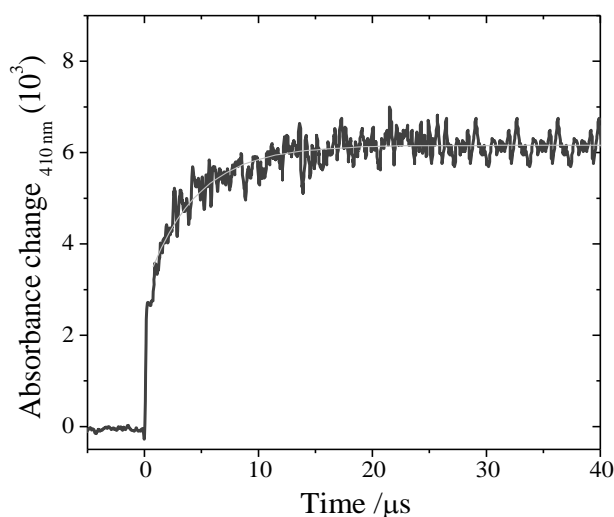


Figure 4.8: Transient absorption vs. time signals observed at 410 nm upon laser excitation of 1.3×10^{-5} mol particles l^{-1} TiO_2 , 1×10^{-3} M, 5×10^{-5} M HQ at pH 2.5, photon concentration is 5×10^{-5} mol photons l^{-1} . Solid line represents the first order fit.

On the other hand in the wavelength range 500-600 significant decays were observed. The transient absorption vs. time signal at 600 nm is shown in Figure 4.9. The rate constant ($1.7 \times 10^5 \text{ s}^{-1}$) is obtained from the first order fit of the signals decay at 600 nm. Since the redox potential of the two electron reduction of Cu^{2+} is more positive (0.34 vs. NHE) than the one electron redox potential (0.159 vs. NHE), the two electron reduction of Cu^{2+} rather than the one electron reduction might be responsible for that decay (Eq. 4.12).



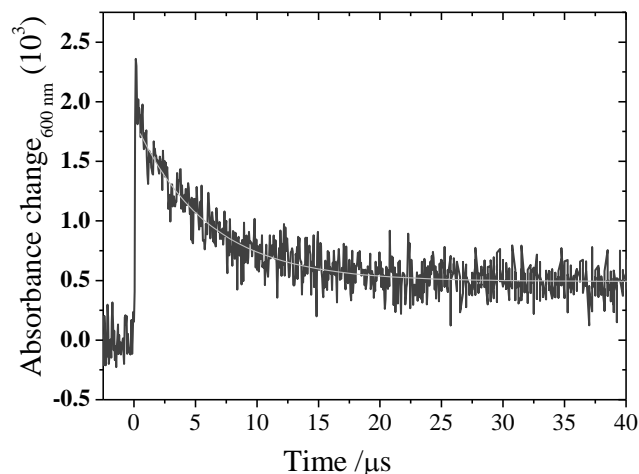


Figure 4.9: Transient absorption vs. time signals at 600 nm observed upon band gap irradiation (355 nm) of a deaerated aqueous colloidal suspension of 1.3×10^{-5} mol particle l^{-1} TiO_2 containing HQ (5×10^{-4} M) and $CuCl_2$ (1×10^{-3} M). Photon concentration 5×10^{-5} mol photon l^{-1} . Solid line represents the first order fit.

Using the kinetic traces at the whole wavelength regime (380-600 nm), the time resolved transient absorbance spectra were recorded after different times (1 μs -400 μs) of excitation (see Figure 4.10). The spectra show maxima at 410 and 440 nm. It was found that the spectra depicted in Figure 4.10 is the typical spectra of phenoxyl radical obtained after the reaction of HQ with hydroxyl radical generated from pulse radiolysis of water^{182, 183} or after the flash photolysis of HQ aqueous solution in presence of tris(oxaloferrate) complexes.¹⁸⁴

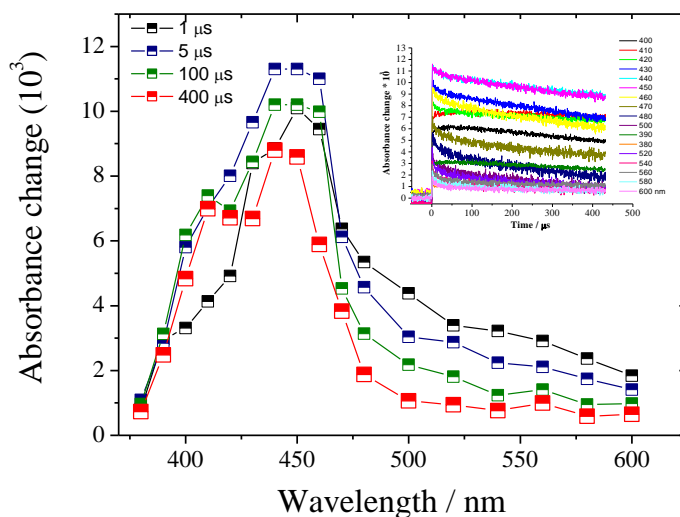


Figure 4.10: Time-resolved transient absorption spectra recorded after the laser excitation (355 nm) of an aqueous colloidal suspension of 1.3×10^{-5} mol particles l^{-1} TiO_2 containing 5×10^{-4} M hydroquinone and 1×10^{-3} M $CuCl_2$, photon concentration 5×10^{-5} mol photons l^{-1} . Inset shows the time profiles observed at the whole wavelength range.

As a blank experiment the system of $\text{TiO}_2/\text{Cu}^{2+}$ /methanol were excited by laser pulses (355 nm) and the change in the absorbance vs. time was followed at the wavelength regime of interest (400-620 nm). Figure 4.11 shows the time resolved transient absorbance spectra recorded at the initial height and at the end of the signals. Inset of Figure 4.11 shows the transient decay observed at 580 nm after laser excitation. Obviously, the initial broad spectrum with a maximum at 580 nm (which is indeed attributed to the trapped electrons) damped with time due to the reaction of trapped electrons with Cu^{2+} ions to give a featureless spectrum without any maximum in the range 380-600 nm at the time domain of interest. Hence, the final spectrum observed after the reduction of Cu^{2+} does not contribute to the spectrum of the phenoxyl radical.

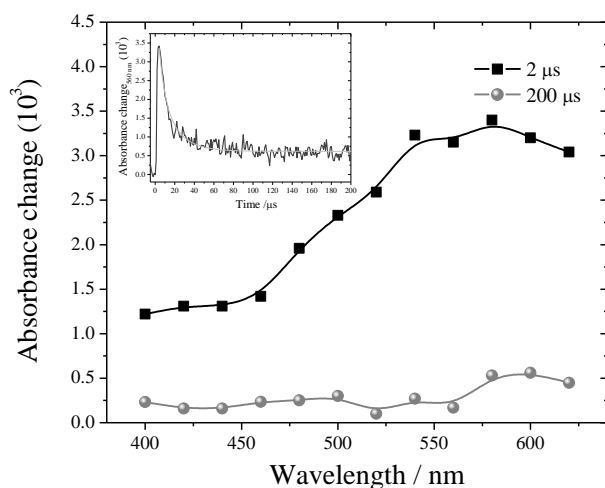
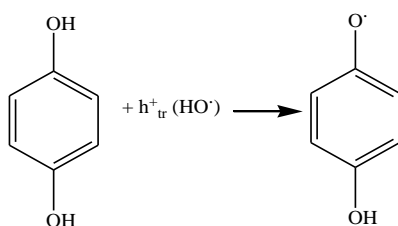


Figure 4.11: Time-resolved transient absorption spectra recorded after the laser excitation (355 nm) of an aqueous colloidal suspension of 1.3×10^{-5} mol particle l^{-1} TiO_2 containing 1×10^{-3} M methanol and 1×10^{-3} M CuCl_2 , photon concentration 5×10^{-5} mol photon l^{-1} . Inset shows the decay observed at 580 nm.

According to the results shown in Figure 4.8 and 4.10, it can be concluded that the TiO_2 surface trapped hole reacts with adsorbed hydroquinone molecule by one electron oxidation process giving the corresponding phenoxyl radical (Eq. 4.13):



(Eq. 4.13)

The rate constant of the one electron oxidation of HQ due to the reaction with the TiO₂ surface trapped hole was obtained from the data analysis at different HQ concentrations and at 1×10⁻³ M CuCl₂. It was found that the rate constants of the significant build-up at 410 nm were increasing linearly with increasing the HQ concentration (Figure 4. 11 (a)) and a second order rate constant of the hole transfer (k_{ht}) is obtained from this linearship (Figure 4.11 (b)) to be $k_{ht} = 4.9 \times 10^8 \text{ M}^{-1} \text{ s}^{-1}$. In absence of HQ an exponential decay was observed which is indeed due to the electron hole pair recombination. The rate constant obtained here for the heterogeneous one electron oxidation of hydroquinone at TiO₂ surfaces is considerably smaller than the rate constants obtained in homogeneous solution.

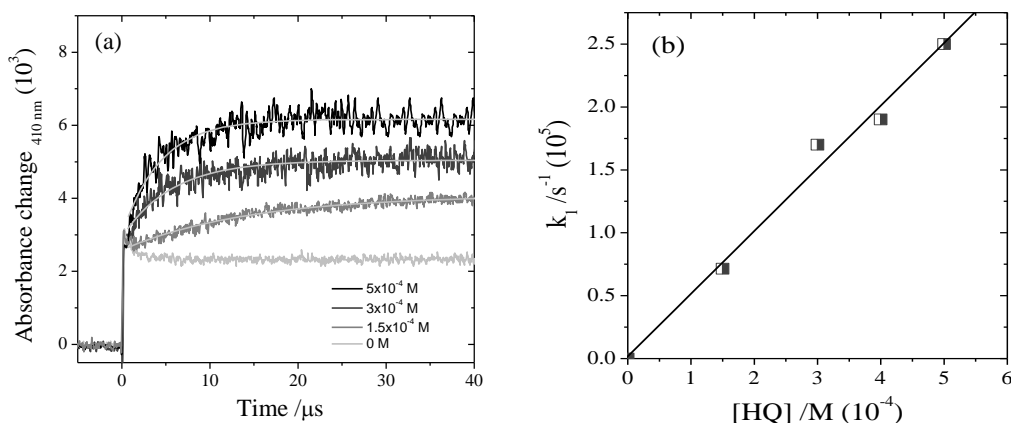


Figure 4.12: (a) Transient absorption vs. time signals at 410 nm observed upon laser excitation of 1.3×10⁻⁵ mol particle l⁻¹ TiO₂, 1×10⁻³ M CuCl₂, at different concentrations of HQ, pH 2.5, photon concentration 5×10⁻⁵ mol photon l⁻¹. (b) Linear dependency of the observed rate constants determined from first order fitting of the build-up at 410 nm as a function of HQ concentrations.

The kinetics of the trapped electron transfer can be calculated from the data analysis at different Cu²⁺ concentrations where [HQ]= 5×10⁻⁴ M. The decay kinetics obey pseudo first order rate law and a second order rate constant $k_2 = 1.6 \times 10^8 \text{ M}^{-1} \text{ s}^{-1}$ is obtained from the linear dependency of the observed first order rate constants and Cu²⁺ concentrations (Figure 4.13). This value is in good agreement with the second order rate constant of Cu²⁺ reduction in presence of methanol instead of HQ (1.8×10⁸ M⁻¹ s⁻¹, obtained from the analysis of the data in Figure 4.11 at 1×10⁻³ M CuCl₂).

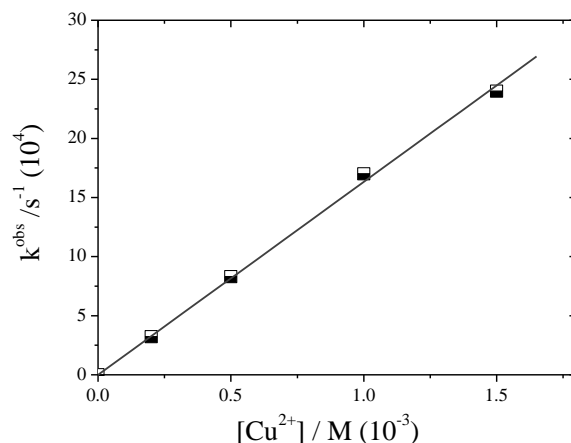
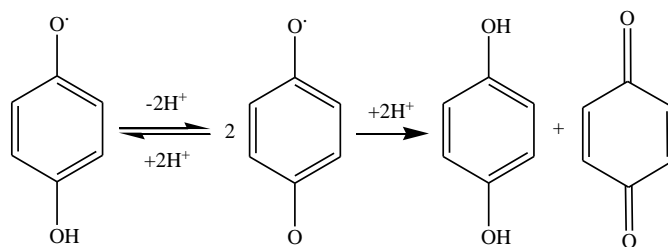


Figure 4.13: Linear dependency of the observed rate constants determined from first order fitting of the decay at 600 nm as a function of Cu^{2+} concentrations.

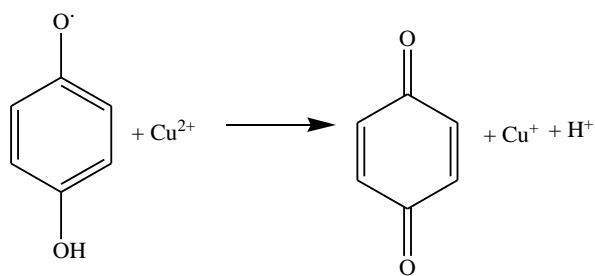
In order to elucidate the overall mechanism it was important to follow the fate of the transient radical by following its kinetic in longer time domain. Figure 4.14 shows the longer time scale of the transient absorption vs. time signals observed at 410 nm. It was found that the transient radical decay with a first order rate law which depends on the initial concentration of HQ. It was reported that the phenoxyl radical disproportionate giving benzoquinone by acid catalyzed second order rate law (Eq. 4.14).¹⁸²



(Eq. 4.14)

Here the decay kinetics of the transient radical does not obey the second order rate law but rather a first order law was obeyed with rate constant $k = 638 \text{ s}^{-1}$ (cf. Figure 4.14).

It is a well known that copper ions are highly reactive toward phenoxyl radicals.¹⁸⁵ From the data of the present work it follows that the decay of the phenoxyl radical can be due to its reaction with Cu^{2+} ions according to Eq. 4.15. Hence, the decay of the hydroquinone radical formed here can be assigned to Eq. 4.15. A second order rate constant can be calculated knowing the concentration of copper ions ($[\text{Cu}^{2+}] = 1 \times 10^{-3} \text{ M}$) to be $k_2 = 6.38 \times 10^5 \text{ M}^{-1} \text{ s}^{-1}$. This rate constant was found to be in a good agreement with the literature values.¹⁸⁵



(Eq. 4.15)

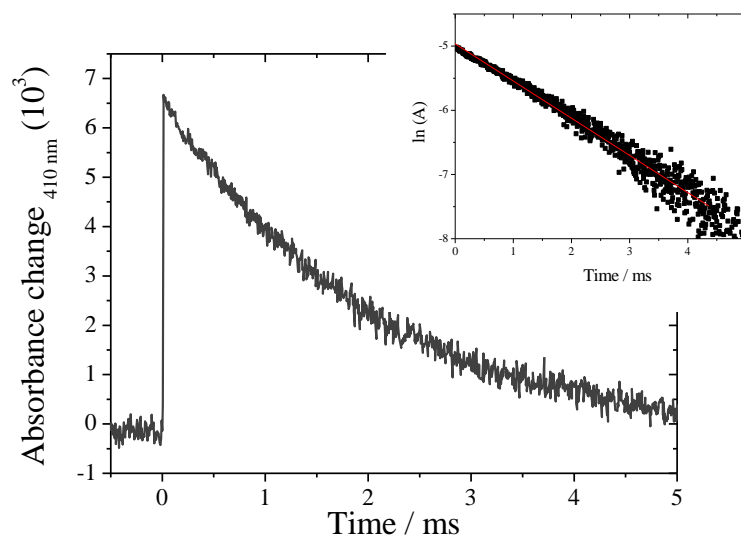


Figure 4.14: Transient absorption vs. time signals at 410 nm shows the longer time scale decay of the transient radical formed upon band gap excitation of a deaerated aqueous colloidal suspension of 1.3×10^{-5} mol particles l^{-1} TiO_2 containing 5×10^{-4} M HQ and 1×10^{-3} M CuCl_2 . Photon concentration 3×10^{-5} mol photons l^{-1} , inset shows the plot of $\ln(\text{Absorbance})$ vs. Time.

5. Conclusions

This thesis presents a comprehensive and detailed study of the kinetics and mechanism of various charge carrier transfer reactions at TiO₂ nanoparticles performing stopped flow and laser flash photolysis techniques.

The stopped flow method was successfully used to study the kinetics of a variety of electron transfer reactions. This study focuses on the analysis of the dynamics of one- and multi-electron transfer reactions in photocatalytic systems and utilizing the stored electrons in TiO₂ nanoparticles for the reactions with various electron acceptors. The TiO₂ conduction band electrons have been photo-generated on nano-sized TiO₂ particles upon UV (A) illumination in the presence of a hole scavenger (methanol) and stored on them in the absence of molecular oxygen to be used in the reduction of various electron acceptors.

The reduction of viologen compounds was studied as models for the one electron transfer reaction and the rate constant obtained here was compared with the rate constant obtained using laser flash photolysis technique. The factors influencing the formation kinetics of V^{•+} such as the initial concentration of V²⁺ compounds and the ionic strength have been studied. It was shown that the rate constants of the one electron reduction of MV²⁺ increase linearly with the concentration of MV²⁺. In addition, the rate constants increase as the ionic strength increasing owing to the decreasing in the electrostatic repulsion between the positively charged TiO₂ surface and MV²⁺ ions. Furthermore, a consequence decay of the reduced viologen radicals is observed when metal clusters exist. This confirms an electron transfer process from viologen radical in the solution to the adsorbed hydrogen ions on the surfaces of the metal clusters. The decay of viologen radical obeys pseudo first order rate law depending linearly on the metal clusters concentrations.

The multi-electron reductions of common electron acceptors that are often present in the photocatalytic systems such as O₂, H₂O₂ and NO₃⁻ were investigated. The main results obtained from this study can be summarized as follows: (1) the stored TiO₂ electrons reduce O₂ and H₂O₂ to water by multi-electron transfer process; (2) the stored TiO₂ electrons are able to reduce nitrate ions to ammonia through the transfer of 8 electrons with the intermediate formation of molecular nitrogen.

The kinetics of transition metal ions reduction, such as Mn²⁺, Zn²⁺, Cd²⁺, Cu²⁺, Hg²⁺, Ag⁺ and Au³⁺ has been studied after mixing with the stored TiO₂ electrons. It was found that while neither the reduction of Zn²⁺ nor that of Mn²⁺ is occurred using stored TiO₂ electrons, the

other metal ions are reduced into their metallic forms which were characterized by their surface plasmon absorbance bands. The kinetic results show the expected trend concerning the relationship between the interfacial electron transfer rate constant and the driving force of metal ions reduction. The kinetics of the metal particles growth was also studied. While Cu^0 and Cd^0 particles grow through a coalescence of the reduced metal atoms, Hg^0 particles grow through an autocatalytic mechanism including the association of the metal ions and the electrons. It was also shown that the metal deposits are very sensitive towards oxygen, a partial-or a complete-oxidation of the particles occurred upon exposure to air.

Furthermore, the mechanisms of the formation and growth of noble metal nanoparticles (Ag^0 and Au^0) on the surface of TiO_2 and the ensuing electron transfer to the surface of the deposited metal nanoparticles via the transfer of the stored electrons on TiO_2 were investigated. It was shown that:

- 1- The formation process of metal nanoparticles on the surface of TiO_2 is a multistep process comprising three main steps: (i) reduction of metal ions forming metal atoms which are getting together to form metal nuclei, (ii) autocatalytic surface growth, which is composed of hundreds of elementary steps of the association of metal nuclei with metal ions analogous to those hypothesized to be involved in latent image formation in silver halide photography, and (iii) coalescence of the formed metal particles to form even bigger particles.
- 2- The subsequent transfer of excess TiO_2 electrons to the surface of the deposited metal nanoparticles results in a slight blue-shift in the surface plasmon absorbance band in case of silver metal particles. This shift is due to the Fermi level equilibration of $\text{Ag}_n^0/\text{TiO}_2$ composite. In case of the gold metal nanoparticles, the shifting in the Fermi level of metallic gold nanoparticles is indicated by the damping in the surface plasmon resonance band.
- 3- The accumulated electrons on the surface of the deposited metal nanoparticles are reacted with the adsorbed H^+ ions producing H_2 gas.
- 4- PVA plays a vital role in the stabilization of the formed metal particles. The presence of PVA chains during the reduction of metal ions retards their reduction and limits the growth of metal nuclei which consequently decreases the particle size. They are stabilizing the metal nanoparticles and protecting them from coagulation.
- 5- While the deposited silver nanoparticles were sensitive toward oxygen; partial oxidation of the particles is occurred by reacting with dissolved oxygen giving back the silver ions, the deposited gold nanoparticles were stable towards oxygen.

Moreover, the kinetics of hydrogen production upon the reaction of the TiO₂ electrons with adsorbed H⁺/H₂O on the surface of the noble metal nanoparticles (Au⁰, Pt⁰) was studied under various conditions of different H⁺ (6.3×10⁻⁴-6×10⁻³ M) and different metal concentrations (1×10⁻⁴-5×10⁻⁴ M). The decay of the TiO₂ electrons obeys a pseudo first order rate law with linear dependencies on the H⁺ and the metal concentrations. The results show that hydrogen produced mostly by the reduction of H⁺ and to a lesser extent by H₂O reduction. The rate of the H⁺/H₂O reduction reaction is higher on Pt⁰ surfaces than on Au⁰ surfaces. The smaller particle size (i. e., higher surface area) of Pt⁰ particles (2.5 nm) compared to the particle size of Au⁰ (15-20 nm) might explain this higher rate.

In the second part of this thesis the laser flash photolysis technique was used to study the charge carrier transfer processes which are not possible to investigate using the stopped flow technique. The primary processes under band gap irradiation of colloidal TiO₂ suspension under various conditions were investigated and the results were found to be in good agreement with the literature. The one electron reduction of MV²⁺ was performed and the rate constant was compared to the one obtained from the stopped flow measurements. The rate constant ($k_2 = 1.64 \times 10^5 \text{ M}^{-1} \text{ s}^{-1}$) of the one electron reduction of MV²⁺ using laser flash photolysis technique is higher than the value obtained from the stopped flow experiments ($k_2 = 1.03 \times 10^4 \text{ M}^{-1} \text{ s}^{-1}$). However, in both technique one electron transfer reaction is occurred, in the laser flash photolysis experiment the TiO₂ colloidal suspension are in equilibrium with adsorbed and bulk MV²⁺ while there is no adsorbed MV²⁺ on TiO₂ surfaces employing stopped flow technique.

Furthermore, the simultaneous oxidation of phenolic compounds by TiO₂ trapped holes and reduction of metal ions by trapped TiO₂ electrons was investigated using hydroquinone (HQ) as a model of phenolic compounds and Cu²⁺ as a model of metal ions. It was shown that while the adsorbed HQ reacts quickly with surface trapped holes (OH[•]) producing the phenoxyl radical which is characterized by maxima at 410 and 440 nm, the trapped electrons react slowly with the adsorbed Cu²⁺ ion. The second order rate constant of the trapped electron transfer as well as the trapped hole transfer were determined. It was shown also that the phenoxyl radical decayed with a pseudo first order rate law which is supposed to be due to its oxidation through the reaction with the Cu²⁺ ions in the solution.

6. References

1. A. Henglein, M. Gutierrez, K. Weller, A. Foeti, J. Jirkovský, “Photochemistry of Colloidal Semiconductors. 30. Reactions and Fluorescence of AgI and AgI-Ag₂S Colloids”, *Ber. Bunsenges. Phys. Chem. Chem. Phys.*, **1989**, 93, 593–600.
2. H. Weller, “Quantized Semiconductor Particles: A Novel State of Matter for Materials Science”, *Adv. Mater.*, **1993**, 5, 88–95.
3. M. C. Schlamp, X. G. Peng, and A. P. Alivisatos, “Improved Efficiencies in Light Emitting Diodes Made with CdSe(CdS) Core/Shell Type Nanocrystals and a Semiconducting Polymer”, *J. Appl. Phys.*, **1997**, 82, 5837–5842.
4. S. Coe, W-K Woo, M. Bawendi and V. Bulovi, “Electroluminescence from Single Monolayers of Nanocrystals in Molecular Organic Devices”, *Nature*, **2002**, 420, 800–803.
5. N. C. Greenham, X. G. Peng, and A. P. Alivisatos, “Charge Separation and Transport in Conjugated-Polymer/Semiconductor-Nanocrystal Composites Studied by Photoluminescence Quenching and Photoconductivity”, *Phys. Rev. B*, **1996**, 54, 17628–17637.
6. W. U. Huynh, J. J. Dittmer, W. C. Libby, G. L. Whiting and A. P. Alivisatos, “Controlling the Morphology of Nanocrystal Polymer Composites for Solar Cells”, *Adv. Funct. Mater.*, **2003**, 13, 73–79.
7. V. I. Klimov, “Optical Nonlinearities and Ultrafast Carrier Dynamics in Semiconductor Nanocrystals”, *J. Phys. Chem. B*, **2000**, 104, 6112–6123.
8. N. Suzuki and Y. T. Kojima, “Holographic Recording in TiO₂ Nanoparticle Dispersed Methacrylate Photopolymer Film”, *App. Phys. Lett.*, **2002**, 81, 4121–4123.
9. R. J. Walters, P. G. Kik, J. D. Caspersen and H. A. Atwater, “Silicon Optical Nanocrystal Memory”, *App. Phys. Lett.*, **2004**, 85, 2622–2624.
10. M. Bruchez, M. Moronne, P. Gin, S. Weiss, A. P. Alivisatos, “Semiconductor Nanocrystals as Fluorescent Biological Labels”, *Science*, **1998**, 281, 2013–2016.
11. R. M. Dickson, D. J. Norris, Yih-Ling Tzeng and W. E. Moerner, “Three-Dimensional Imaging of Single Molecules Solvated in Pores of Poly(acrylamide) Gels”, *Science*, **1996**, 274, 966–969.
12. A. P. Alivisatos, “Semiconductor Clusters, Nanocrystals, and Quantum Dots”, *Science*, **1996**, 271, 933–937.

13. C. M. Niemeyer, "Nanoparticles, Proteins, and Nucleic Acids: Biotechnology Meets Materials Science", *Angew. Chem. Int. Ed.*, **2001**, 40, 4128–4158.
14. C. M. Niemeyer, B. Ceyhan, and P. Hazarika, "Oligofunctional DNA-Gold Nanoparticle Conjugates", *Angew. Chem. Int. Ed.*, **2003**, 42, 5766–5770.
15. M. C. Daniel and D. Astruc, "Gold Nanoparticles: Assembly, Supramolecular Chemistry, Quantum-Size-Related Properties and Applications toward Biology, Catalysis and Nanotechnology", *Chem. Rev.*, **2004**, 104, 293–346.
16. Y. Yin, Zhi-Yuan Li, Z. Zhong, B. Gates, Y. Xia and S. Venkateswaranc, "Synthesis and Characterization of Stable Aqueous Dispersions of Silver Nanoparticles through the Tollens Process", *J. Mater. Chem.*, **2002**, 12, 522–527.
17. Ki-Sub Kim, N. D. j. Dembereinyamba, Sun-Wha Yeon, S. Choi, Jong-Ho Cha and H. Lee , "One-Phase Preparation of Palladium Nanoparticles Using Thiolfunctionalized Ionic Liquid", *Korean J. Chem. Eng.*, **2005**, 22, 717–720.
18. C. Kormann, D. W. Bahnemann and M. R. Hoffmann, "Preparation and Characterization of Quantum-Size Titanium Dioxide", *J. Phys. Chem.*, **1988**, 92, 5196–5201.
19. D. W. Bahnemann, C. Kormann, and M. R. Hoffmann, "Preparation and Characterization of Quantum Size Zinc-Oxide: a Detailed Spectroscopic Study", *J. Phys. Chem.*, **1987**, 91, 3789–3798.
20. Z. A. Peng and X. G. Peng, "Mechanisms of the Shape Evolution of CdSe Nanocrystals", *J. Am. Chem.Soc.*, **2001**, 123, 1389–1395.
21. W. Z. Wang, I. Germanenko and M. S. El-Shall, "Room-Temperature Synthesis and Characterization of Nanocrystalline CdS, ZnS, and $CdxZn_{1-x}S$ ", *Chem. Mater.*, **2002**, 14, 3028–3033.
22. A. L. Rogach , L. Katsikas, A. Kornowski, D. Su, A. Eychmüller and H. Weller, "Synthesis and Characterization of Thiol-Stabilized CdTe Nanocrystals", *Ber. Bunsenges. Phys. Chem. Chem. Phys.*, **1996**, 100, 1772–1778.
23. C. B. Murray, C. R. Kagan, and M. G. Bawendi, "Synthesis and Characterization of Monodisperse Nanocrystals and Close-Packed Nanocrystal Assemblies", *Annu. Rev. Mater. Sci.*, **2000**, 30, 545–610.
24. R. L. Wells and W. L. Gladfelter, "Pathways to Nanocrystalline III-V (13–15) Compound Semiconductors", *J. Cluster Science*, **1997**, 8, 217–238.
25. O. I. Micic, and A. J. Nozik, "Synthesis and Characterization of Binary and Ternary III-V Quantum Dots", *J. Luminescence*, **1996**, 70, 95–107.

26. H. Uchida, C. J. Curtis and A. J. Nozik, "Gaas Nanocrystals Prepared in Quinoline", *J. Phys. Chem.*, **1991**, 95, 5382–5384.
27. M. A. Malik, P. O'Brien, S. Norager and J. Smith, "Gallium Arsenide Nanoparticles: Synthesis and Characterisation", *J. Mater. Chem.*, **2003**, 13, 2591–2595.
28. O. I. Micic, C. J. Curtis, K. M. Jones, J. R. Sprague and A. J. Nozik, "Synthesis and Characterization of Inp Quantum Dots", *J. Phys. Chem.*, **1994**, 98, 4966–4969.
29. T. Schneider, M. Haase, A. Kornowski, S. Naused, H. Weller, S. Förster and M. Antonietti, "Synthesis and Characterization of PbS Nanoparticles in Block Copolymer Micelles", *Ber. Bunsenges. Phys. Chem. Chem. Phys.*, **1997**, 101, 1654–1656.
30. L. E. Brus, "A Simple-Model for the Ionization-Potential, Electron-Affinity, and Aqueous Redox Potentials of Small Semiconductor Crystallites", *J. Chem. Phys.*, **1983**, 79, 5566–5571.
31. L. E. Brus, "Electron–Electron and Electron–Hole Interactions in Small Semiconductor Crystallites: the Size Dependence of the Lowest Excited Electronic State", *J. Chem. Phys.*, **1984**, 80, 4403–4409.
32. E. M. Wong and P.C. Searson, "ZnO Quantum Particle Thin Films Fabricated by Electrophoretic Deposition", *App. Phys. Lett.*, **1999**, 74, 2939–2941.
33. M. Grätzel, "Photoelectrochemical Cells", *Nature*, **2001**, 414, 338–344.
34. M. Faraday, "The Bakerian Lecture: Experimental Relations of Gold (and Other Metals) to Light", *Philos. Trans. Soc., London*, **1857**, 197, 145–181.
35. P. Jena, B. K. Rao, S. N. Khanna, Eds., "Physics and Chemistry of Small Clusters" *Plenum Press*, New York, **1986**.
36. G. Schmid, "Large Clusters and Colloids. Metals in the Embryonic State", *Chem. Rev.*, **1992**, 92, 1709–1727.
37. C. N. R. Rao, G. U. Kulkarni, P. J. Thomas and P. P. Edwards, "Metal Nanoparticles and their Assemblies", *Chem. Soc. Rev.*, **2000**, 29, 27–35.
38. A. C. Templeton, W. P. Wuelfing and R. W. Murray, "Monolayer-Protected Cluster Molecules", *Acc. Chem. Res.*, **2000**, 33, 27–36.
39. G. Markovich, P. Collier, S. E. Henrichs, F. Remacle, R. D. Levine, J. R. Heath, "Architectonic Quantum Dot Solids", *Acc. Chem. Res.*, **1999**, 32, 415–423.
40. L. N. Lewis, "Chemical Catalysis by Colloids and Clusters", *Chem. Rev.*, **1993**, 93, 2693–2730.

41. G. Schön and U. Simon, "A Fascinating New Field in Colloid Science: Small Ligand-Stabilized Metal Clusters and Possible Application in Microelectronics", *Colloid. Polym. Sci.*, **1995**, 273, 101–117.
42. (a) G. Schmid, M. Bäuml, M. Geerkens, I. Heim, C. Osemann and T. Sawitowski, "Current and Future Applications of Nanoclusters", *Chem. Soc. Rev.*, **1999**, 28, 179–185, (b) S. Eustis and M. A. El-Sayed, "Why Gold Nanoparticles are More Precious than Pretty Gold: Noble Metal Surface Plasmon Resonance and its Enhancement of the Radiative and Nonradiative Properties of Nanocrystals of Different Shapes", *Chem. Soc. Rev.*, **2006**, 35, 209–217.
43. G. Schmid and R. Ugo, "Aspects of Homogeneous Catalysis", *Kluwer Academic Press*, **1991**, 7, 1–36.
44. A. J. Bard and M. A. Fox, "Artificial Photosynthesis: Solar Splitting of Water to Hydrogen and Oxygen", *Acc. Chem. Res.*, **1995**, 28, 141–145.
45. L. A. Harris and R. H. Wilson, "Semiconductor for Photocatalysis", *Annu. Rev. Mater. Sci.*, **1978**, 8, 99–134.
46. A. L. Linsebigler, G. Q. Lu and J. T. Yates, "Photocatalysis on TiO₂ Surfaces: Principles, Mechanisms, and Selected Results", *Chem. Rev.*, **1995**, 95, 735–758.
47. A. J. Nozik, "Photoelectrochemistry: Applications to Solar Energy Conversion", *Annu. Rev. Phys. Chem.*, **1978**, 29, 189–222.
48. M. Tomkiewicz and H. Fay, "Photoelectrolysis of Water with Semiconductors", *Appl. Phys.*, **1979**, 18, 1–28.
49. T. A. Kandiel, R. Dillert and D. W. Bahnemann, "Enhanced Photocatalytic Production of Molecular Hydrogen on TiO₂ Modified with Pt–Polypyrrole Nanocomposites". *Photochem. Photobiol. Sci.*, **2009**, 8, 683–690.
50. N. Chandrasekharan and P. V. Kamat, "Improving the Photoelectrochemical Performance of Nanostructured TiO₂ Films by Adsorption of Gold Nanoparticles", *J. Phys. Chem. B.*, **2000**, 104, 10851–10857.
51. Y. Nakato, K. Ueda, H. Yano and H. Tsubomura, "Effect of Microscopic Discontinuity of Metal Overlayers on the Photovoltages in Metal-Coated Semiconductor-Liquid Junction Photoelectrochemical Cells for Efficient Solar Energy Conversion", *J. Phys. Chem.*, **1988**, 92, 2316–2324.
52. Y. Nakato, M. Shioji and H. Tsubomura, "Photoeffects on the Potentials of Thin Metal Films on an n-TiO₂ Crystal Wafer: The Mechanism of Semiconductor Photocatalysts", *Chem. Phys. Lett.*, **1982**, 90, 453–456.

53. R. Hiesgen and D. Meissner, "Cooperative Nature of Complex Formation in Mixed Polyelectrolyte–Surfactant Systems", *J. Phys. Chem. B.*, **1998**, 102, 6549–6557.
54. J. S. Curran and D. Lamouche, "Transport and Kinetics in Photoelectrolysis by Semiconductor Particles in Suspension", *J. Phys. Chem.*, **1983**, 87, 5405–5411.
55. H. A. Gerischer, "Mechanism of Electron Hole Pair Separation in Illuminated Semiconductor Particles", *J. Phys. Chem.*, **1984**, 88, 6096–6097.
56. M. Hilgendorf, L. Spanhel, C. Rothenhausler and G. Muller, "From ZnO Colloids to Nanocrystalline Highly Conductive Films", *J. Electrochem. Soc.*, **1998**, 145, 3632–3637.
57. A. J. Bard, "Design of Semiconductor Photoelectrochemical Systems for Solar Energy Conversion", *J. Phys. Chem.*, **1982**, 86, 172–177.
58. R. Baba, S. Nakabayashi, A. Fujishima and K. Honda, "Investigation of the Mechanism of Hydrogen Evolution during Photocatalytic Water Decomposition on Metal-Loaded Semiconductor Powders", *J. Phys. Chem.*, **1985**, 89, 1902–1905.
59. A. Heller, "Optically Transparent Metallic Catalysts on Semiconductors", *Pure Appl. Chem.*, **1986**, 58, 1189–1192.
60. A. A. Ismail, D. W. Bahnemann, L. Robben, V. Y. and M. Wark, "Palladium Doped Porous Titania Photocatalysts: Impact of Mesoporous Order and Crystallinity", *Chem. Mater.*, **2010**, 22, 108–116.
61. A. A. Ismail, D. W. Bahnemann, I. Bannat and M. Wark, "Gold Nanoparticles on Mesoporous Interparticle Networks of Titanium Dioxide Nanocrystals for Enhanced Photonic Efficiencies", *J. Phys. Chem. C*, **2009**, 113, 7429–7435.
62. M. Anpo, K. Chiba, M. Tomonari, S. Coluccia, M. Che and M. A. Fox, "Photocatalysis on Native and Platinum-Loaded TiO₂ and ZnO Catalysts—Origin of Different Reactivities on Wet and Dry Metal Oxides", *Bull. Chem. Soc. Jpn.*, **1991**, 64, 543–551.
63. K. D. Schierbaum, U. K. Kirner, J. F. Geiger and W. Gopel, "Schottky-Barrier and Conductivity Gas Sensors Based upon Pd/SnO₂ and Pt/TiO₂", *Sens. Actuators B*, **1991**, 4, 87–94.
64. M. Gao, W. Lee, R. Trehan, R. Kershaw, K. Dwight and A. Wold, "Improvement of Photocatalytic Activity of Titanium (IV) Oxide by Dispersion of Au on TiO₂", *Mater. Res. Bull.*, **1991**, 26, 1247–1254.
65. V. Subramanian, E. E. Wolf and P. V. Kamat, "Catalysis with TiO₂/Gold Nanocomposites. Effect of Metal Particle Size on the Fermi Level Equilibration", *J. Am. Chem. Soc.*, **2004**, 126, 4943–4950.

66. M. Jacob, H. Levanon and P. V. Kamat, "Charge Distribution between UV-Irradiated TiO₂ and Gold Nanoparticles: Determination of Shift in the Fermi Level", *Nano Lett.*, **2003**, 3, 353–358.
67. T. Hirakawa and P. V. Kamat, "Photoinduced Electron Storage and Surface Plasmon Modulation in Ag@TiO₂ Clusters", *Langmuir*, **2004**, 20, 5645–5647, (b) T. Hirakawa and P. V. Kamat, "Charge Separation and Catalytic Activity of Ag@TiO₂ Core–Shell Composite Clusters under UV–Irradiation", *J. Am. Chem. Soc.*, **2005**, 127, 3928–3934.
68. A. Wood, M. Giersig and P. Mulvaney, "Fermi Level Equilibration in Quantum Dot–Metal Nanojunctions", *J. Phys. Chem. B*, **2001**, 105, 8810–8815.
69. V. Subramanian, E. E. Wolf and P. V. Kamat, "Green Emission to Probe Photoinduced Charging Events in ZnO–Au Nanoparticles: Charge Distribution and Fermi-Level Equilibration", *J. Phys. Chem. B*, **2003**, 107, 7479–7485.
70. P. V. Kamat, "Photophysical, Photochemical and Photocatalytic Aspects of Metal Nanoparticles", *J. Phys. Chem. B*, **2002**, 106, 7729–7747, (b) P. V. Kamat, "Photoinduced Transformations in Semiconductor–Metal Nanocomposite Assemblies", *Pure Appl. Chem.*, **2002**, 74, 1693–1706.
71. P. D. Cozzoli, E. Fanizza, R. Comparelli, M. L. Curri, D. Laub and A. Agostiano, "Role of Metal Nanoparticles in TiO₂/Ag Nanocomposite-Based Microheterogeneous Photocatalysis", *J. Phys. Chem. B*, **2004**, 108, 9623–9630.
72. A. Fujishima and K. Honda, "Electrochemical Photolysis of Water at a Semiconductor Electrode", *Nature*, **1972**, 238, 37–38.
73. R. Memming, "Semiconductor Electrochemistry", *Wiley-VCH*, Weinheim, **2001**.
74. D. W. Bahnemann, A. Henglein, J. Lili and L. Spanhel, "Flash Photolysis Observation of the Absorption Spectra of Trapped Positive Holes and Electrons in Colloidal Titanium Dioxide", *J. Phys. Chem.*, **1984**, 88, 709–711.
75. B. O'Regan, M. Grätzel, D. Fitzmaurice, "Optical Electrochemistry I: Steady-State Spectroscopy of Conduction-Band Electrons in a Metal Oxide Semiconductor Electrode", *Chem. Phys. Lett.*, **1991**, 183, 89–93.
76. G. Boschloo and D. Fitzmaurice, "Spectroelectrochemical Investigation of Surface States in Nanostructured TiO₂ Electrodes", *J. Phys. Chem. B*, **1999**, 103, 2228–2231.
77. A. Safrany, R. Gao, J. Rabani, "Optical Properties and Reactions of Radiation Induced TiO₂ Electrons in Aqueous Colloid Solutions", *J. Phys. Chem.*, **2000**, 104, 5848–5853.
78. M. R. Hoffmann, S. T. Martin, W. Choi and D. W. Bahnemann, "Environmental Applications of Semiconductor Photocatalysis", *Chem. Rev.*, **1995**, 95, 69–96.

79. (a) D. Duonghong, J. Ramsden, and M. Grätzel, "Dynamics of Interfacial Electron-Transfer Processes in Colloidal Semiconductor Systems", *J. Am. Chem. Soc.*, **1982**, 104, 2977–2985, (b) J. Moser and M. Grätzel, "Light-Induced Electron Transfer in Colloidal Semiconductor Dispersions: Single vs. Dielectronic Reduction of Acceptors by Conduction-Band Electrons", *J. Am. Chem. Soc.*, **1983**, 105, 6547–6555.
80. M. Grätzel and A. J. Frank, "Interfacial Electron-Transfer Reactions in Colloidal Semiconductor Dispersions. Kinetic Analysis", *J. Phys. Chem.*, **1982**, 86, 2964–2967.
81. M. Grätzel and J. Moser, "Multielectron Storage and Hydrogen Generation with Colloidal Semiconductors", *Proc. Natl. Acad. Sci.*, **1983**, 80, 3129–3132.
82. A. I. Krasna, "Acridines, Deazaflavins, and Tris (2,2'-Bipyridine) Ruthenium as Catalysts for Photoreduction of Hydrogen from Organic Compounds", *Photochem. Photobiol.*, **1980**, 31, 75–82.
83. J. R. Darwent, "Photoreduction of Methyl Viologen in Micellar Solutions Sensitized by Zinc Phthalocyanine", *J. Chem. Soc. Chem. Commun.*, **1980**, 17, 805–807.
84. R. J. Crutchley and A. B. P. Lever, "Ruthenium(II) Tris(bipyrazyl) Dication: a New Photocatalyst", *J. Am. Chem. Soc.*, **1980**, 102, 7128–7129.
85. T. Tanno, D. Wöhrle, M. Kaneko and A. Yamada, "Rapid Photoreduction of Methyl Viologen with Visible Light using Metal-Phthalocyanines as Sensitizers", *Ber. Bunsenges. Phys. Chem.*, **1980**, 84, 1032–1034.
86. D. Meisel, W. A. Mulac and M. S. Matheson, "Catalysis of Methyl Viologen Radical Reactions by Polymer-Stabilized Gold Sols", *J. Phys. Chem.*, **1981**, 85, 179–187.
87. I. Okura and N. Kim-Thuan, "Kinetic Studies of Photoinduced Methyl Viologen Reduction with Ruthenium Complexes and Hydrogen Evolution from Water by Hydrogenase", *J. Chem. Soc. Faraday Trans. 1*, **1981**, 77, 1411–1415.
88. A. Harriman, G. Porter, and M. C. Richoux, "Photosensitized Reduction of Water to Hydrogen using Water-Soluble Zinc Porphyrins", *J. Chem. Soc. Faraday Trans. 2*, **1981**, 77, 833–844.
89. J. S. Bus, S. D. Aust, J. E. Gibson, "Superoxide- and Singlet Oxygen-Catalyzed Lipid Peroxidation as a Possible Mechanism for Paraquat (Methyl Viologen) Toxicity", *Biochem. Biophys. Res. Commun.*, **1974**, 58, 749–752.
90. A. G. Evans, N. K. Dodson and N. H. Rees, "Study of Bipyridyl Radical Cations. Part III. Reaction of Paraquat Radical Cation with Oxygen and with Chromic Ions in Methanol", *J.C.S. Perkin II*, **1976**, 859–863.

91. T. W. Ebbesen and G. Ferraudi, "Photochemistry of Methyl Viologen in Aqueous and Methanolic Solutions", *J. Phys. Chem.* **1983**, 87, 3717–3721.
92. G. A. Somorjai and Y. G. Borodko, "Research in Nanosciences – Great Opportunity for Catalysis Science", *Catal. Lett.*, **2001**, 76, 1–5.
93. Z. Ma and F. Zaera, "*Encyclopedia of Inorganic Chemistry*", 2nd ed. King, B. R., Ed. John Wiley & Sons Ltd: West Sussex, **2005**, 3, 1768–1784.
94. M. Che and C. O. Bennett, "The Influence of Particle Size on the Catalytic Properties of Supported Metals", *Adv. Catal.*, **1989**, 36, 55–172.
95. G. C. Bond, "Strategy of Research on Supported Metal Catalysts. Problems of Structure-Sensitive Reactions in the Gas Phase", *Acc. Chem. Res.*, **1993**, 26, 490–495.
96. G. A. Somorjai, "The Structure Sensitivity and Insensitivity of Catalytic Reactions in Light of the Adsorbate Induced Dynamic Restructuring of Surfaces", *Catal. Lett.*, **1990**, 7, 169–182.
97. J.-F. Lambert and M. Che, "The Molecular Approach to Supported Catalysts Synthesis: State of the Art and Future Challenges", *J. Mol. Catal. A: Chem.*, **2000**, 162, 5–18.
98. A. Henglein, P. Mulvaney and T. Linnert, "Chemistry of Ag_n Aggregates in Aqueous Solution: Non-Metallic Oligomeric Clusters and Metallic Particles", *Faraday Discuss.*, **1991**, 92, 31–44.
99. (a) M. I. Litter, "Heterogeneous photocatalysis Transition metal ions in photocatalytic systems", *Applied Catalysis B: Environmental* , **1999**, 23, 89–114. (b) W. Salomons, U. Förstner, P. Mader, "*Heavy Metals, Problems and Solutions*", *Springer: Berlin*, **1995**, 386.
100. H. Reiche, W. W. Dunn and A. J. Bard, "Heterogeneous Photocatalytic and Photosynthetic Deposition of Copper on Titanium Dioxide and Tungsten(VI) Oxide Powders", *J. Phys. Chem.*, **1979**, 83, 2248–2251.
101. M. D. Ward and A. J. Bard, "Photocurrent Enhancement via Trapping of Photogenerated Electrons of Titanium Dioxide Particles", *J. Phys. Chem.*, **1982**, 86, 3599–3805.
102. J.-M. Herrmann, J. Disdier and P. Pichat, "Photoassisted Platinum Deposition on TiO₂ Powder using Various Platinum Complexes", *J. Phys. Chem.*, **1986**, 90, 6028–6034.
103. C. N. Sawyer, P. L. McCarty and G. F. Parkin, "Chemistry for Environmental Engineering", *McGraw-Hill*, New York, **1994**, 10.
104. T. W. Clarkson, "Mercury: Major Issues in Environmental Health", *Environ. Health Perspect*, **1992**, 100, 31–38.

105. K. Tanaka, K. Harada and S. Murata, "Photocatalytic Deposition of Metal Ions onto TiO₂ Powder", *Solar Energy*, **1986**, 36, 159–161.
106. Z. Wang and Q. Zhuang, "Photocatalytic Reduction of Pollutant Hg(II) on Doped WO₃ Dispersion", *Photochem. Photobiol. A*, **1993**, 75, 105–111.
107. (a) H. A. Wiatrowski, S. Das, R. Kukkadapu, E. S. Ilton, T. Barkay and N. Yee, "Reduction of Hg(II) to Hg(0) by Magnetite", *Environ. Sci. Technol.*, **2009**, 43, 5307–5313, (b) W. Salomons, U. Förstner and P. Mader (Eds.), "Heavy Metals, Problems and Solutions", *Springer, Berlin, Heidelberg*, **1995**.
108. M. R. V. Sahyun and N. Serpone, "Primary Events in the Photocatalytic Deposition of Silver on Nanoparticulate TiO₂", *Langmuir*, **1997**, 13, 5082–5088.
109. D. Friedmann, H. Hansing, and D. W. Bahnemann, "Primary Processes During the Photodeposition of Ag Clusters on TiO₂ Nanoparticles", *Z. Phys. Chem.*, **2007**, 221, 329–348.
110. E. Borgarello, R. Harris, N. Serpone, "Photochemical Deposition and Photorecovery of Gold using Semiconductor Dispersions. A Practical Applications of Photo catalysis", *Nouv. J. Chim.*, **1985**, 9, 743.
111. N. Serpone, E. Borgarello, R. Harris, P. Cahill, M. Borgarello, "Photocatalysis over TiO₂ Supported on a Glass Substrate", *Solar Energy Mater.*, **1986**, 14, 121–127.
112. S. O. Obare, T. Ito, and G. J. Meyer, "Multi-Electron Transfer from Heme-Functionalized Nanocrystalline TiO₂ to Organohalide Pollutants", *J. Am. Chem. Soc.*, **2006**, 128, 712–713.
113. (a) R. Gao, A. Safrany and J. Rabani, "Reactions of TiO₂ Excess Electron in Nanocrystallite Aqueous Solutions Studied in Pulse and Gamma-Radiolytic Systems", *Rad. Phys. Chem.*, **2003**, 67, 25–39, (b) Z. Kasarevic-Popovic, D. Behar and J. Rabani, "Role of Excess Electrons in TiO₂ Nanoparticles Coated with Pt in Reduction Reactions Studied in Radiolysis of Aqueous Solutions", *J. Phys. Chem. B*, **2004**, 108, 20291–20295. (c) F. H. Hussein, R. Rudham, "Photocatalytic Dehydrogenation of Liquid Propan-2-ol by Platinized Anatase and other Catalysts", *J. Chem. Soc., Faraday Trans. 1*, **1987**, 2817–2825, (d) D. Behar and J. Rabani, "Kinetics of Hydrogen Production upon Reduction of Aqueous TiO₂ Nanoparticles Catalyzed by Pd⁰, Pt⁰, or Au⁰ Coatings and an Unusual Hydrogen Abstraction; Steady State and Pulse Radiolysis Study", *J. Phys. Chem. B*, **2006**, 110, 8750–8755.

114. K. Aika, L. L. Ban, I. Okura, S. Namba and J. Turkevich, "Chemisorption and Catalytic Activity of a Set of Platinum Catalysts", *J. Res. Inst. Catal., Hokkaido Univ.*, **1976**, 24, 54–64.
115. K. Rajeshwar, "Photoelectrochemistry and the Environment", *J. Appl. Electrochem.*, **1995**, 25, 1067–1082.
116. C. Wang, D. W. Bahnemann and J. K. Dohrmann, "Determination of Photonic Efficiency and Quantum Yield of Formaldehyde Formation in the Presence of Various TiO₂ Photocatalysts", *Water Sci. Technol.*, **2001**, 44, 279–286.
117. N. Serpone, R. Terzian, D. Lawless, P. Kennepohl and G. Sauve, "On the Usage of Turnover Numbers and Quantum Yields in Heterogeneous Photocatalysis", *J. Photochem. Photobiol. A*, **1993**, 73, 11–16.
118. U. Koelle, J. Moser and M. Grätzel, "Dynamics of Interfacial Charge-Transfer Reactions in Semiconductor Dispersions: Reduction of Cobaltoceniumdicarboxylate in Colloidal Titania", *Inorg. Chem.*, **1985**, 24, 2253–2258.
119. (a) P. A. Trudinger, "On the Absorbency of Reduced Methyl Viologen", *Anal. Biochem.*, **1970**, 36, 222. (b) S. Heinen, W. Meyer and L. Walder, "Charge Trapping in Dendrimers with a Viologen Skeleton and a Radial Redox Gradient", *J. Electroanalytical Chem.*, **2001**, 498, 34–43
120. M. Venturi, Q. G. Mulazzani and M. Z. Hoffman, "Radiologically-Induced One-Electron Reduction of Methyl Viologen in Aqueous Solution: Stability of the Radical Cation in Acidic and Highly Alkaline Media", *Radiat. Phys. Chem.*, **1984**, 23, 229–236.
121. C. L. Bird and A. T. Kuhn, "Electrochemistry of the Viologens", *Chem. Soc. Rev.*, **1981**, 10, 49–82.
122. (a) E. Steckhan and T. Kuwana, *Ber. Bunsenges. Phys. Chem.*, **1974**, 78, 253, (b) J. N. Brønsted, "Zur Theorie der chemischen Reaktionsgeschwindigkeit", *Z. Phys. Chem.*, **1922**, 102, 169–207. (c) P. Debye and E. Hückel, "The Theory of Electrolytes. I. Lowering of Freezing Point and Related Phenomena", *Phys. Z.*, **1923**, 24, 185–206, (d) J. A. Nóbrega and F. R. P. Rocha, "Ionic Strength Effect on the Rate of Reduction of Hexacyanoferrate (III) by Ascorbic Acid A Flow Injection Kinetic Experiment", *J. Chem. Ed.*, **1997**, 74, 560–562.
123. G. T. Brown, J. R. Darwent and P. D. I. Fletcher, "Interfacial Electron Transfer in TiO₂ Colloids", *J. Am. Chem. Soc.*, **1985**, 107, 6446–6451.

124. T. Nakahira and M. Grätzel, "Fast Electron Storage with Colloidal Semiconductors Functionalized with Polymeric Viologen", *J. Phys. Chem.*, **1984**, 88, 4006–4010.
125. H. Gerischer and A. Heller, "The Role of Oxygen in Photooxidation of Organic Molecules on Semiconductor Particles", *J. Phys. Chem.*, **1991**, 95, 5261–5267.
126. H. Gerischer and A. Heller, "Photocatalytic Oxidation of Organic Molecules at TiO₂ Particles by Sunlight in Aerated Water", *J. Electrochem. Soc.*, **1992**, 139, 113–118.
127. J. Schwitzgebel, J. G. Ekerdt, H. Gerischer and A. Heller, "Role of the Oxygen Molecule and of the Photogenerated Electron in TiO₂-Photocatalyzed Air Oxidation Reactions", *J. Phys. Chem.*, **1995**, 99, 5633–5638.
128. J. M. Kesselman, G. A. Shreve, M. R. Hoffmann and N. S. Lewis, "Flux-Matching Conditions at TiO₂ Photoelectrodes: is Interfacial Electron Transfer to O₂ Rate-Limiting in the TiO₂-Catalyzed Photochemical Degradation of Organics?" *J. Phys. Chem.*, **1994**, 98, 13385–13395.
129. S. Upadhyaya and D. F. Ollis, "Simple Photocatalysis Model for Photoefficiency Enhancement via Controlled, Periodic Illumination", *J. Phys. Chem. B*, **1997**, 101, 2625–2631.
130. C. Kormann, D. W. Bahnemann, M. R. Hoffmann, "Photocatalytic Production of Hydrogen Peroxides and Organic Peroxides in Aqueous Suspensions of Titanium Dioxide, Zinc Oxide, and Desert Sand", *Environ. Sci. Technol.*, **1988**, 22, 798–806.
131. D. W. Bahnemann, M. Hilgendorff and R. Memming, "Charge Carrier Dynamics at TiO₂ Particles: Reactivity of Free and Trapped Holes", *J. Phys. Chem. B*, **1997**, 101, 4265–4275.
132. F. Shiraishi, T. Nakasako and Z. Hua, "Formation of Hydrogen Peroxide in Photocatalytic Reactions", *J. Phys. Chem. A.*, **2003**, 107, 11072–11081.
133. D. M. Stanbury, "Reduction Potentials Involving Inorganic Free Radicals in Aqueous Solution", *Adv. Inorg. Chem.*, **1989**, 33, 69–138.
134. K. T. Ranjit and B. Viswanathan, "Photocatalytic Reduction of Nitrite and Nitrate Ions to Ammonia on M/TiO₂ Catalysts", *J. Photochem. Photobiol. A*, **1997**, 108, 73–78.
135. K. T. Ranjit, B. Viswanathan and T. K. Varadarajan, "Photocatalytic Reduction of Nitrite and Nitrate Ions over TiO₂ Semiconductors", *J. Mat. Sci. Lett.*, **1996**, 15, 874–877.
136. K. T. Ranjit, T. K. Varadarajan, B. Viswanathan, "Photocatalytic Reduction of Nitrite and Nitrate Ions to Ammonia on Ru/TiO₂ Catalysts", *J. Phys. Chem. A*, **1995**, 99, 67–68.

137. F. Zhang, Y. Pi, J. Cui, Y. Yang, X. Zhang, and N. Guan, "Unexpected Selective Photocatalytic Reduction of Nitrite to Nitrogen on Silver-Doped Titanium Dioxide", *J. Phys. Chem. C*, **2007**, 111, 3756–3761.
138. M. Halmann and K. Zuckerman, "Nitrite Ion Reduction to Ammonia in Illuminated Aqueous Suspensions of Powdered Semiconductors in Alkaline Sulphide Solutions", *J. Chem. Soc. Chem. Commun.*, **1986**, 455–462.
139. F. Vicente, J. J. Garcia-Jareño, R. Tamarit, A. Cervilla and A. Domenech, "Electrochemical Reduction of the Nitrite to Ammonium Ions in Presence of $[\text{MoO}_2(\text{O}_2\text{CC}(\text{S})\text{C}_6\text{H}_5)_2]^{2-}$ ", *Electrochem. Acta*, **1995**, 40, 1121–1126.
140. B. Douglas, D. H. McDaniel and J. J. Alexander, "Concepts and Model of Inorganic Chemistry", 2nd Ed. Wiley, New Yourk, **1983**.
141. G. Booth, B. McDuel, J. Sears, "Wold of Science", Oxford, **1999**.
142. B. Langea, Z. J. Vejdělek , "Photometrische Analyse", *Verlag Chemie*, Weinheim, **1980**.
143. (a) A. Henglein, "Formation and Absorption Spectrum of Copper Nanoparticles from the Radiolytic Reduction of $\text{Cu}(\text{CN})_2^{2-}$ ", *J. Phys. Chem. B*, **2000**, 104, 1206–1211, (b) R. Suryanarayanan, C. A. Frey, and S. M. L. Sastry, "Deformation, Recovery, and Recrystallization Behavior of Nanocrystalline Copper Produced from Solution-Phase Synthesized Nanoparticles", *J. Mater. Res.*, **1996**, 11, 439–457, (c) P.K. Khanna, S. Gaikwad, P.V. Adhyapak, N. Singh and R. Marimuthu, "Synthesis and Characterization of Copper Nanoparticles", *Mater. Lett.* , **2007**, 61, 4711–4714, (d) A. Henglein and M. Giersig, "Optical and Chemical Observations on Gold-Mercury Nanoparticles in Aqueous Solution", *J. Phys. Chem. B*, **2000**, 104, 5056–5060, (f) J. A. Creighton and D. J. Eadon, *J. Chem. Soc. Faraday Trans.* **1991**, 87, 3881. (g) S. Kapoor, S. Adhikari, C. Gopinathan, and J.P. Mittal, "Radiolytic Production of Metallic Nanoclusters in a Quaternary Microemulsion System", *Mater. Res. Bull.*, **1999**, 34, 1333–1343.
144. (a) D. F. Shriver, P. W. Atkins and C. H. Langford, "Inorganic Chemistry", *University Press*, Oxford, **1990**. (b) A. J. Bard, R. Parsons and J. Jordan, "Standard Potential in Aqueous Solution", *Dekker*, New York, **1985**.
145. (a) P. Mulvaney, "Surface Plasmon Spectroscopy of Nanosized Metal Particles", *Langmuir*, **1996**, 12, 788–800. (b) Y. Sun and Y. Xia, "Shape-Controlled Synthesis of Gold and Silver Nanoparticles", *Science*, **2002**, 298, 2176–2179.

146. Y. Liu, C. Lui, Z. Zhang and C. Wang, "The Surface Enhanced Raman Scattering Effects of Composite Nanocrystals of Ag-TiO₂", *Spectrochem. Acta A*, **2001**, 57, 35–39.
147. M. D. Malinsky, K. L. Kelly, G. C. Schatz and P. Van Duyne, "Chain Length Dependence and Sensing Capabilities of the Localized Surface Plasmon Resonance of Silver Nanoparticles Chemically Modified with Alkanethiol Self-Assembled Monolayers", *J. Am. Chem. Soc.*, **2001**, 123, 1471–1482.
148. D. H. Napper, "Polymeric Stabilization of Colloidal Dispersions"; *Academic Press*, London, **1983**, 414–424.
149. T. G. Schaaf and R. L. Whetten, "Giant Gold-Glutathione Cluster Compounds: Intense Optical Activity in Metal-Based Transitions", *J. Phys. Chem. B*, **2000**, 104, 2630–2641.
150. M. K. Chow and C. F. Zukoski, "Gold Sol Formation Mechanisms: Role of Colloidal Stability", *J. Colloid Interface Sci.*, **1994**, 165, 97–109.
151. G. A. Gaddy, A. S. Korchev, J. L. McLain, J. R. Black, G. Mills, M. Bratcher and B. L. Slaten, "Reversible Formation of Silver Clusters and Particles in Polymer Films", *Proceedings of the 24th Army Science Conference, Orlando, Florida, USA*, **2004**.
152. (a) T. Ung, L. M. Liz-Marzan and P. Mulvaney, "Redox Catalysis Using Ag@SiO₂ Colloids", *J. Phys. Chem. B*, **1999**, 103, 6770–6773, (b) T. Ung, M. Giersig, D. Dunstan and P. Mulvaney, "Spectroelectrochemistry of Colloidal Silver", *Langmuir*, **1997**, 13, 1773–1782.
153. T. HiraKawa and P. V. Kamat, "Charge Separation and Catalytic Activity of Ag@TiO₂ Core-Shell Composite Clusters under UV-Irradiation", *J. Am. Chem. Soc.*, **2005**, 127, 3928–3934.
154. Z.-Y. Huang, G. Mills and B. Hajek, "Spontaneous Formation of Silver Particles in Basic 2-Propanol", *J. Phys. Chem.*, **1993**, 97, 11542–11550.
155. A. Slistan-Grijalva, R. Herrera-Urbina, J. F. Rivas-Silva, M. A'valos-Borja, F. F. Castillo'n-Barraza and A. Posada-Amarillas, "Classical Theoretical Characterization of the Surface Plasmon Absorption Band for Silver Spherical Nanoparticles Suspended in Water and Ethylene Glycol", *Physica E*, **2005**, 27, 104–112.
156. M. K. Chow and C. F. Zukoski, "Gold Sol Formation Mechanisms: Role of Colloidal Stability", *J. Colloid Interface Sci.*, **1994**, 165, 97–109.
157. M. A. El-Sayed, "Some Interesting Properties of Metals Confined in Time and Nanometer Space of Different Shapes", *Acc. Chem. Res.*, **2001**, 34, 257–264.

158. (a) K. Esumi, T. Hosoya, A. Yamahira and K. Torigoe, "Formation of Gold and Silver Nanoparticles in Aqueous Solution of Sugar-Persubstituted Poly(amidoamine) Dendrimers". *J. Colloid Interface Sci.*, **2000**, 226, 346–352.
159. K. Esumi, T. Hosoya, A. Suzuki, and K. Torigoe, "Spontaneous Formation of Gold Nanoparticles in Aqueous Solution of Sugar-Persubstituted Poly (amidoamine) dendrimers", *Langmuir*, **2000**, 16, 2978–2980.
160. D. G. Du., A. Baiker and P. P. Edwards, "A New Hydrosol of Gold Clusters. 2: A Comparison of some Different Measurement Techniques", *Langmuir*, **1993**, 9, 2310–2317, (b) E. Gachard, H. Remita, J. Khatouri, B. Keita, L. Nadjjo and J. Belloni, "Radiation-Induced and Chemical Formation of Gold Clusters", *New J. Chem.*, **1998**, 1257–1265.
161. A. S. Gosh-Mazumdar and E. J. Hart, "A Pulse Radiolysis Study of Bivalent and Zerovalent Gold in Aqueous Solutions", *Adv. Chem. Ser.*, **1968**, 81, 193–209.
162. J. Belloni, J. Amblard, J. L. Marignier and M. Mostafavi, "Clusters of Atoms and Molecules", *ed. H. Haberland, Springer-Verlag, Berlin*, **1994**, 290-311. (b) M. A. Hayat, "Colloidal Gold, Principles, Methods and Applications"; *Academic Press*, New York, **1989**.
163. D. H. Napper, "Polymeric Stabilization of Colloidal Dispersions", *Academic Press*, London, **1983**.
164. T. S. Ahmadi, Z. L. Wang, T. C. Green, A. Henglein and M. A. El-Sayed, "Shape-Controlled Synthesis of Colloidal Platinum Nanoparticles", *Science*, **1996**, 272, 1924–1926.
165. (a) T. G. Schaaf and R. L. Whetten, "Giant Gold-Glutathione Cluster Compounds: Intense Optical Activity in Metal-Based Transitions", *J. Phys. Chem. B*, **2000**, 104, 2630–2641, (b) A. Fernández-Nieves, F. J. de las Nieves and C. Richter, "Point of Zero Charge Estimation for a TiO₂/Water Interface", *Progr. Colloid. Polym. Sci.*, **1998**, 110, 21–24.
166. A. Henglein, "Physicochemical Properties of Small Metal Particles in Solution: "Microelectrode" Reactions, Chemisorption, Composite Metal Particles, and the Atom-to-Metal Transition", *J. Phys. Chem.*, **1993**, 5457–5471.
167. A. Henglein, "Small-Particle Research: Physicochemical Properties of Extremely Small Colloidal Metal and Semiconductor Particles", *Chem. Rev.*, **1989**, 89, 1861–1873.

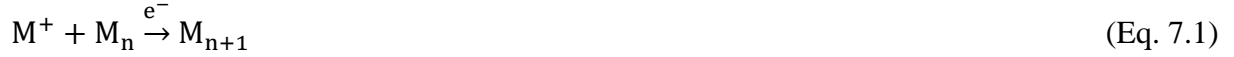
168. B. G. Ershov and N. L. Sukhov, "A Pulse Radiolysis Study of the Process of the Colloidal Metal Formation in Aqueous Solution", *Radiat. Phys. Chem.*, **1990**, 36, 93–97.
169. A. S. Gosh-Mazumdar and E. J. Hart, "A Pulse Radiolysis Study of Bivalent and Zerovalent Gold in Aqueous Solutions", *Adv. Chem. Ser.*, **1968**, 81, 193–209.
170. M. A. Watzky and R. G. Finke, "Transition Metal Nanocluster Formation Kinetic and Mechanistic Studies. A New Mechanism when Hydrogen is the Reductant: Slow, Continuous Nucleation and Fast Autocatalytic Surface Growth", *J. Am. Chem. Soc.*, **1997**, 119, 10382–10400.
171. A. Henglein, "Reduction of $\text{Ag}(\text{CN})_2^-$ on Silver and Platinum Colloidal Nanoparticles", *Langmuir*, **2001**, 17, 2329–2333.
172. T. Shibata, B. A. Bunker, Z. Y. Zhang, D. Meisel, C. F. Vardemann and J. D. Gezelter, "Size-Dependent Spontaneous Alloying of Au–Ag Nanoparticles", *J. Am. Chem. Soc.*, **2002**, 124, 11989–11996.
173. A. Henglein and D. Meisel, "Radiolytic Control of the Size of Colloidal Gold Nanoparticles", *Langmuir*, **1998**, 14, 7392–7396.
174. P. V. Kamat, "Photoinduced Transformations in Semiconductor–Metal Nanocomposite Assemblies", *Pure Appl. Chem.*, **2002**, 74, 1693–1706.
175. T. S. Ahmadi, S. L. Logunov and M. A. El-Sayed, "Picosecond Dynamics of Colloidal Gold Nanoparticles", *J. Phys. Chem.*, **1996**, 100, 8053–8056.
176. A. Henglein and J. Lilie, "Storage of Electrons in Aqueous Solution: the Rates of Chemical Charging and Discharging the Colloidal Silver Microelectrode", *J. Am. Chem. Soc.*, **1981**, 103, 1059–1066.
177. A. Henglein, B. G. Ershov and M. Malow, "Absorption Spectrum and Some Chemical Reactions of Colloidal Platinum in Aqueous Solution", *J. Phys. Chem.*, **1995**, 99, 14129–14136.
178. J. Turkevich, B. C. Stevenson and J. Hilleir, "A Study of the Nucleation and Growth Processes in the Synthesis of Colloidal Gold", *Discuss. Faraday Soc.*, **1951**, 11, 55–75.
179. J. Kimling, M. Maier, B. Okenve, V. Kotaidis, H. Ballot, and A. P. Turkevich "Method for Gold Nanoparticle Synthesis Revisited", *J. Phys. Chem. B*, **2006**, 110, 15700–15707.

180. G. R. Bamwenda, S. Tsubota, T. Nakamura, M. J. Haruta, "Photoassisted Hydrogen Production from a Water-Ethanol Solution: a Comparison of Activities of Au-TiO₂ and Pt-TiO₂", *J. Photochem. Photobiol. A*, **1995**, 89, 177–189.
181. M. von Smoluchowski, "Versuch Einer Mathematischen Theorie der Koagulationshinetik Kolloder Losungen", *Z. Phys. Chem.*, **1917**, 92, 129.
182. (a) E. Adams and B. Michael, "Pulse Radiolysis Investigations of Unimolecular Elimination Reactions in Free Radicals Produced by OH addition to Hydroxybenzenes", *Nature*, **1966**, 211, 293–294. (b) E. Adams and B. Michael, "Pulse Radiolysis of Benzoquinone and Hydroquinone: Semiquinone Formation by Water Elimination from Trihydroxycyclohexadienyl Radicals", *Trans. Faraday. Soc.*, **1967**, 63, 1171–1180.
183. E. J. Land and M. Ebert, "Pulse Radiolysis Studies of Aqueous Phenol Water Elimination from Dihydroxycyclohexadienyl Radicals to form Phenoxy", *Trans. Faraday Soc.*, **1967**, 63, 1181–1190.
184. V. Nadtochenko and J. Kiwi, "Dynamics of Adduct Formation of Hydroquinone under Oxidative Conditions Observed by Laser Spectroscopy", *Chem. Commun.*, **1997**, 41–42.
185. (a) I. V. Renge, I. V. Khudyakov, and M. Ya. Gubergrits, "The interaction of 3-hydroxyphenoxy and 5-methyl-3-hydroxyphenoxy radicals with copper(II) ions", *Russian Chemical Bulletin*, **1979**, 28, 278–281. (b) I. V. Khudyakov, P. P. Levin, M. V. Voevodskaya and V. A. Kuz'min, "Reaction Rate for Oxidation of Neutral p-Benzosemiquinone Radicals with Phenyl Substituents by Copper(II) Compounds", *Russian Chemical Bulletin*, **1979**, 28, 1068–1070.

7. Appendix

7.1. Derivation of the Autocatalytic Model

The autocatalytic growth of metal particles in the association of metal ions and metal nuclei can be expressed by the following reaction:



The rate law of Eq. 7.1 is

$$\frac{d[M_{n+1}]}{dt} = k[M^+][M_n] \quad (\text{Eq. 7.2})$$

where M^+ is the metal ion, M_n is the metal nuclei and M_{n+1} is the metal particle. The solution of Eq. 7.2 is

$$\frac{1}{[M^+]_0 + [M_n]_0} \left\{ \ln \left(\frac{[M^+]_0}{[M^+]_t} \right) + \ln \left(\frac{[M_n]_t}{[M_n]_0} \right) \right\} = kt \quad (\text{Eq. 7.3})$$

Since the concentration of metal particles needed to initiate the autocatalytic reaction ($[M_n]_0$) is very small it can be assumed that $[M_n]_0 \ll [M^+]_0$. Then, Eq. 7.3 reduces to

$$\frac{1}{[M^+]_0} \left\{ \ln \left(\frac{[M^+]_0}{[M^+]_t} \right) + \ln \left(\frac{[M_n]_t}{[M_n]_0} \right) \right\} = kt \quad (\text{Eq. 7.4})$$

According to the principle of mass conversion

$$[M^+]_0 = n[M_n]_\infty \quad (\text{Eq. 7.5})$$

where $[M_n]_\infty$ is the concentration of M particles when all M^+ ions are reduced. Since $n[M_n]_\infty$ is equivalent to the concentration of M^+ ions that have been reduced at time t, it follows that:

$$[M^+]_t = [M^+]_0 - n[M_n]_t = n[M_n]_\infty - n[M_n]_t = n([M_n]_\infty - [M_n]_t) \quad (\text{Eq. 7.6})$$

Therefore, the third term on the left hand side of Eq. 7.1 is equal to:

$$\ln \left(\frac{[M_n]_t}{[M^+]_t} \right) = \ln \left(\frac{1}{n} \right) + \ln \left(\frac{[M_n]_t}{[M_n]_\infty - [M_n]_t} \right) \quad (\text{Eq. 7.7})$$

Using $a = \frac{[M_n]_t}{[M_n]_\infty}$, Eq. 7.7 transform into Eq. 7.8:

$$\ln \left(\frac{[M_n]_t}{[M^+]_t} \right) = \ln \left(\frac{1}{n} \right) + \ln \left(\frac{a}{1-a} \right) \quad (\text{Eq. 7.8})$$

A combination of Eq. 7.4 and Eq. 7.8 give:

$$\frac{1}{[M^+]_0} \ln \left\{ \left(\frac{[M^+]_0}{n[M_n]_0} \right) + \ln \left(\frac{a}{1-a} \right) \right\} = kt \quad (\text{Eq. 7.9})$$

After rearrangement Eq. 7.10 is obtained which is equivalent to Eq. 3.43:

$$\ln \left(\frac{a}{1-a} \right) = (k[M^+]_0)t - \ln \left(\frac{[M^+]_0}{n[M_n]_0} \right) \quad (\text{Eq. 7.10})$$

According to Beer's law:

$$A_t = [M_n]_t \cdot \epsilon \cdot d \quad (\text{Eq. 7.11})$$

where A_t is the optical absorption of the metal particles at time t and ϵ is the extinction coefficient, d is the optical path length.

$$a = \frac{[M_n]_t}{[M_n]_\infty} = A_t/A_\infty \quad (\text{Eq. 7.12})$$

7.2. List of Abbreviations and Symbols

A	Absorbance
A, A⁺	Electron acceptor
CB	Conduction band
c	Concentration
cm	Centimeter
D	Electron donor
D	Diffusion coefficient
d	Particle size
<i>d_{sc}</i>	The dimension of space charge region
E	Light energy
E	Applied voltage or potential
et al.	Latin: et alii (English: and others)
eV	Electron volt
E_{CB}	Conduction band potential
E_F	Fermi level energy
E_g	Band gap energy
E_{redox}	Standard redox potential
E_{VB}	Valance band energy
e⁻_{CB}	Conduction band electron
e⁻_t	Trapped electron
e⁻_{TiO₂}	Electrons on TiO ₂
g	Gram
GC	Gas Chromatograph
h	Planck constant
HR-TEM	High resolution transmission electron microscopy
HOMO	Highest occupied molecular orbital
HPIC	High performance ionic chromatography
h⁺_{VB}	Valance band hole
I	Light intensity after it passes through the sample
IR	Infrared spectra
i. e.	Latin: id est (English: that is)
I₀	Initial light intensity
J	Joule
J₀	Photon flux
k^{obs}	Observed rate constant

k_{ct}	Electrochemical charge transfer rate constant
k_2	Second order rate constant
K	Boltzmann constant
K	Kelvin
l	Liter
LUMO	Lowest unoccupied molecular orbital
M	Molar (moles per liter)
m_0	Electron mass in vacuum
m^*	Effective mass of electron
mbar	Millibar
mM	Milimolar
mg	Milligram
ml	Milliliter
mm	Millimeter
mol	Mole
ms	Millisecond
mW	Milliwatt
MΩ	Mega ohm
N	The number of atoms in one particle
NHE	Normal Hydrogen Electrode
nm	Nanometer
N_A	Avogadro's number
SP	Surface Plasmon
T	Temperature
TCD	Thermal conductivity detector
TEM	Transmission electron microscopy
UV	Ultraviolet light
UV(A)	Ultraviolet light in the range of 315 nm to 380 nm
UV-vis	Ultraviolet and visible light
V	Volt
V	Volume
VB	Valance band
vs.	Versus
W	Watt
XRD	X-ray diffraction
α	reciprocal absorption length

$\Delta\phi_H$	A potential drop of Helmholtz double layer
$\Delta\phi_\infty$	A potential drop across the space charge region
δ	Reaction layer thickness
ε	Extinction coefficient
ζ	Photonic efficiency
θ	Theta
λ	Wavelength
λ_{\max}	Maximum wavelength
μl	Microliter
μs	Microsecond
ν	Frequency
$\rho(x)$	charge density
τ_{tr}	Transit time
\AA	Ångström
$^\circ\text{C}$	Degree Celsius

7.3. List of Tables

Table 3.1: Summary of the extinction coefficient values determined for different TiO ₂ suspensions.....	39
Table 3.2: Second order rate constant values obtained from the half life time at $[MV^{2+}]_0 = 1 \times 10^{-3}$ M and various ionic strengths.....	50
Table 3.3: Summary of rate constants of the reaction of TiO ₂ electrons with different electron acceptors and their corresponding reactions.....	63
Table 3.4: Summary of rate constants of the reaction of TiO ₂ electrons with different metal ions and their corresponding reactions.....	76
Table 3.5: Variation of the amount of H ₂ gas measured after mixing of an aqueous suspension of TiO ₂ electrons (0.9×10^{-4} M) and aqueous Ag ⁺ solution with various of silver ion concentrations at pH 2.7.....	81
Table 3.6: The rate constants of the build-up of SP at 400 nm obtained from the data represented in Figure 3.45.....	87
Table 3.7: The rate constants of the build-up of SP at 400 nm ($[e^-_{TiO_2}] = 2.2 \times 10^{-4}$ M, $2.4 e^-_{TiO_2}/$ particle) and AgClO ₄ solution ($[Ag^+]_0 = 5 \times 10^{-3}$ M) in the absence and the presence of PVA obtained from the data represented in Figure 3.47.....	88
Table 3.8: Rate constants of growth of Au at different concentrations of Au ³⁺ , $e^-_{TiO_2}$ and PVA obtained from the slope of the linear dependency of $\ln(a/(1-a))$ vs. time.....	98
Table 3.9: Summary of the electron transfer rate constants of the reaction of stored TiO ₂ electrons with transition metal ions, their corresponding reactions and the corresponding redox potentials.....	108
Table 3.10: Comparison of produced hydrogen concentrations at different metals and different metal concentrations.....	115

7.4. List of Figures

Figure 1.1: The separation of the energy bands in the molecular system, semiconductor quantum dots and bulk semiconductors.....	3
Figure 1.2: Band edge position of several semiconductors in contact with aqueous electrolyte at pH 1. The lower edge of the conduction band (red color) and upper edge of the valence band (green color) are presented along with the band gap in electron volts. The energy scale is indicated in electron volts using either the normal hydrogen electrode (NHE) or the vacuum level as a reference. ³³	5
Figure 1.3: Origin of surface plasmon resonance due to coherent interaction of the electrons in the conduction band with electromagnetic field, reproduced from reference 42 (b).....	7
Figure 1.4: Fermi level equilibration at bulk semiconductor- metal junction and semiconductor- metal nanocomposite system.....	9
Figure 1.5: Equilibration of semiconductor- metal nanocomposite with redox couple before and after irradiation. Electron storage in metal nanoparticles causes Fermi level to shift closer to conduction band of the semiconductor.....	9
Figure 1.6: Schematic presentation of the photocatalytic processes.....	10
Figure 1.7: Potential distribution at the semiconductor–electrolyte interface. ⁷³	11
Figure 1.8: Charge transfer at the n-type semiconductor–solution interface under illumination. ⁷³	13
Figure 1.9: Charge–carrier transfer at large (<i>left</i>) and small (<i>right</i>) semiconductor particles in the presence of an electron donor D and an acceptor A. ⁷³	14
Figure 1.10: Schematic representation of the general mechanistic steps in heterogeneous photocatalysis on TiO ₂ nanoparticles.....	17
Figure 1.11: Positions of the redox potentials of various metallic couples related to the energy levels of the conduction and valence bands of TiO ₂ (P25). ^{99(a)}	19
Figure 2.1: TiO ₂ preparation from organic- (Titan (IV)-isopropoxid) and inorganic precursor (TiCl ₄).....	26
Figure 2.2: Schematic representation of the stopped flow apparatus set up.....	29
Figure 2.3: Schematic illustration of the stopped flow experiment for the multi-electron transfer reactions induced by stored electrons in TiO ₂ nanoparticles.....	30
Figure 2.4: Schematic representation of the set up of a Nanosecond laser flash photolysis spectrometer.....	32
Figure 3.1: (a) UV–vis absorbance of an aqueous suspension of as prepared TiO ₂ nanoparticles (3 g l ⁻¹), (b) XRD pattern of as-prepared TiO ₂ (blue line), XRD of pure anatase (red line), difference between pure anatase and sample (grey line) , (c) TEM micrograph of as prepared TiO ₂	34

Figure 3.2: (a) Build up of the TiO₂ electron spectrum of a 3.8×10⁻² M deaerated aqueous TiO₂ suspension (freshly prepared) in the presence of 0.02 M methanol at pH 2.3 recorded following different periods of UV irradiation. (b) Change in absorbance at 600 nm as a function of the employed irradiation time.....35

Figure 3.3: Build up of the TiO₂ electron spectrum of a 3.8×10⁻² M deaerated aqueous TiO₂ suspension (aged for 2 weeks) in the presence of 0.02 M methanol at pH 2.3 recorded following different periods of UV irradiation, (a) 100, (b) 200, (c) 250, (d) 400 min.....36

Figure 3.4: Build up of the TiO₂ electrons spectra of a 3.8×10⁻² M deaerated aqueous TiO₂ suspension in the absence of methanol at pH 2.3 recorded following different periods of UV irradiation.....38

Figure 3.5: The dependency of the absorbance change of TiO₂ electrons at 600 nm due to the titration of the stored electrons with different concentration of benzoquinone on BQ concentrations (a) using freshly prepared aqueous TiO₂ suspension and (b) 2 weeks aged TiO₂ suspensions (b). Insets show the final absorbance of stored electrons after their titration with different BQ concentrations.....40

Figure 3.6: Change in concentrations of TiO₂ stored electrons as a function of the employed irradiation time, the concentration data were obtained from the absorbance measurements shown in Figure 3.2 and providing that the average extinction coefficient is 600 M⁻¹s⁻¹.....41

Figure 3.7: (a) Transient absorption spectra measured after 5 ms of mixing a deaerated aqueous suspension of 3.8×10⁻² M TiO₂ molecules (9.2×10⁻⁵ mol TiO₂ particles l⁻¹ loaded with about 7.7 electrons per TiO₂ particle) at pH 2.3, inset shows transient absorbance vs. time signals observed at 600 nm after mixing of an aqueous TiO₂ electrons suspension with deaerated water at pH 2.3 (HCl), (b) Steady state absorbance of a deaerated aqueous TiO₂ electron suspension after 1:1 mixing with deaerated H₂O at pH 2.3 under the identical experimental conditions of (a).....42

Figure 3.8: Steady state UV-vis absorbance spectra of methyl viologen radical (MV^{•+}) and benzyl viologen radical (BV^{•+}) measured after mixing of electrons loaded TiO₂ suspension ([TiO₂] = 9.2×10⁻⁵ mol particles l⁻¹, [e⁻_{TiO₂}] = 1×10⁻⁴ M, ~1 electron/ particle) with an Ar-saturated aqueous solutions of the corresponding dication ([V²⁺] = 1×10⁻³ M) at pH 2.7, the final concentration of viologen radicals calculated from the final absorbance value and the corresponding extinction coefficient values are 9×10⁻⁵ M and 8.5×10⁻⁵ M respectively, for MV^{•+} and BV^{•+} respectively.....44

Figure 3.9: Time profiles of the build-up of methyl viologen radical and benzyl viologen radical absorbance at 600 nm observed upon mixing of electrons loaded TiO₂ suspension ([TiO₂] = 9.2×10⁻⁵ mol particles l⁻¹, [e⁻_{TiO₂}] = 1×10⁻⁴ M, 1 electron/ particle) with an Ar-saturated aqueous solutions of the corresponding dication ([V²⁺] = 1×10⁻³ M) at pH 2.7, the final concentration of viologen radicals calculated from the final absorbance value and the corresponding extinction coefficient values are 9×10⁻⁵ M and 8.6×10⁻⁵ M respectively for MV^{•+} and BV^{•+} respectively.....45

Figure 3.10: Transient absorption spectra measured after various time of mixing of an Ar-saturated aqueous solution of methyl viologen dication (1×10⁻³ M) with TiO₂ electron

suspension ($[e^-_{TiO_2}] = 1 \times 10^{-4}$ M) at pH 2.7, experimental conditions are identical to that in Figure 3.8 and 3.9.....46

Figure 3.11: Time profiles of the build-up of viologen radicals absorbance at 600 nm observed upon mixing of aqueous suspensions of TiO_2 nanoparticles loaded with electrons ($[TiO_2] = 9.2 \times 10^{-5}$ M (particles), $[e^-_{TiO_2}] = 1 \times 10^{-4}$ M, 1 electron/ particle) with Ar-saturated aqueous solutions containing different concentrations of viologen dication at pH 2.7.....47

Figure 3.12: Linear dependency of the observed first order rate constants on the V^{2+} concentrations. First-order rate constants k^{obs} were determined from the data analysis according to Figure 3.11.....48

Figure 3.13: Time profiles of the formation of methyl viologen radical absorbance at 600 nm observed upon mixing of electrons loaded TiO_2 suspension ($[e^-_{TiO_2}] = 1 \times 10^{-4}$ M) with Ar-saturated methyl viologen dication aqueous solutions (1×10^{-3} M) at different concentration of NaCl at pH 2.7..... 50

Figure 3.14: Effect of ionic strength on the rate of reaction applying limiting Debey-Hückel law (a) and extended Debey-Hückel law (b).....51

Figure 3.15: (a) Time profiles of the formation and decay of the methyl viologen radical absorbance at 600 nm observed upon mixing of electron loaded TiO_2 suspension ($[e^-_{TiO_2}] = 1 \times 10^{-4}$ M) with an Ar-saturated methyl viologen dication aqueous solutions (1×10^{-3} M) at pH 2.7 ($[H^+] = 3.2 \times 10^{-3}$ M) in absence and in presence of different concentrations of gold metal particles, solid lines represent the first order fits. (b) Linear dependency of the concentration of the gold particles on the rate constant of the methyl viologen radical decay at 600 nm, the slope corresponding to $2.6 \times 10^6 M^{-1} s^{-1}$ 52

Figure 3.16: Time profile of the absorbance decay at 600 nm observed after mixing of an electron loaded TiO_2 suspension ($[e^-_{TiO_2}] = 3.7 \times 10^{-4}$ M, $4 e^-_{TiO_2}$ /particles) with an Ar-saturated aqueous colloidal gold solution (6.5×10^{-8} M (particles)). The solid line shows the first order fit.....55

Figure 3.17: Schematic illustration of the electron transfer processes from TiO_2 nanoparticles to the viologen dication forming the viologen radical cation and the ensuing electron transfer from the radical cation to the metal particles forming H_2 gas.....55

Figure 3.18: (a) Time profiles of the decay of the $e^-_{TiO_2}$ absorbance at 600 nm ($[e^-_{TiO_2}] = 5.7 \times 10^{-4}$ M, $6 e^-_{TiO_2}$ /particle) observed upon mixing of their aqueous suspension with different concentration of dissolved O_2 saturated aqueous solutions at pH 2.3 (HCl). The solid lines show the double exponential fits, (b) Linear dependency of the observed first order rate constants on the O_2 concentrations. First-order rate constants determined from the data analysis according to (a).....57

Figure 3.19: (a) Time profiles of the decay of the $e^-_{TiO_2}$ absorbance at 600 nm ($[e^-_{TiO_2}] = 6.9 \times 10^{-4}$ M, $7 e^-_{TiO_2}$ /particle) observed upon mixing of their aqueous suspension with Ar-saturated H_2O_2 aqueous solutions at pH 2.3 (HCl), (b) Linear dependency of the observed first order rate constants on the H_2O_2 concentrations. First-order rate constants determined from the data analysis according to (a).....58

- Figure 3.20:** (a) Time profiles of the decay of $e^-_{\text{TiO}_2}$ absorbance at 600 nm ($[e^-_{\text{TiO}_2}] = 5.5 \times 10^{-4}$ M, $6 e^-_{\text{TiO}_2}/\text{particle}$) observed upon mixing of their aqueous suspension with Argon-saturated aqueous NaNO_3 solutions at pH 2.3, the solid lines show the double exponential fits. (b) Linear dependency of the observed first order rate constants on the NO_3^- concentrations. First-order rate constants determined from the data analysis according to (a).....62
- Figure 3. 21:** Time profile of the decay of $e^-_{\text{TiO}_2}$ absorbance at 600 nm ($[e^-_{\text{TiO}_2}] = 2.5 \times 10^{-3}$ M, $27 e^-_{\text{TiO}_2}/\text{particle}$) observed upon mixing of their aqueous suspension with N_2 saturated aqueous solutions at pH 2.3.....64
- Figure 3.22:** Steady state UV–vis measurements showing the growth of the Cu^0 nanoparticle absorption as indicated from the surface plasmon absorbance with max. at 570 nm after mixing of an aqueous suspension of TiO_2 electrons ($[e^-_{\text{TiO}_2}] = 5.5 \times 10^{-4}$ M, $6 e^-_{\text{TiO}_2}/\text{particle}$) with an Ar- saturated aqueous solution of Cu^{2+} (CuCl_2), $[\text{Cu}^{2+}] = 2.5 \times 10^{-4}$ M, (a) stored TiO_2 electrons before mixing (b) immediately after mixing, (c) after 2 min, (d) after 4 min of mixing with Cu^{2+} ions, (e) after the exposure of the final colloidal metal deposits to air. The light scattering above 400 nm can be attributed to a coagulation of TiO_2 particles.....66
- Figure 3.23:** Time profiles of the decay of the $e^-_{\text{TiO}_2}$ absorbance at 600 nm ($[e^-_{\text{TiO}_2}] = 1.5 \times 10^{-4}$ M, $1.6 e^-_{\text{TiO}_2}/\text{particle}$) observed after mixing of their aqueous suspension with Ar-saturated aqueous CuCl_2 solutions at pH 2.3, solid lines show the first order fits.....67
- Figure 3.24:** Linear dependency of the observed first order rate constants on the Cu^{2+} concentrations. First-order rate constants determined from the data analysis according to Figure 3.23.....68
- Figure 3.25:** Long time scale profile at 570 nm observed after mixing of stored TiO_2 electrons suspension ($[e^-_{\text{TiO}_2}] = 1.5 \times 10^{-4}$ M, $1.6 e^-_{\text{TiO}_2}/\text{particle}$) with deaerated aqueous CuCl_2 solution ($[\text{Cu}^{2+}] = 1 \times 10^{-3}$ M) at pH 2.3, solid line shows data fitting..... 68
- Figure 3.26:** Time resolved absorption spectra measured at different time after 1:1 mixing of stored TiO_2 electrons suspension ($[e^-_{\text{TiO}_2}] = 1.5 \times 10^{-4}$ M, $1.6 e^-_{\text{TiO}_2}/\text{particle}$) with deaerated aqueous CuCl_2 solution ($[\text{Cu}^{2+}] = 1 \times 10^{-3}$ M) at pH 2.3.....69
- Figure 3.27:** Time profile of the decay of the SP absorbance of copper particles observed at 570 nm after 1:1 mixing of oxygen saturated aqueous solution with an aqueous solution of Cu/TiO_2 which was prepared in advance by mixing of 2.5×10^{-4} M CuCl_2 with an aqueous suspension of 5.5×10^{-4} M $e^-_{\text{TiO}_2}$69
- Figure 3.28:** Steady state UV–vis measurements showing the growth of the Hg^0 nanoparticles as indicated from its absorbance after mixing of an aqueous suspension of TiO_2 electrons ($[e^-_{\text{TiO}_2}] = 8.3 \times 10^{-4}$ M, $9 e^-_{\text{TiO}_2}/\text{particle}$) with an Ar-saturated aqueous solution of HgCl_2 (5×10^{-4} M). (a) Stored TiO_2 electrons before mixing (b) immediately after mixing, (c) after 2 min, (d) after the exposure of the final colloidal metal deposits to air.....69
- Figure 3.29:** Time profiles of the decay of the $e^-_{\text{TiO}_2}$ absorbance at 600 nm ($[e^-_{\text{TiO}_2}] = 1.5 \times 10^{-4}$ M, $1.6 e^-_{\text{TiO}_2}/\text{particle}$), observed after mixing of their aqueous suspension with Ar-saturated

HgCl ₂ aqueous solutions containing different concentrations of Hg ²⁺ at pH 2.3. Solid lines show the single exponential fits.....	71
Figure 3.30: Linear dependency of the observed first order rate constants on the Hg ²⁺ concentrations. First order rate constants determined from the data analysis according to Figure 3.29.....	72
Figure 3.31: Time profile of the absorbance build-up at 420 nm observed upon mixing of an aqueous suspension of TiO ₂ electrons ([e ⁻ _{TiO₂] = 1.5×10⁻⁴ M) with an Ar-saturated HgCl₂ aqueous solution (2×10⁻³ M) at pH 2.3.....}	72
Figure 3.32: Time resolved absorption spectra measured at different time after 1:1 mixing of an aqueous suspension of TiO ₂ electrons ([e ⁻ _{TiO₂] = 1.5×10⁻⁴ M) with an Ar-saturated HgCl₂ aqueous solution (2×10⁻³ M) at pH 2.3.....}	73
Figure 3.33: Steady state UV-vis measurements showing the growth of the Cd ⁰ nanoparticles as indicated from its absorbance after mixing of an aqueous suspension of TiO ₂ electrons ([e ⁻ _{TiO₂] = 5×10⁻⁴ M, 5.5 e⁻_{TiO₂/particle) with an Ar-saturated aqueous solution of Cd(ClO₄)₂ (2×10⁻⁴M). (a) Stored TiO₂ electrons before mixing (b) after 1 min, (c) after 2 min, (d) after the exposure of the final colloidal metal deposits to air.....}}	74
Figure 3.34: Time profiles of the decay of e ⁻ _{TiO₂ ([e⁻_{TiO₂] = 2.5×10⁻⁴ M, 2.7 e⁻_{TiO₂/particle) absorbance at 600 nm, upon mixing of their aqueous suspension with deaerated aqueous Cd (ClO₄)₂ solutions containing different concentrations of Cd²⁺, pH 2.3.....}}}	75
Figure 3.35: Linear dependency of the observed first order rate constants on the Cd ²⁺ concentrations. First order rate constants determined from the data analysis according to Figure 3.34.....	75
Figure 3.36: Build-up of the transient absorbance at 420 nm showing the growth of Cd ⁰ clusters observed after mixing of stored TiO ₂ electrons suspension ([e ⁻ _{TiO₂] = 2.5×10⁻⁴ M, 2.7 e⁻_{TiO₂/particle) with deaerated aqueous Cd(ClO₄)₂ solutions ([Cd²⁺] = 2×10⁻³ M) at pH 2.3, solid line shows first order data fitting.....}}	76
Figure 3.37: Steady state UV-vis measurements of the growth of the Ag ⁰ nanoparticles as indicated from the evolution of the surface plasmon absorbance with a maximum at 400 nm after mixing of electrons loaded TiO ₂ ([e ⁻ _{TiO₂] = 1.2×10⁻³ M, 13 e⁻_{TiO₂/particle) with an Ar-saturated AgClO₄ aqueous solution ([Ag⁺] = 1×10⁻⁴ M) at pH 2.7 and the effect of O₂ on the formed Ag⁰ particles.....}}	79
Figure 3.38: Steady state UV-vis absorption spectra recorded after mixing of electrons loaded TiO ₂ suspension ([e ⁻ _{TiO₂] = 1.2×10⁻³ M, 13 e⁻_{TiO₂/particle) with an Ar-saturated AgClO₄ aqueous solution ([Ag⁺] = 1×10⁻⁴ M) in the presence and the absence of PVA (0.5×10⁻³ M) at pH 2.7.....}}	80
Figure 3.39: Change in the absorbance vs. time signals at 600 nm (a) and at 400 nm (b) observed after 1:1 mixing of electrons loaded TiO ₂ suspension ([e ⁻ _{TiO₂] = 9×10⁻⁴ M, 10 e⁻_{TiO₂/particle) with an Ar-saturated AgClO₄ aqueous solution ([Ag⁺] = 2.5×10⁻⁴ M) at pH 2.7.....}}	81

- Figure 3.40:** Time resolved absorption spectra measured at different times after 1:1 mixing of electron loaded TiO₂ suspension ($[e^-_{\text{TiO}_2}] = 9 \times 10^{-4} \text{ M}$, $10 e^-_{\text{TiO}_2}/ \text{particle}$) and an Ar-saturated AgClO₄ aqueous solution ($[\text{Ag}^+] = 2.5 \times 10^{-4} \text{ M}$) at pH 2.7.....82
- Figure 3.41:** Change in the absorbance vs. time signals at 600 nm (a) and at 400 nm (b) observed after 1:1 mixing of electrons loaded TiO₂ suspension ($[e^-_{\text{TiO}_2}] = 2.2 \times 10^{-4} \text{ M}$, $2.4 e^-_{\text{TiO}_2}/ \text{particle}$) with an Ar-saturated AgClO₄ aqueous solution ($[\text{Ag}^+] = 5 \times 10^{-3} \text{ M}$) at pH 2.7.....84
- Figure 3.42:** Time resolved absorption spectra measured at different times after 1:1 mixing of electron loaded TiO₂ suspension ($[e^-_{\text{TiO}_2}] = 2.2 \times 10^{-4} \text{ M}$, $2.4 e^-_{\text{TiO}_2}/ \text{particle}$) with deaerated aqueous AgClO₄ solution ($[\text{Ag}^+] = 5 \times 10^{-3} \text{ M}$) at pH 2.7.....85
- Figure 3.43:** (a) Changes in the absorbance vs. time signals at 600 nm observed after 1:1 mixing of electrons loaded TiO₂ suspension ($[e^-_{\text{TiO}_2}] = 2.2 \times 10^{-4} \text{ M}$, $2.4 e^-_{\text{TiO}_2}/ \text{particle}$) with Ar-saturated AgClO₄ aqueous solution with different concentrations of Ag⁺ ions, pH 2.7, solid lines present the first order fits. (b) Linear dependency of the observed first order rate constants for phase 1 and 2 on the Ag⁺ concentrations.....86
- Figure 3.44:** (a) Changes in the absorbance vs. time signals at 400 nm observed after 1:1 mixing of electrons loaded TiO₂ suspension ($[e^-_{\text{TiO}_2}] = 2.2 \times 10^{-4} \text{ M}$, $2.4 e^-_{\text{TiO}_2}/ \text{particle}$) with Ar-saturated AgClO₄ aqueous solutions with different concentrations of Ag⁺ ions, pH 2.7. (b) Linear dependency of the observed first order rate constants for phase 1 on the Ag⁺ concentrations.....86
- Figure 3.45:** Autocatalytic plot of $\ln(a/(1-a))$ vs. reaction time using the data obtained in Figure 3.44 (a).....87
- Figure 3.46:** Linear dependency of the observed autocatalytic first order rate constants (phase 2) on the Ag⁺ concentrations, the rate constants data obtained from the autocatalytic fits in Figure 3.45.....88
- Figure 3.47:** Change in the absorbance vs. time signals at 400 nm observed after 1:1 mixing of electrons loaded TiO₂ suspension ($[e^-_{\text{TiO}_2}] = 2.2 \times 10^{-4} \text{ M}$, $2.4 e^-_{\text{TiO}_2}/ \text{particle}$) and AgClO₄ solution ($[\text{Ag}^+]_0 = 5 \times 10^{-3} \text{ M}$) in the absence and the presence of PVA at pH 2.7.....89
- Figure 3.48:** Time resolved absorption spectra measured after 1:1 mixing of electrons loaded TiO₂ suspension ($[e^-_{\text{TiO}_2}] = 5 \times 10^{-4} \text{ M}$, $5.4 e^-_{\text{TiO}_2}/ \text{particle}$) at pH 2.7 and oxygen saturated aqueous AgClO₄ solution ($[\text{Ag}^+] = 3 \times 10^{-4} \text{ M}$). Inset shows the decay of the build-up signals of the plasmon absorbance of silver particles at 420 and 410 nm in absence and presence of oxygen.....90
- Figure 3.49:** Time profile of the decay of the SP absorbance signals observed at 400 nm after 1:1 mixing of oxygen saturated aqueous solution with an aqueous solution of Ag/TiO₂ which was prepared in advance by mixing of $3 \times 10^{-4} \text{ M}$ AgClO₄ with an aqueous suspension of $5 \times 10^{-4} \text{ M } e^-_{\text{TiO}_2}$91
- Figure 3.50:** Steady state UV-vis spectra of the growth of Au⁰ nanoparticles observed after mixing electron loaded TiO₂ aqueous suspension ($1 \times 10^{-3} \text{ M}$, $11 e^-_{\text{TiO}_2}/ \text{particle}$) with Au³⁺ ions from HAuCl₄ ($3 \times 10^{-4} \text{ M}$) at pH 2.2 and the effect of O₂ on the Au⁰ deposits.....94

- Figure 3.51:** Time resolved spectra measured after mixing of an Ar-saturated Au^{3+} solution (3×10^{-4} M) with stored TiO_2 electrons suspension ($[\text{e}^-_{\text{TiO}_2}] = 1 \times 10^{-3}$ M, $11 \text{ e}^-_{\text{TiO}_2}/\text{particle}$) at pH 2.2. Inset shows the transients build-up at the whole wavelength range.....95
- Figure 3.52:** Time profile of the build-up of the absorbance of Au nanoclusters at 540 nm observed after mixing of an Ar-saturated HAuCl_4 solution ($[\text{Au}^{3+}] = 3 \times 10^{-4}$ M) with a stored TiO_2 electrons suspension ($[\text{e}^-_{\text{TiO}_2}] = 1 \times 10^{-3}$ M, $11 \text{ e}^-_{\text{TiO}_2}/\text{particle}$) at pH 2.2. Inset shows the plot of $\ln(a/(1-a))$ vs. time.....96
- Figure 3.53:** Time profiles of the build-up of the absorbance of Au nanoclusters at 540 nm after mixing of Ar-saturated 3×10^{-4} M Au^{3+} solutions with different concentrations of stored TiO_2 electrons suspensions at pH 2.2.....97
- Figure 3.54:** Time profiles of the build-up of the absorbance of Au nanoclusters at 540 nm observed after mixing of an Ar-saturated aqueous HAuCl_4 solutions containing different concentrations of the Au^{3+} ions with 7.5×10^{-4} M of stored TiO_2 electrons suspension ($8 \text{ e}^-_{\text{TiO}_2}/\text{particle}$) at pH 2.2.....98
- Figure 3.55:** Time profiles of the build-up of the absorbance of Au nanoclusters at 540 nm observed after mixing an Ar-saturated aqueous HAuCl_4 solution (3×10^{-4} M) with an aqueous suspension of stored TiO_2 electrons (1×10^{-3} M, $11 \text{ e}^-_{\text{TiO}_2}/\text{particle}$) at pH 2.2 in the absence and in the presence of PVA.....99
- Figure 3.56:** Time profiles of the build-up of the absorbance of Au nanoclusters at 540 nm observed after mixing stored TiO_2 electrons suspension ($[\text{e}^-_{\text{TiO}_2}] = 5 \times 10^{-4}$ M, $5.4 \text{ e}^-_{\text{TiO}_2}/\text{particle}$) with Ar-saturated aqueous HAuCl_4 solutions (2.5×10^{-4} M) at pH 2.2 in the absence and in the presence of oxygen.....100
- Figure 3.57:** Steady state UV-vis spectra show the damping of the spectra of Au nanoclusters with time (time interval is 1 min) observed after mixing of an Ar-saturated aqueous HAuCl_4 solution (1×10^{-4} M) with an aqueous suspension of TiO_2 loaded with electrons ($[\text{e}^-_{\text{TiO}_2}] = 1 \times 10^{-3}$ M, $11 \text{ e}^-_{\text{TiO}_2}/\text{particle}$) at pH 2.2.....101
- Figure 3.58:** Time profiles of the build up and decay of absorbance of Au nanoclusters at 540 nm observed after mixing of Au^{3+} aqueous solution (1×10^{-4} M) with stored TiO_2 electrons suspension (1×10^{-3} M, $11 \text{ e}^-_{\text{TiO}_2}/\text{particle}$) at pH 2.2, solid lines represent the first order fits of the decay signals. The inset shows the same data in the millisecond time scale.....102
- Figure 3.59:** Time resolved spectra measured after mixing of 1×10^{-4} M Au^{3+} solution with 1×10^{-3} M stored TiO_2 electrons suspension ($11 \text{ e}^-_{\text{TiO}_2}/\text{particles}$) at pH 2.2.....102
- Figure 3.60:** XRD patterns for as prepared Au/ TiO_2 and pure TiO_2 . Au (111) and (200) diffraction planes are recognizable in the Au/ TiO_2 sample, while anatase TiO_2 (101) and (200) lattice planes are detectable in the two samples.....104
- Figure 3.61:** (a) STEM dark field micrograph showing gold particles (ca. 5nm diameter) by bright contrast and an agglomerated carpet of smaller TiO_2 nanocrystals (ca. 2-3nm) by grey contrast. (b): HR-TEM micrograph showing (111) lattice fringes of a gold nanocrystal, surrounded by smaller TiO_2 crystallites. (c): SAED pattern of a 560 nm circular specimen area showing two sets of Debye Scherrer rings, as a consequence of crystal structures and crystallite sizes. The rings corresponding to (002) and (111) of Au are relatively narrow. The

rings corresponding to (020) and (011) of TiO ₂ in the anatase modification are relatively broad. (d): Radial intensity distribution of the SAED pattern.....	105
Figure 3.62: Schematic illustration of the deduced mechanism of the formation and growth of gold nanoparticles on TiO ₂ surfaces using stored electrons.....	107
Figure 3.63: Dependency of interfacial electron transfer rates on the driving forces.....	109
Figure 3.64: UV–vis absorption spectra of (a) colloidal platinum and (b) colloidal gold nanoparticles prepared by citrate method (Section 2.3) : 3.4×10 ⁻³ M sodium citrate, 1×10 ⁻³ M metal salt (H ₂ PtCl ₆ , HAuCl ₄).....	110
Figure 3.65: Time profiles of the decay of e ⁻ _{TiO₂} absorbance at 600 nm observed after mixing aqueous suspension of stored TiO ₂ electrons (5×10 ⁻⁴ M, 5.4 e ⁻ _{TiO₂} /particle) with an Ar-saturated water in the absence of metal particles (a), Ar-saturated aqueous colloidal gold solution (5×10 ⁻¹⁰ M (particles)) (b), or colloidal platinum solution (9.1×10 ⁻⁷ M (particles)) (c) at pH 2.5. The solid lines represent the first order fit.....	111
Figure 3.66: Time profiles of the decay of the e ⁻ _{TiO₂} absorbance at 600 nm observed after mixing aqueous suspension of the stored TiO ₂ electrons (5×10 ⁻⁴ M, 5.4 e ⁻ _{TiO₂} /particle) with Ar-saturated aqueous colloidal gold solutions with different metal particles concentrations at pH 2.2.....	113
Figure 3.67: Linear dependency of the observed first order rate constants (obtained from the kinetic analysis of the data in Figure 3.66 and the concentrations of gold metal atoms. The slope = 2.7×10 ⁷ M ⁻¹ s ⁻¹	113
Figure 3.68: Time profiles of the decay of e ⁻ _{TiO₂} absorbance at 600 nm observed after mixing aqueous suspension of stored TiO ₂ electrons (5×10 ⁻⁴ M, 5.4 e ⁻ _{TiO₂} /particle) with (a) an Ar-saturated aqueous colloidal gold solution (5×10 ⁻¹⁰ M (particles)), (b) an Ar-saturated aqueous colloidal platinum solution (9.1×10 ⁻⁷ M (particles)) at different pH, solid lines represent the first order fit.....	114
Figure 3.69: Linear dependency of the observed first order rate constants (obtained from the kinetic analysis of the data in Figure 3.68 and H ⁺ concentrations.....	115
Figure 4.1: Absorption spectra of freshly prepared 2 g l ⁻¹ colloidal TiO ₂ aqueous suspension at pH 2.5.....	118
Figure 4.2: XRD pattern of as-prepared TiO ₂ powder.....	119
Figure 4.3: Transient absorption vs. time signals at 580 nm (a) and 400 nm (b) observed upon laser excitation of a deaerated aqueous suspension of TiO ₂ particles (1.3×10 ⁻⁵ mol particles l ⁻¹) at pH 2.5, absorbed photon concentration is 5×10 ⁻⁵ mol photons l ⁻¹	120
Figure 4.4: Transient absorption spectrum measured at the height of the absorbance signals (25 ns) under the experimental conditions in Figure 4.3.....	121
Figure 4.5: Transient absorption vs. time signals at 560 nm, the inset shows the same data in the ns time scale (a) and 480 nm (b) observed upon laser excitation (λ= 355 nm) of aqueous suspension of TiO ₂ (1.3×10 ⁻⁵ mol particles l ⁻¹) /colloidal gold (5×10 ⁻⁵ M) at pH 2.5, absorbed photon concentration 5×10 ⁻⁵ mol photons l ⁻¹	122

Figure 4.6: Transient absorption spectra measured various time after the laser excitation ($\lambda=355$ nm) of aqueous suspension of TiO_2 (1.3×10^{-5} mol particles l^{-1}) /colloidal gold (4×10^{-8} mol particles l^{-1}) at pH 2.5, absorbed photon concentration 5×10^{-5} mol photons l^{-1}	123
Figure 4.7: (a) Time profiles at 600 nm observed upon laser excitation (355 nm) of the system of TiO_2 (1.3×10^{-5} mol particles l^{-1})/ MV^{2+} at different concentrations of MV^{2+} , absorbed photon concentration is 2×10^{-5} mol photons l^{-1} , pH 2.7, (b) Linear dependency of the observed first order rate constants obtained from the data analysis of the kinetic curves in (a) on the initial concentration of MV^{2+}	124
Figure 4.8: Transient absorption vs. time signals observed at 410 nm upon laser excitation of 1.3×10^{-5} mol particles l^{-1} TiO_2 , 1×10^{-3} M, 5×10^{-5} M HQ at pH 2.5, photon concentration is 5×10^{-5} mol photons l^{-1} . Solid line represents the first order fit.....	126
Figure 4.9: Transient absorption vs. time signals at 600 nm observed upon band gap irradiation (355 nm) of a deaerated aqueous colloidal suspension of 1.3×10^{-5} mol particle l^{-1} TiO_2 containing HQ (5×10^{-4} M) and CuCl_2 (1×10^{-3} M). Photon concentration 5×10^{-5} mol photon l^{-1} . Solid line represents the first order fit.....	127
Figure 4.10: Time-resolved transient absorption spectra recorded after the laser excitation (355 nm) of an aqueous colloidal suspension of 1.3×10^{-5} mol particles l^{-1} TiO_2 containing 5×10^{-4} M hydroquinone and 1×10^{-3} M CuCl_2 , photon concentration 5×10^{-5} mol photons l^{-1} . Inset shows the time profiles observed at the whole wavelength range.....	127
Figure 4.11: Time-resolved transient absorption spectra recorded after the laser excitation (355 nm) of an aqueous colloidal suspension of 1.3×10^{-5} mol particle l^{-1} TiO_2 containing 1×10^{-3} M methanol and 1×10^{-3} M CuCl_2 , photon concentration 5×10^{-5} mol photon l^{-1} . Inset shows the decay observed at 580 nm.....	128
Figure 4.12: (a) Transient absorption vs. time signals at 410 nm observed upon laser excitation of 1.3×10^{-5} mol particle l^{-1} TiO_2 , 1×10^{-3} M CuCl_2 , at different concentrations of HQ, pH 2.5, photon concentration 5×10^{-5} mol photon l^{-1} . (b) Linear dependency of the observed rate constants determined from first order fitting of the build-up at 410 nm as a function of HQ concentrations.....	129
Figure 4.13: Linear dependency of the observed rate constants determined from first order fitting of the decay at 600 nm as a function of Cu^{2+} concentrations.....	130
Figure 4.14: Transient absorption vs. time signals at 410 nm shows the longer time scale decay of the transient radical formed upon band gap excitation of a deaerated aqueous colloidal suspension of 1.3×10^{-5} mol particles l^{-1} TiO_2 containing 5×10^{-4} M HQ and 1×10^{-3} M CuCl_2 . Photon concentration 3×10^{-5} mol photons l^{-1} , inset shows the plot of $\ln(\text{Absorbance})$ vs. time.....	131

7.5. Curriculum Vitae

Personal Information

Name	Hanan Hussein Amin Mohamed
Date of birth	24.12. 1977, Egypt, Gharbia
Gender	Female
Nationality	Egyptian
Marital status	Married, 3 children

Education

2007- present: PhD work (Photocatalysis and Nanotechnology group), Institute of Technical Chemistry, Hannover University.

2001-2003: Master of Science (Physical Chemistry), Helwan University, Cairo, Egypt. Thesis title: "Synthesis and Application of Molecular Sieves as Heterogeneous Catalysts in some Organic Reactions"

1995-1999: Bachelor of Chemistry, Helwan University, Cairo, Egypt. Major: General Chemistry. Cumulative GPA: 87.34 % (Excellent with honor degree).

Juni 1995: Graduation from High School, Gedda, Saudi Arabia. Cumulative GPA: 94 % (Excellent)

Positions

January 2001- Present: Assistant lecturer at Department of Chemistry, Faculty of Science, Helwan University, Cairo, Egypt.

November 1999- December 2000: Assistant researcher at Department of Microwave Chemistry, Division of Physics, National Research Centre, Dokki, Cairo, Egypt.

Research Experiences and interests

March 2007/current: Kinetics and Mechanism of Charge Carrier Transfer Reactions on TiO₂ Nanoparticles: Stopped Flow and Laser Flash Photolysis Studies (the work have been done at Technical Chemistry Institute, Hannover University, Germany and EPFL, Switzerland).

April 2002- Sep. 2002: Fluorescence Spectroscopic Studies on the Energy Transfer between Coupled Chromophors (The work have been done at Physical Chemistry Institute, Tübingen University, Germany).

Jan. 2001- 2007: 1- Synthesis and Characterization of Mesoporous Molecular Sieves, MCM-41 by Modern Techniques and Elucidation of their Structures using ²⁹Si and ¹H MAS NMR, ESR and Absorption IR Spectroscopy. 2- Selective Oxidation Reactions of Aromatic

compounds over Metalated MCM-41 in the Presence of H₂O₂ (The work have been done at Physical Chemistry Institute, Helwan University, Cairo, Egypt).

Nov.1999- December 2000: Synthesis and Dielectric Properties of Liquid Crystal Materials (The work have been done at the National Research Center, Egypt).

Teaching Experiences

1999-2001, 2004-2006: Practical courses of Physical Chemistry and Inorganic Chemistry for Undergraduate Students, Helwan University, Cairo, Egypt.

Publications

1. Hanan H. Mohamed, Ralf Dillert and Detlef W. Bahnemann, "Reaction dynamics of the transfer of stored electrons on TiO₂ nanoparticles: a stopped flow study", *J. Photochem. Photobiol. A* , **2011**, 217, 271–274.
2. Hanan H. Mohamed, Cecilia B. Mendive, Ralf Dillert and Detlef W. Bahnemann," Kinetic and Mechanistic Investigations of Multi-Electron Transfer Reactions Induced by Stored Electrons in TiO₂ Nanoparticles: A Stopped Flow Study", *J. Phys. Chem. A*, **2011**, 115, 2139–2147.
3. Hanan H. Mohamed, Ralf Dillert and Detlef W. Bahnemann, "Growth and Reactivity of Silver Nanoparticles on the Surface of TiO₂: A Stopped Flow Study", accepted, *J. Phys. Chem. C*, DOI: 10.1021/jp2031576.
4. Hanan H. Mohamed and Detlef W. Bahnemann, "TiO₂ Nanoparticles as Electron Pools: Single- and Multi-Step Electron Transfer Processes", submitted.
5. Hanan H. Mohamed and Detlef W. Bahnemann, "Kinetic and Mechanistic Investigations of the Light Induced Formation of Gold Nanoparticles on the Surface of TiO₂", submitted.

Scientific Meetings

1. Hanan H. Mohamed, Ralf Dillert and Detlef W. Bahnemann NanoDay des Laboratoriums für Nano- und Quantenengineering (LNQE) on 25 September 2008 Hannover, Germany, Poster Presentation.
2. Hanan H. Mohamed, Ralf Dillert and Detlef W. Bahnemann, Photocatalytic Products and Technologies Conference – PPTC'09 on 11-13 May 2009 Guimaraes, Portugal, Poster Presentation.
3. Hanan H. Mohamed, Ralf Dillert and Detlef W. Bahnemann, XXIV International Conference on Photochemistry (ICP09) on 19-24 July 2009 Toledo, Spain, Poster Presentation.

4. Hanan H. Mohamed and Detlef W. Bahnemann, Reactivity of Nanoparticles for more Efficient and Sustainable Energy Production Summer School on 22-27 August 2009 Sandbjerg Gods, Denmark, Poster Presentation.
5. Hanan H. Mohamed and Detlef W. Bahnemann, NanoDay 2009 des Laboratoriums für Nano- und Quantenengineering (LNQE) on 30 September 2009 Hannover, Germany, Poster Presentation.
6. Hanan H. Mohamed, Julia Stützner, Ralf Dillert and Detlef Bahnemann SP3- Third International Conference on Semiconductor Photochemistry on 12-16 April 2010 Glasgow, Scotland, Poster Presentation.
7. Hanan H. Mohamed and Detlef W. Bahnemann X International Conference on Nanostructured Materials (NANO 2010) on 13-17 September, 2010, Rome, Italy, Oral presentation.
8. Hanan H. Mohamed and Detlef W. Bahnemann, Nano Day 2010 des Laboratoriums für Nano- und Quantenengineering (LNQE) on 30 September 2010 Hannover, Germany, Poster Presentation.
9. Hanan H. Mohamed, Ralf Dillert and Detlef W. Bahnemann. The 15th International Conference on TiO₂ Photocatalysis: Fundamentals and Applications (TiO₂-15) on 15-18 November , 2010, San Diego, California (USA), Poster presentation.